# Two Techniques Produce Slow Antihydrogen

A thesis presented
by

Andrew J. Speck

to
The Department of Physics
in partial fulfillment of the requirements
for the degree of
Doctor of Philosophy
in the subject of

Physics

Harvard University
Cambridge, Massachusetts
May 2005

Thesis advisor

**Gerald Gabrielse**

Author

**Andrew J. Speck**

**Two Techniques Produce Slow Antihydrogen**

# Abstract

Two techniques demonstrated to produce slow antihydrogen bring us closer to the spectroscopic comparison of antihydrogen and hydrogen — a comparison that will require atoms both cold enough to be trapped as well as in their ground-state. Refined accumulation, efficient reutilization, and improved counting techniques allow for the use of larger number of positrons and antiprotons than employed in our previous experiments as well as an accurate determination of the size of the confined plasmas. Two different methods make the positrons and antiprotons interact and form antihydrogen. In the first method radio-frequency drives applied to the antiprotons coax collisions between them and the positrons. Field ionization probes the internal atomic state revealing the first atoms are identified which are too tightly bound to be guiding center atoms. An extension of this method allows us to measure the first slow antihydrogen velocity distribution revealing a higher velocity than expected from a thermal distribution. The second $\overline{\mathrm{H}}$ production method utilizes a two step laser-controlled charge exchange to produce antihydrogen with a predetermined internal state distribution and likely with a low temperature. Confinement of the produced $\overline{\mathrm{H}}$ atoms will require an Ioffe-Pritchard quadrupole magnetic field trap superimposed on the existing axial trapping field which removes the cylindrical symmetry responsible for charged particle confinement in a Penning trap. Preliminary experiments show that charged particles survive more than long enough for the production and trapping of $\overline{\mathrm{H}}$.

# Contents

# List of Figures

# List of Tables

# Papers and Publications

1. *First Laser-Controlled Antihydrogen Production*
   C.H. Storry, A. Speck, D. Le Sage, N. Guise, G. Gabrielse, D. Grzonka, W. Oelert, G. Scheppers, T. Sefzick, J. Walz, H. Pittner, M. Herrmann, T.W. Haensch, D. Comeau, E. A. Hessels, Phys. Rev. Lett. 93, 263401 (2004).

2. *Laser-controlled production of Rydberg positronium via charge exchange collisions*
   A. Speck, C.H. Storry, E.A. Hessels, G. Gabrielse, Phys. Lett. B 597, 257 (2004).

3. *First Measurement of the Velocity of Slow Antihydrogen Atoms*
   G. Gabrielse, A. Speck and C.H. Storry, D. Le Sage, N. Guise, D. Grzonka, W. Oelert, G. Schepers, T. Sefzick, H. Pittner, J. Walz, T.W. Haensch, D. Comeau, E.A. Hessels, Phys. Rev. Lett. 93, 073401 (2004).

4. *First Evidence for Atoms of Antihydrogen Too Deeply Bound to be Guiding Center Atoms*
   G. Gabrielse, A. Speck, C.H. Storry, D. Le Sage, N. Guise, D. Grzonka, W. Oelert, G. Schepers, T. Sefzick, H. Pittner, J. Walz, T.W. Haensch, D. Comeau, E.A. Hessels, Submitted for Publication.

5. *Aperture method to determine the density and geometry of antiparticle plasmas*
   P. Oxley, N.S. Bowden, R. Parrott, A. Speck, C.H. Storry, J.N. Tan, M. Wessels, G. Gabrielse, D. Grzonka, W. Oelert, G. Schepers, T. Sefzick, J. Walz, H. Pittner, T.W. Hänsch, E.A. Hessels, Phys. Lett. B 595, 60 (2004).

6. *Driven Production of Cold Antihydrogen and the First Measured Distribution of Antihydrogen States*
   G. Gabrielse, N.S. Bowden, P. Oxley, A. Speck, C.H. Storry, J.N. Tan, M. Wessels, D. Grzonka, W. Oelert, G. Schepers, T. Sefzick, J. Walz, H. Pittner, T.W. Haensch, E.A. Hessels, Phys. Rev. Lett. 89, 233401 (2002).

7. *Background-Free Observation of Cold Antihydrogen and a Field-Ionization Analysis of Its States*
   G. Gabrielse, N.S. Bowden, P. Oxley, A. Speck, C.H. Storry, J.N. Tan, M. Wessels, D. Grzonka, W. Oelert, G. Schepers, T. Sefzick, J. Walz, H. Pittner, T.W. Haensch, E.A. Hessels, Phys. Rev. Lett. 89, 213401 on line (2002).

8. *Stacking of Cold Antiprotons*
   G. Gabrielse, N.S. Bowden, P. Oxley, A. Speck, C.H. Storry, J.N. Tan, M. Wessels, D. Grzonka, W. Oelert, G. Schepers, T. Sefzick, J. Walz, H. Pittner, T.W. Haensch, E.A. Hessels, Phys. Lett. B 548, 140 (2002).

# Acknowledgments

I am grateful for the opportunity to participate in an exciting and interesting research project. The subject of this thesis, the production and study of antihydrogen, is an endeavor undertaken by the ATRAP collaboration which is composed of scientists from 4 institutions – Harvard University, the IKP Forschungszentrum in Jülich, Germany, the Max-Planck-Institute for Quantum Optics in Garching, Germany, and York University in Toronto, Canada. The help and support from people at these institutions has been in large part responsible for my successes in the last few years.

Firstly I would like to thank my advisor, Jerry Gabrielse, for his support and encouragement. It is through his perseverance and vision that this project has reached the state that it is currently at. As an advisor, he was always willing to discuss current successes and difficulties and to offer advice on the path forward. He was also willing to tolerate my sometimes forceful expression of opinions after long shifts.

I owe a large debt to the efforts of the graduate students who preceded me. Without the many years of work by Peter Yesley, John Estrada, Paul Oxley, and Nathaniel Bowden, the experiment would be in a very different place today. I would also like to thank Paul and Nathaniel for showing me the basics of running the experiment in a mad rush before they graduated and I wish that I had had more time to work with them. I am also indebted to the efforts of the graduate students at Harvard who worked with me on the ATRAP experiment. David LeSage was willing to take over running the experiment when the demands of the long shifts of CERN became too much. In addition, while not at CERN, David, Phil Larochelle, and Nick Guise were willing to handle the day to day annoyances of shipping items to Switzerland and taking care of the other nuisance chores that we are unable to perform at CERN.

Finally, Melissa Wessels was always willing to discuss problems and the design of the next generation experiment while she was still working on the project.

In addition, I had the opportunity to work with several superb postdocs: Cody Storry, Joseph Tan, and Ben Levitt. Cody Storry was around throughout most of my graduate student career and his knowledge and skills both taught me much about how research should be done as well as raised the bar in the design and construction of our pieces of apparatus.

I would also like to thank Jan Ragusa for her willingness to deal with the various financial and other problems I ran into. She was always willing to spend the time to resolve whatever problem I had run into. Jim MacArthur designed countless pieces of electronics for our experiment that always worked as specified and were easy to use. He also was always willing to help me with designing and troubleshooting the various electronic circuits we needed. Lastly I had the pleasure to get to know a number of other graduate students in the Gabrielse lab at Harvard: Brian D'Urso, Brian Odom, David Hanneke, and Dan Farkas amongst them.

The part of the collaboration from Jülich was lead by Walter Oelert along with Dieter Grzonka, Frank Goldenbaum, and Georg Schepers. It is a testament to their skill with detector systems that we rarely had problems with the antiproton detectors and when we did they were able to fix them immediately. Dieter was also willing to lend a helping hand regardless of what was needed. The scientists from the Max Planck Institute at Garching, Heiko Pittner, Max Hermann, and Jochen Walz developed robust laser system that performed well when needed. Hopefully in the future they will be able to employ their skills on the spectroscopy of trapped $\overline{\mathrm{H}}$ atoms, but

while waiting they have provided invaluable help on all parts of the experiment. From York University, Eric Hessels was always willing to discuss and refine experimental ideas as well as to get his hands dirty fixing whatever part of the experiment had broken that time. Daniel Comeau was eager to take on whatever project needed doing regardless of how exciting it was.

My family has been incredibly supportive throughout my education. I would not have been able to reach this point without them and I am grateful for their encouragement to pursue my dreams.

Lastly, Emily Simpson has been a source of tremendous encouragement throughout my graduate student career. She has been around to both celebrate when the experiment was working well as well as to commiserate when it was not.

# Chapter 1

# Introduction

Antihydrogen ($\overline{\mathrm{H}}$), the simplest neutral antimatter atom, is composed of a bound state of a positron ($e^+$) and an antiproton ($\overline{p}$). An antimatter atom inspires many questions. Can antihydrogen atoms be produced? Do they have the same spectrum and energy levels as a hydrogen atom as CPT invariance requires? Do they have the same gravitational and inertial masses and thus experience the same gravitational acceleration as hydrogen atoms as required by the weak equivalence principle? The question of existence was answered by the production of 9 antihydrogen atoms traveling at almost the speed of light at CERN in 1996 [1].

Probing the structure and behavior of these atoms however requires much slower antihydrogen that can be trapped and observed for a long period of time. The nested Penning trap [2] was invented to simultaneously confine antiprotons and positrons at cryogenic temperatures and thus to likely produce $\overline{\mathrm{H}}$ atoms slow enough for a spectroscopic comparison with hydrogen. After the interaction of oppositely charged particles was initially demonstrated with protons and electrons in a nested trap [3]

and then with positrons and antiprotons [4], ATRAP demonstrated positron cooling of antiprotons [5]. Not long after, we [6, 7] and another group [8] proved that antihydrogen was being produced through this technique. The central challenges now facing the further study of antihydrogen atoms are thus two-fold:

1. Ground-state $\overline{\mathrm{H}}$ atoms must be produced
2. $\overline{\mathrm{H}}$ atoms must be produced with a speed low enough to be caught in a neutral atom trap

This work reports on the progress that the ATRAP collaboration has made in the development of two robust techniques for producing cold antihydrogen and our progress towards meeting the two major challenges.

The first $\overline{\mathrm{H}}$ production technique utilizes recombination in a nested Penning trap which simultaneously confines both antiprotons and positrons. After an introduction to our apparatus and particle accumulation methods in Chapters 2 – 4, this work describes in Chapter 5 the further understanding of this production method that we have gained since then. In particular, we have demonstrated a method to measure the speed of slow $\overline{\mathrm{H}}$ atoms. Unfortunately, so far we have measured the mean axial energy to be approximately 200 meV, corresponding to a temperature almost 2 orders of magnitude higher than the hoped for 4.2 K distribution [9]. In addition, we have proved the existence of atoms whose internal radius is less than 0.1 µm, which corresponds to an internal orbit that is no longer described by the simple guiding center atom model used so far for theoretical studies of $\overline{\mathrm{H}}$ formation.

Our ATRAP collaboration recently developed and demonstrated a second method for producing slow antihydrogen atoms [10]. A two-step charge exchange transfers the

binding energy of an excited Rydberg cesium atom ($Cs^*$) to a Rydberg positronium atom ($Ps^*$) and finally to a Rydberg antihydrogen atom ($\overline{H}^*$) [11]. This work reports on the development of the methods necessary to implement this idea in Chapter 6. First came the demonstration of high rate production of positronium through a single charge exchange [12], followed by the detection of $\overline{H}^*$ atoms produced through laser-controlled charge exchange [10].

Both of these techniques require large numbers of stable positrons and antiprotons confined within a cryogenic apparatus. Chapter 2 discusses the Penning trap we use to confine charged particles. Chapter 3 then describes the methods used to accumulate particles into the Penning traps, as well as the techniques used to manipulate antiprotons and positrons into interacting. Chapter 4 reports the methods we use to characterize up to 5 million positrons and 750,000 antiprotons accumulated in the Penning trap as well as the shape of the trapped plasma clouds created by the trapped particles.

Finally, Chapter 7 describes preliminary investigations into the stability of charged particles when placed in the magnetic field of a combined Penning and Ioffe neutral atom trap. This configuration is one possibility for trapping antihydrogen atoms but unfortunately it lacks the cylindrical symmetry of a simple Penning trap. Angular momentum is no longer conserved which removes the core reason for long confinement times of charged antiprotons and positrons within a Penning trap. As the depth of the neutral atom trap is increased the stability of trapped positrons and antiprotons decreases.

The work presented here is the combined effort of many people within the ATRAP

collaboration. As the graduate student primarily responsible for the day to day operation of the Penning trap and associated devices for the last two years, I was heavily involved in the design, implementation, and data taking of almost all of the experiments conducted by ATRAP during this time. This thesis concentrates on those parts in which I was actively involved.

The remainder of this chapter will first describe more fully the motivation for these experiments. This will be followed by a brief review of the antihydrogen recombination processes most likely to be occurring in our experiments.

All the formulas in this thesis will employ SI units unless otherwise specified.

## 1.1 $CPT$ Theorem

Testing the fundamental $CPT$ theorem is a major point of our antihydrogen studies. If this theorem, which is required by any quantum field theory that obeys both Lorentz invariance and locality, is true then the properties of both antihydrogen and hydrogen should be the same. In particular, determining the frequency of the forbidden $1S \rightarrow 2S$ transition in H and $\overline{\mathrm{H}}$ to within its 1.3 Hz natural linewidth allows at least in principle for a determination of the frequency of this transition to 5 parts in $10^{16}$ and then a comparison of the frequencies for both H and $\overline{\mathrm{H}}$ at this level of precision as well.

The $CPT$ theorem states that all physical processes are invariant under a combined charge conjugation, parity inversion, and time reversal. Understanding symmetries similar to $CPT$ in physical laws is a fruitful method to predict which sort of processes are possible, make model independent predictions of reaction dependencies,

| Quantity | $C$ | $P$ | $T$ | $CPT$ |
|---|---|---|---|---|
| Position ($\vec{R}$) | $\vec{R}$ | $-\vec{R}$ | $\vec{R}$ | $-\vec{R}$ |
| Linear Momentum ($\vec{P}$) | $\vec{P}$ | $-\vec{P}$ | $-\vec{P}$ | $\vec{P}$ |
| Angular Momentum ($\vec{J}$) | $\vec{J}$ | $\vec{J}$ | $-\vec{J}$ | $-\vec{J}$ |
| Charge ($Q$) | $-Q$ | $Q$ | $Q$ | $-Q$ |
| Electric Field ($\vec{E}$) | $-\vec{E}$ | $-\vec{E}$ | $\vec{E}$ | $\vec{E}$ |
| Magnetic Field ($\vec{B}$) | $-\vec{B}$ | $\vec{B}$ | $-\vec{B}$ | $\vec{B}$ |

Table 1.1: The effect of $C$, $P$, $T$, and $CPT$ transformations on various physical quantities.

and to put constraints on the forms of possible theories of interactions. Mathematically a symmetry requires that $\Theta H \Theta^{-1} = H$ or equivalently

$$[H, \Theta] = 0 \tag{1.1}$$

where $H$ is the Hamiltonian of the system and $\Theta$ is the symmetry operator. From this definition it follows that the expectation value of the operator of a valid symmetry does not change in time.

While $\Theta$ can be either a continuous or a discrete operator, we will only consider the three primary discrete symmetry operators — charge conjugation, parity inversion, and time reversal [13]. Charge conjugation ($C$) is defined to replace a particle by its antiparticle (reversing the sign of the particle's charge in the process). Parity inversion ($P$) inverts spatial coordinates by taking $\vec{x} \rightarrow -\vec{x}$ as in a three dimensional mirror. This changes the coordinate system between a left-handed one and a right-handed one. The final symmetry operator is time reversal ($T$) which changes $t \rightarrow -t$. A more precise definition of these two operators considers their effect on operators

and other physical quantities as shown in Table 1.1.

Until the 1950's it was widely believed that all physical systems were independently invariant under each of these discrete symmetries. However in 1956, Lee and Wang noticed that this assumption of invariance under $P$ had not been tested experimentally for weak interactions [14]. Shortly thereafter, Wu *et al.* showed that during the $\beta$ decay of polarized $^{60}$Co, the electrons were emitted preferentially in the direction opposite to the nuclear spin [15]. Since under $P$ the momentum of the emitted electrons is reversed but the nuclear spin is the same, parity conservation would require that there be no asymmetry in the direction of the emitted electrons. $P$ is thus not conserved by the weak interaction. Note that this result does not violate $T$ or $CP$ as under $T$ the nuclear spin flips as does the electron's momentum and for $CP$ violation to be observed would require a similar experiment with the antimatter $^{60}$Co in which the result is that the positron is not emitted preferentially with the nuclear spin.

History then repeated itself and most physicists assumed the combined operation, $CP$, was a good symmetry. However, Christenson *et al.* found in 1964 that the $K_2^0$ kaon which has a $CP$ eigenvalue of -1, decayed into 2 $\pi^0$ pions with $CP$ eigenvalue of $+1$. If $CP$ were a valid symmetry this would not be allowed by Eq. 1.1 and thus $CP$ is not conserved in this process.

We now believe that $CPT$ is a valid symmetry for all physical laws. This belief has a more valid basis in that any quantum field theory obeying Lorentz symmetry and locality must be invariant under $CPT$ [16]. However as proved repeatedly, the degree of our belief in a certain symmetry should be determined entirely by the precision of

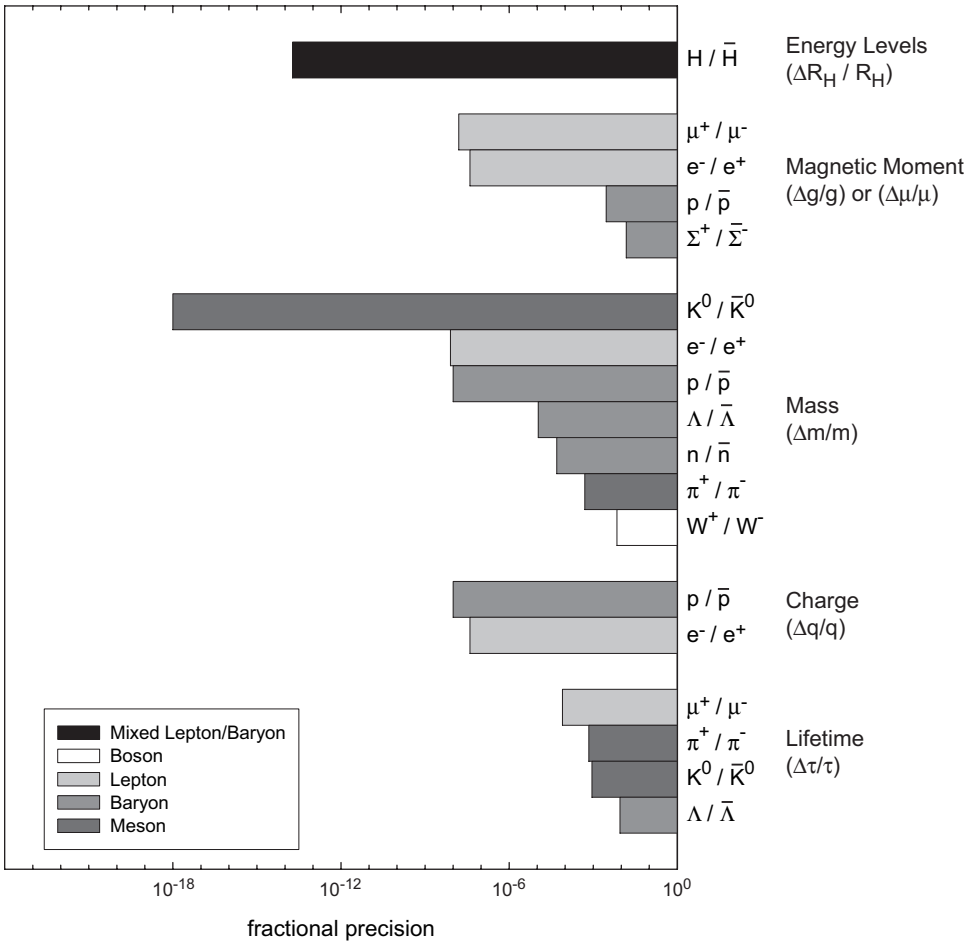


Figure 1.1: Fractional precision of current $CPT$ tests [17]. The estimated value for a future H-$\overline{\text{H}}$ test is based on the best current $1S-2S$ spectroscopy [18].

the experiments supporting that symmetry. We thus must consider what properties should be invariant under the combined $CPT$ operation alone and continue searching for violations of these invariants to either deepen our belief in $CPT$ conservation or reject $CPT$ invariance as a general principle.

$CPT$ invariance requires that all physically valid processes be invariant under the $CPT$ operator. For example for a proton the magnetic moment coupling to the magnetic field, $\mu_{\text{p}}\vec{s}\cdot\vec{B}$, becomes $\mu_{\overline{\text{p}}}(-\vec{s})\cdot\vec{B}$ under the $CPT$ operator as the spin

direction is the only available vector to associate with the magnetic moment. In order for the physical interaction to be invariant we must then have that $\mu_{\mathrm{p}} = -\mu_{\overline{\mathrm{p}}}$. $CPT$ invariance requires in a similar manner that the masses, lifetimes, charges, and magnetic moments of all particle-antiparticle pairs must be equal in magnitude (with the last two opposite in sign). Each of these predictions can be experimentally tested in many different systems. The most precise current $CPT$ invariance measurement compares the difference in mass between the $\mathrm{K}^0$ and $\overline{\mathrm{K}}^0$ relative to their mass though this precision is model dependent. Meson systems are comprised of a bound-state of an antiquark and a quark as opposed to the bound state of three quarks (antiquarks) for baryons (anti-baryons) or the point particle of a lepton and hence are qualitatively different than baryon and lepton systems. It is thus important to increase the precision of the $CPT$ tests for baryons and leptons.

The comparison of hydrogen and antihydrogen will provide an ideal system for improving the precision of the $CPT$ test for baryon and lepton systems. Hydrogen's forbidden $1S \rightarrow 2S$ transition has been measured to 2 parts in $10^{14}$ [18] and a similar precision measurement in antihydrogen should be feasible at least in principle although it will require quite different techniques. The comparison of these two results is equivalent to a comparison of the Rydberg constants for each atom, assuming that the form of the Coulomb interaction remains the same, and would be given by

$$\frac{R_{\overline{\mathrm{H}}}}{R_H} = \frac{\left(1+\frac{m_{\mathrm{e}^-}}{m_{\mathrm{p}}}\right)}{\left(1+\frac{m_{\mathrm{e}^+}}{m_{\overline{\mathrm{p}}}}\right)} \left(\frac{m_{\mathrm{e}^+}}{m_{\mathrm{e}^-}}\right) \left(\frac{q_{\overline{\mathrm{p}}}}{q_{\mathrm{p}}}\right)^2 \left(\frac{q_{\mathrm{e}^+}}{q_{\mathrm{e}^-}}\right)^2 \tag{1.2}$$

If $CPT$ is conserved, then $R_{\overline{\mathrm{H}}}/R_H = 1$. A more detailed consideration of the manner in which the standard model could be extended to include $CPT$ violation also suggests that experiments with $\overline{\mathrm{H}}$ could further constrain the possibilities by which $CPT$ is

violated [19].

## 1.2 Cold Antihydrogen Production Methods

Prior to being able to trap and then spectroscopically study antihydrogen, large number of atoms must be produced. To do so requires several steps. First, the constituent particles, an $\overline{\mathrm{p}}$ and a $\mathrm{e}^+$, must be confined simultaneously in the same region of space. Second, through some collision process energy must be removed from the pair to form an atom in a bound state. It can be shown that to conserve energy and momentum in this process requires a third body to participate in the collision. Finally, through a combination of radiative decay and more collisions, the atom must be de-excited to the ground state.

### 1.2.1 Three-Body Recombination

The highest rate reaction at cryogenic temperatures appears to be the simple three body collisional process [2]

$$\overline{\mathrm{p}} + \mathrm{e}^+ + \mathrm{e}^+ \rightarrow \overline{\mathrm{H}}^* + \mathrm{e}^+ \tag{1.3}$$

where the spare $\mathrm{e}^+$ carries away the excess energy and momentum. The $\overline{\mathrm{H}}^*$ atoms thus formed have an average radius estimated by the classical distance of closest approach, $\rho_{\mathrm{tbd}} = e^2/(4\pi\epsilon_0 k_b T)$, between the positron and the antiproton. For 4.2 K, $\rho_{\mathrm{tbd}} = 4\,\mu\mathrm{m}$, equivalent to an electric field binding the positron and antiproton of only 1 V/cm which is much less than the typical fields in charged particle traps or even those due to the charged particles in the positron plasma. For atoms to survive, the atoms must

decay to a lower radius before experiencing any large electric fields. In particular, atoms whose binding energy exceeds $10k_bT$ (implying that $\rho < 0.4\,\mu\text{m}$) are rarely re-ionized. This decay is enhanced in a positron plasma through the combination of short-range replacement collisions where the bound positron is replaced by a new positron at a shorter radius [20, 21] along with longer range diffusion collisions that gently drive the bound positron to a lower radius [22, 23].

The rate for three-body recombination has been calculated for astrophysical systems in many ways and has been found to scale as $T^{-9/2}$ [24, 25] resulting in a massive rate at 4.2 K if this scaling holds to low temperatures and large magnetic fields [2]. When the effect of a strong magnetic field is included ($B \to \infty$) the stable $\overline{\text{H}}^*$ production rate per antiproton including only replacement collisions is given by [20]

$$\Gamma_{\text{tbd}} = 4 \times 10^{-}10\frac{n_{\text{e}^+}^2}{T^{9/2}} = 60\,\text{s}^{-1} \tag{1.4}$$

for a typical positron density, $n_{\text{e}^+} = 10^7/\,\text{cm}^3$, and $T = 4.2\,\text{K}$. This rate is a factor of 10 less than that predicted for no magnetic field. A later simulation suggests that for $B = 5.3\,\text{T}$, as in our experiments, this rate may increase by another 60 % compared to that when $B \to \infty$ [26]. This enormous rate means that for 200,000 $\overline{\text{p}}$, a $\overline{\text{H}}$ atom should be formed every 100 ns under our conditions.

There are however several caveats to this result. First there have been no experimental confirmations that the $T^{-9/2}$ scaling continues to 4.2 K and furthermore that the calculated magnetic field dependencies are correct. Second, the analytical calculations assumed an infinitely long positron plasma allowing long times for the atoms to reach a binding energy of $10k_bT$. Practical positron plasmas in our traps

have lengths of order 1 mm and thus the recombination process is arrested resulting in a likely slower rate and atoms with smaller binding energies [27]. In addition, combining the two clouds of positrons and antiprotons within a nested Penning trap requires the addition of energy to one species. This will likely raise the temperature of the produced $\overline{\mathrm{H}}$ atoms and make it more difficult to trap and study them.

### 1.2.2 Resonant Charge Exchange

While the production rate for three body recombination is very attractive, the lack of control over the internal state distribution of the $\overline{\mathrm{H}}^*$ means de-excitation to the $1S$ ground state will likely be very difficult. A charge exchange process [28, 29]

$$\mathrm{Ps} + \overline{\mathrm{p}} \rightarrow \overline{\mathrm{H}} + \mathrm{e}^- \tag{1.5}$$

whereby the positronium atom, Ps, resonantly transfers its binding energy to the $\overline{\mathrm{H}}$ atom allows this control through varying the initial state of the Ps atom. This reaction rate is very small for ground state Ps but scales as [11]

$$\sigma_{\overline{\mathrm{H}}} = 58\pi a_0^2 n_{\mathrm{Ps}}^4 \tag{1.6}$$

where $n_{\mathrm{Ps}}$ is the positronium principal quantum number and $a_0 = 0.5\mathring{\mathrm{A}}$ is the Bohr radius. A calculation including a magnetic field suggests that this rate may be a factor of two too high [30]. While the efficiency of this process is smaller than that of three-body recombination due to the solid angle constraints that occur because the positron and antiproton clouds are spatially separated, the combination of a smaller range of states produced as well as a likely slower velocity distribution due to no need

for additional energy to be added to either the positrons or antiprotons may allow this process to produce more $\overline{\mathrm{H}}$ atoms that can be trapped and studied.

### 1.2.3 Comparison of Antihydrogen Recombination Processes

There are many other reactions that have been proposed as a feasible technique to compel an antiproton and a positron to recombine and produce cold antihydrogen. These include using an external electric field to induce recombination [31] which has been attempted by ATRAP but which we were for unknown reasons unable to get to work and the use of a $CO_2$ laser to stimulate the formation of $n \approx 10$ $\overline{\mathrm{H}}$ states [2, 32]. However, three-body recombination and resonant charge exchange are the most likely reactions to have produced the cold antihydrogen observed so far.

Each $\overline{\mathrm{H}}$ formation reaction has its own advantages and disadvantages though. Three-body recombination is a high rate process that will produce large numbers of antihydrogen atoms. However, in a Penning trap three-body recombination requires addition of axial energy to one species to produce spatial overlap thus likely producing higher velocity $\overline{\mathrm{H}}$ atoms. In addition, there is no process that restricts the range of $\overline{\mathrm{H}}$ states produced rendering it more difficult to de-excite the resultant atoms. In comparison, resonant charge exchange will likely produce fewer atoms but they are in a much tighter state distribution and probably have a thermal energy distribution set by the 4.2 K trap environment. Regardless, both three-body recombination and resonant charge exchange have the potential to produce $\overline{\mathrm{H}}$ atoms that are useable for spectroscopy,

# Chapter 2

# Apparatus

In order to produce antihydrogen it is first necessary to confine its constituent charged particles, positrons and antiprotons. The Penning trap, a combination of a static axial magnetic field and electrostatic quadrupole potential, provides the means to do so in a cryogenic environment. This chapter describes our Penning traps and the considerations involved in their design.

## 2.1 Theory

To confine charged particles, we employ a Penning trap which is composed of an axial magnetic bias field, $\vec{B} = B_0\hat{z}$, and a quadrupole electric field, $\phi(\rho, z) = \frac{C_2 V_0}{2d^2}\left(z^2 - \frac{\rho^2}{2}\right)$ where $C_2$ and $d$ are geometrical constants. For a charged particle, the equation of motion in these fields is [33, 34]:

$$m\ddot{\vec{r}} = q\left(-\nabla\phi + B_0\dot{\vec{r}} \times \hat{z}\right) \tag{2.1}$$

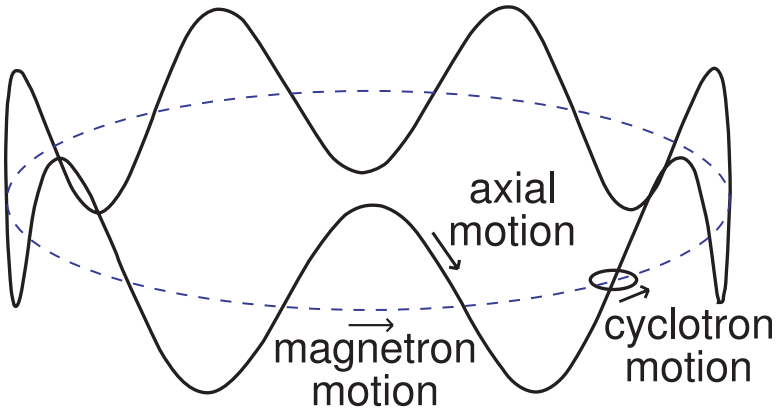


Figure 2.1: Single particles in an ideal Penning trap exhibit three distinct motions.

thus

$$m\ddot{z} = \frac{-qC_2V_0}{d^2}z \tag{2.2a}$$

$$m\ddot{x} = \frac{qC_2V_0}{2d^2}x - qv_yB_0 \tag{2.2b}$$

$$m\ddot{y} = \frac{qC_2V_0}{2d^2}y + qv_xB_0 \tag{2.2c}$$

The axial motion is just a simple harmonic motion with frequency:

$$\omega_z = \sqrt{\frac{qC_2V_0}{md^2}} \tag{2.3}$$

Substituting $u = x + iy$ and the cyclotron frequency, $w_c = \frac{qB_0}{m}$, into the radial equations we find:

$$\ddot{u} + i\omega_c\dot{u} - \frac{1}{2}\omega_z^2 u = 0 \tag{2.4}$$

This is solved by $u = e^{-i\omega_\pm t}$ when:

$$\omega_\pm = \frac{1}{2}\left(\omega_c \pm \sqrt{\omega_c^2 - 2\omega_z^2}\right) \tag{2.5}$$

In order for this to result in confined periodic motion in the radial plane, $\omega_\pm$ must be

| | $e^+$ | $\overline{p}$ |
|---|---|---|
| Magnetic Field | 5.3 T | |
| Trapping Voltage ($V_0$) | -15 V | 15 V |
| Electrode Length ($d$) | 5.11 mm | |
| Magnetron Frequency | 4.5 kHz | 4.5 kHz |
| Axial Frequency | 37 MHz | 860 kHz |
| Cyclotron Frequency | 145 GHz | 80 MHz |

Table 2.1: Typical parameters for particles in our 5.3 T Penning traps.

real giving the trapping requirement:

$$\omega_c \geq \sqrt{2}\omega_z \tag{2.6}$$

In general the radial motion is composed of a superposition of motion at the two frequencies, $\omega_\pm$.

The trapping fields result in the three harmonic motions shown in Fig. 2.1. They are the axial motion, a large magnetron motion at a frequency $\omega_m = \omega_- = \frac{\omega_z^2}{2\omega_c'}$, which can be considered as an $\vec{E} \times \vec{B}$ drift, and a cyclotron motion at the modified cyclotron frequency, $\omega_c' = \omega_+ = \omega_c - \omega_m$. In a standard trap, $\omega_c' \gg \omega_z \gg \omega_m$ which allows each of these motions to be considered as independent. Table 2.1 shows the typical frequencies in one of our Penning traps.

## 2.2 Cylindrical Electrodes in a Penning Trap

A Penning trap can be constructed from electrodes that follow equipotential surfaces of a quadrupole potential. Unfortunately, these surfaces are hyperboloids, as shown in Fig. 2.2a, which creates electrodes that are both difficult to machine to ex-

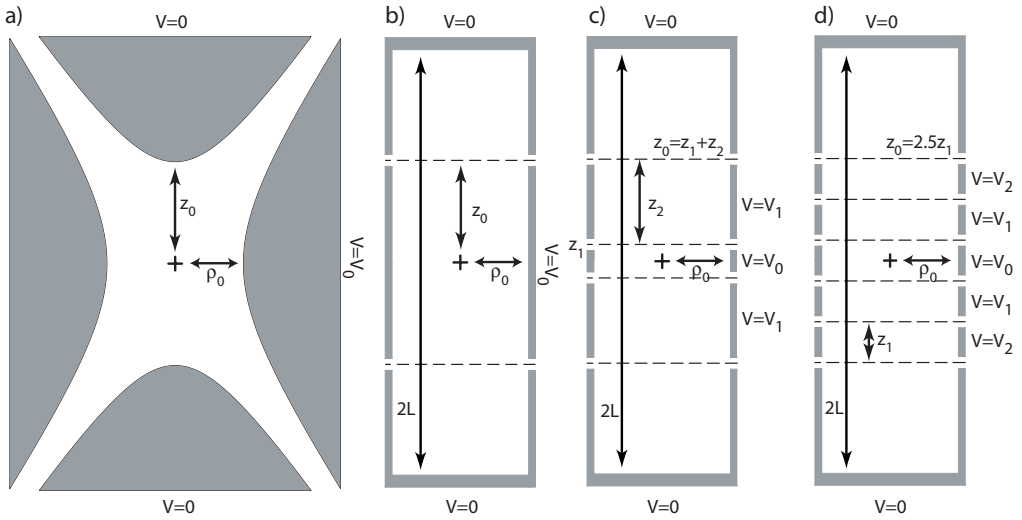


Figure 2.2: (a) Hyperbolic, (b) 3 electrode, (c) 5 electrode, and (d) 5 single length electrode Penning trap geometries and electrode potentials used for calculating the complete symmetric potential within a trap.

acting tolerances and also prevent easy access for injecting particles into the trap. To rectify these problems our Penning traps are constructed out of a stack of cylindrical electrodes [35] resulting in a trap that is open at both ends to allow for particle loading.

To discuss the implications of a cylindrical geometry, we first note that the potential at the center of an axisymmetric Penning trap can be expanded in terms of even Legendre polynomials, $P_j\left(\cos[\theta]\right)$, assuming axial reflection symmetry about the $z = 0$ plane:

$$\phi(\rho, z) = \frac{V_0}{2} \sum_{\substack{j=0 \\ even}}^{\infty} C_j \left(\frac{r}{d}\right)^j P_j\left(\cos[\theta]\right) \tag{2.7}$$

where $d^2 = \frac{1}{2}\left(z_0^2 + \frac{1}{2}\rho_0^2\right)$, $V_0$ is the applied trapping potential, $r^2 = z^2 + \rho^2$, and $z_0$ and $\rho_0$ are defined as in Fig. 2.2. For an ideal quadrupole field $C_{j>2} = 0$, while for cylindrical electrodes the constants $C_n$ are in general not equal to 0.

For an arbitrary cylindrical geometry, it is more convenient to first calculate the

potential using an expansion in terms of modified Bessel functions, $I_0(z)$:

$$\phi(\rho, z) = \sum_{n=0}^{\infty} S_n I_0\left(k_n \rho\right) \cos\left(k_n z\right) \tag{2.8}$$

where

$$k_n = \frac{\left(n + \frac{1}{2}\right)\pi}{L}, \tag{2.9}$$

$$S_n = \frac{2}{I_0\left(k_n \rho_0\right) L} \int_0^L V\left(\rho_0, z\right) \cos\left(k_n z\right) dz, \tag{2.10}$$

$2L$ is the length of the electrode stack, and $V\left(\rho_0, z\right)$ is the potential on the electrodes as a function of axial position. Note that this sum is an approximation for the correct open-endcap electrode expansion due to the closed potential surfaces at the end of the stack. However, a realistic electrode stack can not be infinite and thus must have a defined length, $L$. For the geometry in Fig. 2.2b, we thus have that:

$$S_n = -\frac{2V_0}{k_n L} \frac{\sin\left(k_n z_0\right)}{I_0\left(k_n \rho_0\right)} \tag{2.11}$$

This formalism can then be expanded to the geometry in Fig. 2.2c by defining the total potential as the superposition of the potentials from the individual electrodes, $\phi(\rho, z) = \phi_0(\rho, z) + \phi_1(\rho, z)$ where:

$$\phi_0(\rho, z) = \sum_{n=0}^{\infty} S_n^0 I_0\left(k_n \rho\right) \cos\left(k_n z\right); \qquad S_n^{(0)} = -\frac{2V_0}{k_n L} \frac{\sin\left(k_n z_0\right)}{I_0\left(k_n \rho_0\right)} \tag{2.12}$$

$$\phi_1(\rho, z) = \sum_{n=0}^{\infty} S_n^1 I_0\left(k_n \rho\right) \cos\left(k_n z\right); \qquad S_n^{(1)} = -\frac{2V_1}{k_n L} \frac{\sin\left[k_n\left(z_1 + z_0\right)\right] - \sin\left[k_n z_0\right]}{I_0\left(k_n \rho_0\right)} \tag{2.13}$$

For application to the detection and damping of particles discussed later, the solution to an antisymmetric potential applied to the nearest electrode pair to the

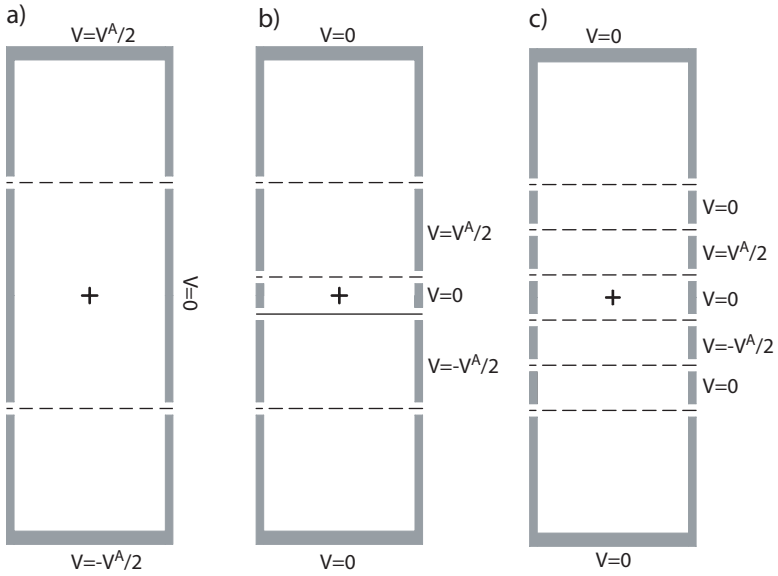


Figure 2.3: (a) 3 electrode, (b) 5 electrode, and (c) 5 single length electrode Penning trap geometries and electrode potentials used for calculating the complete antisymmetric potential within a trap.

center of the trap is useful. In this case, the Legendre polynomial expansion is in terms of odd $j$:

$$\phi_0^A(\rho, z) = 0 \tag{2.14}$$

$$\phi_1^A(\rho, z) = \frac{V_1^A}{2} \sum_{\substack{j=1 \\ odd}}^{\infty} D_j \left(\frac{r}{z_0}\right)^j P_j\left(\cos[\theta]\right) \tag{2.15}$$

The Bessel expansion also slightly changes:

$$\phi_1^A(\rho, z) = \sum_{n=1}^{\infty} A_n^{(1)} I_0\left(a_n \rho\right) \sin\left(a_n z\right) \tag{2.16}$$

where

$$A_n^{(1)} = \frac{2V_1^A}{a_n L} \frac{\cos\left[a_n\left(z_1 + z_0\right)\right] - \cos\left[a_n z_0\right]}{I_0\left(a_n \rho_0\right)} \tag{2.17}$$

$$a_n = \frac{n\pi}{L} \tag{2.18}$$

| | Hyperbolic Trap | 3 electrode trap | | 5 electrode trap | 7 electrode trap |
|---|---|---|---|---|---|
| $\rho_0$ | 6.00 mm | | | | |
| $z_0$ | 5.12 mm | 5.12 mm | 3.00 mm | 5.86 mm | 10.56 mm |
| $z_1$ | ··· | ··· | ··· | 0.97 mm | 4.23 mm |
| $z_2$ | ··· | ··· | ··· | 4.89 mm | ··· |
| $d$ | 4.702 mm | 4.702 mm | 3.674 mm | 5.116 mm | 8.047 mm |
| $\frac{V_1}{V_0}$ | ··· | ··· | ··· | 0.8811 | -0.3856 |
| $\frac{V_2}{V_0}$ | ··· | ··· | ··· | ··· | 0.4830 |
| $C_2$ | 1.0000 | 0.5734 | 0.5092 | 0.5449 | 1.2706 |
| $C_4$ | 0.0000 | 0.0135 | -0.1080 | 0 | 0 |
| $C_6$ | 0.0000 | -0.0486 | 0.0036 | 0 | 0 |
| $C_8$ | 0.0000 | 0.0039 | 0.0061 | -0.0366 | -0.451 |
| $D_1$ | ··· | 0.3738 | 0.3803 | 0.8996 | 1.0171 |

Table 2.2: Expansion coefficients values for several electrode geometries with given potential ratios.

The Bessel function expansion for the symmetric case can be related back to the Legendre expansion in Eq. 2.7 by expanding $\cos(k_n z)$ in powers of $z^k$ and equating these terms with the terms in Eq. 2.7 along the axis ($\rho = 0$):

$$C_j = 2\frac{(-1)^{\frac{j}{2}}}{j!}\sum_{n=0}^{\infty}(k_n d)^j \frac{S_n}{V_0} \tag{2.19}$$

for even $j$. As an ideal trap has $C_{j>2} = 0$ and in many cases only small radiuses, $\rho \ll \rho_0$, need be considered, this is a good expansion to consider as only the lower order terms are non-negligible and the simple goal for the optimum configuration is to minimize all the coefficients $C_{j>2}$. Table 2.2 lists the values of the lower order coefficients for typical trap geometries used in our experiments. The excellent performance of the 5 electrode trap is due to the choice of a specific geometry and potential applied to the compensation electrodes [35].

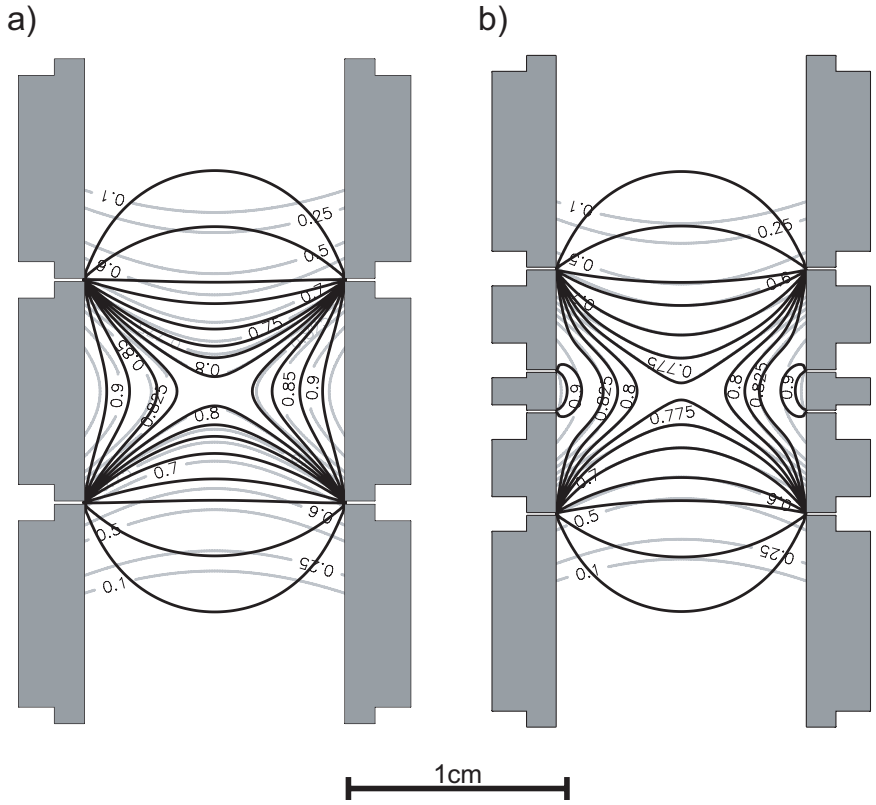


Figure 2.4: Comparison of an ideal quadrupole potential (gray contours) and the actual potential within an electrode (black contours) for two different electrode geometries.

Unfortunately as the number of particles increases, the above formalism becomes less applicable. The effects of space charge within the cloud of particles as well as a cloud radius approaching that of the electrode result in a potential that is no longer described by only the low order terms in the Legendre polynomial expansion (Eq. 2.7). The root difficulty is that while with an infinite number of electrodes one could exactly match the quadratic boundary conditions necessary for a quadrupole potential, practical considerations reduce the fidelity of the actual potentials by limiting the number of electrodes. In addition, while carefully adjusting each electrode length may improve the fidelity of one specific potential configuration, choosing a fixed single electrode geometry for all electrodes results in a much more flexible trap for larger particle numbers.

To avoid the convergence issues at larger radii inherent in the above analytical formalism, all the remaining potential calculations in this thesis have been performed using numerical relaxation on a fixed grid. In this method, Laplace's equation, $\nabla^2 u = 0$, is rewritten as a diffusion equation [36, 37]:

$$\frac{\partial u}{\partial t} = \nabla^2 u \tag{2.20}$$

As $t \to \infty$, $\partial u/\partial t \to 0$ which implies that $u(t = \infty)$ is a solution of Laplace's equation. This equation can be solved by an iterative method where $u_{i+1} = u_i + (\nabla^2 u)\,\Delta t$. To calculate $\nabla^2 u$ we utilize the fact that on an axisymmetric grid with grid points defined by $u_{i,j}$ where $i$ ($j$) is the axial (radial) coordinate and $h_r$ and $h_z$ are the axial and radial grid spacings, Laplace's operator can be discretized as

$$\nabla^2 u_{i,j} = \frac{u_{i-1,j} + u_{i+1,j} + 2u_{i,j}}{h_z^2} + \frac{u_{i,j-1} + u_{i,j+1} + 2u_{i,j}}{h_r^2} + \frac{1}{\rho}\frac{u_{i,j-1} - u_{i,j+1}}{2h_r} \tag{2.21}$$

As this equation contains a singularity at $r = 0$, we replace it by recognizing that

$$\left.\frac{\partial^2 u}{\partial x^2}\right|_{\rho=0} = \left.\frac{\partial^2 u}{\partial y^2}\right|_{\rho=0} = \left.\frac{\partial^2 u}{\partial \rho^2}\right|_{\rho=0} \tag{2.22}$$

so that

$$\nabla^2 u(z, \rho = 0) = \left.\frac{\partial^2 u}{\partial x^2}\right|_{\rho=0} + \left.\frac{\partial^2 u}{\partial y^2}\right|_{\rho=0} + \left.\frac{\partial^2 u}{\partial z^2}\right|_{\rho=0} \tag{2.23}$$

$$= 2\left.\frac{\partial^2 u}{\partial \rho^2}\right|_{\rho=0} + \left.\frac{\partial^2 u}{\partial z^2}\right|_{\rho=0} \tag{2.24}$$

and discretized over the grid of points

$$\nabla^2 u(z, \rho = 0) = \frac{u_{i-1,0} + u_{i+1,0} + 2u_{i,0}}{h_z^2} + 2\frac{2u_{i,1} + 2u_{i,0}}{h_r^2} \tag{2.25}$$

which is no longer infinite at $\rho = 0$.

The final solution is calculated by choosing an initial solution, $u_{i,j}(0)$, defined by the boundary conditions given by the electrode voltages and then using these results to iteratively converge to the true solution, $u_{i,j}$. Through superposition this solution, $\phi_i$, need only be calculated once per electrode with the boundary conditions of 1 V on the particular electrode and 0 V on all other. The potential in the trap is then given by:

$$\phi(\rho, z) = \sum_{i}^{\substack{\text{all} \\ \text{electrodes}}} V_i \phi_i(\rho, z) \tag{2.26}$$

where $V_i$ is the voltage of electrode $i$, and $\phi_i(\rho, z)$ is the solution calculated above for electrode $i$. For more details on the actual software code used for these calculations see Appendix A.

Using this code we can consider the two competing considerations that suggest an optimal choice of electrode geometry to be $\rho_0 \approx z_1$ (*i.e.* the length of the electrode is

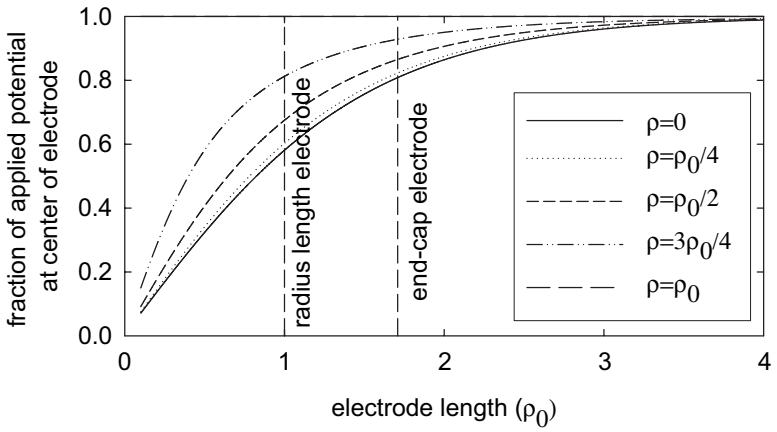


Figure 2.5: The potential at the axial center of an electrode as a function of electrode length and radius off of the axis in terms of the electrode radius $\rho_0$.

the same as its radius). First, as the length of the electrode is reduced the fraction of the potential applied to the electrode surface reaching the center of the electrode becomes smaller (Fig. 2.5). Note that an electrode length of one radius is approximately at the knee of the curves. Second, the fidelity of the quadrupole potential reproduction is reduced as the number of electrodes is reduced. Figure 2.6 shows the fractional deviation of the actual potential relative to an ideal quadrupole potential as the individual electrode length is varied. The standard deviation is calculated over the inner 1 cm of a 5 cm long electrode stack. Here electrode lengths smaller than $\rho_0$ show little advantage. For future traps, a slightly smaller electrode length, $z_l = 0.704\rho_0$, will have an advantage in terms of the ability to minimize low order $C_j$ coefficients [38] as shown in Table 2.2. A harmonic trap is necessary for robust RF counting of the number of particles (Chapter 4) in clouds containing over 1 million $e^+$. From experiments in HBAR2 comparing the particle number counted in a 5 electrode trap with $C_4/C_2 = 0$ to that of a 3 electrode trap with $C_4/C_2 = -0.21$, we found the counts in the 3 electrode trap varied by a factor of 2 depending on how perturbed

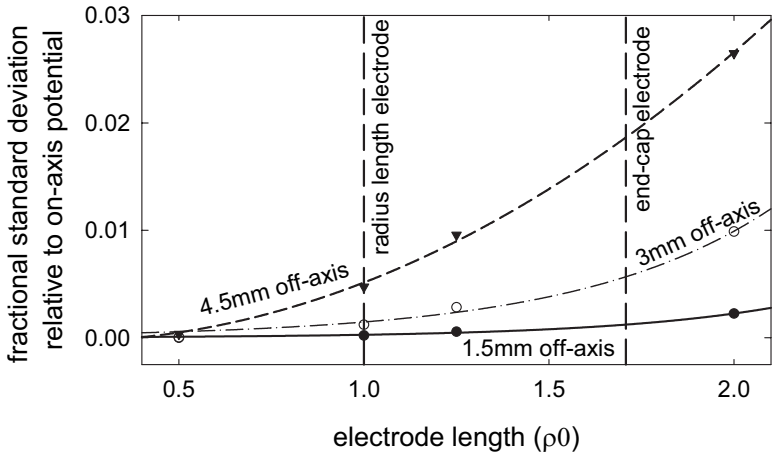


Figure 2.6: The fractional standard deviation relative to an ideal quadrupole potential as a function of electrode length. The curves are just to guide the eye.

the particle cloud had been previously.

## 2.3 Actual Penning Traps

Within the course of this research we used three different Penning trap assemblies. As a detailed description of these traps has been discussed previously [39, 40], I will only provide a cursory description of the essential features.

All the trap assemblies are composed of a series of cylindrical open-ended electrodes enclosed within a sealed vacuum enclosure with 10 µm Ti windows on each end for positron and antiproton loading. The whole assembly is cooled to 4.2 K via thermal contact with a liquid helium dewar. Cryo-pumping within the vacuum enclosure results in a vacuum of better than $5 \times 10^{-17}$ Torr [41] which is equivalent to an antiproton lifetime in the trap of better than 1 month. Above the sealed vacuum enclosure is the liquid helium dewar and a thermal isolation stage consisting of fiber-

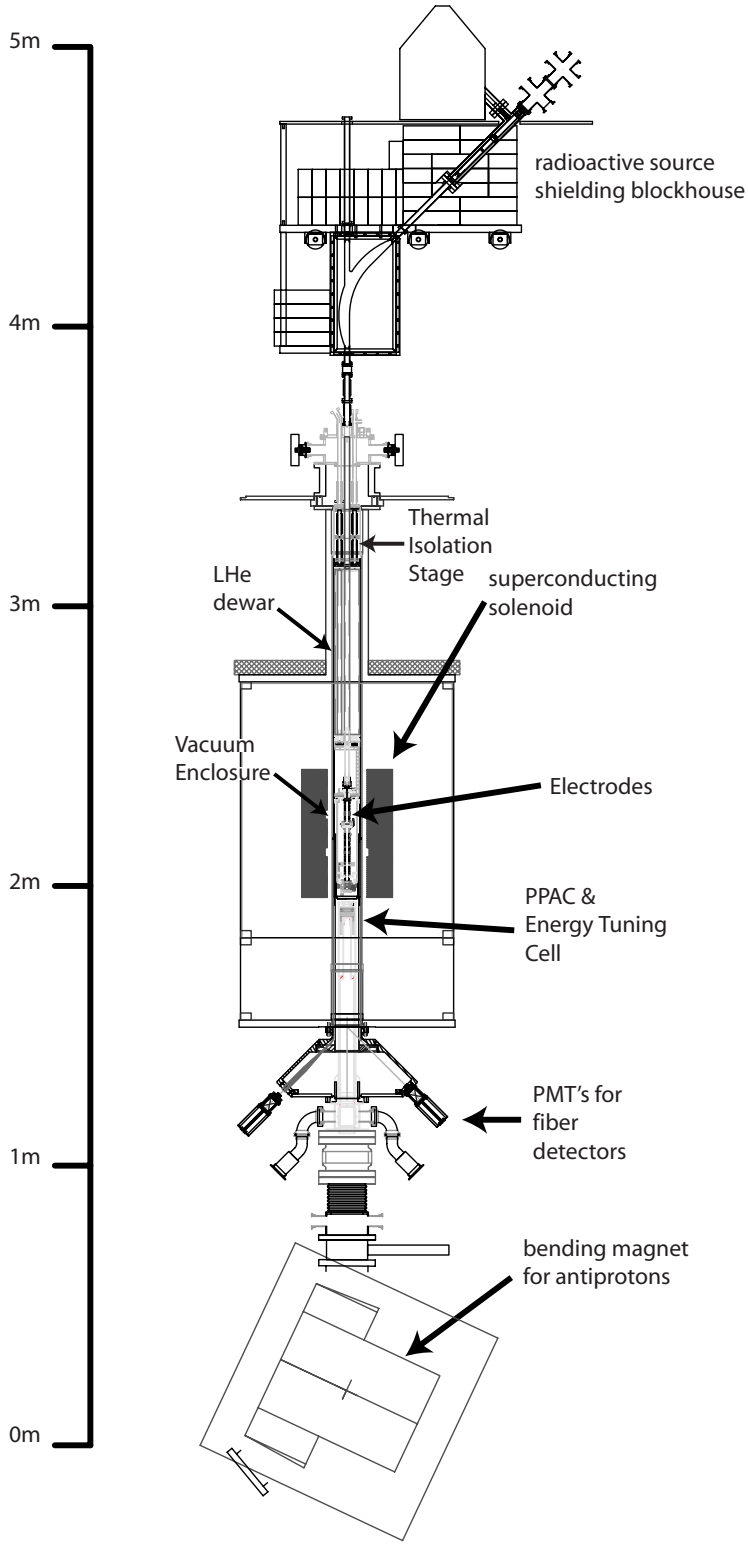


Figure 2.7: The complete experimental system that is employed at CERN.

glass G-10 rods used to reduce thermal conduction from room temperature to the 4.2 K dewar. Finally, at the top of the assembly, is a series of electrical feedthroughs which allow connections to the various circuits within the trap. This complete system is lowered into a superconducting magnet which is normally configured to provide an axial bias field of 5.3 T. Above this system resides a lead shielding system to protect the radioactive source used for positron loading when it is not in use. Below the trap assembly (for those traps used at CERN) is the equipment necessary to reliably inject antiprotons into the Penning trap. Figure 2.7 shows the entire apparatus that is used for our experiments at CERN.

The simplest trap we employed was the Cs-Ps trap that was used only at Harvard University (as distinguished from the HBAR1 and HBAR2 traps to be discussed later). This trap was only capable of loading electrons and positrons and was utilized to test positronium production as discussed in Chapter 6. Figure 2.8 shows the essential features of this trap. It is composed of 14 electrodes and contains a unique electrode ($CS$) for producing the cesium beam necessary for positronium production.

We used two more complex traps (nicknamed HBAR1 and HBAR2) at CERN to produce antihydrogen. These traps are capable of loading positrons, electrons, and antiprotons and both contain on the order of 35 electrodes. Both traps also contain a rotating ball valve [40] to protect the tungsten transmission moderator used for loading positrons from exposure to high energy antiprotons. As discussed later the ball valve contains a secondary reflection moderator and a field emission point for loading electrodes.

While in general the two traps are similar there are several differences between

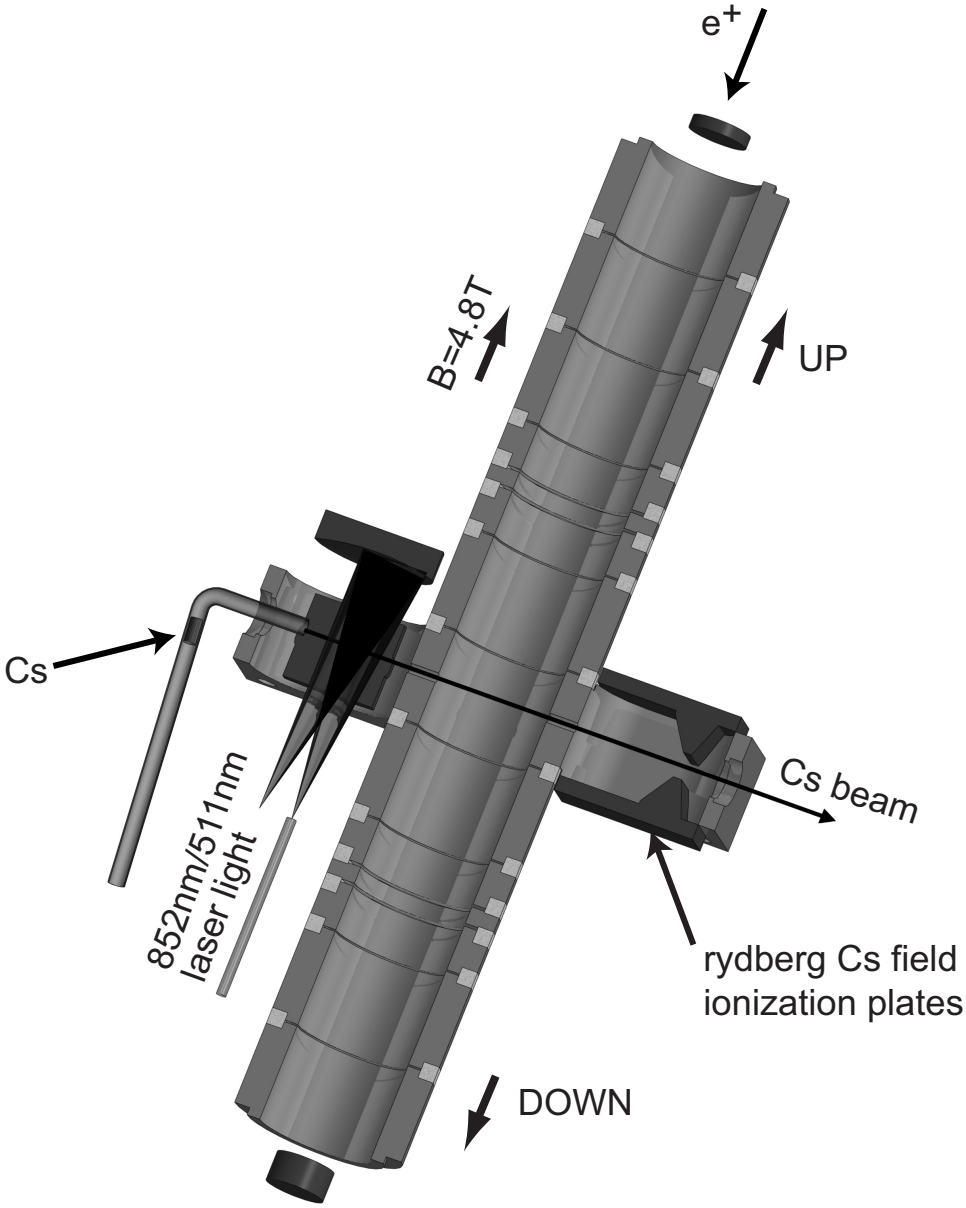


Figure 2.8: The Cesium-Positronium Penning trap used at Harvard.

them. First, HBAR1 (Fig. 2.9) contains a copper ball valve with an aperture whose radius is only 2.5 mm as opposed to the electrode radius of 6 mm. The aperture results in reduced transmission of particles through this region of the trap as particles who have a larger radius than the aperture are clipped off in transit. HBAR2, in contrast, has a ball valve with an opening the same 6 mm radius as the electrodes. This ball valve is constructed out of BeCu for structural stability. Second, the HBAR2 lower trap region has a series of shorter electrodes to allow for more control of the potentials, particularly for experiments utilizing charge exchanges to produce antihydrogen (as discussed in Chapter 6). These electrodes have a length the same as the radius of the trap (6.0 mm) instead of the standard electrode length of 10.1 mm. Finally, HBAR2 has an electrode ($CS$) which is equipped to produce a cesium beam directed through the center of the electrode.

In order to contain and manipulate particles, all the electrode potentials can be adjusted independently through bias circuits. These circuits are heavily filtered to prevent electrical noise from disturbing the trapped particles. In addition, most electrodes have the circuitry necessary to apply either fast voltage pulses or radio-frequency drives to them in order to further manipulate the particle geometry as discussed later in this chapter. The complete wiring diagram for HBAR2 is shown in Fig. 2.11; the wiring for the Cesium-Positronium and HBAR1 traps are essentially similar.

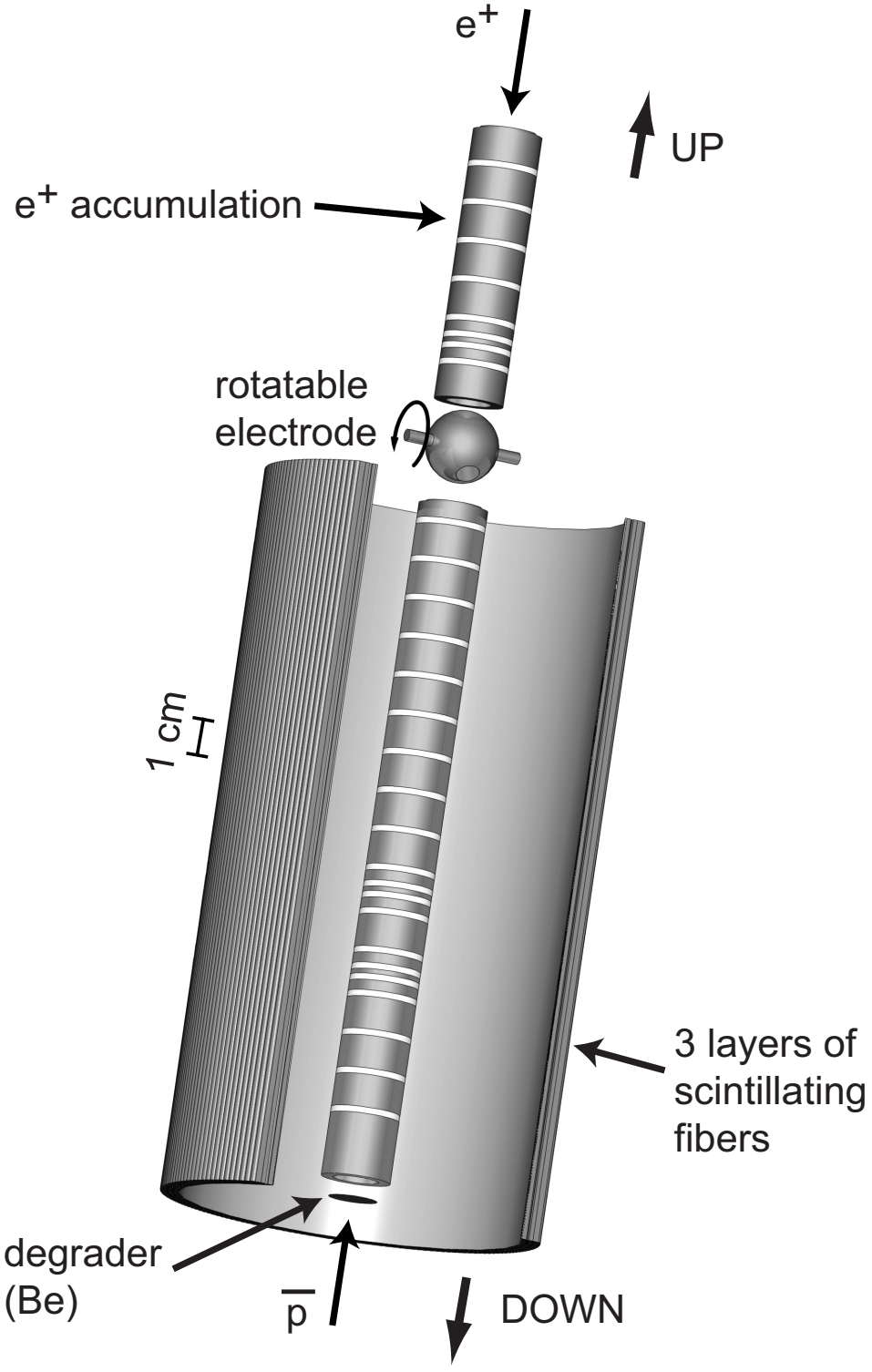


Figure 2.9: The HBAR1 Penning trap as used in 2003 and 2004.

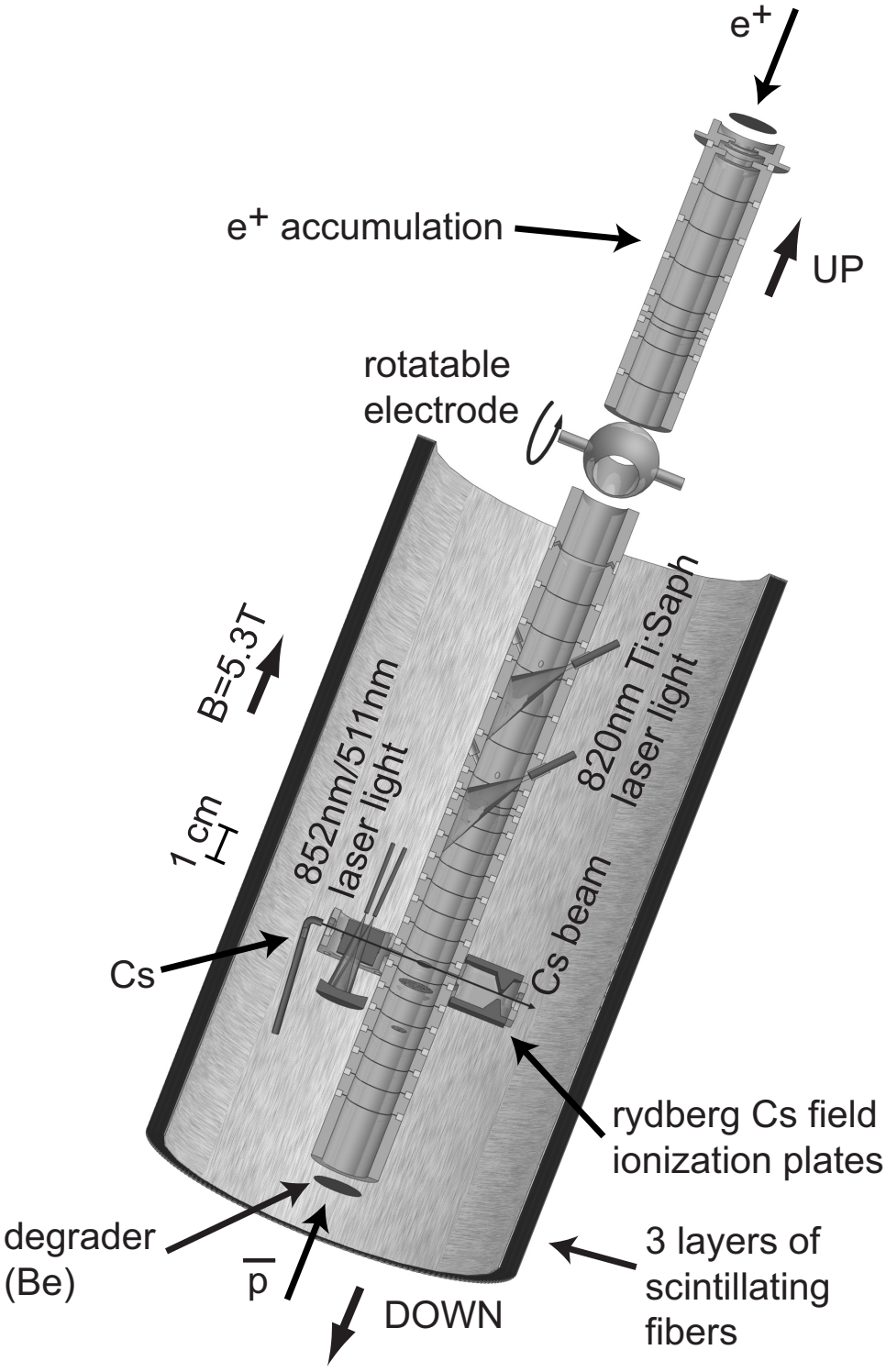


Figure 2.10: The HBAR2 Penning trap as used in 2004.

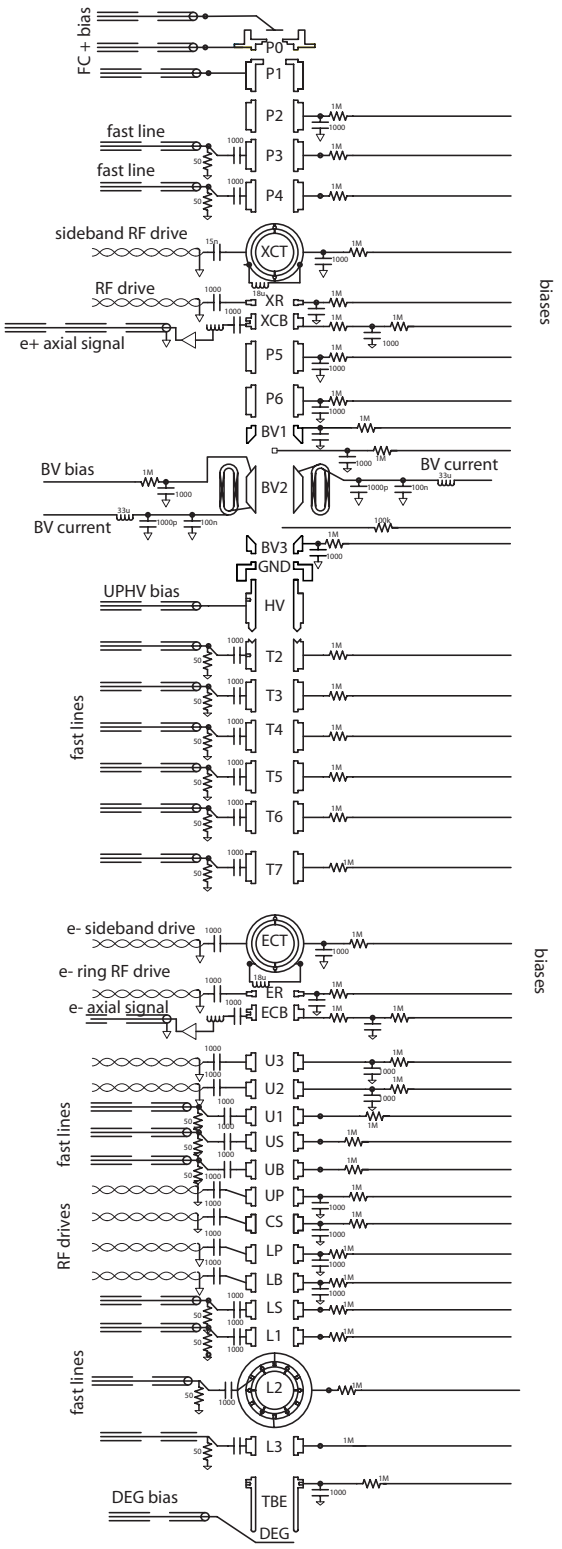


Figure 2.11: Wiring of the HBAR2 trap

# Chapter 3

# Antiproton and Positron Accumulation in a Penning Trap

The previous chapter showed how to accumulate the constituents of antihydrogen. To produce antihydrogen atoms, the accumulated positrons and antiprotons must be coaxed into interacting. This chapter discusses the techniques we use to acquire and manipulate charged particles.

## 3.1 Particle Accumulation

In order to load particles into a well within our Penning traps, some mechanism must be employed to lower the energy of the incoming particles enough to confine them inside the axial potential well. The several different techniques used to accumulate electrons, positrons, and antiprotons are discussed in the next few sections.

### 3.1.1 Electrons

Electrons are quite easy to accumulate in large numbers and are our standard diagnostic tool for testing trap functionality. They are also used to collisionally cool antiprotons as discussed later.

#### Field-Emission Point Loading

The simplest method to load electrons is through the use of a field emission point (FEP) which is in essence a sharp metallic point (in our case it is formed from tungsten wire chemically etched to a fine point). In this technique, a single well for electrons is created (Fig. 3.1a). The field emission point located on the ball valve is then biased to around 700 V. At this potential, an approximately 10 nA beam of electrons is emitted due to the high electric field surrounding the FEP tip. This beam has too high an energy to be directly trapped but it can ionize gas atoms cryo-pumped onto trap surfaces. These ionized electrons are then captured in a potential well located in the center of the electrode stack through collisions with residual gas atoms or already trapped electrons which result in energy loss.

FEP $e^-$ loading has the unfortunate characteristic of being quite variable in both the number of particles loaded as well as in the particle cloud shape. To create a more regulated technique, the potential depth of the well into which the electrons is loaded is lowered after firing the FEP (Fig. 3.1b). Electrons whose energies are greater than the lowered well depth can then escape the well leaving only a more controlled number of electrons behind. Figure 3.2 shows the linear dependency of the number of electrons loaded on the well depth.

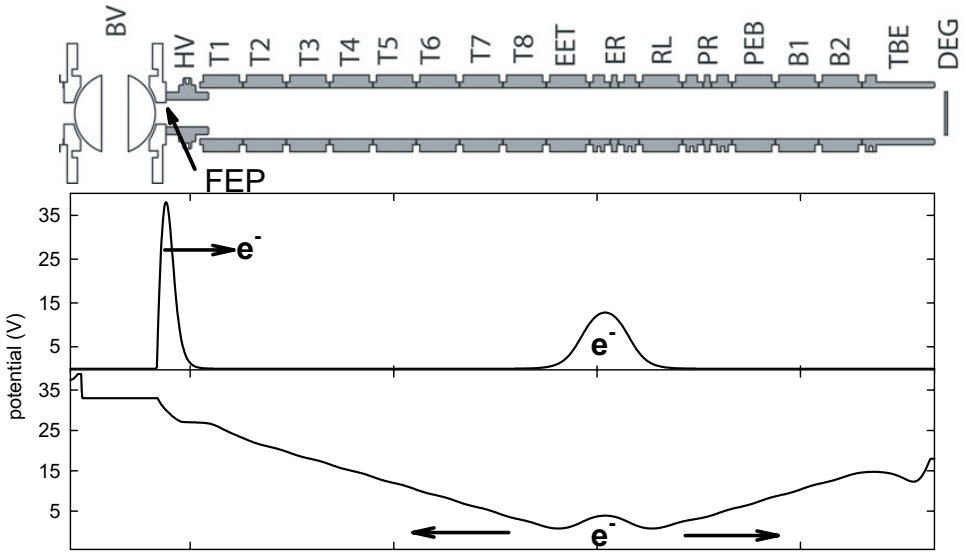


Figure 3.1: Potentials used in loading electrons from the field emission point.

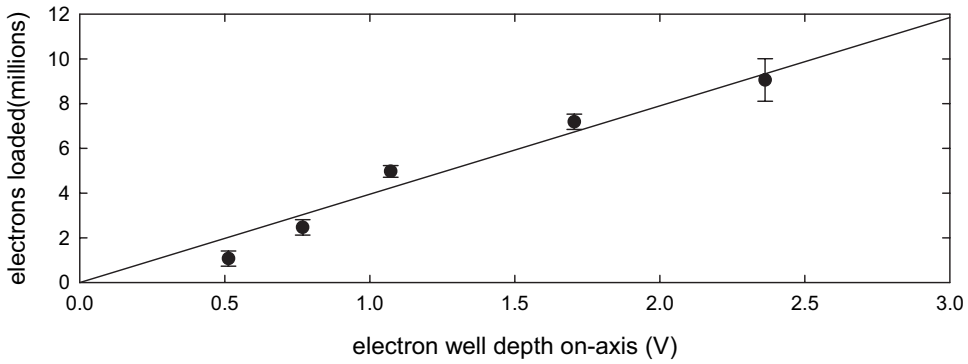


Figure 3.2: The number of electrons loaded from the FEP as a function of the depth that the electron well is reduced to. This curve was measured using $e^-$ loaded in HBAR2's *ER*.

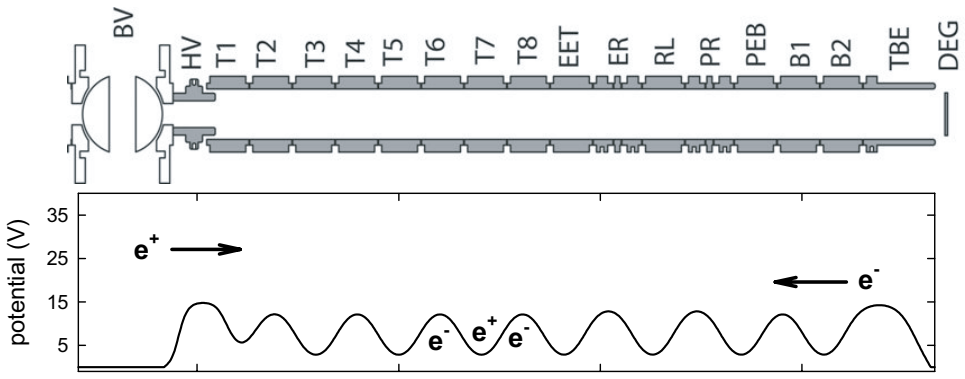


Figure 3.3: Potentials used for source $e^-$ loading.

**Radioactive Source Loading**

While FEP electron loading is robust and simple, if any other particles such as positrons or antiprotons are simultaneously confined in the lower stack when the FEP is fired they are perturbed and have high probability to be ejected from the trap. To allow for loading electrons while particles are located in the lower trap, we use secondary electrons emitted from collisions of high energy positrons with the degrader. Empirically these high energy positrons do not cause the heating effects observed with electrons from the FEP which is likely due to their much higher energies and thus much smaller interaction time with trapped particles.

In this technique, positrons from the $^{22}$Na source, discussed later in this section, are allowed to impinge upon the degrader. As $^{22}$Na emits positrons with energy up to approximately 500 keV, these positrons have the energy necessary to both ionize cryo-pumped gas as occurs in FEP electron loading as well as to emit secondary electrons from the Be degrader. These secondary electrons are then captured in wells adjoining the existing positron well (Fig. 3.3). This technique also works when there are no

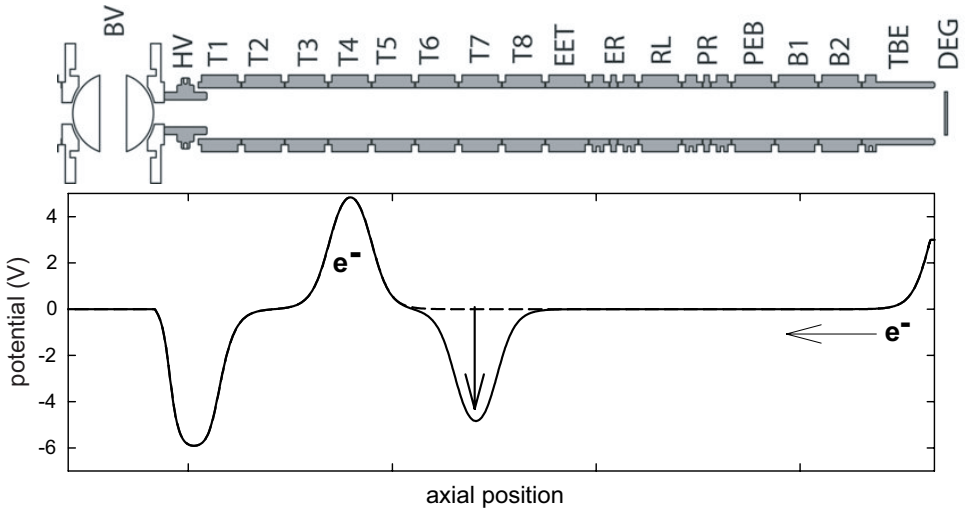


Figure 3.4: Potentials used for loading secondary $e^-$ emitted from antiproton collisions with the degrader foil.

$e^+$ trapped in the lower stack [42]. In this case, background gas collisional cooling results in initial confinement for the $e^-$. The collisional cooling from the trapped positrons results in an order of magnitude more efficient trapping rate as compared to situations where there are initially no other particles in the lower trap

### Antiproton Secondary Electron Loading

One final technique has been used to load electrons. In this case secondary electrons resulting from antiproton collisions with the Be degrader foil, located at the bottom of the electrode stack, are captured. These secondary electrons are emitted with energies comparable to the work-function of Be (4.98 eV) and are produced in a pulse given by the length of the 200 ns incoming antiproton shot from the AD facility.

The pulsed nature of the emitted secondary electrons makes it possible to capture them in flight. To do this the trap is configured as shown in Fig. 3.4. On the right, the degrader is biased to +3 V to reduce the speed at which the emitted electrons are

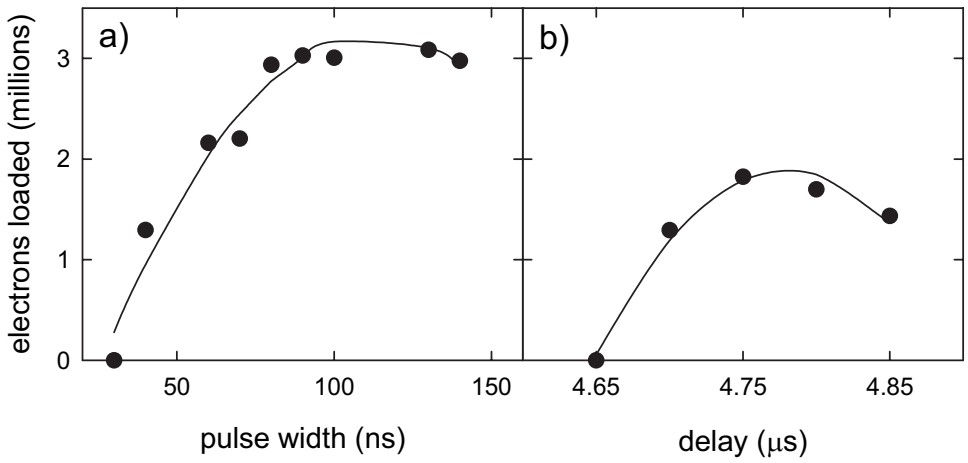


Figure 3.5: The effect of the width of the voltage pulse and the delay relative to CERN's $\overline{\text{p}}$ ejection warning signals on the number of electrons loaded.

traveling. On the left, an extended well is created between *HV* and *T7* to capture the electrons. Just before the antiproton pulse arrives, a fast voltage pulse is applied to *T7*. This changes the potential to the dashed line and allows secondary electrons to enter the well. After the electrons enter the well, the fast voltage pulse is removed closing the door of the well which traps the electrons within the well structure. The electrons eventually end up within *T4* after enough time has past for radiative synchrotron cooling to reduce their energy. Figure 3.4 shows the effects on the number of electrons loaded of tuning either the high voltage pulse delay relative to the antiproton ejection timing signal delivered from CERN or the width of the high voltage pulse.

### Future Electron Loading Techniques

While the above techniques sufficed to provide the electrons necessary for this research, they share several drawbacks. First, in order to load the typical 5 million electrons required for stacking antiprotons takes approximately 10 minutes which

when compared to the average hour long experiment is a limitation. Second, all the techniques became less reliable as the number of electrons is increased above 10 million. While it may be possible to reliably extend the number of electrons loaded for future requirements, a new technique will quite likely be necessary.

One promising technique utilizes photoemission from a metallic surface to generate a pulse of electrons that can be trapped using the same technique as that used for antiproton secondary electron loading. In this implementation, 248 nm pulsed light from a KrF excimer laser impinging on a gold surface would emit the electrons [43]. The advantage of this technique is that both the number of electrons and length of the electron pulse can be controlled by varying respectively the intensity and length of the excimer laser pulse. With an estimated quantum efficiency of $10^{-4}$ electrons per photon, a single 18 mJ, 10 ns laser pulse would result in $10^{12}$ electrons available which is an improvement of over 15 orders of magnitude in the loading time required per electron.

### 3.1.2 Antiprotons

To form cold antihydrogen, we need large numbers of cold antiprotons. In this case, cold means at the same temperature as that of the trap environment (4.2 K or 0.345 meV). However, the coldest available source of antiprotons produces antiprotons at an energy of 5.3 MeV. To slow antiprotons the remaining 10 orders of magnitude, we utilize techniques refined over many years by the TRAP collaboration, the predecessor to ATRAP. These techniques include the slowing of antiprotons in matter [44], trapping them while in flight [45], and finally cooling them to 4.2 K through collisions

with electrons [46]. While the basic techniques remain the same, this section will discuss several refinements that allow for the stable capture of more antiprotons [47] by repeated stacking of antiproton shots on top of each other.

### Antiproton Production

The coldest source of available antiprotons is currently at CERN near Geneva, Switzerland through the Antiproton Decelerator (AD) facility (Fig. 3.6) [48]. The AD receives bunches of approximately $10^{13}$ protons accelerated to 25 GeV by CERN's primary accelerator, the proton synchrotron (PS). The protons then collide with an iridium wire target. From this collision, approximately $3\times10^7$ antiprotons at 2.75 GeV are produced and directed into the AD ring. In a series of steps taking approximately 90 seconds, the 2.75 GeV antiprotons are slowed to 5.3 MeV while applying both stochastic and collisional electron cooling to maintain a small momentum spread. The antiprotons are then diverted from the AD ring towards our experimental zones in a 200 ns bunch of $2.5 \times 10^7$ antiprotons before finally being turned upwards into our experiment through two 45° bending magnets (Fig. 2.7).

### Antiproton Steering and Slowing

In order to center the incoming antiproton beam onto our trap electrodes, we use a parallel plate avalanche counter (PPAC) which monitors the position and intensity of the incoming beam [39, 49]. This detector consists of two sets of anode-cathode pairs each consisting of 5 thin 2 mm wide parallel conducting strips separated by a 0.5 mm gap. These sets are oriented in the $x$-$y$ plane perpendicular to the beam with one set of electrodes aligned along the $x$-axis and one set aligned along the $y$-axis. A

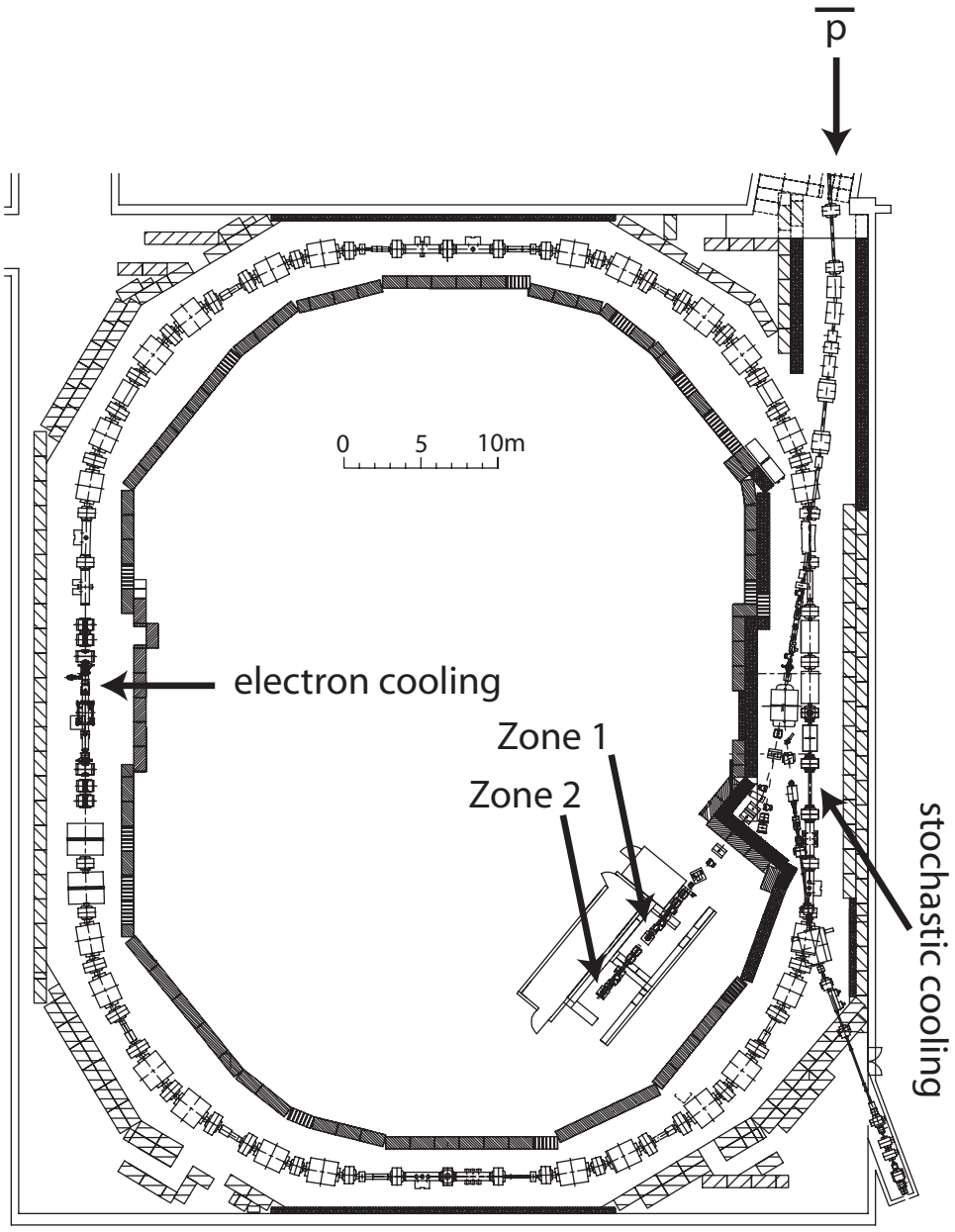


Figure 3.6: The layout of the Antiproton Decelerator (AD) at CERN showing the locations of the antiproton cooling devices and ATRAP's two experimental zones.

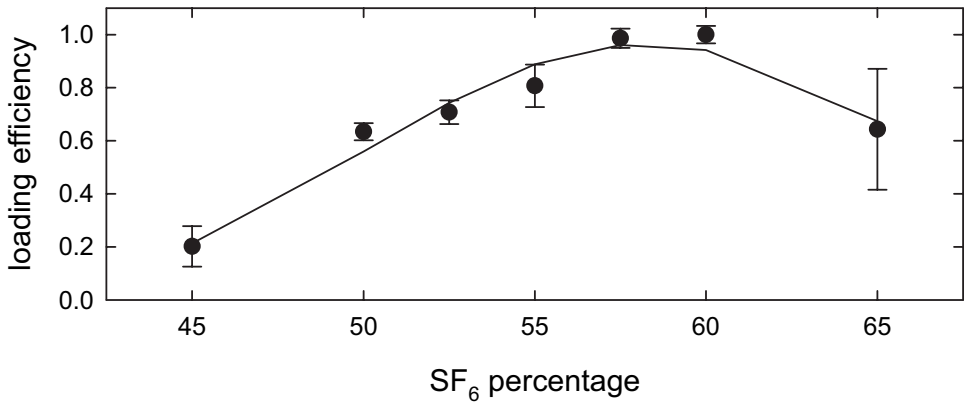


Figure 3.7: Optimization of $SF_6$-He mixture in the gas tuning energy cell.

200 V potential difference is maintained between each anode-cathode pair and argon gas is continuously flowed inside the space between the pairs of electrodes.

Incoming antiprotons ionize argon atoms inside the PPAC plates releasing electrons which are accelerated by the potential difference and then ionize further atoms creating an avalanche process. The released electrons are constrained by the magnetic bias field to travel only axially along field lines, so by monitoring the current collected on each parallel conducting strip, the beam profile can be inferred and then corrected by adjusting the currents within the beam-line steering magnets.

The 5.3 MeV incoming antiproton energy is much too high to trap via an electrostatic field created by an electrode within our Penning trap. To reduce the energy the three orders of magnitude necessary for trapping, we utilize several stages of thin foils as well as a gas tuning cell which incrementally lower the antiproton energy. These stages have been discussed previously [44] so I will concentrate on the two primary stages.

In the first stage, antiprotons pass through a 13 mm thick gas cell located just

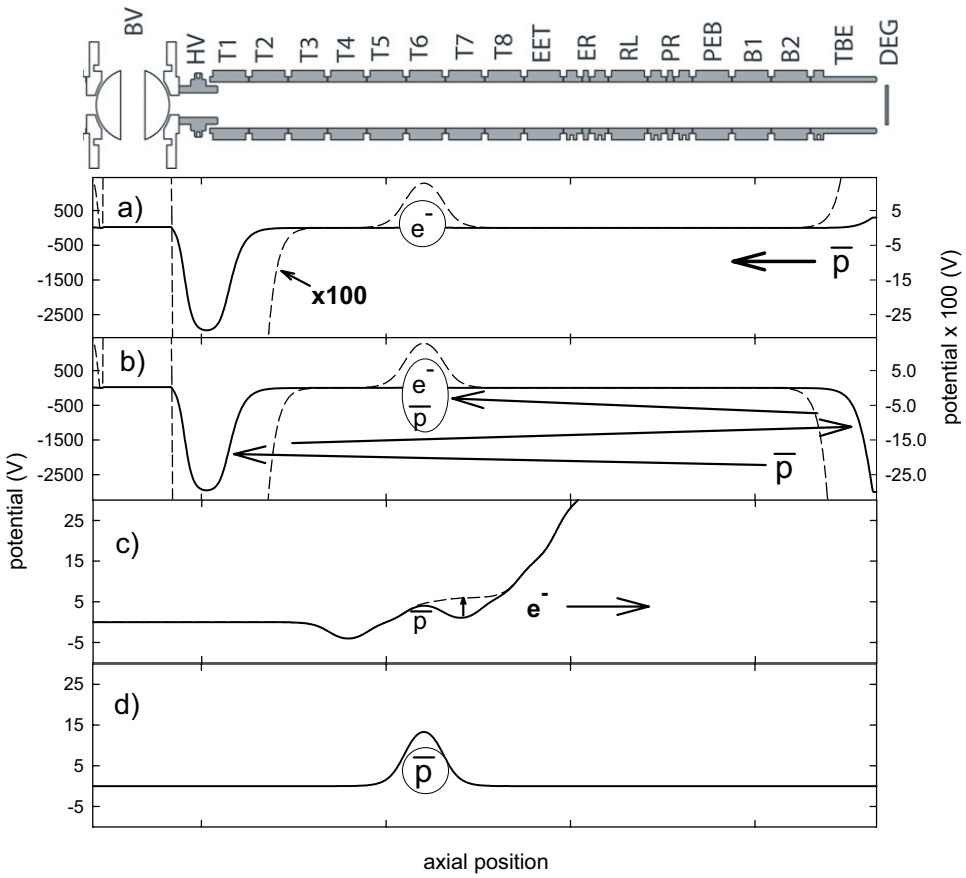


Figure 3.8: Potentials used for trapping $\overline{\mathrm{p}}$: (a) the trap is ready for $\overline{\mathrm{p}}$ to enter, (b) $\overline{\mathrm{p}}$ enter and are trapped electrostatically, (c) electrons are ejected, and (d) $\overline{\mathrm{p}}$ loaded.

above the PPAC assembly. This gas cell is composed of a 1 atm mixture of He and $SF_6$ in which the amount of energy loss can be changed by varying the percentage of each gas. The tuning of this percentage is done empirically to maximize the number of antiprotons loaded (Fig. 3.7). The second stage is a 125 µm Beryllium foil(*DEG*) located at the end of the Penning trap in which most of the energy loss (approximately 3.5 MeV) occurs.

**Antiproton Trapping**

Figure 3.8 shows the basic technique for trapping the resulting keV antiprotons in the trap. First, electrons are loaded into a well on *T6* and *HV* is biased to −3000 V creating one end of the well for the antiprotons. Next, antiprotons enter the electrode with *DEG* biased to 300 V to minimize the production of secondary electrons (Fig. 3.8a). After the pulse is entirely contained within the trap, the potential on *DEG* is suddenly pulsed to -3000 V using a high voltage switch (Behlke HTS-301) (Fig. 3.8b). This closes the potential well and confines the antiprotons. For the next 70 seconds, antiprotons are allowed to collide with the previously trapped electrons thus cooling them into the small electron well in *T6* and eventually to the 4.2 K temperature of the trap environment. Almost 25,000 $\overline{\mathrm{p}}$ have been cooled from the most intense AD pulses of high energy $\overline{\mathrm{p}}$ but between 10,000 to 15,000 $\overline{\mathrm{p}}$ is more typical [47]. After this cooling time, elapses the trap is reset for the next incoming bunch of antiprotons. We repeat this cycle as many times as necessary to load the total number of required antiprotons with a linear dependence of antiprotons loaded versus the number of shots (Fig. 3.9). The last few steps involve ejecting the cooling electrons by removing the electron and antiproton potential well for a duration of 100 ns (Fig. 3.8c). During this time period, the electrons can escape but the antiprotons are too slow due to their large comparative mass and thus unable to leave the well.

The time delay of the high voltage pulse relative to a signal generated by the AD when antiprotons are ejected is the one parameter that can be easily adjusted to optimize the loading process (Fig. 3.10). If the timing is too short relative to the warning signal, no antiprotons will have entered the trap before the high voltage pulse

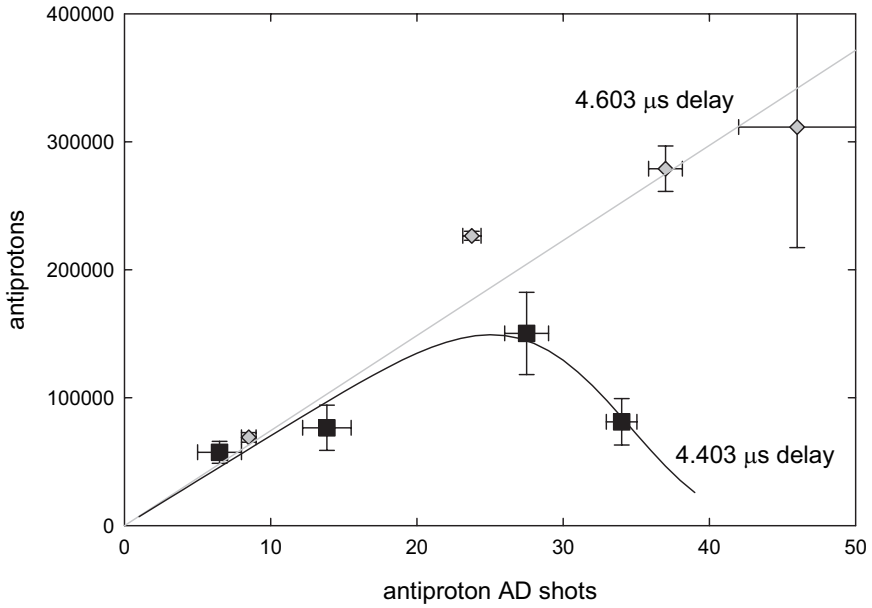


Figure 3.9: Stacking of multiple $\overline{\mathrm{p}}$ bunches. The 4.603 μs points show normal linear loading. The 4.403 μs points show the effects of loading secondary $\mathrm{e}^-$.

is triggered and thus no antiprotons will be trapped as they will have too much energy to be reflected and trapped by the potential on *HV*. If the timing is too late, high energy antiprotons will have bounced off of *HV* and exited through the other end of the trap before the high voltage pulse is triggered thus lowering the loading efficiency.

A second more subtle effect is also related to the timing of the high voltage pulse where if very specific conditions are met secondary electrons will also be trapped and cooled resulting in a steadily increasing number of electrons in the well on *T6*. When the number of electrons reaches a certain level, the trapped antiprotons become unstable and are almost entirely lost radially through annihilations at the electrode surfaces. In one particular experiment, an initial cloud of 1.8 million electrons grew to over 5.5 million $\mathrm{e}^-$ after 5 $\overline{\mathrm{p}}$ shots. The 4.403 μs points in Fig. 3.9 show the limit on the number of antiprotons loaded due to this effect. By increasing the high voltage

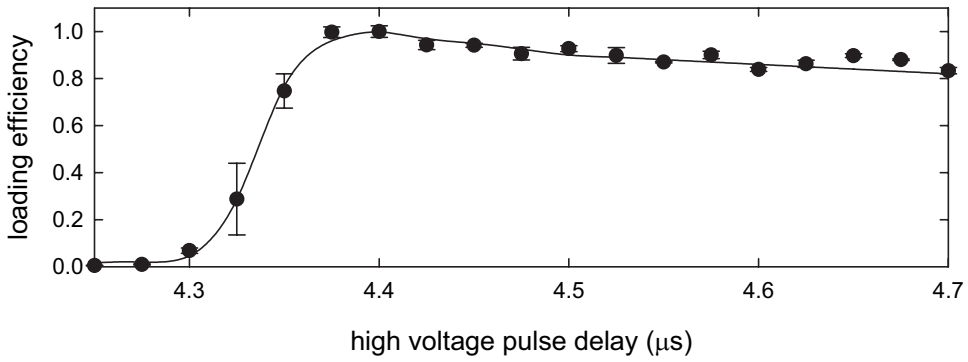


Figure 3.10: High voltage pulse delay optimization for $\overline{\mathrm{p}}$ loading.

delay by 200 ns, additional electrons were no longer loaded and in one run over 900,000 antiprotons were stacked. In fact additional electrons were trapped only when the pulse delay was near the sudden increase in antiprotons loaded at 4.4 µs; varying the potentials on *DEG* or *HV* had no effect. This suggests that the additional electrons were loaded because of slightly overlapping the antiproton beam with the high voltage trapping pulse. Some secondary electrons will then be emitted when the potential on *DEG* is slightly less than -3000 V during the rising edge of the pulse. The energy of these electrons is not enough to escape the final potential well. In contrast, if electrons were emitted when *DEG* is at -3000 V, the small additional energy gained from the work-function of Be (5.0 eV) allows the emitted electrons to be recaptured by *DEG* after one round trip of the trap.

The magnetic bias field plays a key role in the capture of antiprotons by ensuring the high energy antiprotons are still bound to field lines and thus unable to escape radially annihilating on electrodes. In the future, however, it will be necessary to use lower bias fields in order to trap neutral antihydrogen atoms. To investigate this effect, the magnetic field was varied while monitoring the number of high energy antiprotons

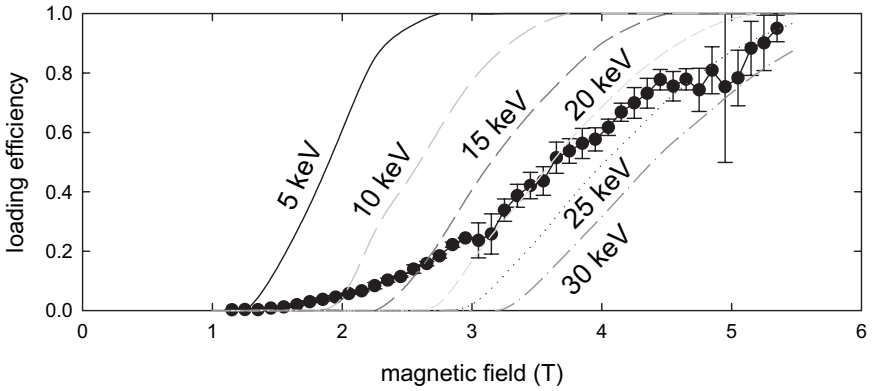


Figure 3.11: Antiproton loading efficiency as a function of magnetic field.

captured (Fig. 3.11). The number of antiprotons captured is still increasing even at our typical 5.3 T bias field. A simple model may account for the magnetic field dependencies. Here we assume that low energy antiprotons are emitted from the Be foil (*DEG*) in all directions with varying energies due to the collisional processes inherent in the energy loss occurring within the foil. However, any radial energy is immediately converted to energy in the particle's cyclotron motion due to the strong magnetic field. Since the cyclotron radius is:

$$r_c = \frac{\sqrt{2E_c m}}{qB_0} \tag{3.1}$$

where $E_c$ is the cyclotron energy, as the energy increases the cyclotron radius also increases eventually resulting in antiprotons annihilating on the trap walls before cooling. The solid curves in Fig. 3.11 show a simulation of the number of antiprotons stacked with a given radial energy and a 2 keV axial energy suggesting that on average the antiprotons that are trapped have an initial radial energy of 20 keV. The incoming 5.3 MeV antiprotons are assumed to be contained in an initial 2 mm spot as measured from the PPAC. The 20 keV radial energy is quite different than the approximately

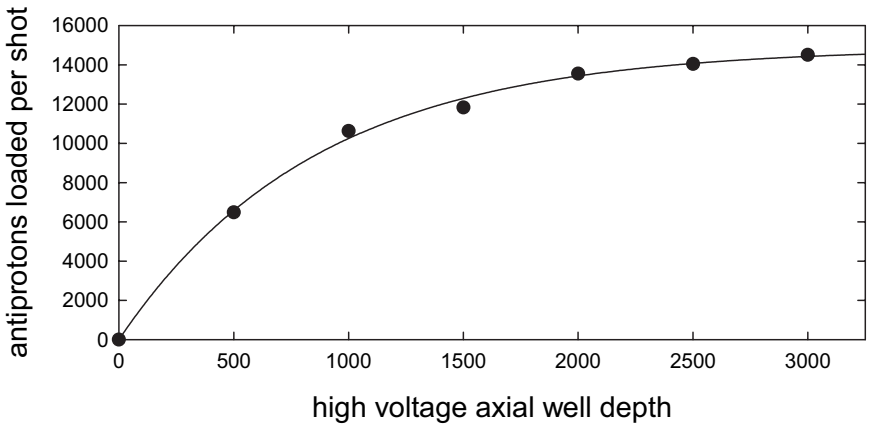


Figure 3.12: Antiprotons loaded as a function of the high voltage axial potential well depth.

1 keV average axial energy of the $\overline{\mathrm{p}}$ (Fig. 3.12).

### 3.1.3 Positrons

Positrons are the second critical component for the production of antihydrogen. There is a long history of various techniques for loading positrons into a Penning trap [50, 51, 52, 53, 54]. The technique used for this research is the most robust available method for loading $e^+$ directly into a cryogenic ultra-high vacuum. With the current 40 mCi radioactive source, a loading rate of 0.5 million positrons in an hour is achievable.

A 40 mCi $^{22}$Na radioactive source contained in a 3 mm capsule provides the positrons for our experiments. At this strength, the source represents a major health hazard, so a robust technique for remote handling was developed [42]. While the source is not in use it resides in a vacuum system surrounded by lead (Fig. 2.7). In order to protect the antiproton annihilation detectors from the gamma radiation produced by $^{22}$Na, the vacuum system is designed with a 45° bend relative to the trap axis to prevent a

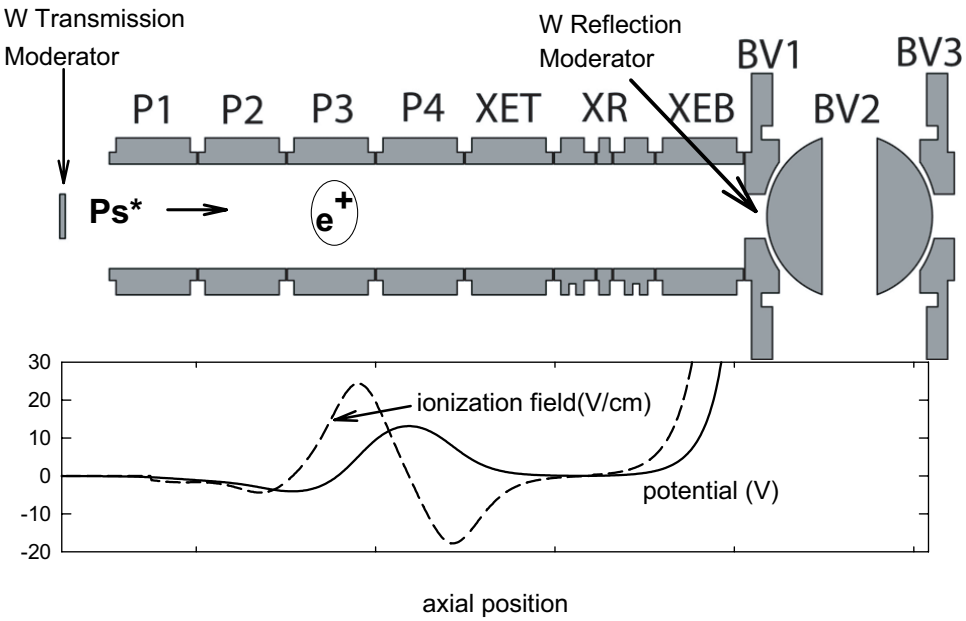


Figure 3.13: Potentials used for loading $e^+$.

direct line of sight between the source and the detectors. When needed the source is then lowered through a tube in the center of the experiment assembly until it rests just above the electrode stack. Positrons can then enter the trap through a 10 µm Ti window.

Once the source is lowered, the positrons are directed onto a 2 µm single crystal W(100) transmission moderator ($MT$). The transmission moderator emits approximately 4 slow positrons per $10^4$ incoming high energy positrons [55]. An even smaller fraction acquires an electron when it is emitted and forms weakly bound magnetized Rydberg positronium atoms [51]. These atoms then proceed into the trap before being field ionized by a small electric field within the trap (approximately 17 V/cm). As the ionization occurs within a potential well, the positrons are trapped within the electrode stack. To improve the loading efficiency a second moderator ($RMOD$)

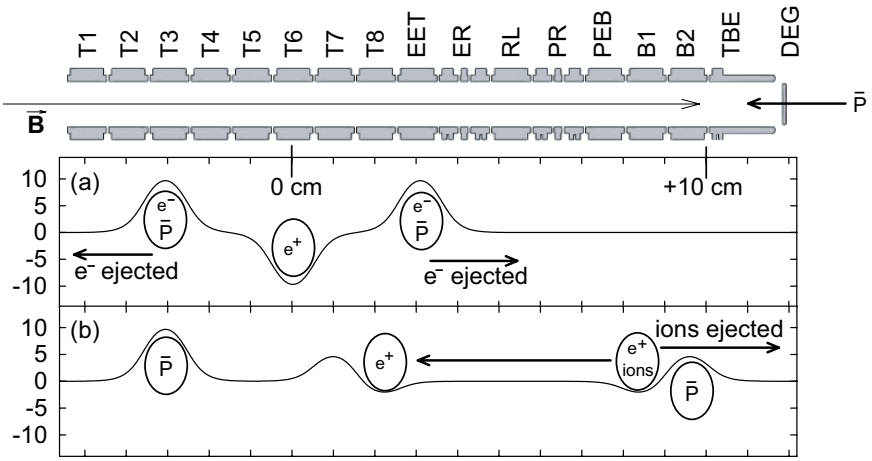


Figure 3.14: Potentials used for (a) stacking $\overline{p}$ with $e^+$ in the lower trap and (b) removing ions from the $e^+$ well.

is placed on the ball valve at the lower end of the upper stack which remoderates and reflects those positrons that did not initially form positronium back towards the *TMOD* resulting in a second chance to form positronium. The net effect of *RMOD* is a gain of a factor of 3 in $e^+$ loading efficiency.

The duration of stacking of antiprotons for a typical experiment is on the order of one hour. The 500,000 $e^+$ that can be loaded in that amount of time is not enough for many experiments requiring us to reuse leftover positrons from one experiment to the next. The first attempt to do so was done in HBAR1 where the restricted aperture of the ball valve precluded moving the $e^+$ to the upper electrodes while stacking antiprotons. To avoid this problem, the positrons were instead kept in the lower trap while antiprotons were loaded (Fig. 3.14a). While stacking, the incoming high energy antiprotons ionize residual cryo-pumped atoms resulting in positive ion cores accumulating in the $e^+$ well. The ions would cause difficulties in actual experiments so they are removed by using 95 ns wide voltage pulses to transfer the positrons to

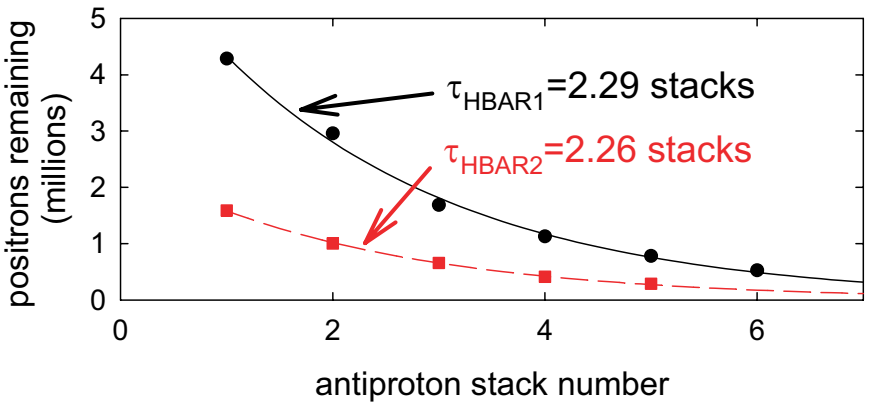


Figure 3.15: Positron loss per antiproton stack when positrons are kept in the lower stack of HBAR1 or adiabatically transferred between the lower and upper stack in HBAR2. The difference in absolute numbers is primarily due to radioactive source decay.

*T8* while the ions remain in *B1*. This pulsing technique is discussed further later in this chapter. The remaining ions are then ejected from the trap. The unfortunate side effect of keeping positrons in the path of incoming antiprotons while loading is a loss of 35 % of the initial positrons after each antiproton load (Fig. 3.15). This is likely due to a combination of collisions with incoming antiprotons and heating of the positrons from the trapped ions.

To avoid this loss, HBAR2 was designed with a ball valve with an aperture the same size as that of the trap electrodes. This design should allow transfer of $e^+$ with no loss through the ball valve as opposed to the maximum transfer of 800,000 $e^+$ in HBAR1 [39] thus one would protect the $e^+$ from antiproton shots by moving them to the upper stack during $\overline{p}$ stacking. However comparable losses of positrons after each experimental cycle to those in the HBAR1 technique were observed. Both using fast voltage pulses and adiabatic transfer as described in the next section to move the $e^+$ through the ball valve had similar particle loss results. In this case, the culprit is

probably the BeCu construction of the ball valve in HBAR2. The resistivity of BeCu at 4.2 K is over 2000 times higher than that of copper which leads to higher particle energy damping compared to that of a standard electrode and likely the increased particle losses.

## 3.2 Particle Manipulation

### 3.2.1 Particle Cooling

A critical component of producing cold antihydrogen is maintaining the constituent particles at a temperature as close as possible to the 4.2 K trap environment. Both passive and active techniques are used to initially cool particles and to ensure they remain at 4.2 K.

#### Radiative Damping

Since particle motion in a Penning trap involves continuous acceleration, energy damping through radiation is constantly occurring [33]. The power radiated is given by the familiar Larmor formula [56]:

$$P = \frac{e^2}{6\pi\epsilon_0 c^3}\left|\ddot{\vec{\rho}}\right|^2 \tag{3.2}$$

We first consider the radiative damping of the cyclotron motion for which this synchrotron radiation is the predominant damping mechanism. Using the fact that $\ddot{\vec{\rho}} = \omega_c \times \dot{\vec{\rho}}$ and $E_c = \frac{1}{2}m\dot{\rho}^2$:

$$\frac{dE}{dt} = -P = -\gamma_c E \tag{3.3}$$

| $\gamma^{-1}$ | $e^+$ | $\overline{p}$ |
|---|---|---|
| Magnetron | $1.0 \times 10^{14}$ s | $1.8 \times 10^{17}$ s |
| Axial | $3.0 \times 10^{6}$ s | $1.0 \times 10^{13}$ s |
| Cyclotron | 0.1 s | $5.9 \times 10^{8}$ s |

Table 3.1: Typical radiative damping times for particles in our Penning trap.

where

$$\gamma_c = \frac{e^2 \omega_c^2}{3\pi\epsilon_0 m c^3} \tag{3.4}$$

As the magnetron motion is formally equivalent to the cyclotron motion

$$\gamma_m = \frac{e^2 \omega_m^2}{3\pi\epsilon_0 m c^3} \tag{3.5}$$

For the axial motion, using $E_z = \frac{1}{2} m \omega_z^2 z^2$ and $\ddot{z} = -\omega_z^2 z$:

$$\gamma_z = \frac{e^2 \omega_z^2}{6\pi\epsilon_0 m c^3} \tag{3.6}$$

Only the $e^-$ and $e^+$ cyclotron motion will decay appreciably without extra coupling (Table 3.1). However, in clouds with many particles, collisions will couple the axial motion to the cyclotron motion increasing the damping rate to a reasonable value for cooling. The axial damping rate can be further improved by coupling the axial motion to an external resistor as described in Chapter 4.

### Axial Sideband Cooling

As discussed above the magnetron motion has effectively no radiation damping. In addition, the motion is unstable and requires energy to reduce the radius of the motion. An active technique is instead required to reduce a particle's radius and

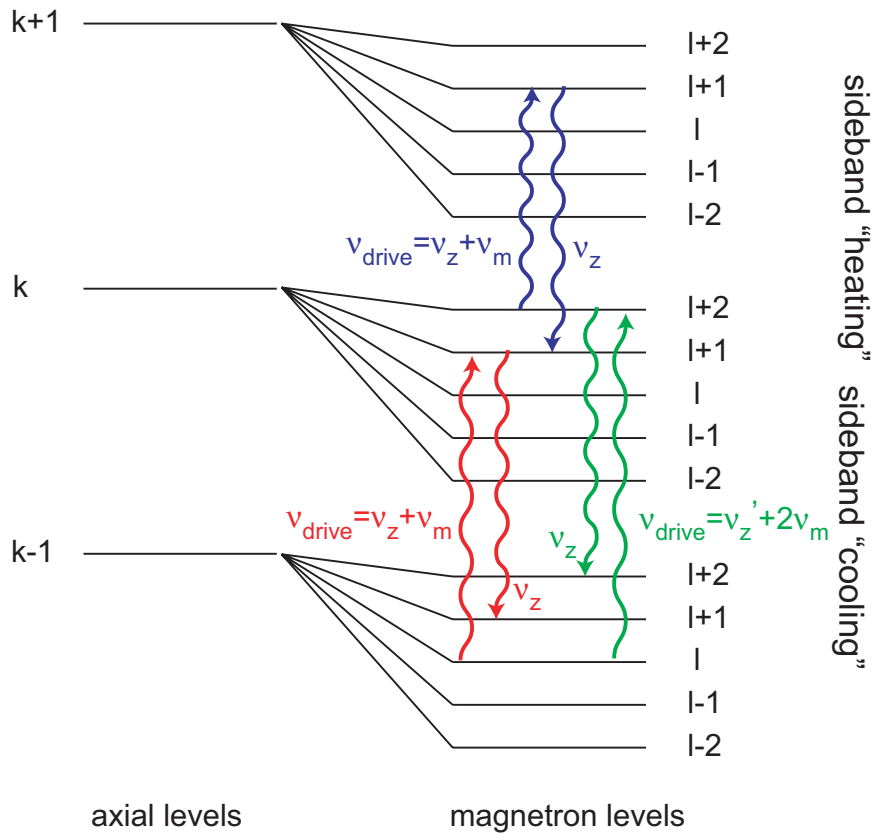


Figure 3.16: Magnetron and axial energy levels.

"cool" it to the center of the trap. Furthermore, the low frequency of the motion means that the interaction strength for an external drive is quite low. To overcome this limitation we use a technique called RF sideband cooling [33] that is equivalent to laser cooling of neutral atoms.

The core idea of this technique is to drive the axial and magnetron motions simultaneously by applying a drive at $\nu_z + \nu_m$. For the necessary symmetry this drive is applied to one half of an electrode split along an axial plane. In a quantum mechanical picture, a charged particle absorbing a $\nu_z + \nu_m$ photon corresponds to an excitation of one energy level in both the axial and magnetron energy levels (Fig. 3.16). The

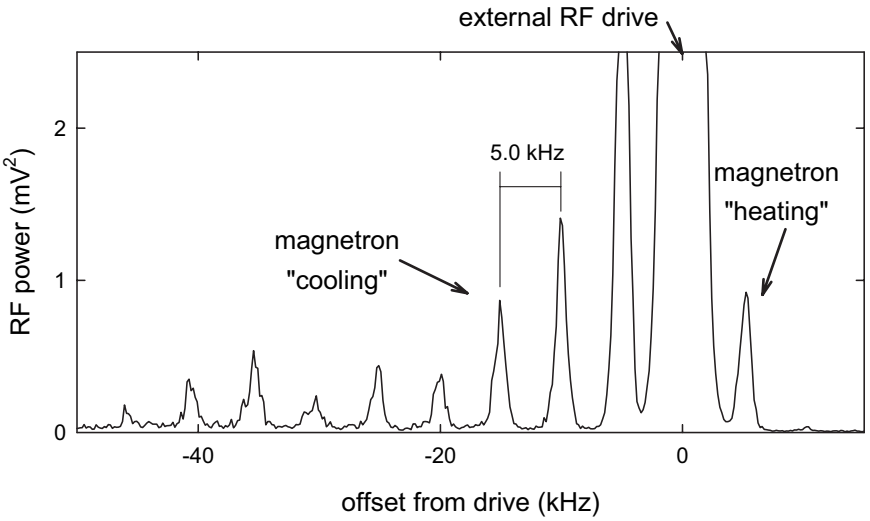


Figure 3.17: A comb of sidebands from magnetron cooling.

particle then spontaneously emits a photon at the axial frequency returning it to the same axial energy level but with one quanta more of magnetron energy (which implies a slightly smaller radius). For a single particle the choice of drive frequency is well defined but for a particle cloud this choice is less clear. The most effective techniques in the case of large numbers involve driving fairly far off resonance (greater than 500 kHz compared to the mean axial frequency) and with a high amplitude (approximately -5 dBm). In this case it is also possible to drive a transition that excites one quanta of axial energy but more than one quanta of magnetron energy due to the large line width induced by space charge and collisional effects within the plasma cloud. Figure 3.17 shows the comb of sidebands produced from the spontaneous emission of an axial photon after excitation.

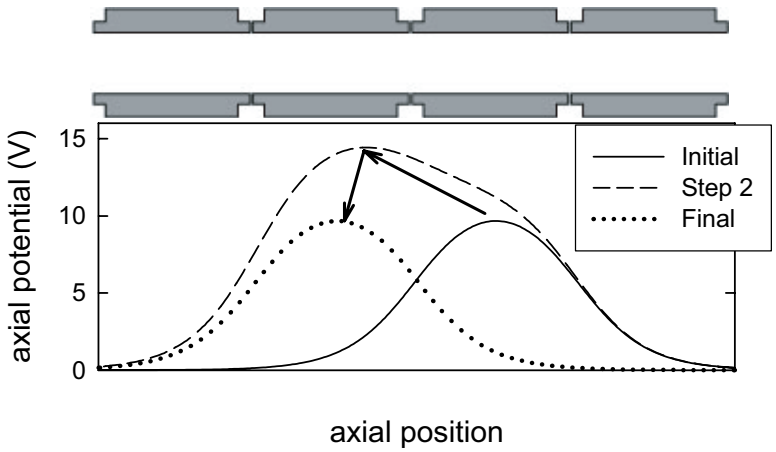


Figure 3.18: Inchworm technique for adiabatic particle transfer.

### 3.2.2 Particle Transfer

With careful control of electrode potentials, it is possible to move particles about the electrode stack with the intent of bringing them together and forcing them to interact. For most particle movements we use a slow adiabatic transfer technique. In this technique, particles are moved one electrode at a time around the trap through an "inchworm" technique on a time scale of several seconds. To do this, the well on the next electrode is first made deeper (in general to 16 V) than the 12 V well on the original electrode (Fig. 3.18). This causes the particles to move to a position centered on the new electrode. The initial electrode's potential can then be brought to zero and the potential on the new electrode brought back to 12 V allowing the process to be repeated as many times as necessary. In order to prevent the particles from becoming heated during this process, the time scale of changes of the axial frequency must be slow compared to the period of an axial oscillation (approximately 100 ns) [57].

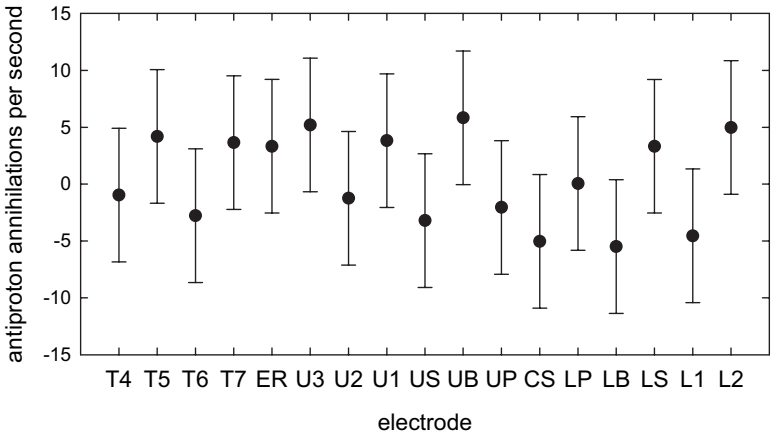


Figure 3.19: Average antiproton loss rates during adiabatic transfers as a function of the electrode the $\overline{p}$ are currently being transferred onto.

Excluding the ball valve, there is no particle loss in most electrodes during adiabatic transfers (Fig. 3.19). This is due to the carefully chosen potentials which avoid long flat potential wells which would result in increased magnetron heating and radial particle loss presumably due to small imperfections in the electrode geometries that predominate when the applied potential is flat.

For most particle transfer requirements, adiabatic transfer works exceedingly well. There are two cases where it is not capable of meeting our requirements. First, particles cannot be adiabatically transfered over the top of an existing particle well to, for example, reverse the spatial orientation of a pair of $e^+$ and $\overline{p}$ wells. Second, it is unable to separate particles of different masses contained within the same well. This is needed to remove $e^-$ from $\overline{p}$ wells as well as to remove contaminant ions from $e^+$ wells.

A non-adiabatic pulse transfer method is used to perform these types of particle transfers. The basic idea is to remove the potential well surrounding the particles in a faster time than a single axial oscillation (Fig. 3.20a). The particles then leave the elec-

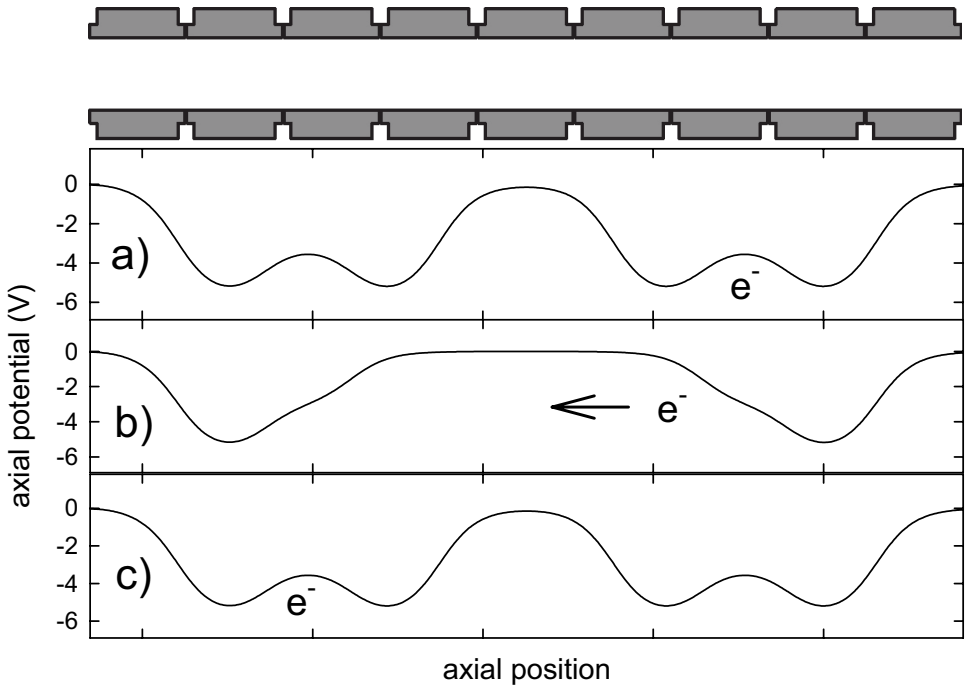


Figure 3.20: Potentials for pulsing $e^-$ from *T3* to *T6*.

trode with a controllable energy and travel towards the catch electrode (Fig. 3.20b). Once the particles are slowed down but before being reflected at the potential barrier at the other end of the transfer, the potential well is closed by a second pulse (Fig. 3.20c).

To not perturb the particle cloud, the pulse that opens and closes the potential well must be much faster than the sub 100 ns axial oscillation time for electrons and positrons. This means that signals with bandwidths greater than 1 GHz must be transmitted to the electrodes requiring carefully terminated transmission lines. Figure 3.21 shows the circuitry necessary to apply these pulses. A saturated switch (Avtech Electrosystems AV-144B1) is triggered and generates a +20V pulse. This pulse can be attenuated by a variable amount (typically -3 dB) before being sent

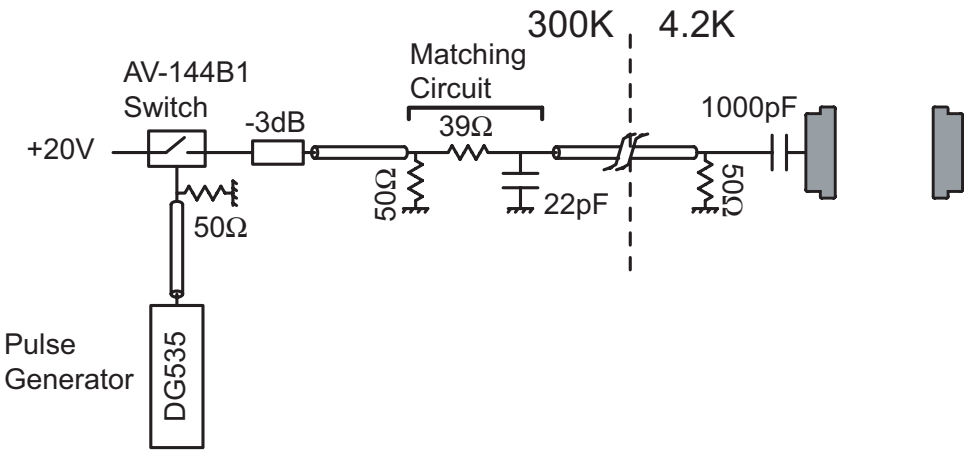


Figure 3.21: Electronics used to apply fast voltage pulses to electrodes.

through a matching circuit located at the top of the experiment and into a 50 Ω stainless steel micro-coax line (Microstock UT-20-SS) that terminates at an electrical feedthrough into the trap vacuum enclosure. At the electrode, a maximum +13 V pulse can be generated but the pulse is typically attenuated to +6 V.

The delay between the launch and capture pulses must also be tuned for maximum efficiency (Fig. 3.22). In practice this delay is tuned empirically but an initial guess can be calculated by integrating the axial equation of motion for a single particle. This calculated value is usually within 10 ns of the correct value but is not exact due to both small electrostatic patches that perturb the potentials within the trap as well as space charge effects within a particle cloud.

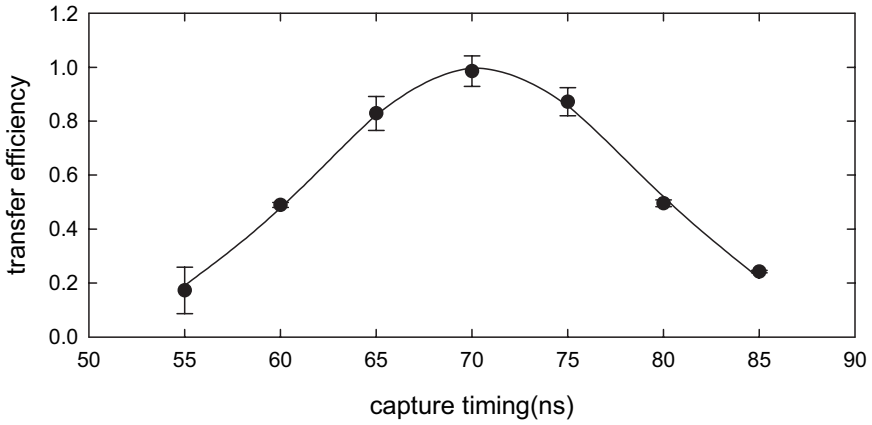


Figure 3.22: Pulse timing for pulsing electrons from *T3* to *T6*.

# Chapter 4

# Plasmas in a Penning Trap

The previous chapter discussed the single particle dynamics in a Penning trap. This is adequate for most experiments that are done in these types of traps but the production of large numbers of antihydrogen atoms necessitates working with clouds containing as many particles as possible. These clouds are non-neutral plasmas in the sense that all of the spatial dimensions are large compared to the typical Debye length, $\lambda_d \equiv \sqrt{\epsilon_0 kT/ne^2}$, of 30 µm where $T$ is the temperature of the plasma, and $n$ is the number density. A consequence of this requirement is that the effect of the space charge of the plasma on the trapping potential is non-negligible and the formalism developed in the previous chapter is no longer a complete description. This chapter will discuss the basic dynamics of these clouds as well as experimental techniques used to characterize them.

## 4.1 Basic Non-neutral Plasmas

We first consider the confinement of a cloud of particles in a Penning trap. From the axial cylindrical symmetry of the trap, the canonical angular momentum, $P_\theta$, is conserved [57]:

$$P_\theta = \sum_{j=1}^{N} m v_{\theta_j} \rho_j + \frac{q}{2} B_0 \rho_j^2 \tag{4.1}$$

where the sum is over all particles in the trap. The first term is the mechanical angular momentum of the particles and the second term is the angular momentum of the magnetic field. The second term dominates for a sufficiently large magnetic field so

$$\text{const} = P_\theta \propto \sum_{j=1}^{N} \rho_j^2 \tag{4.2}$$

which implies that the mean square radius of the cloud is constrained [58]. For example for a spheroidal plasma containing 2.25 million $e^-$ with an axial length of 5 mm and a radius of 3.6 mm, the mechanical angular momentum is only $1.5 \times 10^{-25}\,\text{kg}\cdot\text{m}^2/\text{s}$ while the field angular momentum is $5.0 \times 10^{-18}\,\text{kg}\cdot\text{m}^2/\text{s}$. As all practical traps do not have perfect axial symmetry, this theorem is not absolute, but still results in confinement times on the scale of days in our traps. These times are more than long enough for the plasma to reach thermal equilibrium through internal collisions.

If the density of our plasmas is low enough that correlations between particles can be ignored, thermal equilibrium states can be described with a single particle distribution function. In particular, the correlation parameter, $\Gamma = e^2/(4\pi\epsilon_0 akT)$, must be less than one for a plasma to be uncorrelated, where the distance between particles, $a$, is defined implicitly by $4\pi n_0 a^3/3 = 1$ and $n_0$ is the density [59]. For the

plasma described above, with $n_0 = 1.5 \times 10^7/\,\mathrm{cm}^3$, $\Gamma = 0.16$, and in general $\Gamma < 1$ for our plasma clouds. Furthermore, since the logarithm of the distribution function must be expressible in terms of additive constants of motion from Liouville's theorem [60], the most general single particle distribution function is given by

$$\log f(\vec{p},\vec{q}) = \alpha + \beta\left[E(p,q) + \vec{\gamma}\cdot\vec{p} + \vec{\omega}\cdot(\vec{q}\times\vec{p})\right] \tag{4.3}$$

where $\alpha$, $\beta$, $\vec{\gamma}$, and $\vec{\omega}$ are constant Lagrange multipliers. Because only energy and angular momentum about the $z$-axis are conserved in this system, the thermal distribution function is as follows [59, 61, 62]

$$f(\vec{r},\vec{v}) = \frac{N\exp\left[-\frac{1}{kT}\left(h+\omega_r p_\theta\right)\right]}{\int d^3\vec{r}\,d^3\vec{v}\exp\left[-\frac{1}{kT}\left(h+\omega_r p_\theta\right)\right]} \tag{4.4}$$

where $h$ and $p_\theta$ are the single particle Hamiltonian and canonical angular momentum about the $z$-axis respectively:

$$h = \frac{mv^2}{2} + q\phi(\rho,z); \qquad\qquad p_\theta = mv_\theta\rho + \frac{qB\rho^2}{2} \tag{4.5}$$

and $\omega_r$ will be shown to be the rotation frequency of the plasma. This function can be further simplified to

$$f(\vec{r},\vec{v}) = n(\rho,z)\left(\frac{m}{2\pi kT}\right)^{3/2}\exp\left[-\frac{1}{2}m\frac{\left(\vec{v}+\omega_r\rho\hat{\theta}\right)^2}{kT}\right] \tag{4.6}$$

where the plasma density is given by

$$n(\rho,z) = n_0\exp\left[-\frac{q\phi(\rho,z) + \frac{1}{2}m\omega_r\left(\omega_c-\omega_r\right)\rho^2}{kT}\right] \tag{4.7}$$

This is a Maxwell-Boltzman distribution superimposed on a rigid-body rotation with $v_\theta = -\omega_r\rho\hat{\theta}$ which is shear-free rotation at a frequency of $\omega_r$. The density function

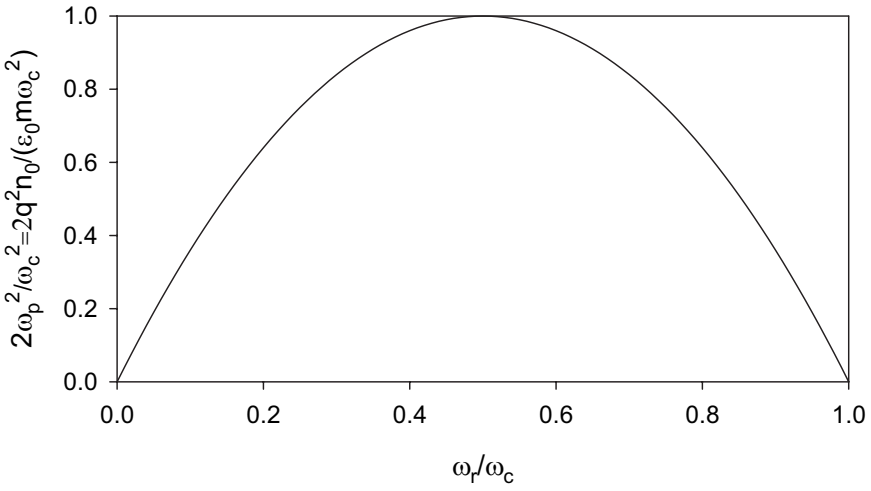


Figure 4.1: The plasma density or plasma frequency as a function of the plasma rotation frequency.

(Eq. 4.7) must also satisfy Poisson's equation requiring a self-consistent solution to $\phi(\rho, z)$:

$$\nabla^2\phi(\rho,z) = \frac{qn(\rho,z)}{\epsilon_0} = \frac{q}{\epsilon_0} n_0 \exp\left[-\frac{q\phi(\rho,z) + \frac{1}{2}m\omega_r\left(\omega_c - \omega_r\right)\rho^2}{kT}\right] \tag{4.8}$$

In the low temperature limit where $T \to 0$, the requirement of a finite plasma density in Eq. 4.7 necessitates

$$q\phi(\rho,z) + \frac{1}{2}m\omega_r\left(\omega_c - \omega_r\right)\rho^2 = 0 \tag{4.9}$$

Thus the plasma must have a constant density, $n_0$. Also, $\phi$ must be independent of $z$ inside the plasma, which is equivalent to the requirement that there be no force on particles along a magnetic field line. Finally, since Poisson's equation (Eq. 4.8) must hold inside the plasma, this constraint implies

$$n_0 = \frac{2\epsilon_0 m\omega_r\left(\omega_c - \omega_r\right)}{q^2} \tag{4.10}$$

The plasma frequency, $\omega_p$, is then given by

$$\omega_p^2 \equiv \frac{q^2 n_0}{\epsilon_0 m} = 2\omega_r \left(\omega_c - \omega_r\right) \tag{4.11}$$

Hence modifying the rotation frequency allows control over the central density of the plasma cloud (Fig. 4.1).

Since the above discussion has been independent of the exact form of the trapping potential, the results of a constant density inside the plasma and a rigid rotation of the cloud apply in general to low temperature plasmas. In addition, these equations imply that only two parameters along with the applied external trapping potential are needed to describe a general plasma cloud at a specified temperature. Thus one only needs to specify the central density and the rotation frequency, the total number and the plasma radius, or many other combinations to completely determine the plasma's shape.

We now assume a Penning trap's quadrupole external potential, $\phi_t$, resulting in a total electrostatic potential, $\phi$, given by

$$\phi = \phi_t + \phi_p \tag{4.12}$$

Solving for the plasma potential, $\phi_p$, using Eq. 4.9 we find

$$\phi_p = \frac{-m}{2q}\left[\omega_r\left(\omega_c - \omega_r\right) - \frac{\omega_z^2}{2}\right]\rho^2 - \frac{m\omega_z^2 z^2}{2q} \tag{4.13}$$

$$= -\frac{m\omega_p^2}{6q}\left(ar^2 + bz^2\right) \tag{4.14}$$

This is just the well-known quadratic potential inside a spheroid charge distribution [63] implying that the equilibrium of a plasma trapped within a quadrupole potential is a spheroid (Fig. 4.2).

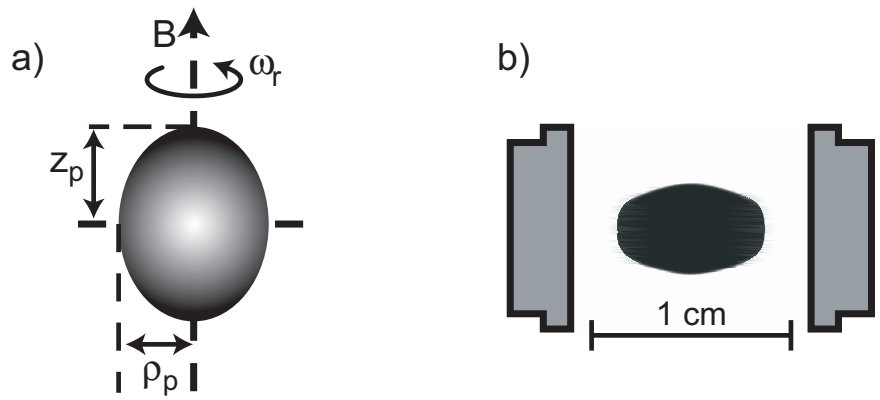


Figure 4.2: Plasma clouds in (a) an ideal Penning trap with quadrupole electric field and (b) an actual cylindrical electrode.

The aspect ratio of the spheroidal plasma cloud, $\alpha = z_p/\rho_p$, can then be related to the plasma frequency and the axial frequency by [64]

$$\frac{\omega_z^2}{\omega_p^2} = \frac{Q_1^0\left(\frac{\alpha}{\sqrt{\alpha^2-1}}\right)}{\alpha^2-1} \tag{4.15}$$

where $Q_1^0$ is the Legendre function of the second kind defined as

$$Q_1(z) = \frac{z}{2}\ln\left(\frac{1+z}{z-1}\right) - 1 \tag{4.16}$$

A final familiar equation for spheroids provides the final formula necessary to link $\alpha$, $\rho_p$, $z_p$, $n_0$, and $N$ together

$$N = \frac{4}{3}\pi\alpha\rho_p^3 n_0 \tag{4.17}$$

In an actual trap, the effect of image charges produced through the interaction of the plasma cloud and the trap electrodes, as well as the deviation of the potential from a pure quadrupole, results in a plasma cloud that is no longer spheroidal. In addition, a finite temperature results in a thin plasma boundary layer proportional to the Debye length, $\lambda_d \equiv \sqrt{\epsilon_0 kT/ne^2}$. The Debye length also plays the important role of determining the screening length within the plasma. This is the length at which

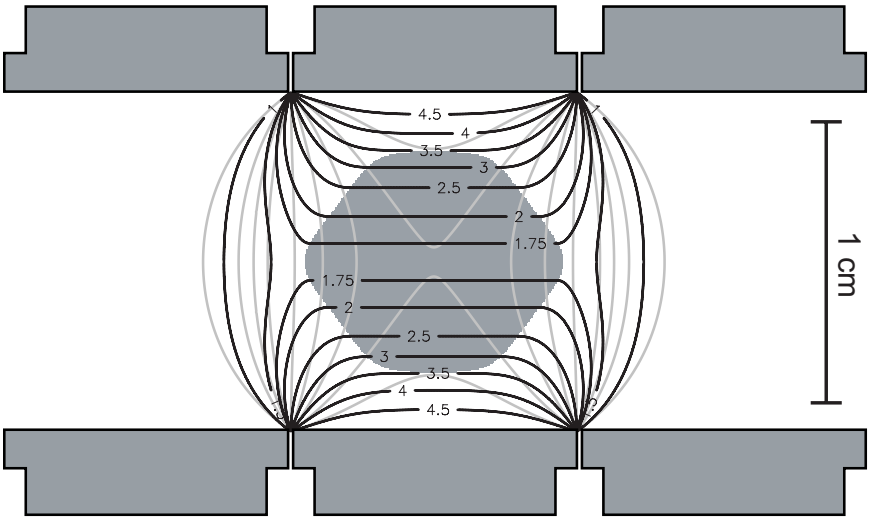


Figure 4.3: Space charge effects of a plasma cloud containing 4.5 million $e^-$ on the potentials within a cylindrical trap. The black contours are the combined potential of the trapping and plasma potentials and the gray contours are the trapping potential alone.

the Coulomb interaction between particles is removed due to the movement of other charges within the plasma to cancel out the field. Figure 4.3 shows the perturbation a plasma cloud induces on the total trap potential as well as the plasma's deviation from an ideal spheroidal shape.

To calculate plasma cloud shapes including these effects we use a computer code, *equilsor2* written initially by Spencer *et al.* [65] and discussed further in Appendix A. This code solves Eqs. 4.7 and 4.8 self-consistently through a combination of the relaxation method discussed in Section 2.2 to solve for the potential and Newton's method to handle the nonlinearity in the function for the plasma density. In practice, Eq. 4.7 describing the plasma density is rewritten as:

$$f(\rho, z) = -\frac{qn_0}{\epsilon_0} \exp\left[-\frac{q}{kT}\left(\phi(\rho, z) - \phi(0, 0)\right) - \kappa\rho^2\right] \tag{4.18}$$

where $\phi(0, 0)$ is the potential at the center of the plasma cloud and the constant $\kappa$ is

adjusted after every iteration to maintain the same plasma radius, $\rho_p$, by the formula

$$\kappa = -\frac{q}{kT\rho_p^2}\left(\phi\left(\rho_p, 0\right) - \phi\left(0, 0\right)\right) \tag{4.19}$$

This iteration technique maintains both a constant central density and plasma radius. However, in our particle clouds the total number is known but not the central density requiring a second adjustment after every 100 or so iterations to adjust the central density to converge on the desired particle number.

### 4.1.1 Dynamics

Within a plasma small deviations from equilibrium can excite collective oscillations whose frequencies depend on the plasma's shape. These modes are classified according to two integers $(l, m)$ with $l > 0$ and $|m| < l$. When $m = 0$ the mode is azimuthally symmetric while $m \neq 0$ modes break this rotational symmetry. The $(1, 0)$ mode is the axial center of mass mode whose frequency is the familiar oscillation frequency for a single particle axial oscillation in the trap, $\omega_1 = \omega_z$. The $(2, 0)$ mode is the quadrupole mode where the plasma remains a spheroid but with an aspect ratio that oscillates in time. Several higher order modes are demonstrated pictorially in Fig. 4.4.

In the low temperature limit, Dubin [67] has analytically calculated the frequencies of these modes. For an arbitrary $(l, 0)$ mode the frequency, $\omega_l$, is given by

$$1 - \frac{\omega_p^2}{\omega_l^2} = \frac{k_2}{k_1}\frac{P_l(k_1)Q_l'(k_2)}{P_l'(k_1)Q_l^(k_2)} \tag{4.20}$$

where

$$k_1 = \frac{\alpha}{\sqrt{\alpha^2 - 1 + \frac{\omega_p^2}{\omega_l^2}}}, \qquad k_2 = \frac{\alpha}{\sqrt{\alpha^2 - 1}}, \tag{4.21}$$

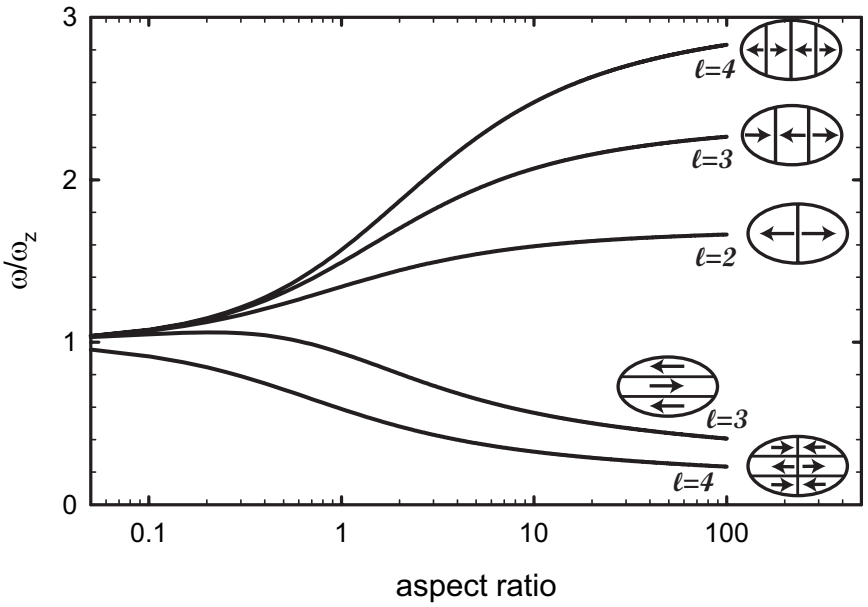


Figure 4.4: The frequency of the low order axisymmetric ($m = 0$) plasma modes as a function of the aspect ratio [66]. Note all frequencies have been scaled to the center of mass ($l = 0$) mode frequency. The axial fluid oscillations inside the plasma are also shown for each mode.

$P_l$ and $Q_l$ are Legendre functions of the first and second kind respectively, and $P_l' = dP_l(z)/dz$ and $Q_l' = dQ_l(z)/dz$ are their derivatives. By combining Eqs. 4.15 and 4.20, the knowledge of $w_1$, $w_2$, and $N$ allows the computation of the aspect ratio of the cloud and thus a complete description of the plasma cloud shape.

As the above result was derived for $T \to 0$, when $T$ is finite the observed quadrupole mode frequency shifts from the cold fluid result, $\omega_2^0$, to [64, 66]:

$$(\omega_2)^2 = \left(\omega_2^0\right)^2 + 5\left[3 - \frac{\alpha^2}{2}\frac{\omega_p^2}{\left(\omega_2^0\right)^2}\frac{\partial^2 A_3}{\partial \alpha^2}\right]\frac{kT}{mz_p} \tag{4.22}$$

where

$$A_3 = \frac{2Q_1(k_2)}{\alpha^2 - 1} \tag{4.23}$$

This shift has been used to determine the temperature of positron plasmas in other experiments [66].

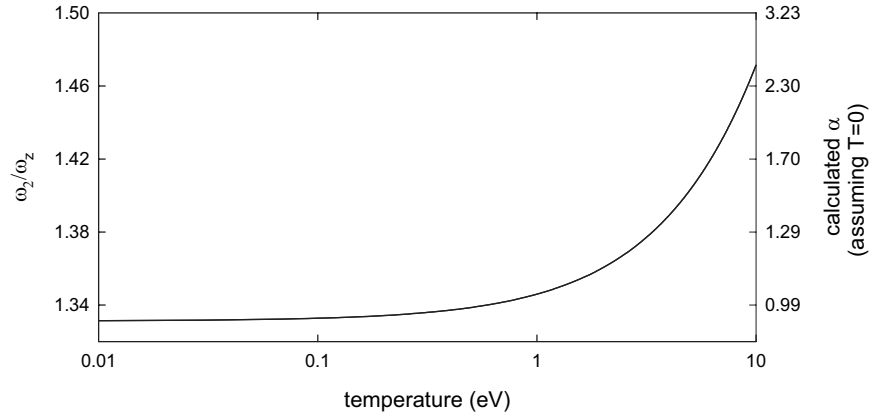


Figure 4.5: Calculated shift in the quadrupole mode as a function of temperature. The plasma cloud is assumed to have 4.4 million $e^-$ with a length of 3.0 mm and aspect ratio of 0.93.

## 4.2 Particle Detection

The most important parameter of a plasma contained in our traps is the number of particles in the plasma. In order to accurately determine this number we have developed several different techniques which are independent cross-checks.

### 4.2.1 Nondestructive Resonant RF Detection of Center-of-Mass Motion

Particles can be counted nondestructively by observing the oscillating image charge induced on nearby trap electrodes. For small numbers of particles this is an excellent technique but, as the particle count increases, axial damping and the increasing anharmonicity of the external potential at large radii creates substantial problems within this technique.

Currents to ground are induced in external circuits connected to a system of conductors, labeled $1 \ldots n$, by a moving point charge with the current on conductor

$i$ given by [68] :

$$I_i = -q\nabla\phi_i\left(\vec{r}\right)\cdot\vec{v} \tag{4.24}$$

Here $\vec{v}$ is the velocity of the moving point charge and $\phi_i\left(\vec{r}\right)$ is the potential induced at the position of the charged particle when conductor $i$ is at a potential of 1 V and all other conductors are at 0 V. For our typical configuration where the amplifier is connected to a nearest neighbor electrode to the central electrode containing the charged particle, the appropriate potential near the center of the trap is (Fig. 4.6):

$$\phi_1\left(\vec{r}\right) = \frac{1}{2}\phi_1^S + \frac{1}{2}\phi_1^A \tag{4.25}$$

$$= \frac{1}{2}\sum_{\substack{j=0\\even}}^{\infty} C_j^1\left(\frac{r}{d}\right)^j P_j\left(\cos[\theta]\right) + \frac{1}{2}\sum_{\substack{j=1\\odd}}^{\infty} D_j^1\left(\frac{r}{z_0}\right)^j P_j\left(\cos[\theta]\right) \tag{4.26}$$

Hence to first order:

$$-\nabla\phi_1 = -\frac{1}{2}\frac{D_1}{z_0}\hat{z} \tag{4.27}$$

so

$$I_1 = -\frac{q}{2}\frac{D_1}{z_0}v_z \tag{4.28}$$

For a positron in a 5 electrode trap with 4.2 K average thermal energy, this corresponds to a current given by $I_1 = 0.1\,\mathrm{fA}\cos\left(\omega_z t\right)$, oscillating at frequency $\omega_z/2\pi \approx 40\,\mathrm{MHz}$.

The induced current on the electrodes results in an additional potential, $V$, applied to the compensation electrode. This potential creates an extra force on the trapped charge particle adding damping to the axial equation of motion [69, 70]:

$$\ddot{z} = -\omega_z^2 z - \gamma\dot{z} - \frac{qD_1V}{2mz_0} \tag{4.29}$$

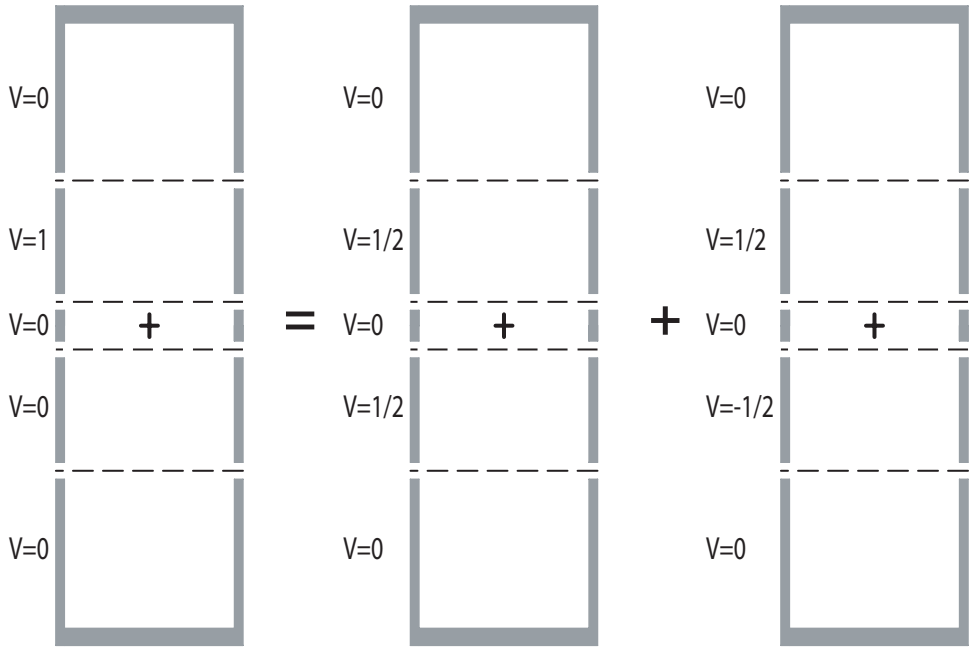


Figure 4.6: Electrode potentials used to calculated the induced image current from a charged particle oscillating in the center of the trap.

where $\gamma$ is the axial damping rate and $\omega_z$ is the characteristic frequency of the harmonic restoring force on the particle. Using Eqs. 4.28 and 4.29, this equation can be rewritten as

$$V = l_{1p}\frac{dI}{dt} + \frac{1}{c_{1p}}\int I dt + r_{1p} I \tag{4.30}$$

where

$$l_{1p} = m\left(\frac{2z_0}{qD_1}\right)^2, \qquad c_{1p} = \frac{1}{l_p\omega_z^2}, \qquad r_{1p} = \gamma m\left(\frac{2z_0}{qD_1}\right)^2 \tag{4.31}$$

This result can be easily be generalized to $N$ particles by noting that $I_N = NI_1$, so

$$l_p = \frac{l_{1p}}{N}, \qquad c_p = Nc_{1p}, \qquad r_p = \frac{r_{1p}}{N} \tag{4.32}$$

Eq. (4.30) thus implies that the center of mass oscillation for a trapped cloud of particles is equivalent to an $r_p l_p c_p$ circuit with a resonant frequency $\omega_z$. Coupling

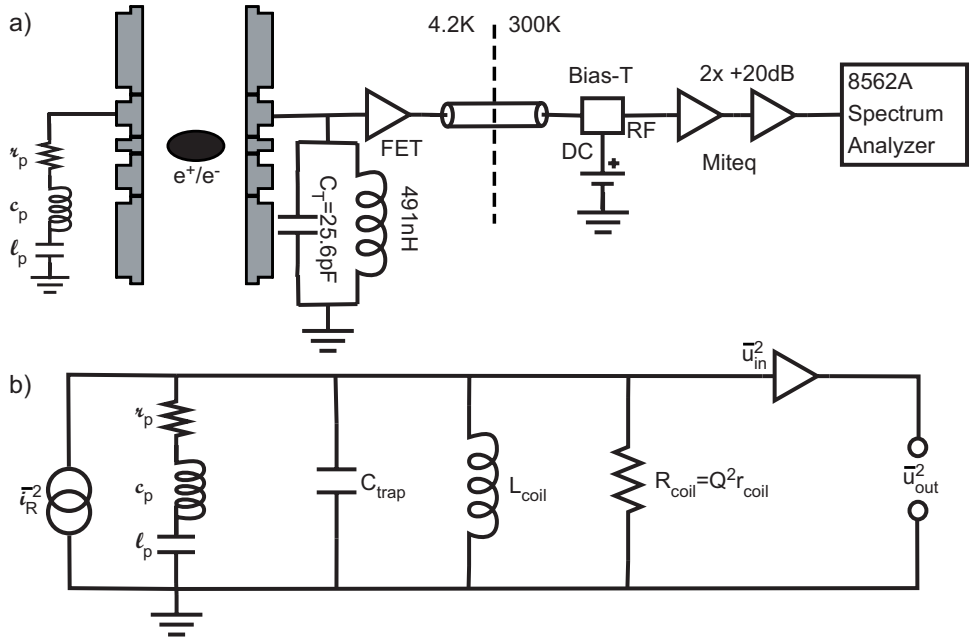


Figure 4.7: (a) The schematic of amplifier circuit used to detect particle. (b) Equivalent circuit.

these particles to an external $LC$ "tank" circuit results in the equivalent circuit given by Fig. 4.7. In this figure the parasitic series resistance, $r_{coil}$, of the inductor has been replaced by the equivalent $R_{coil} = Q^2 r$ where $Q$ is the quality factor of the tank circuit (see below). Note this conversion is valid only for a narrow bandwidth around $\omega_{LC}$ within which we work.

First, we consider the case where there are no particles in the trap. The circuit is driven by the Johnson thermal noise produced by the resistors $R_{coil}$ and $r_p$, but $r_p$ is much smaller and can be neglected. The current noise power spectral density for $R_{coil}$ is then given by $(\bar{i}_R)^2 = 4k_bT/R$ [71] which for our typical inductors at 4.2 K is $1000\,\mathrm{pA}^2/\,\mathrm{Hz}$. The average preamplifier input voltage power spectral density is then

| Parameter | Value |
|---|---|
| $\nu_{LC}$ | 39.164 MHz |
| $Q$ | 597 |
| $L_{coil}$ | 491 nH |
| $r_{coil}$ | 210 mΩ |

| Parameter | Value |
|---|---|
| $C_{trap}$ | 25.6 pF |
| $c_{1p}$ | $4.771 \times 10^{-9}$ pF |
| $l_{1p}$ | 3.461 kH |
| $\gamma_z/2\pi$ | 3.204 Hz |

Table 4.1: Typical amplifier parameters

given by $(\overline{u}_{in})^2 = |Z(\omega)|^2 (\bar{i}_R)^2$ where $Z(\omega)$ is the impedance of the equivalent circuit:

$$Z(\omega) = \frac{1}{\frac{1}{R_{coil}} + \frac{1}{i\omega L_{coil}} + i\omega C_{trap}} \tag{4.33}$$

For $\omega \approx \omega_{LC}$ this power spectrum, $P(\omega)$, reduces to a Lorentzian where $\omega_{LC} = 1/\sqrt{L_{coil}C_{trap}}$ and $\Gamma = 1/C_{trap}R_{coil} = r_{coil}/L_{coil}$:

$$P(\omega) \propto \frac{1}{\left(\frac{\Gamma}{2}\right)^2 + (\omega - \omega_{LC})^2} \tag{4.34}$$

When particles are trapped with axial frequency $\omega_z \approx \omega_{LC}$, the particle $l_p c_p$ circuit shorts out frequencies near the center frequency $\omega_{LC}$ resulting in a frequency spectrum composed of a dip surrounded by two peaks separated by a width proportional to $\sqrt{N}$. Analytically, the impedance changes to

$$Z(\omega) = \frac{1}{\frac{1}{\frac{1}{r_p} + i\omega c_p + \frac{1}{i\omega L_p}} + \frac{1}{R_{coil}} + \frac{1}{i\omega L_{coil}} + i\omega C_{trap}} \tag{4.35}$$

We will first assume that there is very little axial damping resulting in $r_p \approx 0$. Then the observed power spectrum reduces to [72]

$$P(\omega) \propto \frac{\omega_{LC}^4 (\omega_z^2 - \omega^2)}{\left[(\omega_z^2 - \omega^2)(\omega_{LC}^2 - \omega^2) - \omega^2 \Gamma N \gamma_z\right]^2 + \omega^2 \Gamma^2 \left[(\omega_z^2 - \omega^2) + \Gamma N \gamma_z\right]^2} \tag{4.36}$$

where $\gamma_z = \left(\frac{d_1 q}{2 z_0}\right)^2 \frac{R_{coil}}{m}$. Assuming $N\gamma_z \gg \Gamma$, two peaks are formed when the reactive impedance, $Z \approx \frac{2 l_{1p}}{N}(\omega - \omega_z)$, of the particles cancels the imaginary impedance of the

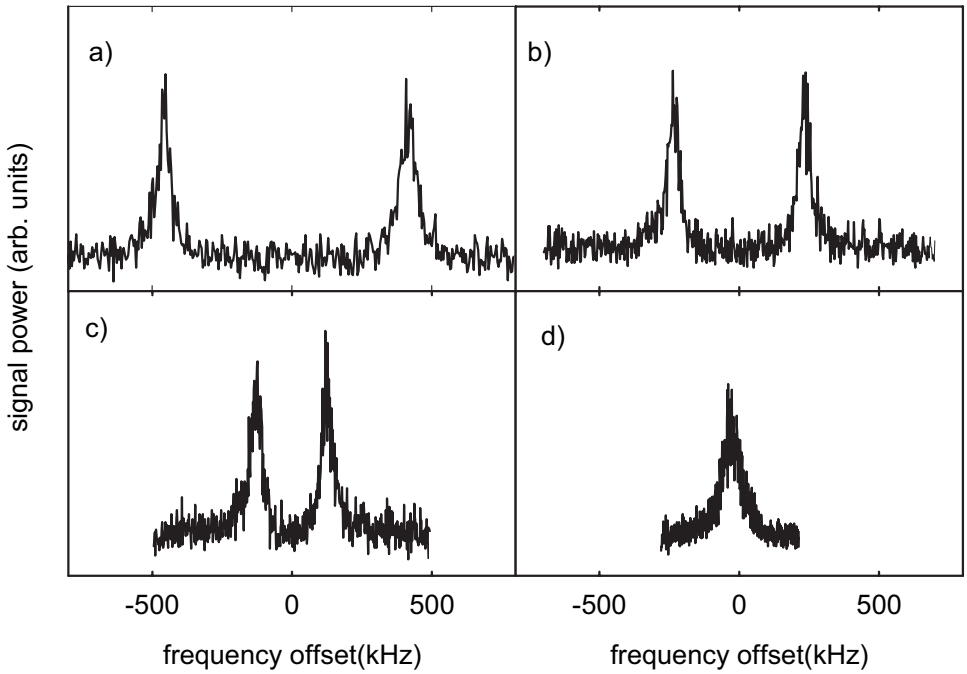


Figure 4.8: Sample amplifier power spectrums for (a) 3.5 million $e^+$, (b) 1.0 million $e^+$, (c) 0.29 million $e^+$, and (d) LC resonance (0 $e^+$).

"tank" circuit, $Z \approx \left(2C_{trap}\left(\omega - \omega_{LC}\right)\right)^{-1}$. The number of particles, $N$ is then given by $\Delta\omega_z = \left(\sqrt{\left(C_{trap} l_{1p}\right)}\right)^{-1} = \sqrt{\left(N\Gamma\gamma_z\right)}$ where $\Delta\omega_z = 2\left(\omega_z - \omega\right)$. Figure 4.8 shows observed power spectrums versus the number of particles.

In a real particle cloud, axial damping external to the circuit shown in Fig. 4.7b can not be ignored [73]. This damping can be due to coupling with other modes (primarily the cyclotron motion or a plasma mode) as well as the anharmonicity caused by the cylindrical electrode stack. We first consider a simplified model where the particle cloud's resistance, as parameterized by $r_n$, is independent of the number of particles. As shown in Fig. 4.9 the effect of the damping is too slow down the growth of the dip width with increasing particle number and to eventually reverse it. The comparison of particle number obtained by dumping the charged particles to a current detector

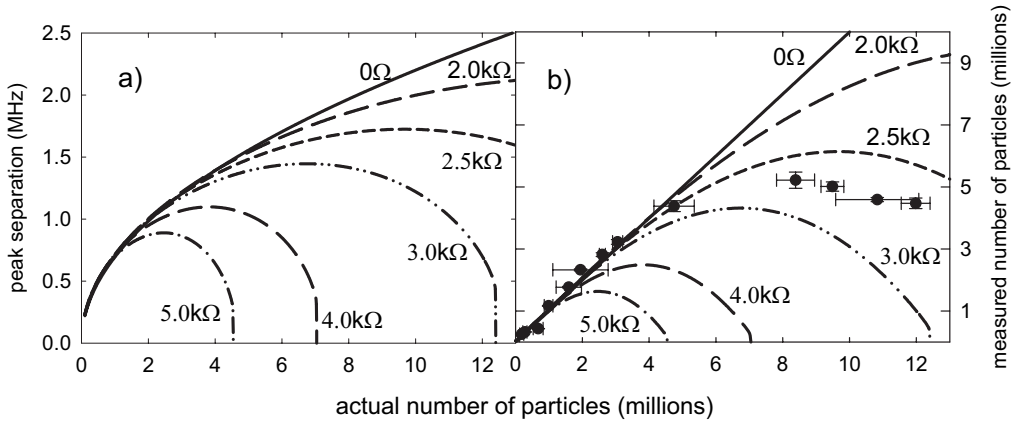


Figure 4.9: The effects of finite particle damping on (a) width of amplifier resonance dip and (b) the number of particles measured assuming zero particle resistance versus the actual number. The experimental data points show the measured number of particles from the width of the particle dip compared to the number measured via a current amplifier as discussed in Section 4.2.3.

(discussed in the next section) with that counted by the RF amplifier assuming $r_n = 0$ shows that $r_n \approx 2.75\,\mathrm{k\Omega}$ in HBAR1. This is much lower than the effective resistance of the tank circuit coil on resonance, which is approximately $75\,\mathrm{k\Omega}$. External axial damping thus has a negligible effect on axial cooling of the trapped particles.

It is remarkable that this simple model of a constant axial damping independent of the number of particles fits well with experiment. From Eqs. 4.31 and 4.32, $r_n \propto \gamma/N$ where $\gamma$ depends on $N$ in a complicated manner. For example, a primary axial damping mechanism is cyclotron damping where Coulomb collisions between the constituent charged particles of the plasma cloud transfer energy from the center of mass motion to cyclotron motion which then decays immediately due to synchrotron radiation (Section 3.2.1). The equipartition rate at which this energy transfer occurs is proportional to the density of the plasma cloud [74]. As the density is approximately linearly dependent on particle number (Fig. 4.23), $r_n$ should be independent of particle

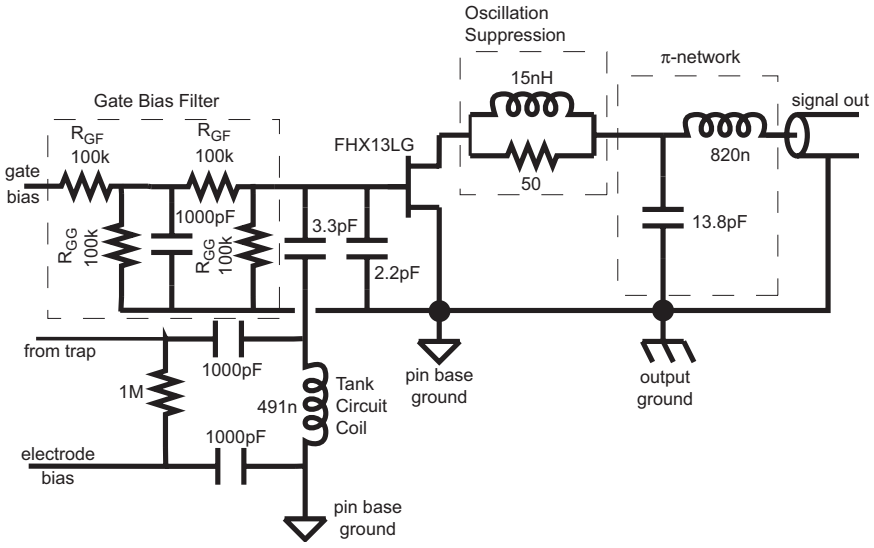


Figure 4.10: HEMT RF amplifier schematic

number to first order.

### Cryogenic Amplifiers

To both transform the high impedance of the equivalent circuit (approximately 70 kΩ) to a lower one that can be coupled to a 50 Ω transmission line as well as to amplify the $5\,\mu A^2/\,Hz$ signal ($\bar{u}_{in}^2$), we utilize a cryogenic FET preamplifier circuit physically located just above the electrode stack (Fig. 4.10). At the heart of the circuit is a Fujitsu FHX13LG HEMT transistor which when operated with a drain-source current of 100 µA has a transconductance, $g_t$, and output resistance, $R_d$, given by [75]

$$g_t = \frac{dI_{ds}}{dV_{gs}} = 10\,\text{mS} \qquad\qquad R_d = \frac{dV_{ds}}{dI_{ds}} = 2\,\text{k}\Omega \tag{4.37}$$

The $\pi$-net section then serves to transfer the 2 kΩ output impedance of the HEMT to the 50 Ω transmission line. The output signal is thus given by

$$\bar{u}_{out}^2 = g_t^2 \bar{u}_{in}^2 R_d^2 = 400 \bar{u}_{in}^2 \tag{4.38}$$

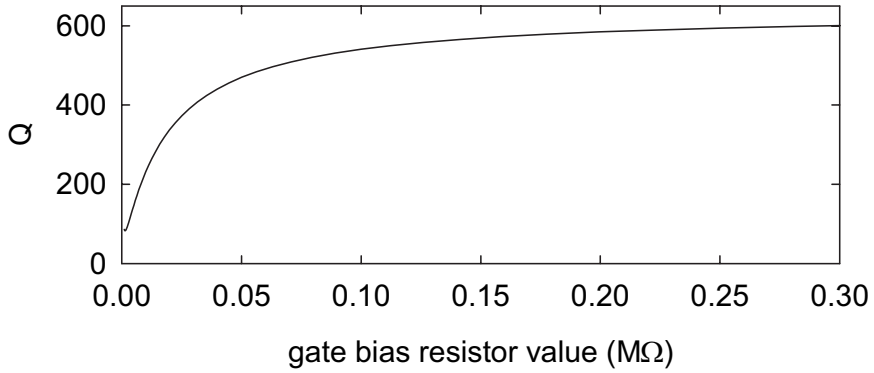


Figure 4.11: Amplifier Q as a function of resistors in the gate biasing circuit ($R_{GG} = R_{GF} = R$). The coil's series resistance is assumed to be $0.3\,\Omega$ resulting in the limiting Q value of 630.

The first attempts at using this amplifier circuit with the large radioactive source employed at CERN resulted in failure. Within a few minutes of the transistor being exposed to the source, the gate insulator was destroyed resulting in the classic symptom of a blown FET whereby the gate can no longer control the current flowing through the FET. In these circuits, several of the resistors in the gate bias circuit had different values than shown in Fig. 4.10. In particular $R_{GF} = 1\,\mathrm{M}\Omega$ and the two resistors labeled $R_{GG}$ were removed. As HEMT transistors are known to be quite resilient to radiation damage [76], the likely culprit was charging of the gate due to the high impedance to ground of the gate bias network resulting in an arc that damaged the gate insulating layer. To prevent this, the two resistors labeled $R_{GG}$ were added. These have the side-effect of reducing the tank circuit $Q$ (Fig. 4.11) so they were initially chosen to be $1\,\mathrm{M}\Omega$ as well. This resulted in a large improvement but after approximately one day of exposure to the radioactive source the FET gate was destroyed. The final configuration was then implemented with $R_{GG} = R_{GF} = 100\,\mathrm{k}\Omega$ which has lasted for over 6 months of use with no signs of degradation.

### 4.2.2 Amplitude RF Detection

The limitations of our currently utilized techniques makes it necessary to develop a new technique for non-destructively counting large number of charged particles if we are to utilize more than 5 million particles in a useful manner. Given the 12 hours needed to load 5 million $e^+$, it is especially imperative to develop an alternative to the destructive counting technique currently necessary for large numbers of positrons.

One alternative technique is the closely related method to our resonant RF detection that is used by ATHENA. Here the plasma is externally driven at the center of mass resonance and the power transmitted through the plasma cloud to another electrode is then measured [77]. In this method the plasma is again replaced by the same equivalent circuit model but the shape and amplitude of the particle's $RLC$ resonance is measured as opposed to its coupling to an external $LC$ circuit. This measurement is then combined with a separate measurement of the quadrupole plasma mode frequency (discussed in Section 4.3.2) to provide a complete description of the plasma cloud. This method does however require a difficult calibration due to the need to know the frequency dependent gain of the external circuit and is likely to change every time the experiment is thermally cycled. Finally it, in a similar manner to the coupled circuit detection technique, under counts large numbers of charged particles although this occurs above $10^8$ particles as compared to $5 \times 10^6$ for our method.

### 4.2.3 Destructive Charge Counting

While resonant RF detection has the major advantage of being non-destructive to the trapped particles, it does have several disadvantages. First, as the particle

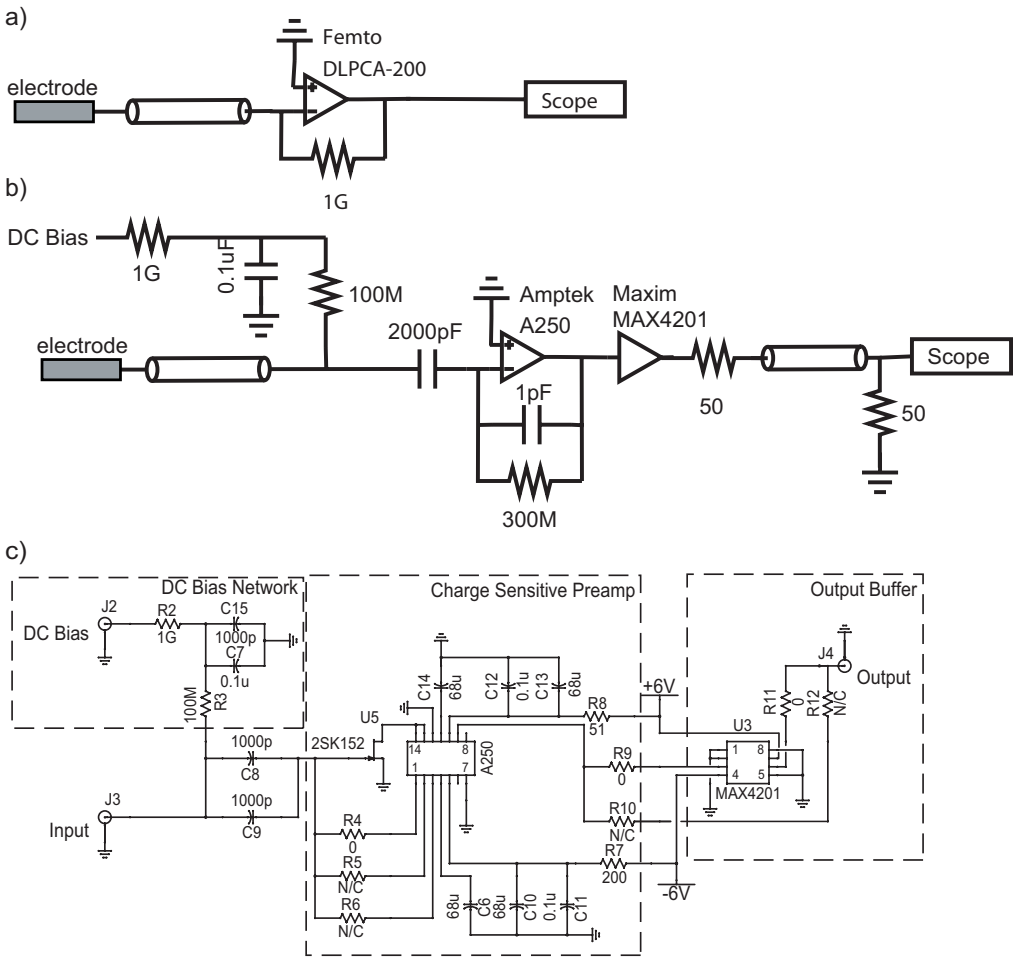


Figure 4.12: Schematics of (a) current and (b) charge detector systems. (c) shows the full charge detector schematic that is shown as an overview in (b).

number grows the reported counts become less accurate and eventually multi-valued as discussed above. Second, calibration of $\gamma_z$ requires a knowledge of the inductance of the tank coil which is located at 4.2K and depends on temperature making it hard to obtain an accurate value once the trap is cold. To avoid the necessity of obtaining a calibration requiring knowledge of component values at 4.2 K, we used techniques based on counting the charge or current resulting from dumping particles onto a Faraday cup electrode (Fig. 4.12).

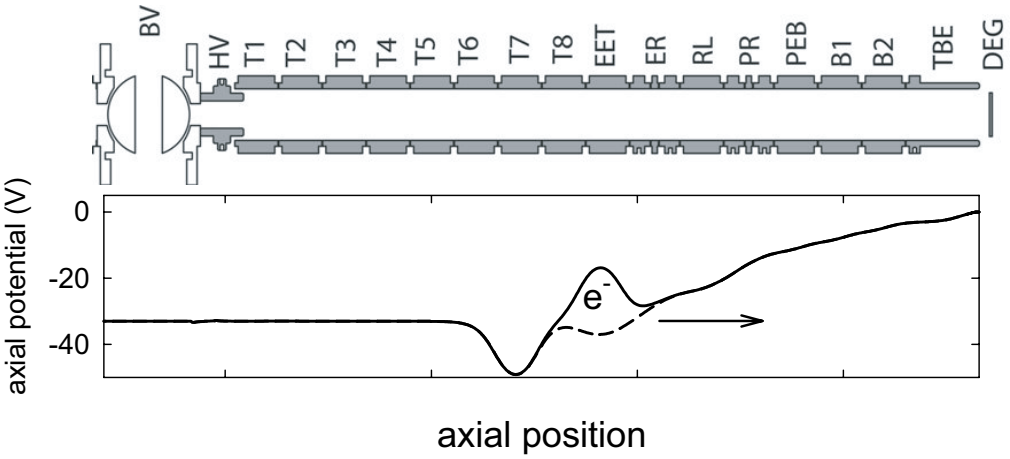


Figure 4.13: Potentials used to ramp $e^-$ onto *DEG* for counting using a current preamplifier.

The first method utilizes a current amplifier (FEMTO DLPCA-200) that has a gain of $10^9\,\mathrm{V/A}$ with a 3 dB bandwidth of 1.2 kHz. This amplifier is, in essence, a carefully constructed operational amplifier with a feedback resistor of 1 GΩ. Particles are then slowly ramped towards the Faraday cup electrode (*DEG*) by applying a linear voltage ramp to the electrode where the particles are initially located (Fig. 4.13). The observed current (Fig. 4.14) can then be integrated to obtain the total number of charge particles detected. Note that the presence of the ramp prevents secondary electrons emitted from *DEG* from escaping and reducing the counted number of $e^-$ (since Be has a yield of over 1 secondary electron per incoming electron [78]). The primary disadvantage to this technique is the wide bandwidth required to ensure an accurate count (which is approximately from 50 Hz to 10 kHz). This area is where $1/f$ noise predominates and it results in a signal to noise ratio that precludes counting clouds composed of much less than 1 million particles. In addition the small amplifier bandwidth prevents ramping particle clouds faster to avoid this noise.

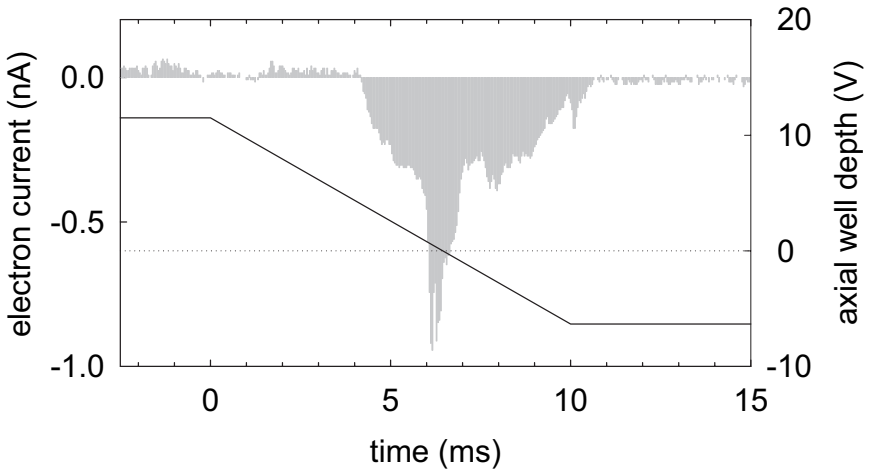


Figure 4.14: Faraday cup current amplifier signal from 12.7 million $e^-$ ramped onto the *DEG* Faraday cup.

To avoid these noise problems, we developed a charge sensitive preamplifier (Fig. 4.12c) which is composed of an operational amplifier with a capacitor, $C_f = 1\,\text{pF}$, in the feedback loop instead of a resistor. From the requirement that the two inputs be at equal voltage, this forces the output to be given by $V_{out} = Q/C_f$ where $Q$ is the input charge. The additional $300\,\text{M}\Omega$ resistor in parallel with $C_f$ causes the charge to be drained away with a characteristic time constant of $300\,\mu\text{s}$ thus resetting the preamplifier for a new charge pulse.

To count particles with this preamplifier, the pulsing techniques described in Section 3.2.2 are employed to transfer an approximately 10 ns long charge pulse containing all the particles in the cloud onto the Faraday cup. The observed signal is then an exponential decay (Fig. 4.15) with the peak of the signal proportional to the number of particles, $N = C_f V_{peak}/q$.

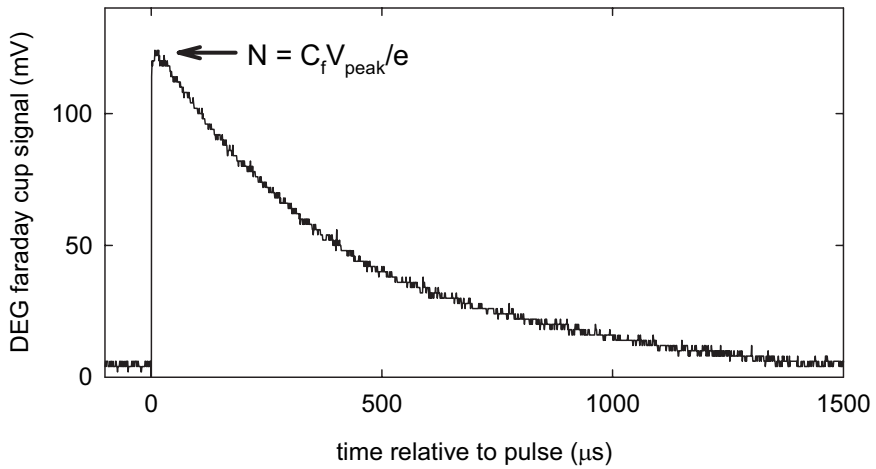


Figure 4.15: Charge sensitive amplifier signal from 2.7 million $e^-$ pulsed onto the *DEG* Faraday cup.

### 4.2.4 Annihilation Detection

One of the advantages of working with antimatter is that it is easy to detect and count annihilations with matter. Antiproton annihilation with protons proceeds with many possible decay channels [79]. However on average the annihilation can be written approximately as

$$\mathrm{p} + \overline{\mathrm{p}} \rightarrow 3.0\pi^{\pm} + 2.0\pi^{0} \tag{4.39}$$

It is instructive to trace the path of a charged pion produced during an antiproton's annihilation on a trap electrode through the two stages of the annihilation detector (Fig. 4.16). The charged pion first reaches the three scintillating fiber layers composed of 1.9 mm diameter optical fibers with the fibers in the inner two layers arranged in a helix oriented at a 30° angle from vertical. Inside these fibers, molecules excited by the passage of a high energy pion emit photons that are then detected in photomultiplier tubes located below the experiment. The small distance from the electrode stack to the fiber detectors results in a high solid angle and a unit efficiency for detection of

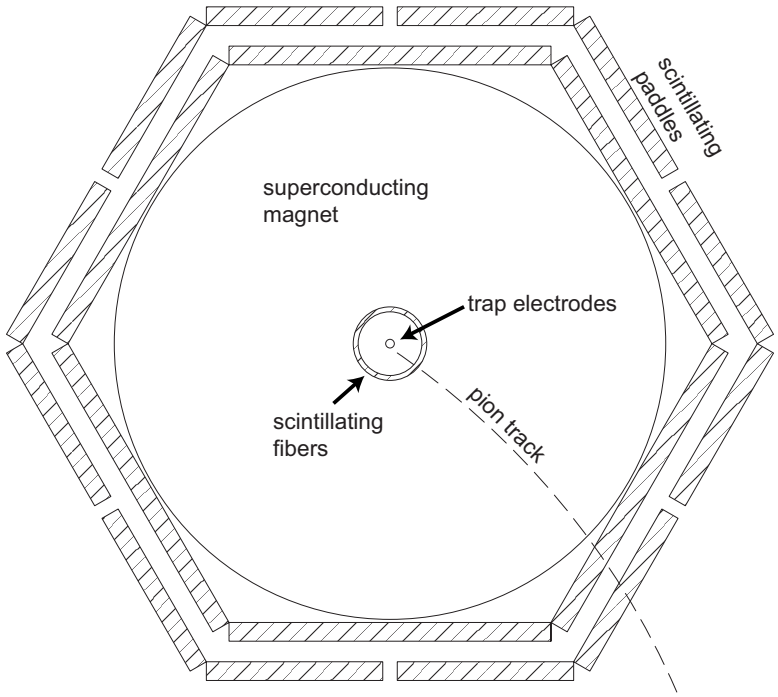


Figure 4.16: The antiproton annihilation detector consists of inner scintillating fibers and outer scintillating paddles.

| Channel | Definition | Antiproton annihilations per count | Background count rate per second |
|---|---|---|---|
| Singles | Count in both scintillating paddle layers | $2.1 \pm 0.1$ | 60 |
| Fibers | Count in 2 out of 3 scintillating fiber layers | $1.0 \pm 0.1$ | 10 |
| Triggers | Coincidence of a fiber and a single count | $2.6 \pm 0.2$ | 1 |

Table 4.2: Calibration parameters for the antiproton annihilation detector channels.

antiproton annihilations as at least one of the on average 3 charged pions will pass through the fiber layers. To be recorded as an annihilation event at least one fiber in two out of the three layers must fire. Background counts from cosmic particles and electronic noise result in a background fiber count rate of approximately 10 per second.

The second stage of the detector is composed of two layers of plastic scintillating paddles located just outside of the superconducting magnet's helium dewar. Again at least two paddles in line with each other and the trap center must fire for an event to be recorded in order to reduce the background count rate. The smaller solid angle due to the larger radius results in a detection efficiency of only 50 % and the greater area of the detector presents an increased cross section for cosmic events leading to a background rate of 60 counts per second.

Further noise reduction at the expense of signal amplitude can be achieved by requiring a temporal coincidence of a count from the fiber detector and outer paddle detector. This results in an efficiency of 38 % with a background rate of 1 count per second.

To increase the signal to noise ratio even more, we apply a short duration linear voltage ramp to the electrode where the particles are initially located which reduces the well depth to 0 V. The trap potential is ramped beforehand so as to then direct the antiprotons towards the ends of the trap where they annihilate (Fig. 4.17). A typical ramp time is 10 ms resulting in only a 1 % chance of one or more noise counts in a typical ramp. By correlating counts with the well depth at the same time, the energy spectrum of antiprotons within the well can also be inferred (Fig. 4.18).

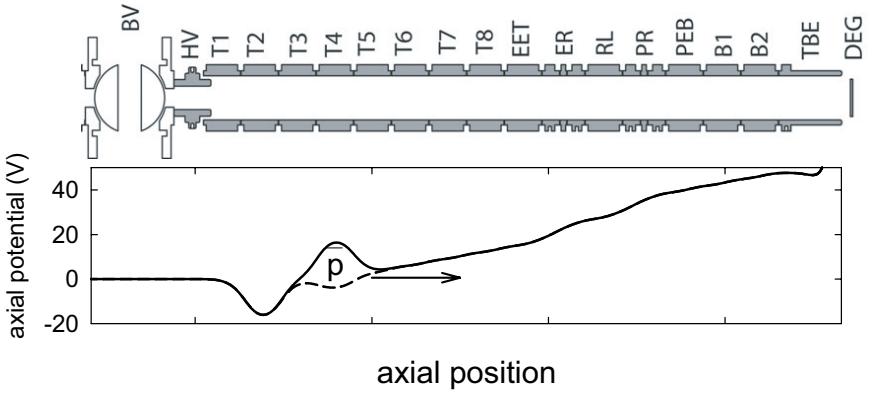


Figure 4.17: Trap potential ramp for $\overline{\mathrm{p}}$ annihilation detection.

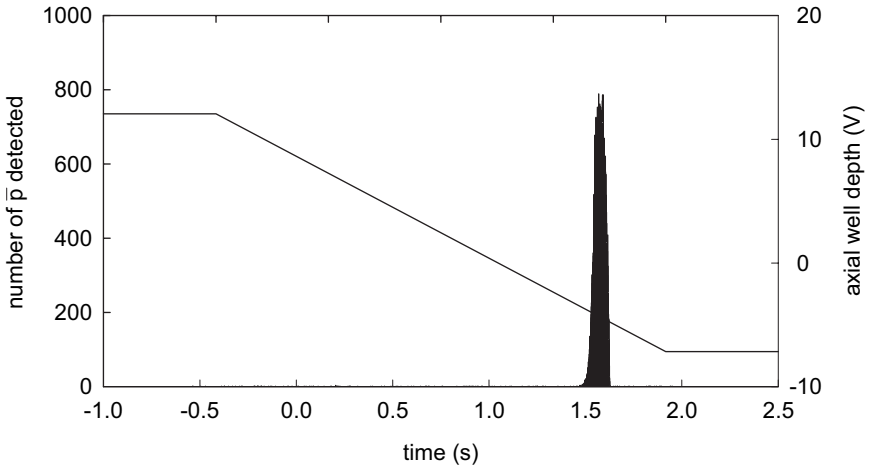


Figure 4.18: Annihilation ramp signal from 40,000 $\overline{\mathrm{p}}$.

### 4.2.5 Counting Techniques Comparison

Typically we measure $e^+$ and $e^-$ numbers using RF center-of-mass detection as this technique is non-destructive. However, after the plasma cloud grows beyond approximately 5 million particles, axial damping precludes accurate counts (Fig. 4.9). In addition accurate calibration of this counting technique is difficult due to the necessity to know component values at 4.2 K. The current, charge, and annihilation detection techniques avoid these problems but come with the major drawback of being destructive to the trapped particles. While the annihilation detection technique has an excellent signal to noise ratio when utilized with careful timing which allows for the detection of a single trapped antiproton, the current and charge detection techniques have a much lower signal to noise ratio. This limits the number of charged particles detected to approximately 1 million for the current amplifier and approximately 50,000 for the charge sensitive amplifier.

## 4.3 Plasma Parameters

A second parameter besides the total particle number, $N$, is needed to fully characterize the shape of the plasma cloud. This parameter can be the axial or radial extent, the rotation frequency, or the central density. Once this parameter has been given all other quantities can be calculated using the formulas described previously. To determine this constant we have developed two independent techniques.

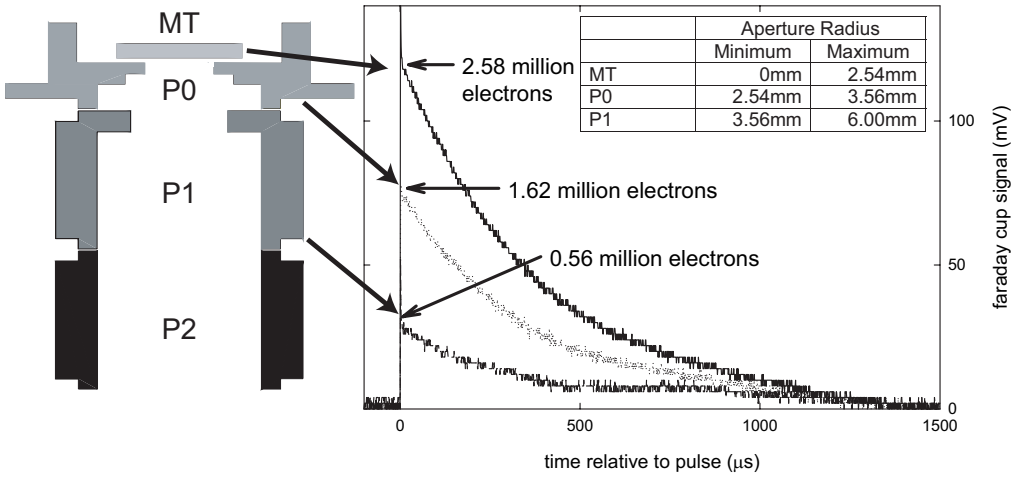


Figure 4.19: Typical response from pulsing $e^-$ at the Faraday cup apertures in HBAR2.

### 4.3.1 Aperture Detection

The first technique [80] utilizes the fact that the transmission efficiency, $P_a$, of particles through a constricted aperture will uniquely determine the radius of a spheroidal cloud

$$P_a = 1 - \left[1 - \left(\frac{a}{\rho_p}\right)^2\right]^{3/2} \tag{4.40}$$

This equation is then combined with three results from Section 4.1 to calculate the remaining plasma cloud parameters:

$$N = \frac{4}{3}\pi\alpha\rho_p^3 n_0 \tag{4.41a}$$

$$\frac{\omega_z^2}{\omega_p^2} = \frac{Q_1^0\left(\frac{\alpha}{\sqrt{\alpha^2-1}}\right)}{\alpha^2-1} \tag{4.41b}$$

$$\omega_p^2 \equiv \frac{q^2 n_0}{\epsilon_0 m} \tag{4.41c}$$

$P_a$ can be determined in several ways. The first method employed was to place a constricted aperture (the ball valve in HBAR1) with a diameter of $2a_{BV} = 5\,\text{mm}$

between two trap electrodes with RF counting amplifiers connected to them [80]. Particles could then be counted initially, pulsed through the aperture, caught, and finally counted on the other side which gives $P_{a_{BV}} = N_f/N_i$. This technique requires careful calibration of both amplifiers to ensure accurate particle counts as well as repeated timing optimizations for all cloud sizes. In addition, the presence of the aperture in the middle of the trap limits the flexibility to move and store particles within the trap reducing the ability to maintain large numbers of positrons.

To avoid these restrictions, the upper part of HBAR2 includes a series of electrodes with increasing aperture diameters, *MT*, *P0*, and *P1*, connected to charge sensitive preamplifiers (Fig. 4.19). By pulsing particles onto these electrodes and recording the amount of charge collected on each electrode both the total number of particles in the cloud as well as the radius can be calculated simultaneously:

$$N_{total} = N_{MT} + N_{P0} + N_{P1} \tag{4.42a}$$

$$P_{a_{MT}} = \frac{N_{MT}}{N_{total}} \tag{4.42b}$$

To remove the assumption of a spheroidal equilibrium, the *equilsor2* code described earlier was modified to solve for a plasma cloud defined by the number of particles, $N^{(goal)}$ and the transmission through an aperture, $P_a^{(goal)}$. In this case, the code modified the midplane plasma radius, $r_p$ and central density, $n_0$ every 100 iterations as follows:

$$r_p^n = r_p^{n-1}\left[\frac{P_a^{(goal)}}{P_a^{(calc)}}\right]^{0.4} \tag{4.43a}$$

$$n_0^n = n_0^{n-1}\left[\left(\frac{N^{(goal)}}{N^{(calc)}}\right)\left(\frac{P_a^{(calc)}}{P_a^{(goal)}}\right)^2\right]^{0.4} \tag{4.43b}$$

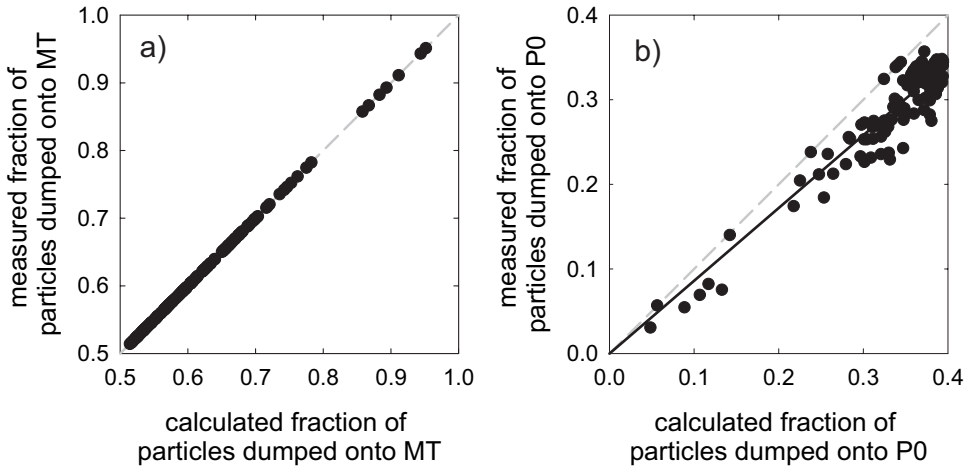


Figure 4.20: The measured fraction of $e^-$ dumped onto (a) *MT* and (b) *P0* compared to the calculated value from the thermal equilibrium code. The grey dashed line shows a one to one correspondence. The perfect one to one correlation of the *MT* particle fraction demonstrates the thermal equilibrium code's iteration technique converges to the measured fraction.

where raising the adjustment factors to the 0.4 power prevents oscillatory behavior in the convergence of the solution. Comparing the measured electron fraction dumped onto the three Faraday cups versus the values calculated using the thermal equilibrium code above based only on the measured electron fraction dumped onto *MT* shows that this code does an excellent job of matching the measured fraction on *MT* to a thermal equilibrium state (Fig. 4.20a). However, the measured value for the fraction dumped onto *P0* is 14 % lower than the calculated value (Fig. 4.20b). This suggests that the thermal equilibrium calculation is missing some important component. The discrepancy could be from small patches of charge on the electrode or thermoelectric effects on the electrode biasing networks both of which alter the trapping potential or it could be from some entirely different cause.

Figures 4.21 and 4.23 compare the measured plasma parameters when assuming a spheroid plasma shape to those calculated utilizing the full *equilsor* equilibrium

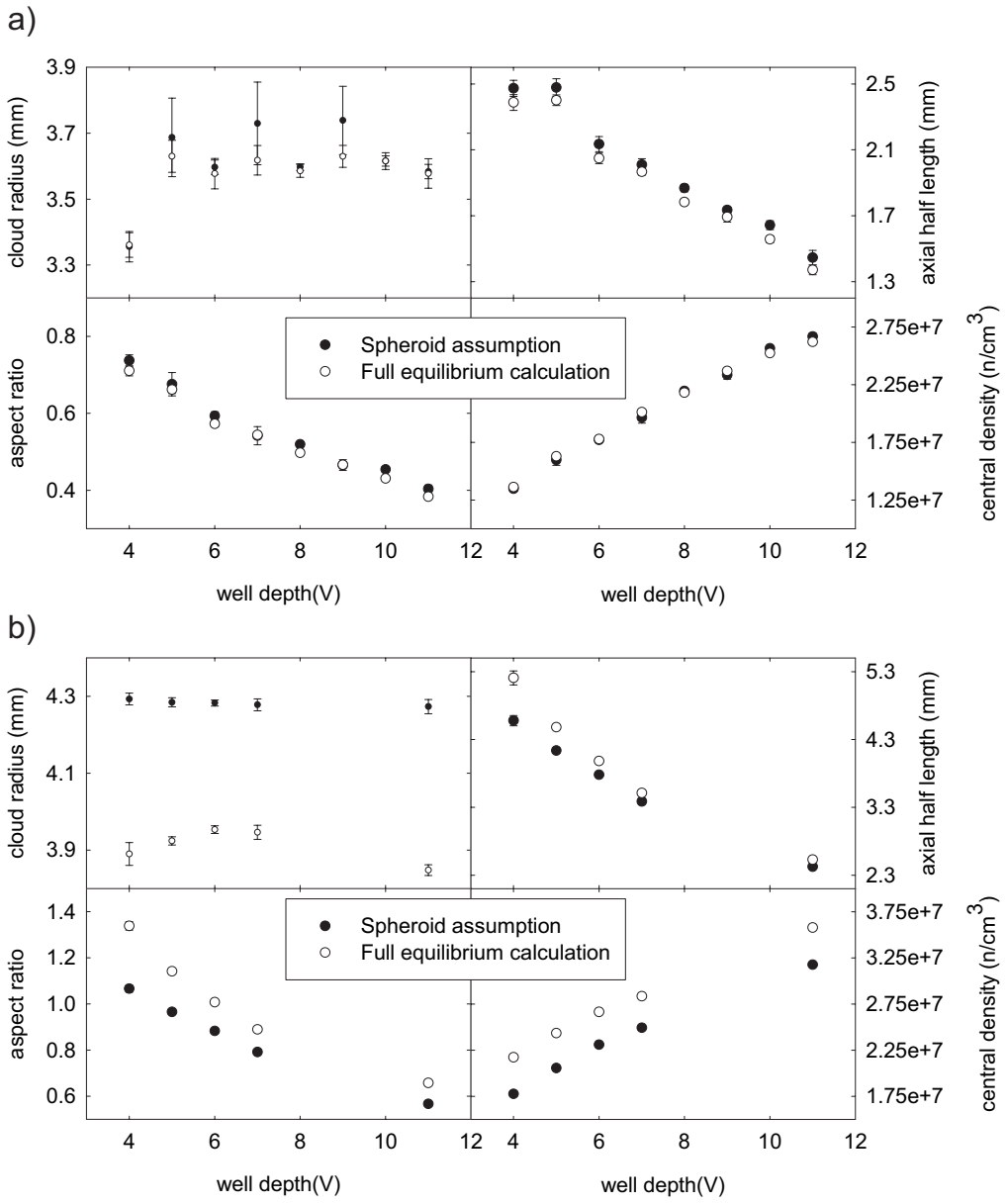


Figure 4.21: Plasma shapes measured by the Faraday cup apertures for clouds of a) 2 million $e^-$ and b) 6 million $e^-$.

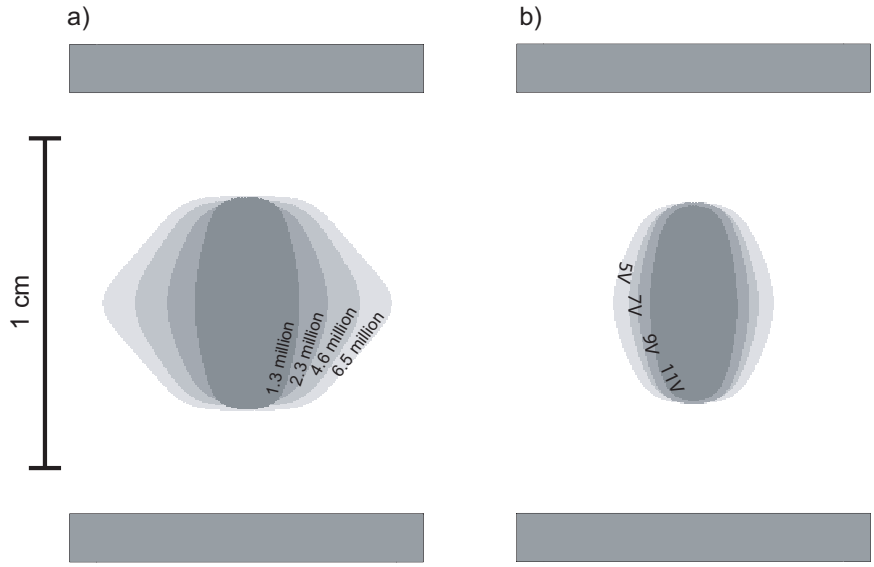


Figure 4.22: Typical $e^-$ clouds (a) in a 5 V well with variable particle numbers and (b) with 2.2 million $e^-$ at various well depths.

calculation. Note that the two methods agree well for the smaller 2 million $e^-$ cloud but diverge for the 6 million $e^-$ cloud. In this case the larger cloud samples a more anharmonic external trapping potential and elongates in the axial direction (Fig. 4.22).

Several other features of the plasma cloud shape's dependency on the well depth are worth discussing. First, there is very little change of the radius with increasing well depth. This is expected as the angular momentum of the cloud should remain approximately constant due to the primary contribution being the field momentum which depends only on the magnetic field and mean radius. Instead as the well depth increases, the plasma is compressed axially increasing the central density. In addition, increasing the particle number primarily results in an axially elongated cloud suggesting that the FEP loading technique used to produce these clouds can only load particles up to a maximum radius of approximately 4 mm. To increase the number of particles in the cloud, the plasma instead elongates axially and the density

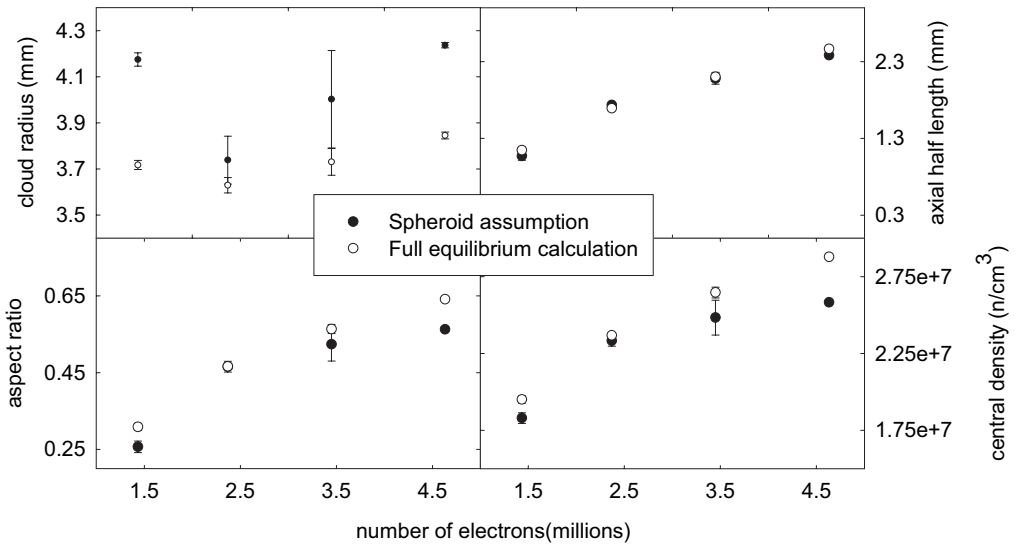


Figure 4.23: Plasma shapes measured by the Faraday cup apertures for $e^-$ clouds in a 9 V well.

increases.

The independence of the angular momentum on the well depth suggests that it is the ideal parameter to characterize these clouds with (Fig. 4.24). Thus for electrons loaded from the FEP and positrons loaded from magnetized positronium atoms:

$$P_\theta^{(e^-)} = 2.71 \times 10^{-18} N_{e^-} \tag{4.44a}$$

$$P_\theta^{(e^+)} = 3.75 \times 10^{-18} N_{e^+} + 3.38 \times 10^{-18} N_{e^+}^2 \tag{4.44b}$$

where $N_{e^-}$ and $N_{e^+}$ are in millions of particles. We can understand the implication of this difference in the angular momentum as a function of particle number between electrons and positrons by noting that the angular momentum of a spheroid is given by

$$P_\theta^{(spheroid)} = \frac{qB_0}{5} N \rho_p^2 \tag{4.45}$$

Since for electrons, $P_\theta$ is linear in $N$ we must have an approximately constant plasma radius regardless of the number of particles. However, for positrons, $P_\theta$ is quadratic in

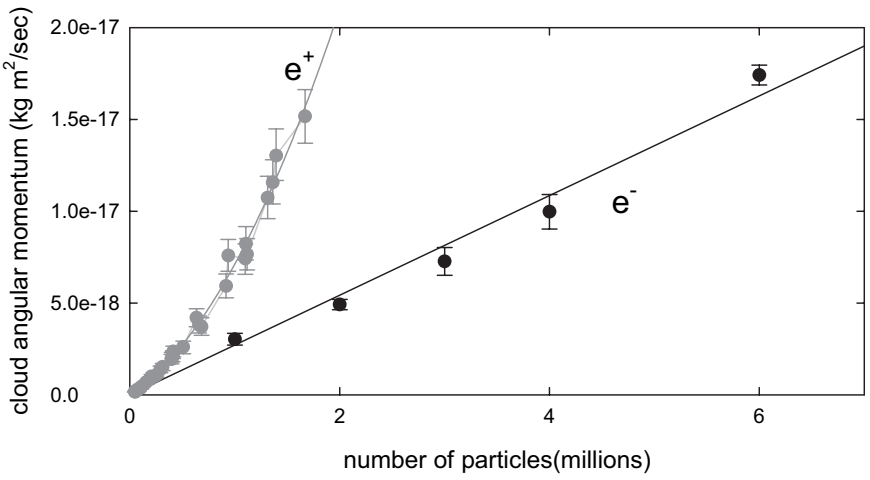


Figure 4.24: Angular momentum of plasma clouds as a function of the $e^-$ or $e^+$ number [80].

$N$ which implies that the plasma radius is proportional to $\sqrt{N}$. This simple estimate will break down once the plasma radius approaches the radius of the electrodes as the plasma cloud will no longer be a simple spheroid.

### 4.3.2 Plasma Mode Frequency Detection

An alternative method for determining the plasma cloud shape is measuring the frequencies of the quadrupole and axial center of mass plasma modes and then using the following formulas to derive the desired cloud parameters:

$$N = \frac{4}{3}\alpha\rho_p^3 n_0 \tag{4.46a}$$

$$\frac{\omega_z^2}{\omega_p^2} = \frac{Q_1^0\left(\frac{\alpha}{\sqrt{\alpha^2-1}}\right)}{\alpha^2-1} \tag{4.46b}$$

$$\frac{\omega_p^2}{\omega_2^2} = 1 - \frac{k_2}{k_1}\frac{P_2(k_1)Q_2'(k_2)}{P_2'(k_1)Q_2^(k_2)} \tag{4.46c}$$

$$\omega_p^2 \equiv \frac{q^2 n_0}{\epsilon_0 m} \tag{4.46d}$$

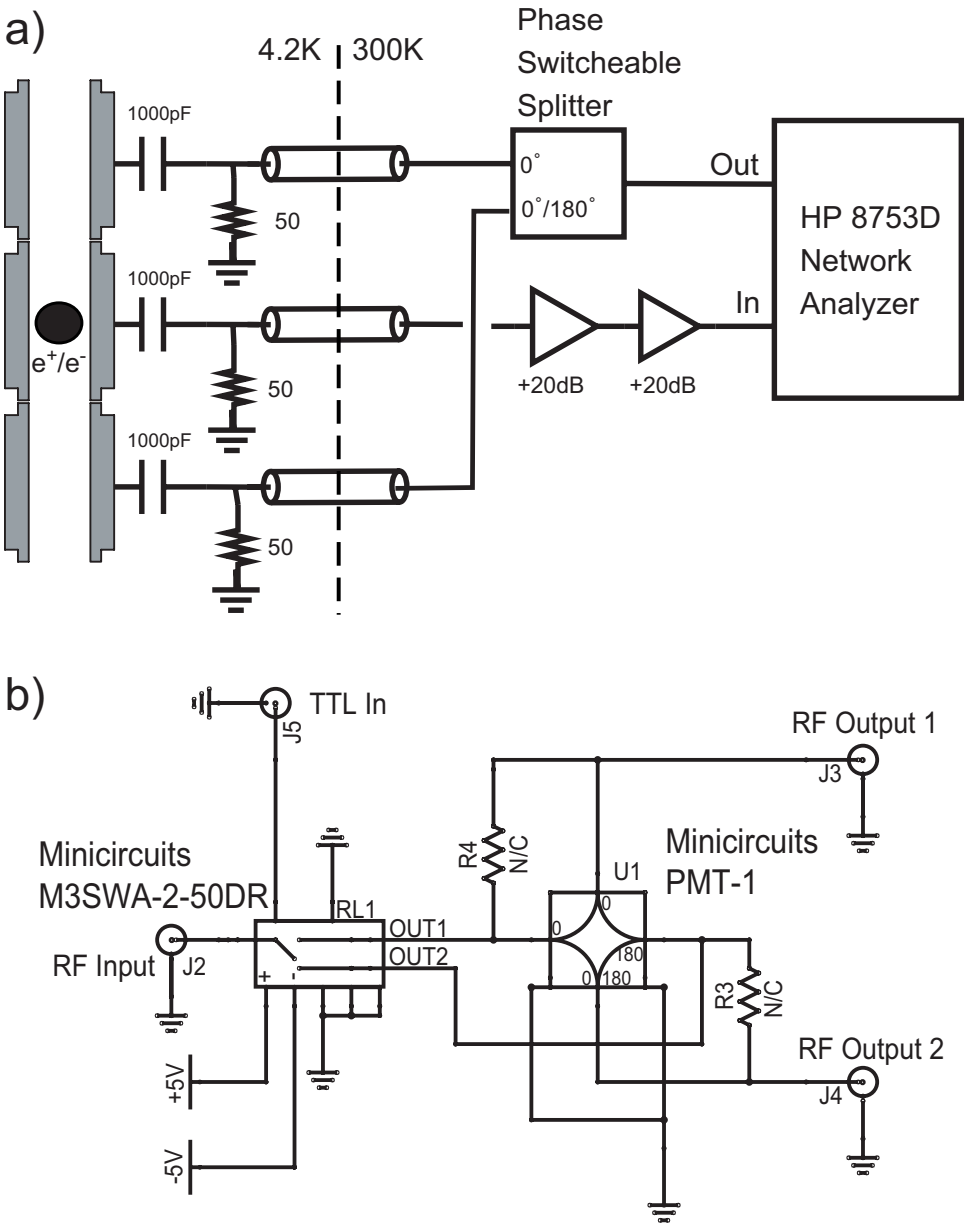


Figure 4.25: (a) Plasma mode detection apparatus. (b) The schematic of the phase variable splitter.

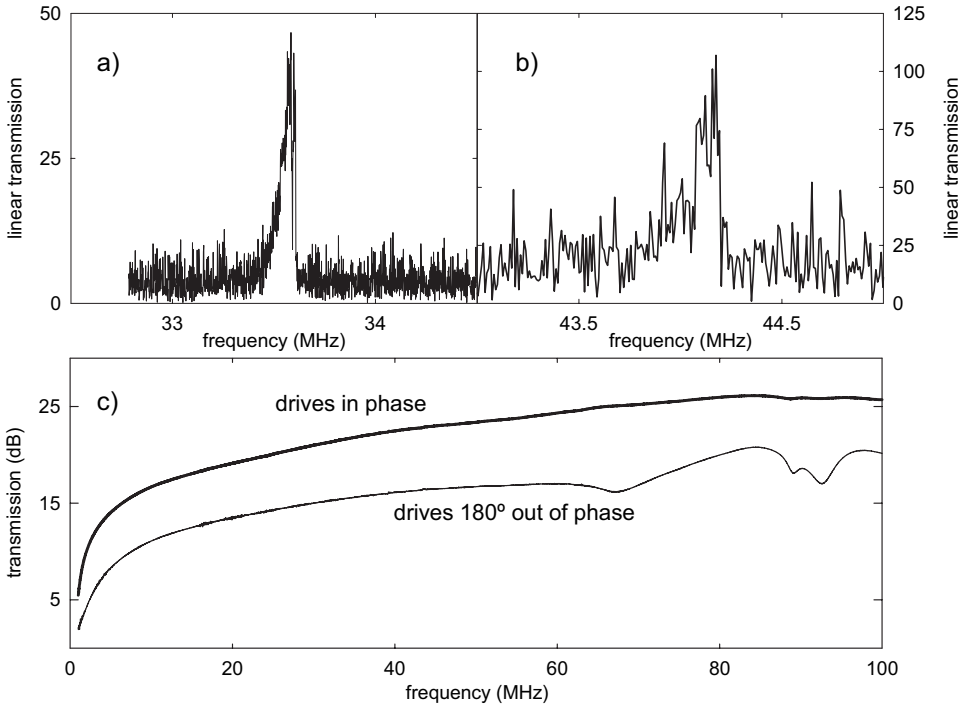


Figure 4.26: Typical frequency response of plasma modes: (a) center of mass mode, (b) quadrupole mode, and (c) background response from the trap alone with no particles confined inside.

where we have assumed $T \rightarrow 0$. This method has the advantage of being non-destructive to the particles in principle but requires the assumption of a spheroidal cloud. In addition, the frequency of the quadrupole mode shifts as the cloud temperature changes introducing an additional systematic source of error as discussed in Section 4.1. This effect also provides the opportunity to measure temperature changes within the plasma cloud in the future assuming it is possible to hold the remaining parameters constant (*i.e.* the particle number, the aspect ratio, etc.).

To measure the frequency of the required plasma modes, the equipment shown in Fig. 4.25 is used. A network analyzer (Hewlett-Packard 8753D) drives the two neighboring electrodes to the particle cloud with a swept frequency in an attempt

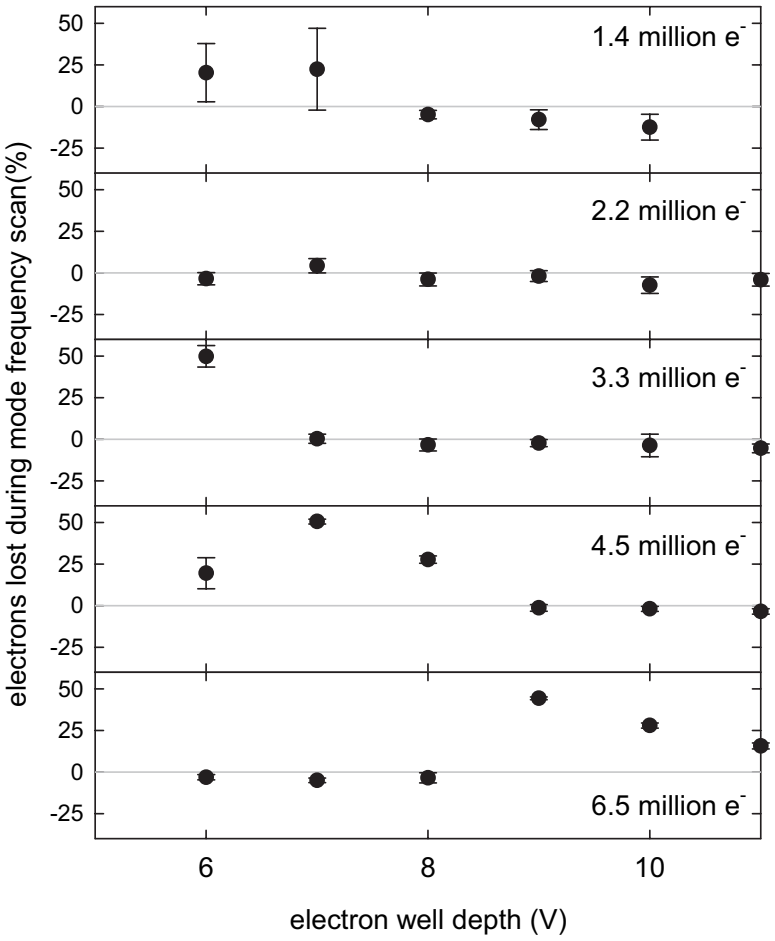


Figure 4.27: Electrons lost during plasma mode frequency scans as a function of well depth and initial number.

to excite a mode. The drives can be either in phase with each other (for modes with $\ell$ even) or 180° out of phase (for odd $\ell$ modes). If a particular mode is excited the oscillating image current (Section 4.2.1) induced on the detection electrode is converted to a voltage signal by a 4.2 K 50 Ω resistor located just above the trap vacuum enclosure, amplified by +40 dB at room temperature, and then detected in quadrature by the network analyzer. Thus when the frequency of the network analyzer is near a plasma mode the transmission through the system increases (Fig. 4.26) and the frequency of the mode can be determined by finding the peak of the signal. The trap itself has a frequency dependent response (Fig. 4.26c) which must be subtracted out from the quadrature signal before converting the signal to an absolute magnitude and looking for a peak. In practice, to reduce the amount of power applied to the particle cloud and thus minimize particle heating only the quadrupole mode frequency is measured as the center of mass mode frequency can be accurately calculated using Eq. 2.3.

At certain well depths and particle numbers, the network analyzer appears to drive particles out of the trap with almost 50 % efficiency (Fig. 4.27). This is likely due to resonances as it is repeatable over multiple scans and dependent on the cloud parameters. Reducing the drive power does not remove the problem until the power is low enough that the plasma modes are no longer detected.

### 4.3.3 Comparison of Techniques

Figure 4.29 shows a comparison of the various cloud parameters measured using both the plasma modes method and the Faraday cup aperture method. For all the

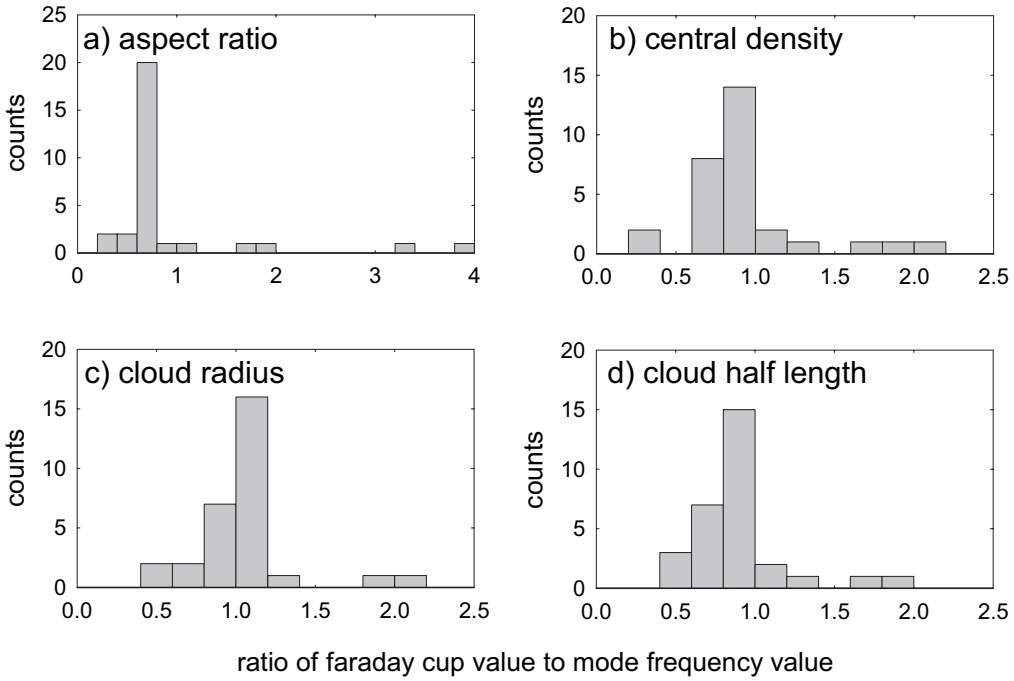


Figure 4.28: Histograms of the ratio of plasma parameters as determined from plasma mode frequencies and the aperture method.

data points, the quadrupole mode frequency was first found and then the particles were pulsed onto the Faraday cup apertures. With the exception of a few outlier points there is a fairly clear correlation between the parameters as measured by the two methods. For example, the aspect ratio determined by the aperture method is 71 % of that measured by plasma modes. Temperature effects alone can not account for the difference as increasing the temperature would increase the aspect ratio inferred from the mode frequencies (Fig. 4.5). In addition, the discrepancy between the calculated and measured $e^-$ fraction dumped onto *P0* implies that the radius of the cloud is likely larger than calculated which brings the two sets of data further out of agreement. The causes for this discrepancy are likely related to the assumption of a spheroidal plasma cloud used in interpreting the plasma mode frequencies; it is plausible that

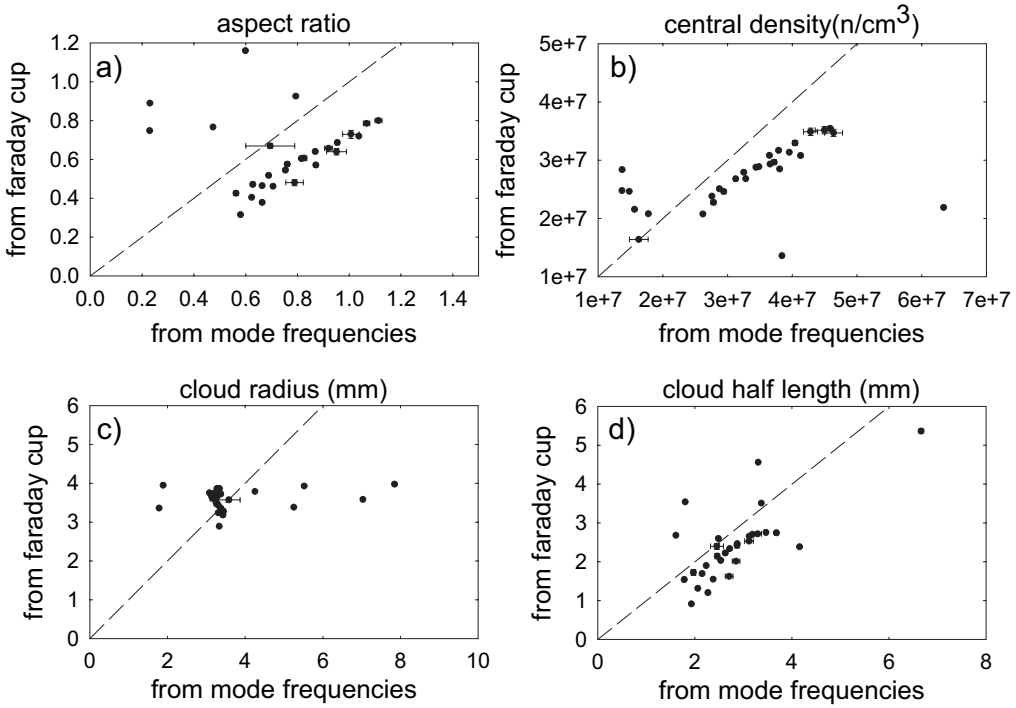


Figure 4.29: Correlation plots of plasma parameters determined from plasma mode frequencies and the aperture method. The dashed lines indicate a one to one correspondence. The outliers in Fig. c are only 7.5 % of the total data which is a similar fraction to the outliers in the other figures (Fig. 4.28.

the anharmonic effects in a cylindrical trap will cause the plasma mode frequency discrepancies described above. Regardless, more investigations will be needed in order to reduce these systematic effects and increase the accuracy with which we can measure these parameters.

# Chapter 5

# Antihydrogen Production in a Nested Well

Long ago, it was recognized that the high rate process of antihydrogen formation at 4.2 K was likely three-body recombination (as discussed in Chapter 1) [2]. For this process to occur, spatial overlap between the antiproton and positron clouds is required. As an individual Penning trap well can only confine a single sign of charge, bringing antiproton and positron clouds into contact in order to produce antihydrogen is not as simple as just placing them in the same well. Recombination instead requires a nested well to confine $\overline{\mathrm{p}}$ and $\mathrm{e}^+$ nearby and then some method to coax the particles into interacting and producing antihydrogen. The nested Penning trap [2] that we and others use to do so is discussed later in this chapter.

After the interaction of oppositely charged particles was initially demonstrated with protons and electrons by the TRAP collaboration [3] and then our demonstration with positrons and antiprotons [4], ATRAP demonstrated positron cooling of

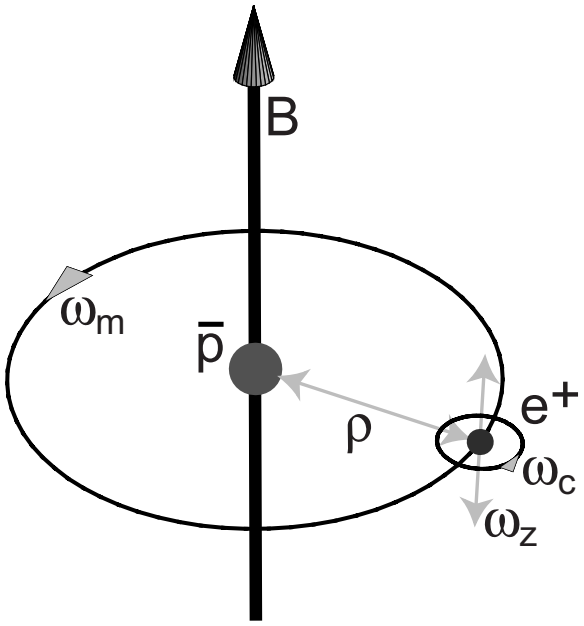


Figure 5.1: Atomic orbits in the guiding center regime of a strong magnetic field and large atomic radius are analogous to the orbits of a charged particle in a Penning trap.

antiprotons [5]. Not long after, we [6, 7] and another group [8] demonstrated that antihydrogen was being produced through this technique. These very satisfying demonstrations of antihydrogen production also raised another level of questions. Were any deeply bound states being produced? What speed were the $\overline{\mathrm{H}}$ atoms traveling at? The experiments we conducted in the last two years have provided initial answers to both of these questions.

Our field ionization technique and an oscillatory variation makes it possible to determine both the sizes of the antihydrogen atoms produced and to learn about their speeds. With this formation method, $\overline{\mathrm{H}}$ atoms are likely to recombine into atoms with a large radius. These atoms have been given the name guiding center atoms as the motion is classical and can be considered using the guiding center approximation where the fast cyclotron motion is averaged out [20]. The large radius of a guid-

ing center atom results in a weakly bound positron that is extremely susceptible to perturbation. For example, in three-body recombination the initial atom is formed with a radius comparable to that of the mean classical distance of closest approach, $\rho = e^2/4\pi\epsilon_0 k_B T = 4\,\mu\text{m}$ at 4 K. At this distance the electric field between the positron and the antiproton is only 1 V/cm so the fields within the Penning trap will be of the same order. Further collisions within the plasma will reduce the radius to the observed sizes of less than 1 µm enabling the atoms to survive within our Penning trap environment but the atoms can still be easily perturbed with laboratory sized fields.

In fact, by applying a large enough electric field the positron and antiproton can be split apart. The ionized antiproton can then be trapped and the number of antiprotons confined at the end of experiment counted by the standard charged particle detection techniques described in Chapter 4. The number of detected antihydrogen atoms is then given by the number of antiprotons counted. While this field ionization method is described more fully in Section 5.6, a simple result gives the axial field, $F$, necessary for ionization in terms of the radius of the atom, $\rho$, by:

$$F \geq 3.60\,\text{V/cm}\left(\frac{\mu\text{m}}{\rho}\right)^2 \tag{5.1}$$

By varying this analyzing electric field in time, we can learn about the speed of the $\overline{\text{H}}$ atoms that we detect.

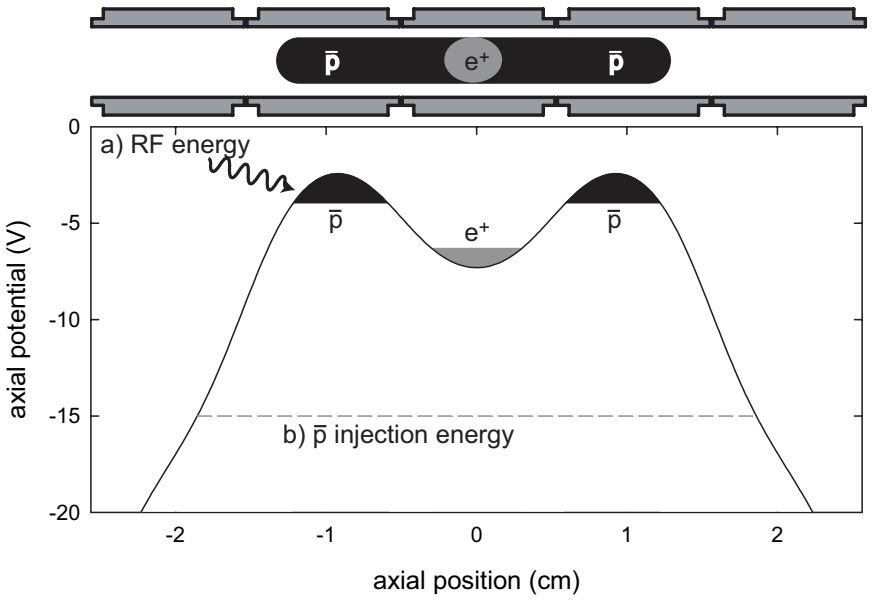


Figure 5.2: A nested Penning trap can contain $\overline{\mathrm{p}}$ in the outer well and $\mathrm{e}^+$ in the inner well. To bring the two species into interaction requires adding energy to the $\overline{\mathrm{p}}$ either through a RF drive (a) or injecting them with enough energy for interaction (b).

## 5.1 Nested Penning Traps

A nested Penning trap (Fig. 5.2) is used to confine the opposite signed charged particles spatially nearby to each other [2]. In this technique, one sign of charge (typically $\mathrm{e}^+$) is confined in the center well. The other sign of charge (in our case $\overline{\mathrm{p}}$'s) are confined in the two small outer wells. The $\overline{\mathrm{p}}$ can then be given enough energy to allow them to oscillate in the large outer well, passing over the top of the $\mathrm{e}^+$ well as they do so.

During each pass over the top of the $\mathrm{e}^+$ well, the antiprotons interact with the trapped positrons and possibly form antihydrogen. In addition, simple two-body collisions with the 4.2 K $\mathrm{e}^+$ cloud reduce the energy of the $\overline{\mathrm{p}}$'s to that of the positron cloud on a time scale of seconds [5, 42]. This cooling increases the interaction time

of the $\overline{p}$'s with the $e^+$ cloud as when the energy of the antiprotons is close to the potential within the $e^+$ cloud the velocity of the $\overline{p}$'s tends to zero.

However, positron cooling does present several challenges in terms of antihydrogen production. First, due to the geometry of the nested trap antiprotons can cool below the level of the $e^+$ cloud through recycled evaporative cooling preventing any further interactions. In this case, collisions between antiprotons decrease the energy of one $\overline{p}$ while bringing the other $\overline{p}$ back into contact with the positrons for further cooling. Second, the energy added to the positrons must be radiated back to the 4.2 K environment primarily through synchrotron radiation. However, the rapid cooling of high energy antiprotons initially heats the positron cloud at a rate much faster than the synchrotron cooling rate. During this process, the positrons can reach temperatures on the order of 200 K which is not consistent with the goal of $\overline{H}^*$ production at the lowest possible temperature [42].

## 5.2 Driving in a Nested Well

The first method we employed to provide the energy necessary for antiprotons initially cooled deeply into a side well to interact with the trapped positrons in the center well was applying radio-frequency drives to the electrodes creating the side antiproton wells. By choosing the frequency of the drive to correspond to the axial oscillation frequency of the antiprotons, the antiprotons can be resonantly driven over the top of the positron well. As shown in Fig. 5.3, the 825 kHz drive frequency for our typical 9 V positron well was chosen to excite only those antiprotons located below the top of the positron well. Once the antiprotons have enough energy to oscillate

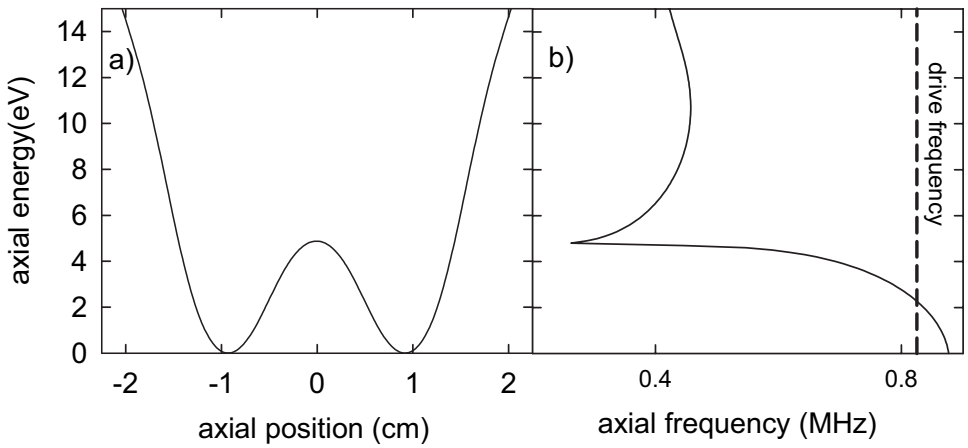


Figure 5.3: The axial oscillation frequency as a function of antiproton axial energy in a nested Penning trap shows a singularity as the antiproton energy passes over the positron well potential energy. (a) Potentials in a 9V nested trap. (b) Axial oscillation frequency as a function of antiproton axial energy.

in the large well the resonant frequency drops precipitously and the drive no longer effectively heats them.

Several different driving methods have been tried. The simplest is a single frequency drive placed a little below the resonant frequency of antiprotons at the top of the side well. A slightly more complicated scheme is to chirp the frequency of the drive from the frequency at the bottom of the side well to the frequency at the top of the side well.

Since the drive is only applied to one side well at a time, an optimum scheme to maximize $\overline{\mathrm{H}}$ production would excite all the antiprotons into the large outer well and then as they cool they would end up into the non-driven side well since otherwise the drive would re-excite them out of the driven side well. Figure 5.4 shows the fraction of the initial antiprotons that are transferred to the other side well during a 10 second drive. In these experiments approximately 250,000 positrons were located in the center well. The experiments discussed in the following sections all used a 9V

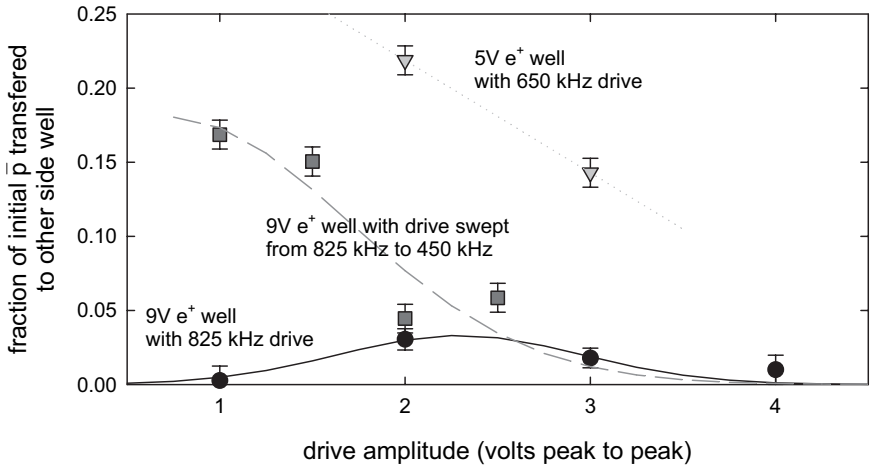


Figure 5.4: Fraction of antiprotons driven over the top of the positron inner well during a single 10 second RF drive application. The curves are just to guide the eye.

$e^+$ well with an 825 kHz drive but it should be more efficient to use a chirped drive.

In a typical experiment, the two side wells are driven in an alternating fashion with a 10 second drive applied to one side well electrode, a dead time of 5 seconds to allow the antiprotons to cool, a 10 second drive applied to the other electrode, and finally another 5 second dead time. This cycle is then repeated 15 to 25 times. As shown in Fig. 5.5, the number of antiproton annihilations during the driving period decays with a time constant of approximately 1.4 cycles.

### 5.2.1 Antihydrogen Production

To detect any produced Rydberg antihydrogen atoms, we then used a field ionization analysis technique. In this scheme two very deep potential wells are placed on either side of the nested well (Fig. 5.6). Any neutral $\overline{\mathrm{H}}$ atoms formed are no longer trapped by the electrostatic potentials of the nested well and escape in all directions. $\overline{\mathrm{H}}^*$ atoms that enter the two detection wells with a large enough radius ionize due to

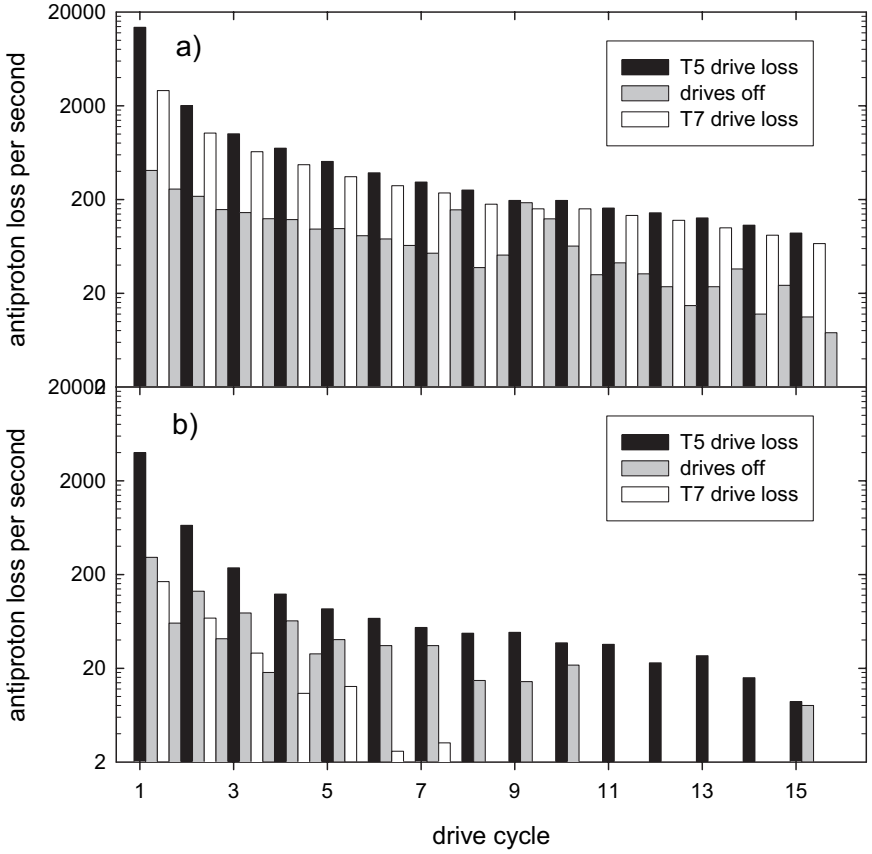


Figure 5.5: The number of antiproton annihilations per second during an experiment decreases over time. The black and white bars show losses while one of the two alternating RF drives are on and the grey bars show losses while the drives are off. (a) shows the symmetric losses when equal numbers of $\overline{\mathrm{p}}$ are placed in each side well initially. (b) shows the asymmetric loss when $\overline{\mathrm{p}}$ are placed only in *T5* initially.

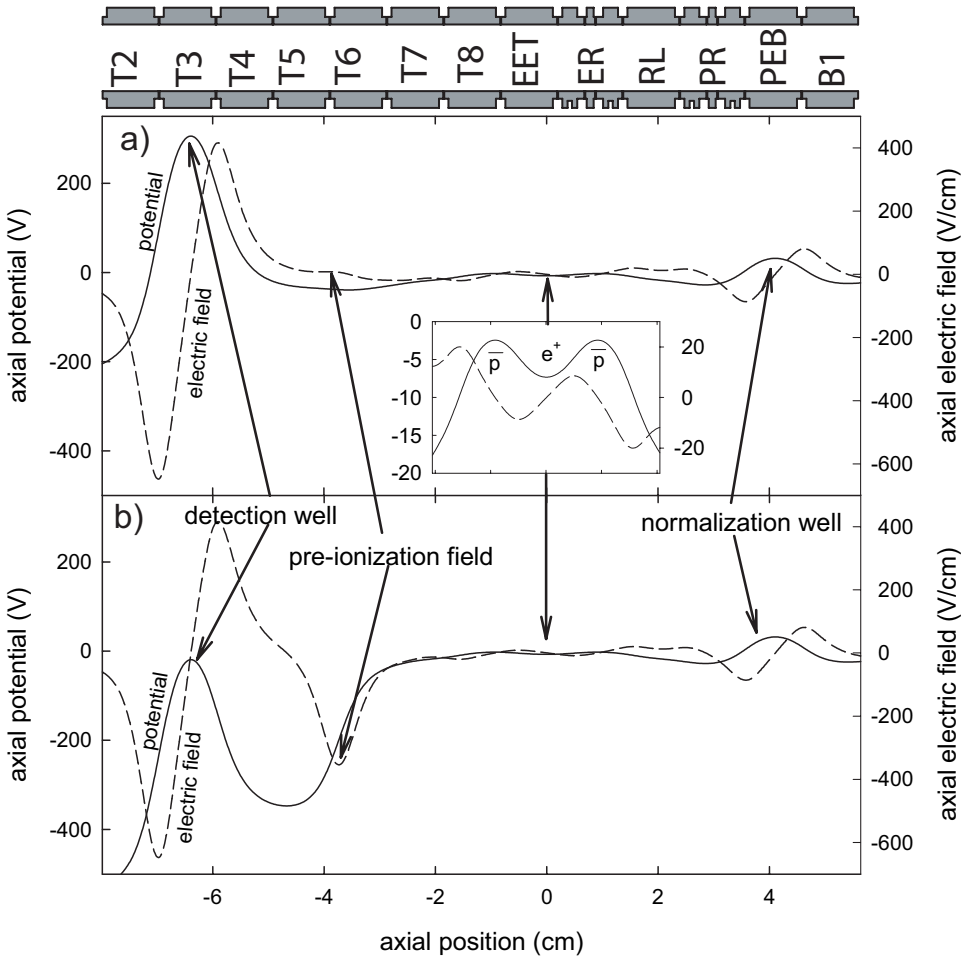


Figure 5.6: Potentials used to detect antihydrogen atoms produced by driving antiprotons within the nested trap — (a) shows a 23 V/cm pre-ionization field and (b) shows a 360 V/cm pre-ionization field.

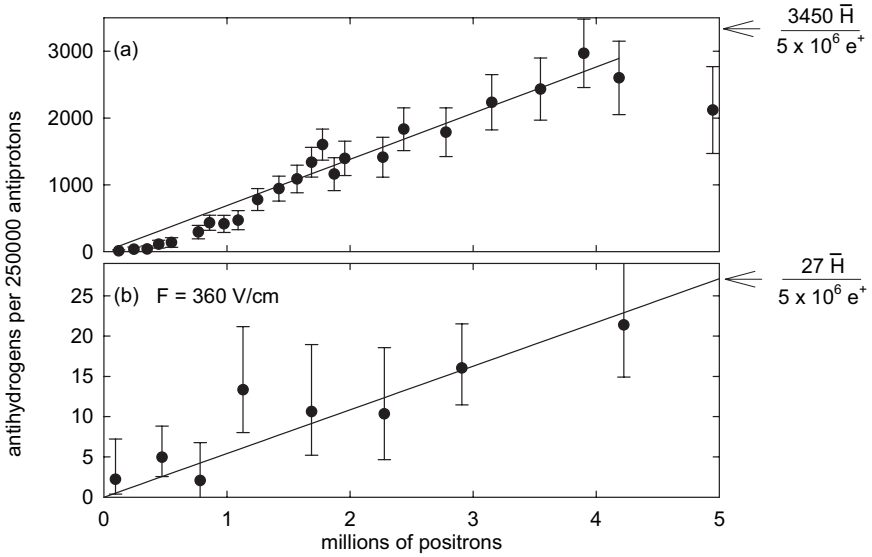


Figure 5.7: $\overline{\mathrm{H}}$ produced from $2.5\times10^5$ $\overline{\mathrm{p}}$ and detected in the (a) normalization and (b) detection wells. To be ionized in the detection well, the incoming $\overline{\mathrm{H}}^*$ atom must have survived a 360 V/cm field.

the strong electric fields (Eq. 5.30). Since the freed $\overline{\mathrm{p}}$ encounters a confining potential upon ionization of the $\overline{\mathrm{H}}^*$ atom and is thus trapped in the detection well, the number of $\overline{\mathrm{H}}^*$ atoms observed is given by the number of trapped $\overline{\mathrm{p}}$ in the detection well at the end of the experiment. To prevent any $\overline{\mathrm{p}}$ from being trapped in the detection well that have not been released from an ionized $\overline{\mathrm{H}}^*$, the potential is designed such that antiprotons from the nested well must climb a substantial potential gradient as well as somehow lose energy while within the detection well. The likelihood of the combination of these requirements being met is negligible resulting in an almost background-free detection method.

Figure 5.7 shows the number of antihydrogen atoms detected to be a linear function of the number of positrons in the center of the nested trap. On average, $2.5\times10^5$ antiprotons were used in the following experiments. The root cause of the linear de-

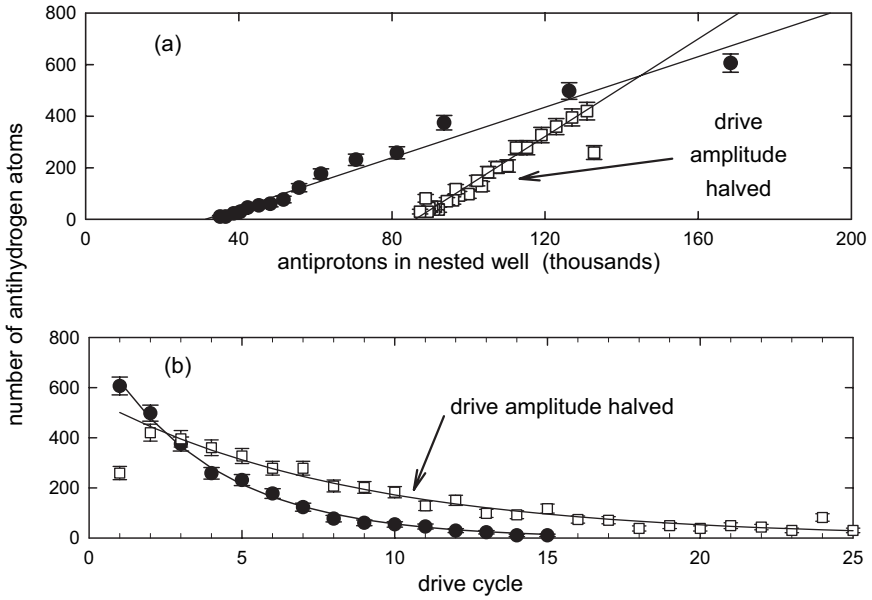


Figure 5.8: The number of $\overline{\mathrm{H}}^*$ atoms detected is linear in the number of $\overline{\mathrm{p}}$ remaining in the nested trap (a), but decreases as a function of drive cycle because of $\overline{\mathrm{p}}$ losses (b).

pendency is still unknown as the recombination rate is likely to involve a non-linear function of the positron cloud's density, length, and radius.

The number of $\overline{\mathrm{H}}^*$ atoms produced is also linear in the number of $\overline{\mathrm{p}}$ remaining in the nested trap (Fig. 5.8). The fact that the intercept is not at zero is presumably related to the fact that some $\overline{\mathrm{p}}$ are never able to produce antihydrogen due to their location at a large radius where there is no overlap with the $\mathrm{e}^+$ cloud. As the drive amplitude is halved, the number of $\overline{\mathrm{H}}^*$ produced is doubled although the rate of production is slower initially. This reduction is consistent with the observation discussed earlier of increased transfer to the other non-driven side well as the drive is reduced up to a certain point. Likely as the drive is reduced, fewer antiprotons are driven outwards radially whereupon they eventually annihilate without producing antihydrogen.

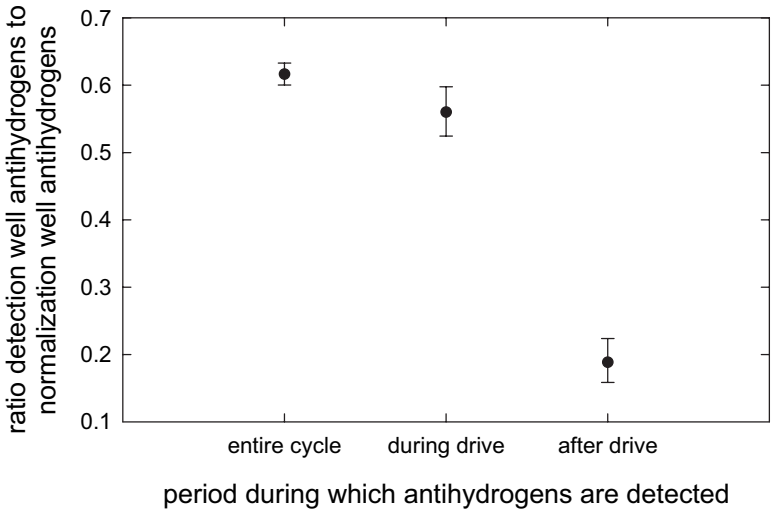


Figure 5.9: Most $\overline{\mathrm{H}}^*$ atoms are produced during the period when the RF heating drive is applied.

By applying a strong ionization field prior to the entrance to the detection well, it is possible to turn off detection of antihydrogen atoms at a controllable time as $\overline{\mathrm{H}}$ atoms are ionized before entering the detection well and thus no $\overline{\mathrm{p}}$ are trapped. By applying this pre-ionization field either during the period when the RF drive is on or during the cooling period after the drive is turned off, we observe that 75 % of the antihydrogen is produced during the drive period (Fig. 5.9).

### 5.2.2 Produced State Distribution

To probe the internal structure of the antihydrogen atoms, we utilize a similar pre-ionization field idea. By changing the magnitude of the field the atoms encounter before entering the detection well we can determine the fraction of atoms that have an internal radius such that they ionize between the pre-ionization field and the maximum field in the detection well. The potential structure used was designed such that the detection well was not affected by the large changes in the pre-ionization field

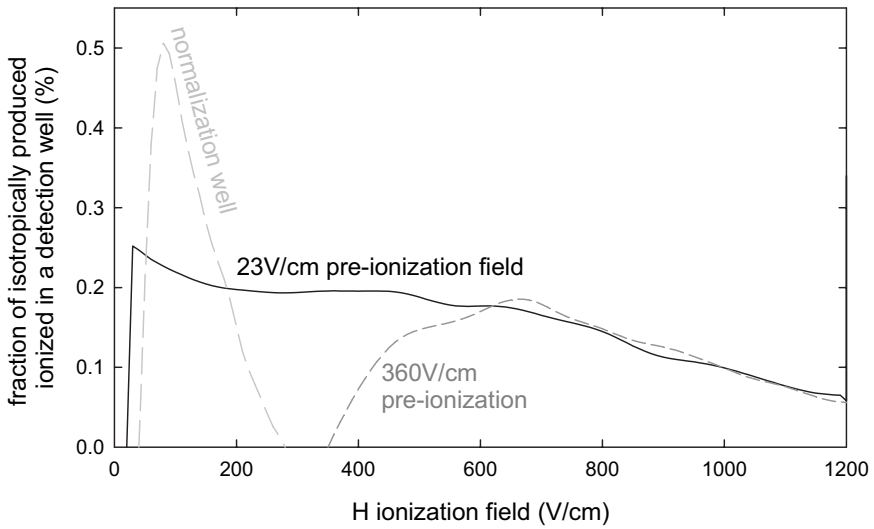


Figure 5.10: The estimated fraction of antihydrogen atoms reaching the detection well for a given field at which the produced $\overline{\mathrm{H}}$ atom will ionize at. The calculation assumed isotropically distributed, ballistic trajectories from the center of the nested Penning trap.

thus allowing a simple interpretation of the detected number of $\overline{\mathrm{H}}^*$ atoms (Fig. 5.6). Figure 5.10 shows the estimated fraction of antihydrogen atoms that will be detected if the atoms have an isotropic distribution. Note that the 360 V/cm pre-ionization field only removes those atoms who ionize at a lower field but does not affect the fraction detected above that field as compared to those detected with a lower pre-ionization field.

The $\overline{\mathrm{H}}^*$ ionization spectrum shown in Fig. 5.11 reveals that the number of atoms that ionize at a given field, $F$, or greater is approximately proportional to $F^{-2}$ and thus has a distribution function

$$dN/dF \propto F^{-3}. \tag{5.2}$$

This spectrum was constructed by measuring the linear dependencies of $\overline{\mathrm{H}}$ atoms produced versus $\mathrm{e}^+$ number (Fig. 5.7) for a number of pre-ionization fields. From the

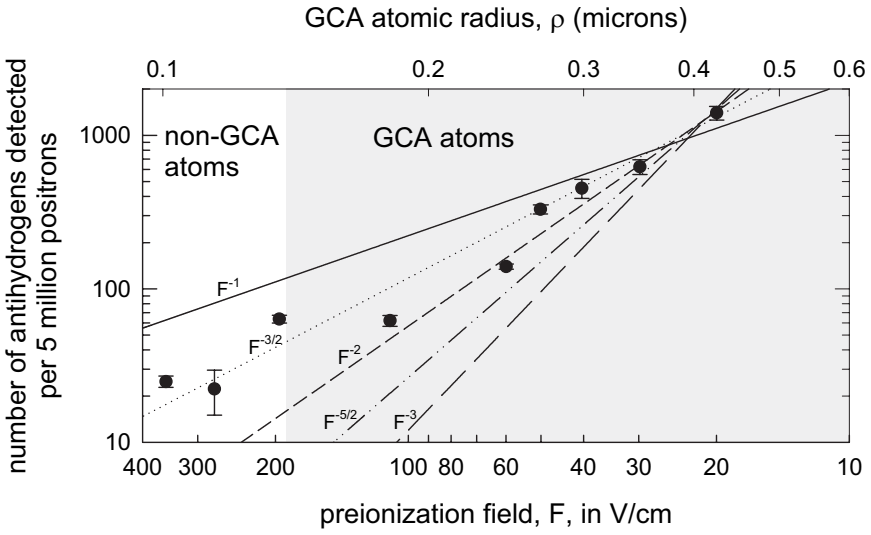


Figure 5.11: The number of antihydrogen atoms, for 250,000 $\overline{\mathrm{p}}$ and 5 million $\mathrm{e}^+$, that survive an ionization field $F$ decreases as a power law.

results in Section 5.6, the atoms that ionize above 190 V/cm are too tightly bound to obey the guiding center Hamiltonian (Eq. 5.24). A simple model may explain this $F^{-3}$ or equivalently $\rho^6$ dependence. The rate for the initial Thompson capture of a positron should go as $\rho^4$ as this process requires two $\mathrm{e}^+$ to be involved in the collision and the rate for de-excitation collisions will scale as $\rho^2$ as these collisions only require one $\mathrm{e}^+$ to participate. Combining these two processes results in a rate that scales as $\rho^6$.

## 5.3 Pulsing into a Nested Well

An alternative method of giving the antiprotons the energy necessary for them to interact with the trapped $\mathrm{e}^+$ is to inject the $\overline{\mathrm{p}}$ into the outer well with high energy. This technique was actually used first in the demonstrations of slow $\overline{\mathrm{H}}$ production [6, 8]. Positron cooling will then bring the antiprotons into contact with the positrons. In

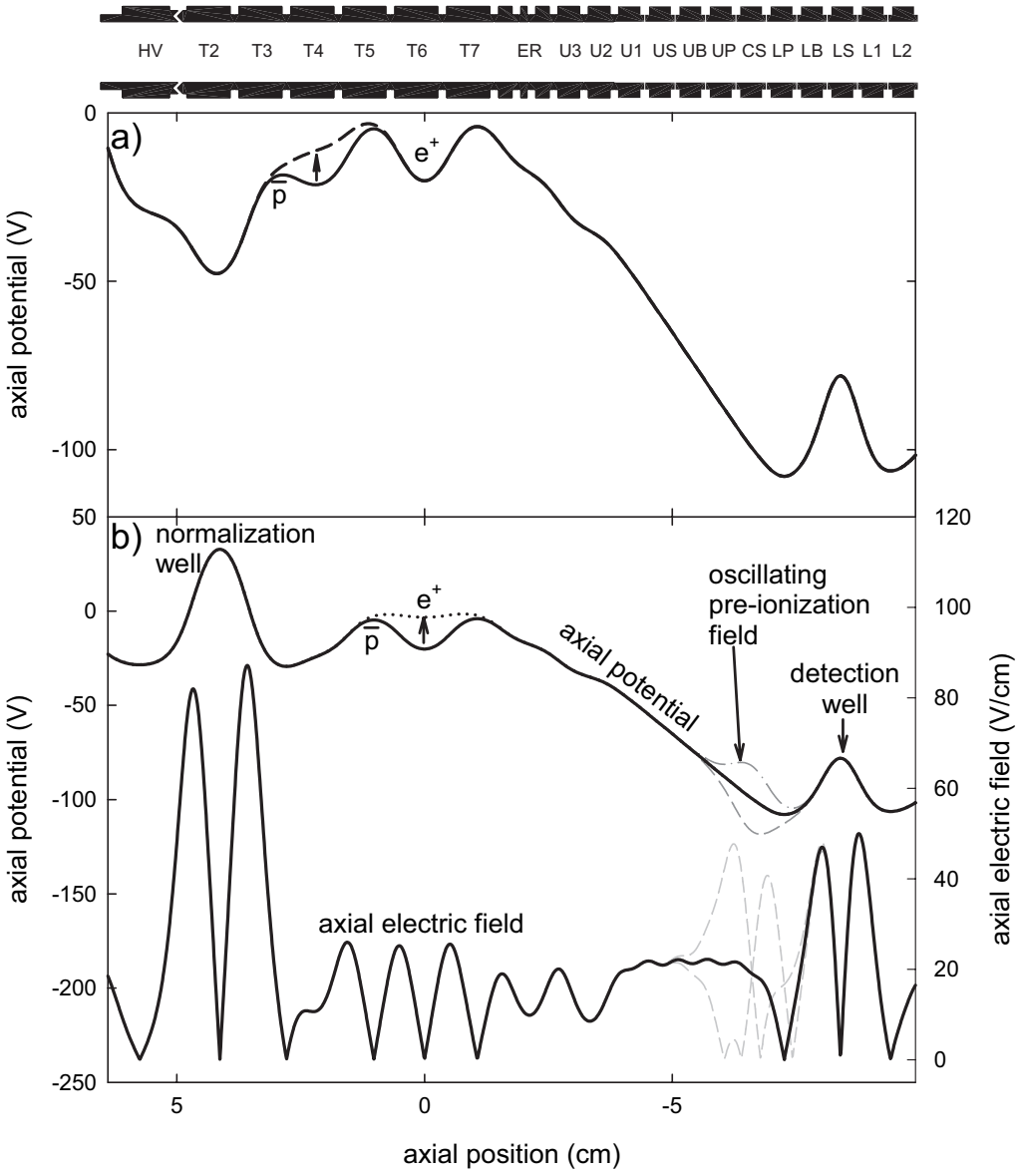


Figure 5.12: The potential structure used to inject antiprotons into the nested well with a high energy (a) and detect the $\overline{\mathrm{H}}$ atoms produced (b).

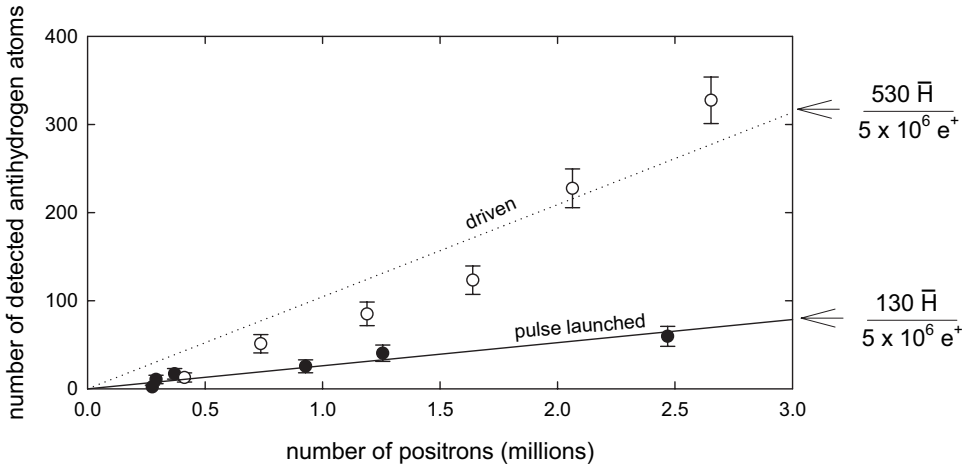


Figure 5.13: The number of $\overline{H}^*$ produced by pulsing into a nested well is a factor of 5 less than the number of $\overline{H}^*$ produced by driving within the nested well. These curves were taken with the detection well and pre-ionization field shown in Fig. 5.12 but with no oscillating field applied.

order to inject the antiprotons we utilize a structure where the antiprotons are initially trapped in a well on one side of the nested trap (Fig. 5.12a). A fast voltage pulse then removes the barriers between the $\overline{p}$ and the nested well allowing the antiprotons to enter the nested well at a high energy relative to the top of the positron well.

The first attempt produced an order of magnitude less antihydrogen than the driving technique [6] and the number of $\overline{H}$ produced became constant once the number of positrons was above 500,000. To improve the production rate we increased the $e^+$ well depth such that the injected antiprotons were initially trapped in a side well. We then lowered the positron well depth slowly allowing the antiprotons to interact with the positrons, cool from collisions, and then collide with the positrons again once the well depth was lowered a small amount (Fig. 5.12b). This restored the linear dependency for large positron numbers and produced a factor of 2 more antihydrogen per positron (Fig. 5.13).

## 5.4 Velocity Distribution

Since the solid angle of the combined detection and normalization wells is less than $4\pi/130$, if the $\overline{\mathrm{H}}$ velocity distribution were isotropic we would expect over 1 million $\overline{\mathrm{H}}$ to be produced based on the 7600 detected $\overline{\mathrm{H}}$ in one trial with 4.5 million $e^+$. As the initial number of antiprotons was only 290,000, the assumption of an isotropic distribution is obviously not valid.

A measurement of the $\overline{\mathrm{H}}$ axial velocity distribution is quite simple in principle. First, with a static pre-ionization field applied the ratio of antihydrogen observed in the detection well to that in the normalization well is measured. This ratio serves to normalize the ratio observed when an oscillating pre-ionization field is generated through an additional AC potential applied to an electrode (Fig. 5.14). This experiment is then repeated for many frequencies (Fig. 5.15). The fraction of $\overline{\mathrm{H}}$ detected decreases as the oscillation frequency, $\omega$, increases since only $\overline{\mathrm{H}}$ atoms that travel quickly through the oscillating field relative to the period of the oscillation avoid ionization.

To quantitatively interpret the observed curve, we consider the distribution function of $N(F, \rho, v, t)dFd\rho dvdt$ $\overline{\mathrm{H}}$ atoms produced in the center of the $e^+$ cloud($z = 0$), at a time between $t$ and $t + dt$, a center of mass radius in the trap between $\rho$ and $\rho + d\rho$, a center of mass velocity between $v$ and $v + dv$, and which are in a state that will be ionized between $F$ and $F + dF$. As a simplifying assumption, we will assume that the trajectory is axially directed and thus $\rho$ is constant.

When no oscillating field is applied, the atoms only experience a static field, $F_{DC}(\rho, z)$ (Fig. 5.14b). The number of atoms detected is determined by the fraction

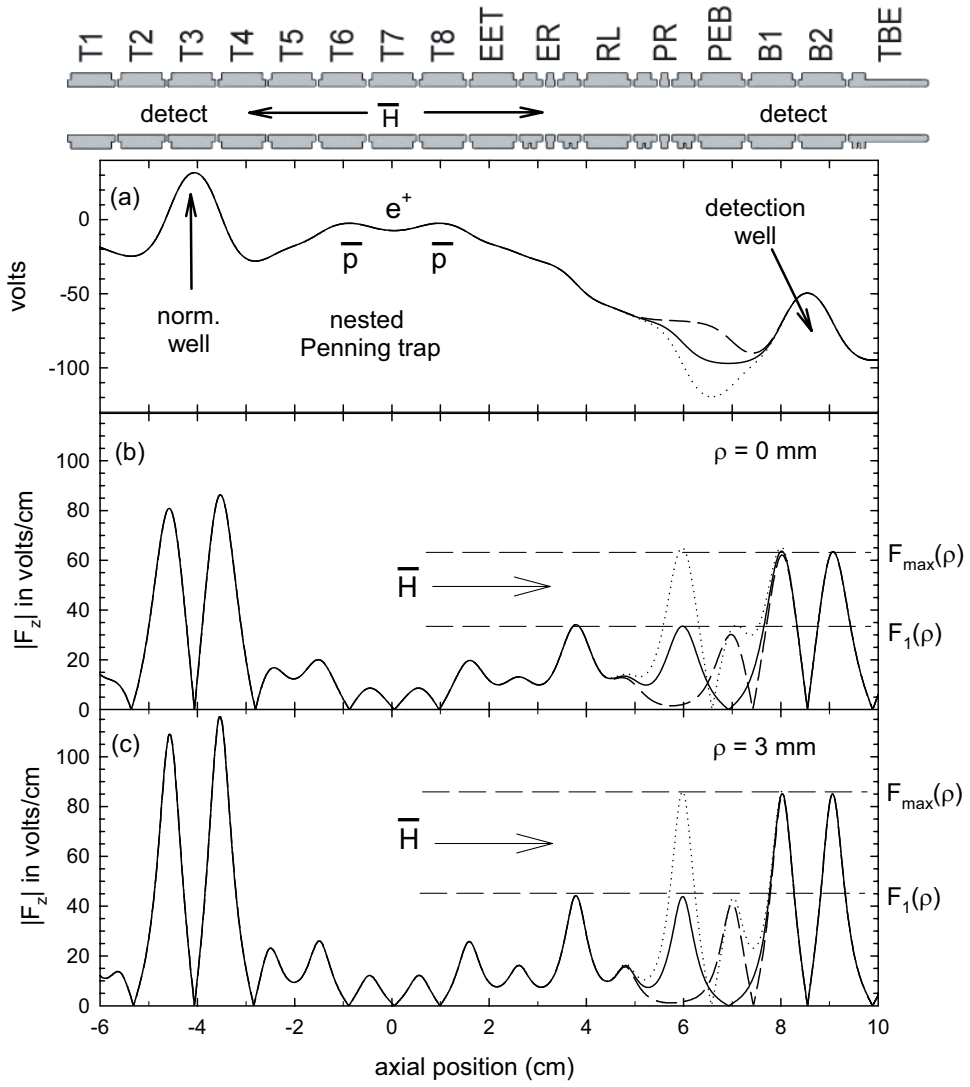


Figure 5.14: The potential (a), electric field on axis (b), and electric field 3 mm off-axis (c) used to determine the axial velocity of $\overline{\mathrm{H}}$ atoms. The solid lines show the static potentials and fields while the dashed lines show the maximum variation when the oscillating field is applied.

that survive the maximum field between $z = 0$ and $z_{\text{detection}} = 8.5\,\text{cm}$ where $z_{\text{detection}}$ is the beginning of the detection well. The maximum field in the detection well, however, still must ionize the $\overline{\text{H}}$ atom. The number of detected $\overline{\text{H}}$ atoms, $N_{\omega=0}$, is then given by

$$N_{\omega=0} = t_{\max} \int_0^{\rho_0} d\rho \int_0^{\infty} dv \int_{F_1(\rho)}^{F_{\max(\rho)}} \bar{N}(F, \rho, v) dF \tag{5.3}$$

where $F_1 = 34\,\text{V/cm}$ (45 V/cm) and $F_{\max} = 63\,\text{V/cm}$ (85 V/cm) on axis (3 mm off-axis), $\rho_0 = 0.6\,\text{cm}$ is the electrode radius, and $t_{max} \approx 750\,\text{s}$ is the duration of the experiment. We have also replaced the instantaneous production rate, $N$, with the average production rate over time, $\bar{N}$.

When the oscillating field is applied the pre-ionization field which determines $F_1$ becomes,

$$\begin{aligned} F(\rho, z) &= F_{DC}(\rho, z) + F_{AC}(\rho, z)\cos(\omega t) \\ &= F_{DC}(\rho, z) + F_{AC}(\rho, z)\cos\left(\omega\frac{z}{v} + \phi\right) \end{aligned} \tag{5.4}$$

where we must now average over the phase, $\phi$ as well. The number of detected $\overline{\text{H}}$ is

$$N_{\omega} = t_{\max} \int_0^{\rho_0} d\rho \int_0^{\infty} dv \int_0^{2\pi} \frac{d\phi}{2\pi} \int_{F_1(\rho,\omega/v,\phi)}^{F_{\max(\rho)}} \bar{N}(F, \rho, v) dF \tag{5.5}$$

$F_1(\rho, \omega/v, \phi)$ is the maximum pre-ionization field the given atom experiences and can be calculated from

$$F_1(\rho, \omega/v, \phi) = \max\left[\left|F_{DC}(\rho, z) + F_{AC}(\rho, z)\cos\left(\omega\frac{z}{v} + \phi\right)\right|\right], z \in (0, z_{\text{detection}}) \tag{5.6}$$

Choosing the simplest assumption about the form of $\bar{N}(F, \rho, v)$ — that the atoms are produced with the state distribution observed previously (Eq. 5.2), the atoms have

a single velocity, $v_0$, and the production occurs in a disc of radius $\rho_{\max}$ — we can write

$$\bar{N}(F,\rho,v) \propto \frac{2\pi\rho}{\pi\rho_{\max}^2}\delta\left(v-v_0\right)F^{-3} \tag{5.7}$$

and thus the two production formulas become

$$N_{\omega=0} \propto \int_0^{\rho_{\max}} \frac{2\pi\rho}{\pi\rho_{\max}^2}d\rho \int_{F_1(\rho)}^{F^{\max(\rho)}} F^{-3}dF \tag{5.8a}$$

$$N_{\omega} \propto \int_0^{\rho_{\max}} \frac{2\pi\rho}{\pi\rho_{\max}^2}d\rho \int_0^{2\pi} \frac{d\phi}{2\pi} \int_{F_1(\rho,\omega/v_0,\phi)}^{F^{\max(\rho)}} F^{-3}dF \tag{5.8b}$$

The solid curves in Fig. 5.15 show the expected number of detected $\overline{\mathrm{H}}$ (Eq. 5.8) normalized to $N_{\omega=0}$ for several values of the center of mass energy ($E_{\mathrm{CM}} = (M/2)v_0^2$). On average $4 \times 10^5$ positrons and $2 \times 10^5$ antiprotons were used. Comparing this to the measured results reveals an axial energy of approximately 200 meV (2400 K) which is much higher than the 4.2 K trap environment that sets a lower limit on the expected velocity distribution. From the comparison of absolute numbers of detected antihydrogen atoms to the initial number of $\overline{\mathrm{p}}$ using the estimated solid angle of the detection well discussed above, we do expect that the radial velocity should be smaller. Note also that this velocity distribution is only measured for atoms who ionize at fields lower than 65 V/cm (*i.e.* atoms with a radius of less than 0.24 µm). The more tightly bound states may still have a lower velocity.

The force on the atom due to electric field gradients could distort these measurements by either slowing down the atoms or speeding them up. However using a simple estimate of the fractional effect on the velocity of the atoms (Eq. 5.38) for the worst case scenario of atoms that just ionize in the detection well ($\rho = 0.3$ µm), this effect produces only a 1 % total change in the velocity and can be ignored. However if the

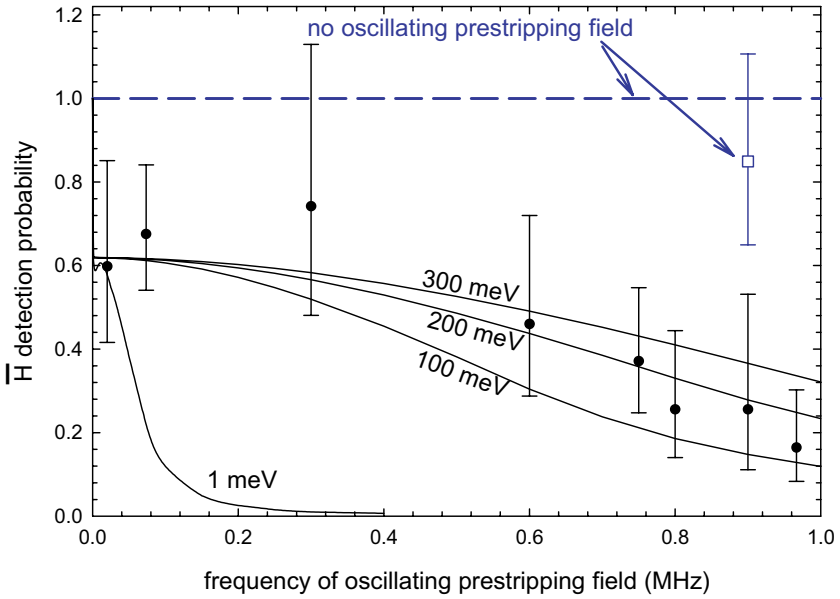


Figure 5.15: The fractional number of $\overline{\mathrm{H}}$ atoms detected decreases as the frequency, $\omega/2\pi$, of the oscillating field increases (solid points). The solid curves show the calculated fraction for a given axial energy. When the oscillating field is not applied the number of $\overline{\mathrm{H}}$ atoms detected increases (dashed line and open point).

atoms had a 4.2 K distribution, up to an order of magnitude change in the velocity is possible. Furthermore, radial fields may direct slow $\overline{\mathrm{H}}^*$ atoms to annihilate on the electrode surfaces prior to entering the detection well [81]. As such one must be careful of polarization effects in future experiments on slower atoms.

Several models may account for the unexpectedly high velocity distribution. First, if the recombination rate is peaked when the relative axial velocity of the $\overline{\mathrm{p}}$ and $\mathrm{e}^+$ are approximately equal, the mean $\overline{\mathrm{H}}$ velocity will be comparable to that of the 4.2 K $\mathrm{e}^+$ distribution which would result in approximately 210 meV $\overline{\mathrm{H}}$ atoms. This agreement is most likely a coincidence given the approximations involved in the estimate.

A second model is based on the idea that the recombination rate is so rapid that any $\overline{\mathrm{p}}$ will recombine into $\overline{\mathrm{H}}$ during a single pass through the positron cloud. In order for the $\overline{\mathrm{H}}$ to survive the fields of the nested Penning trap at least one de-excitation collision must occur before the $\overline{\mathrm{H}}$ atom leaves the positron cloud. The maximum $\overline{\mathrm{p}}$ speed for this to happen is given by

$$v_{\overline{\mathrm{p}}} = 2n_{\mathrm{e}^+}(\pi b^2)v_{\mathrm{e}^+}z_{\mathrm{e}^+} \tag{5.9}$$

where $n_{\mathrm{e}^+} = 1.6 \times 10^7/\,\mathrm{cm}^3$ is the density of the $\mathrm{e}^+$ cloud, $b = e^2/(4\pi\epsilon_0 k_b T) = 4\,\mu\mathrm{m}$ is the classical distance of closest approach between a $\mathrm{e}^+$ and a $\overline{\mathrm{p}}$, and $2z_{\mathrm{e}^+} = 1\,\mathrm{mm}$ is the length of the positron cloud. The $\overline{\mathrm{H}}$ velocity would then correspond to 500 meV. This model has the interesting implication that the speed of the final $\overline{\mathrm{H}}$ atom is proportional to

$$v_{\overline{\mathrm{H}}} \propto n_{\mathrm{e}^+}L/T^{3/2} \tag{5.10}$$

Thus a shorter, lower density, and hotter $\mathrm{e}^+$ cloud should produce slower antihydrogen atoms. These are the exact opposite of the conditions needed to produce the

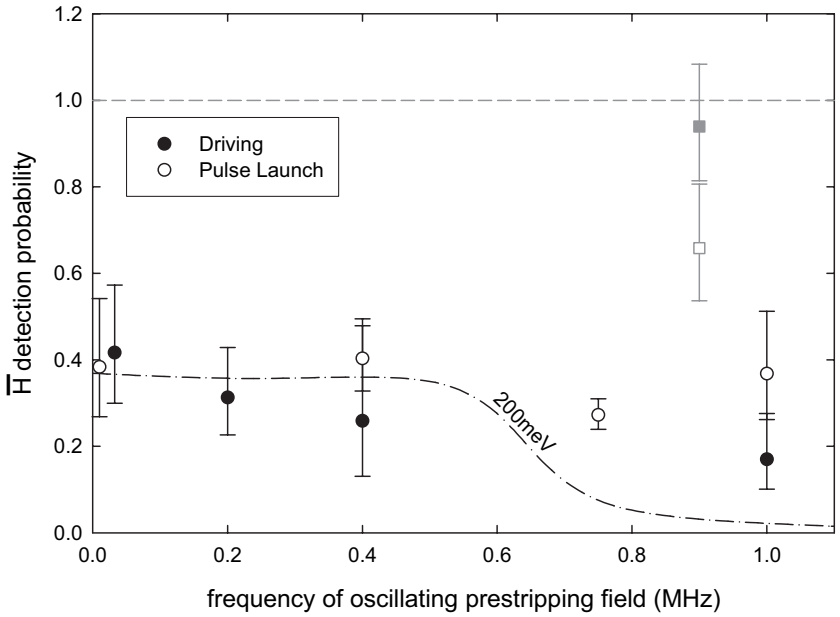


Figure 5.16: Repeating the velocity experiments in HBAR2 for both the driving and pulse launching methods shows an increased velocity. The solid points show the experimentally detected fraction and the dashed curve shows the calculated fraction for a 200 meV axial energy.

maximum total number of $\overline{\mathrm{H}}$ atoms. A simulation of recombination has also shown a similar scaling in the velocity of the resultant $\overline{\mathrm{H}}$ atoms [27].

To compare the effect of pulse launching $\overline{\mathrm{p}}$ into the nested well, these experiments were repeated in HBAR2 for both pulse launching $\overline{\mathrm{p}}$ as well as the standard driving experiments (Fig. 5.16). The resulting velocities are clearly higher even for a similar driving experiment. This may have been due to using on average $1.2 \times 10^6$ ($7 \times 10^5$) positrons for the pulse launched (driven) experiments which would result in an increase $e^+$ cloud length and density.

Finally as discussed earlier, we expect the radial velocity to much slower than the axial velocity since if it were equal to the axial velocity the resulting isotropic distribution would imply a factor of 5 more antihydrogen being produced compared

to the number of initial antiprotons. ATHENA has also observed an anisotropic distribution of $\overline{\mathrm{H}}$ atomic velocities [82]. Their measurement of the axial distribution of $\overline{\mathrm{H}}$ annihilation vertices reveals an enhanced number at large axial distances relative to an isotropic distribution. In a model independent manner, this implies that the axial temperature must be at least a factor of $2.3 \pm 0.6$ greater than the radial temperature however it is not possible to infer an absolute temperature from this data.

## 5.5 Photoionization

While field ionization is an ideal detection method for weakly bound $\overline{\mathrm{H}}$ states, ionizing low-lying $\overline{\mathrm{H}}$ states requires fields on the order $5 \times 10^{10}\,\mathrm{V/cm}$ which are experimentally impossible to create in a Penning trap. The other technique used to detect $\overline{\mathrm{H}}$ atoms relies on detecting temporal and spatial coincidence in annihilations from a $\mathrm{e}^+$ and a $\overline{\mathrm{p}}$ and provides no insight into the internal structure of the atom but can detect all atoms regardless of their internal state [8].

An alternative method that can both detect low-lying atoms as well as probe their internal state is through the use of photo-ionization. Here rather than using an external electric field to remove the axial atomic binding, an incoming photon excites the bound positron to the continuum. The cross-section for this process for a hydrogenic atom with principal quantum number, $n$, is given by Kramer's formula [83]

$$\sigma_n = \frac{64\pi}{3\sqrt{3}} \alpha \left(\frac{\omega_\Gamma}{\omega}\right)^3 \frac{a_0^2}{n^5} \tag{5.11}$$

where $\omega_\Gamma = -13.6\,\mathrm{eV}/\hbar$, $a_0 = 0.5\text{Å}$ is the Bohr radius, and $\alpha = 1/137$ is the fine structure constant. This can be related to the probability of photo-ionization, $P$,

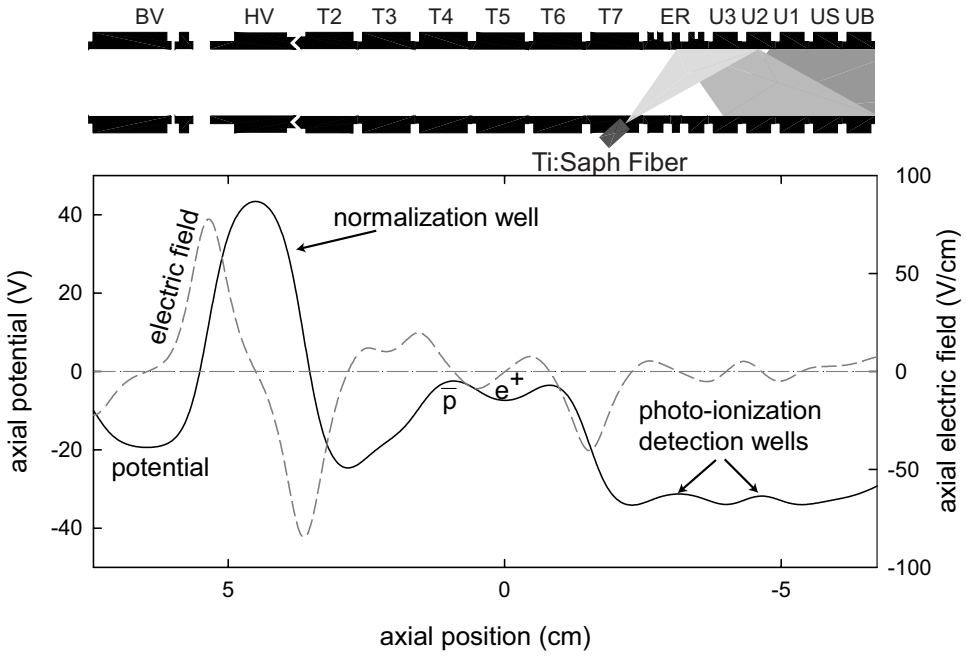


Figure 5.17: Potentials and electric fields used to produce $\overline{\mathrm{H}}$ and then detect the $\overline{\mathrm{p}}$ from photo-ionized atoms. The 821.25 nm Ti:Saph laser enters through an optical fiber glued to the side of *T7*.

through

$$\frac{dP}{dt} = (1-P)\sigma_n \frac{I_0}{\hbar\omega} \tag{5.12}$$

where $I_0$ is the intensity of the applied laser radiation. Thus for a given detection well of length, $\Delta z$, and velocity of the incoming $\overline{\mathrm{H}}$ atoms, $v$,

$$P = 1 - \exp\left[-\sigma_n \frac{I_0}{\hbar\omega}\frac{\Delta z}{v}\right] \tag{5.13}$$

To implement photoionization as a method for detecting low-lying $\overline{\mathrm{H}}$ states, we placed two small detection wells to the side of a standard nested well (Fig. 5.17). As the electric field within the detection wells is smaller than that of the exit to the nested well, the only antihydrogen atoms that can ionize and deposit a $\overline{\mathrm{p}}$ in the well are those that photo-ionize. In particular, any atoms that would have field ionized by

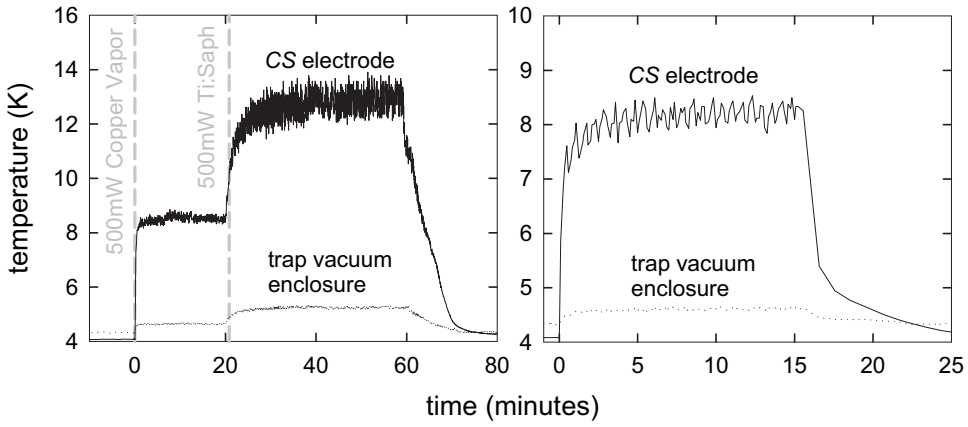


Figure 5.18: (a) Heating of the electrode stack and trap vacuum enclosure due to the application of a 500 mW, 511 nm copper vapor laser to the *Cs* electrode (Chapter 6) and a 500 mW, 821.25 nm Ti:Saph laser to *T7* for over an hour. (b) Heating of the electrode stack due to the 300 mW, 821.25 nm Ti:Saph laser during a typical photoionization experiment.

the 5.5 V/cm maximum field in the detection well would have already been ionized by the 40 V/cm field leaving the nested well. Antihydrogen atoms are produced through driving $\overline{\mathrm{p}}$ over the top of the $\mathrm{e}^+$ well as described before.

Laser light at 821.25 nm is injected into the electrode stack through a 550 µm multi-mode optical fiber glued into the side of *T7*. As the electrode surfaces are plated with a thin gold layer which is reflective at this wavelength, the light bounces down the electrode stack and approximately 10 % of the incoming light is observed at the bottom of the stack. As there are on average 8 bounces, this corresponds to a reflectivity of less than 75 %. The 821.25 nm light is produced from a Ti:Saph laser with a pulse length of 20 ns and a repetition rate of 10 kHz [84]. The output power is adjustable but for these experiments a 300 mW average power was used corresponding to an instantaneous intensity at the first detection well of $6 \times 10^3$ W/cm$^2$ which is reduced to 700 W/cm$^2$ at the second detection well due to the increased distance and

| Ti:Saph power | $\overline{\mathrm{p}}$ loss per second |
|---|---|
| 315 mW | $40 \pm 6$ |
| 810 mW | $200 \pm 40$ |

Table 5.1: $\overline{\mathrm{p}}$ loss rates from the application of the 821.25 nm Ti:Saph laser to *T7* with the antiprotons located on that electrode as well.

one reflection.

The large amount of power dissipated in the electrode stack by the 821.25 nm light results in a temperature increase of over 5 K of the electrode stack (Fig. 5.18). This large amount of heat will release atoms initially cryo-pumped to the electrode surfaces which can collide with trapped $\overline{\mathrm{p}}$ resulting in unwanted annihilations (Table 5.1). These losses are minimized by reducing the laser power as much as possible as well as by repeatedly applying the laser in an effort to clean off the surfaces that are most affected.

For our detection well length of 1.6 cm, Eqs. 5.13 and 5.11 predict a probability of ionization for $n = 3$ of 80 %. However the laser has a duty cycle of 0.02 %, resulting in an averaged probability of only 1 in 6000 atoms in $n = 3$ expected to be ionized in the first well and 1 in 30,000 atoms in the second well. Our observation of no atoms in the detection well during two attempts thus suggests that less than 9000 $n = 3$ atoms were produced. The null result is not unexpected as in total we would expect around 2000 highly excited atoms to have been produced and due to the short distance between the nested well and the detection very few of these atoms would have radiatively decayed to $n = 3$. Furthermore the probability of detecting higher $n$ states scales as $n^{-5}$ so we would expect a factor of 4 less sensitivity to $n = 4$ states

for example. The best method to raise the detection probability would be to increase the duty cycle of the laser. Simply adding more instantaneous laser power will not help however as we already ionize approximately 80 % of any $n = 3$ atoms that are exposed to an 821 nm photon.

## 5.6 Antihydrogen Motion in a Strong Magnetic Field

As we have shown, antihydrogen atoms produced through collisions between positrons and antiprotons are typically created with a large radius. The positron is thus weakly bound to the antiproton and is extremely susceptible to perturbations. In order to understand more fully the observed behavior of these atoms, we will first develop a framework to discuss these atoms in greater detail.

Since the radius is so large compared to the ground state, it is appropriate to consider $\overline{\mathrm{H}}^*$ as a classical system with Hamiltonian given by

$$\begin{aligned} H_{\overline{\mathrm{H}}^*} =& \frac{p_{z_{\overline{\mathrm{p}}}}^2 + p_{x_{\overline{\mathrm{p}}}}^2 + \left(p_{y_{\overline{\mathrm{p}}}} + eBx_{\overline{\mathrm{p}}}\right)^2}{2m_{\overline{\mathrm{p}}}} + \frac{p_{z_{\mathrm{e}^+}}^2 + p_{x_{\mathrm{e}^+}}^2 + \left(p_{y_{\mathrm{e}^+}} - eBx_{\mathrm{e}^+}\right)^2}{2m_{\mathrm{e}^+}} \\ & - \frac{e^2}{4\pi\epsilon_0 \left|\vec{r}_{\mathrm{e}^+} - \vec{r}_{\overline{\mathrm{p}}}\right|} + e\phi\left(\vec{r}_{\mathrm{e}^+}\right) - e\phi\left(\vec{r}_{\mathrm{e}^+}\right) \end{aligned} \tag{5.14}$$

where the external electric field is given by $\vec{E} = -\vec{\nabla}\phi$ and the magnetic vector potential has been chosen as $\vec{A} = Bx\hat{\mathbf{y}}$ to give a uniform axial magnetic field, $\vec{B} = B\hat{\mathbf{z}}$. We have also neglected the spin of the particles as the spin-field interaction energy is constant due to the uniform magnetic field and thus has no effect on the motion of an atom. In addition the spin-orbit coupling is very small because of the large assumed radius.

The magnetic field makes it impossible to completely separate the internal motion

and the center of mass motion. However, by defining the pseudomomentum [85, 86, 81, 87]

$$\vec{K} \equiv M\dot{\vec{R}} + q\vec{B} \times \vec{r} \tag{5.15}$$

where $M = m_{\bar{\mathrm{p}}} + m_{\mathrm{e}^+}$, $\mu = m_{\bar{\mathrm{p}}} m_{\mathrm{e}^+} / \left(m_{\bar{\mathrm{p}}} + m_{\mathrm{e}^+}\right)$, $\vec{R} = \left(m_{\bar{\mathrm{p}}}\vec{r}_{\bar{\mathrm{p}}} + m_{\mathrm{e}^+}\vec{r}_{\mathrm{e}^+}\right)/M$, and $\vec{r} = \vec{r}_{\mathrm{e}^+} - \vec{r}_{\bar{\mathrm{p}}}$, a partial separation can be done at the expense of introducing a pseudo-potential which depends on the motion of the center of mass of the atom. With these definitions the Hamiltonian (Eq. 5.14) becomes

$$\begin{aligned} H =& \frac{|\vec{K}|^2}{2M} - \omega_{cM}\left(K_Y x - K_X y\right) + \frac{M\omega_{cM}^2}{2}\left(x^2 + y^2\right) + \frac{p_x^2}{2\mu} \\ &+ \frac{\left(p_y - \sqrt{1 - \frac{4\mu}{M}}eBx\right)^2}{2\mu} + \frac{p_z^2}{2\mu} - \frac{e^2}{4\pi\epsilon_0\left|\vec{r}\right|} + e\phi\left(\vec{r}_{\mathrm{e}^+}\right) - e\phi\left(\vec{r}_{\mathrm{e}^+}\right) \end{aligned} \tag{5.16}$$

where $\omega_{cM} = eB/M$, $\vec{p} = \mu\dot{\vec{r}} - eB(\vec{R}\cdot\hat{\mathbf{x}})\hat{\mathbf{y}}$, and $x$, $y$, and $z$ denote relative positions. In order for $X$, $Y$, and $Z$ to be canonically conjugate to $K_X$, $K_Y$, and $K_Z$, we must slightly redefine them as compared to the center of mass coordinates. In particular:

$$\vec{R} = \left(X - \frac{K_Y}{eB}, Y - \frac{K_X}{eB}, Z\right) \tag{5.17}$$

For the case of a uniform electric field, $H$ is independent of $X$, $Y$, and $Z$ and thus $\vec{K}$ is a constant of the motion. We will restrict our attention to the case where $\vec{E}$ is constant over the size of the atom enabling us to rewrite $e\phi\left(\vec{r}_{\mathrm{e}^+}\right) - e\phi\left(\vec{r}_{\mathrm{e}^+}\right) \approx -e\vec{E}\cdot\vec{r}$. This enters in same way as $\vec{K} \times \vec{B}/M$ so we can further simplify the Hamiltonian by defining

$$\vec{\mathcal{E}} = \vec{E} + \frac{\vec{K} \times \vec{B}}{M} \tag{5.18}$$

so the Hamiltonian is then given by

$$H = \frac{p_x^2}{2\mu} + \frac{\left(p_y - \sqrt{1 - \frac{4\mu}{M}}eBx\right)^2}{2\mu} + \frac{p_z^2}{2\mu} - \frac{e^2}{4\pi\epsilon_0\left|\vec{r}\right|} + \frac{M\omega_{\mathrm{cM}}^2}{2}\left(x^2 + y^2\right) - e\vec{\mathcal{E}}\cdot\vec{r} \tag{5.19}$$

where we have dropped the constant term $K^2/2M$ as it has no effect on the motion of the atom.

The equations of motion for the relative coordinate, $\vec{r}$, with $\vec{E} = 0$ are equivalent to those of a charged particle in a Penning trap so we expect the same three motions of a rapid cyclotron motion at $\omega_{c\mu} \approx eB/\mu$, the axial motion at $\omega_z \approx \sqrt{e^2/\left(4\pi\epsilon_0\mu\rho^3\right)}$, and a slow $\vec{E} \times \vec{B}$ magnetron drift at $\omega_m = e/(4\pi\epsilon_0 B\rho^3)$. To ensure these motions are separable we must have a well defined frequency ordering

$$\omega_{c\mu} \gg \omega_z \gg \omega_m \tag{5.20}$$

which is satisfied when

$$\rho \gg \rho_{c\mu} = \left(\frac{\mu}{4\pi\epsilon_0 B^2}\right)^{1/3} = 0.07\,\mu\text{m} \tag{5.21}$$

for our 5.3 T field. Note that this is a weak limit and a better requirement, as we will show later, is that $\omega_{c\mu} > 3\omega_z > 3\omega_m$ which implies that $\rho > 0.14\,\mu\text{m}$ is required for regular guiding center motion.

The cyclotron motion is independent of the slower motions within this assumption and, in a uniform magnetic field, is constant so we can replace the cyclotron Hamiltonian,

$$H_c = \frac{p_x^2}{2\mu} + \frac{\left(p_y - \sqrt{1 - \frac{4\mu}{M}}eBx\right)^2}{2\mu} \tag{5.22}$$

with its action form,

$$H_c = I_c\omega_{c\mu} = \omega_{c\mu}\frac{1}{2\pi}\oint p_x\left(H_c, x\right)dx \tag{5.23}$$

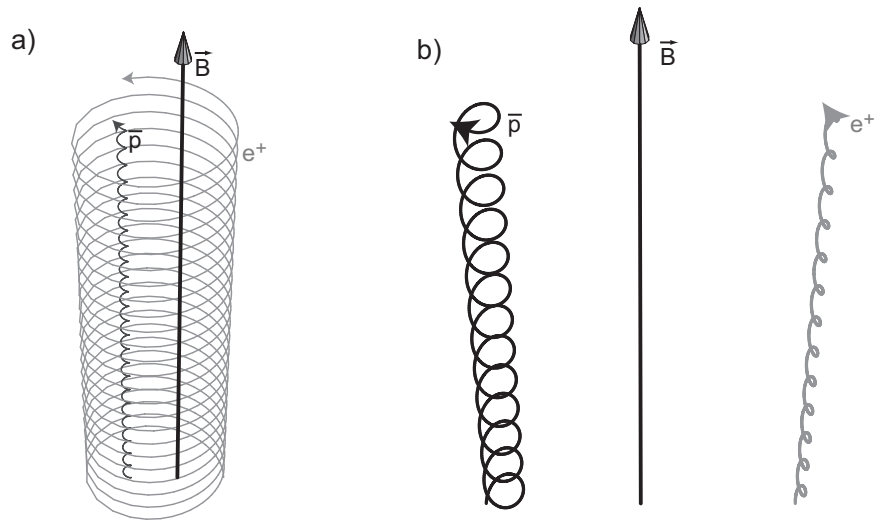


Figure 5.19: The two types of bound orbits for a guiding center atom — (a) a typical guiding center atom and (b) a giant dipole moment atom.

with this replacement, the particle's $x$ position is now given by the guiding center position $x_g = (p_y/eB)(1 - 4\mu/M)^{1/2} \approx p_y/eB$ and the guiding center Hamiltonian is [88]

$$H_g = I_c\omega_{c\mu} + \frac{p_z^2}{2\mu} - \frac{e^2}{4\pi\epsilon_0\sqrt{|\vec{\rho}|^2 + z^2}} - e\mathcal{E}_z z + \frac{M\omega_{cM}^2}{2}|\vec{\rho}|^2 - e\vec{\mathcal{E}}_\perp \cdot \vec{\rho} \qquad (5.24)$$

where $\vec{\rho} = (cp_y/eB, y)$. This Hamiltonian for the internal motion is integrable due to the three adiabatic invariants associated with the cyclotron, axial, and magnetron motions.

Two qualitatively different types of orbits are contained in the guiding center Hamiltonian when no external electric field is applied (Fig. 5.19). Here the $z$ motion is always constrained for finite energy and hence the axial motion exhibits no interesting behavior. We will thus consider only the case where there is no axial oscillation energy. The Hamiltonian then reduces to (again neglecting constant terms and assuming

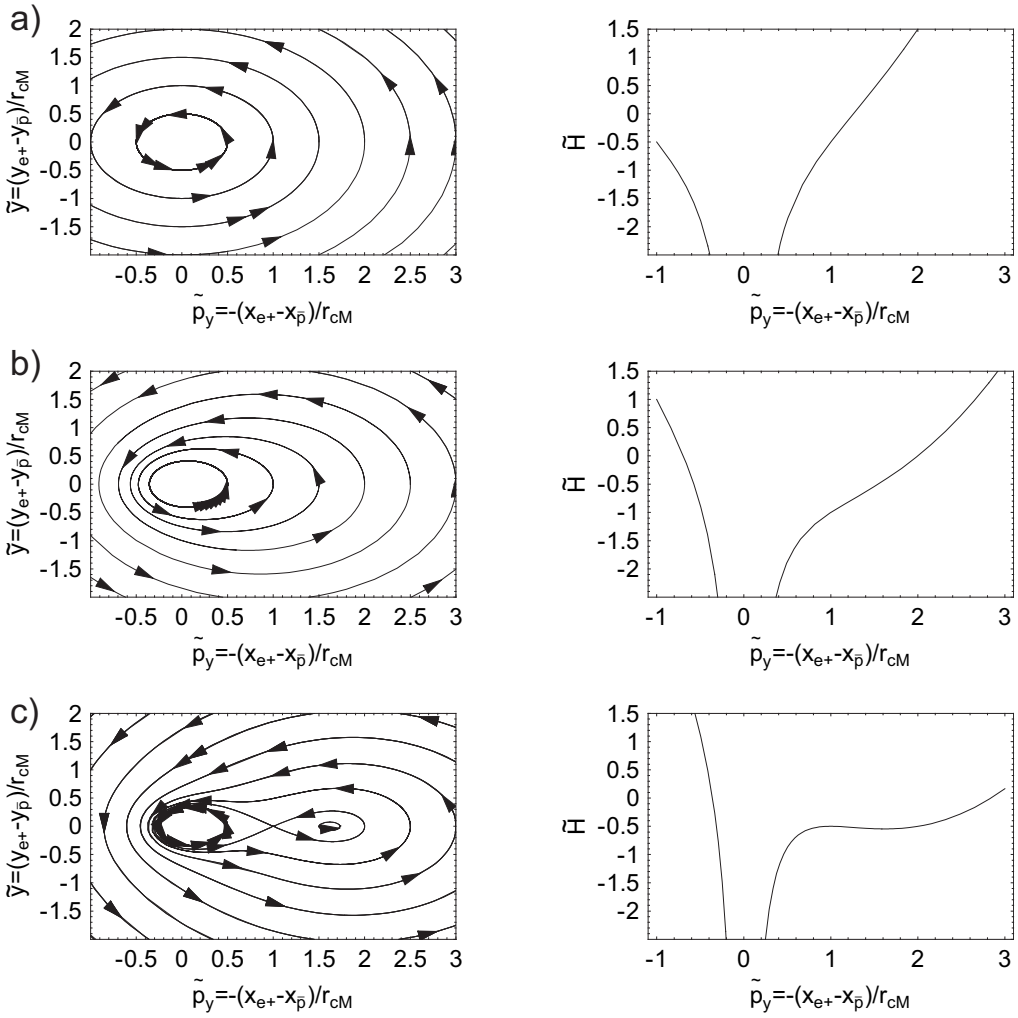


Figure 5.20: Phase trajectories of a guiding center atom and cross sections of $\tilde{H}$ along $\tilde{y}=0$. In (a) $\tilde{K}=0$, (b) $\tilde{K}=1.0$, and (c) $\tilde{K}=2.0>\tilde{K}_c$.

$\vec{K}_\perp = K_\perp \hat{\mathbf{x}}$)

$$H_r = -\frac{e^2}{4\pi\epsilon_0\sqrt{|\vec{\rho}|^2}} + \frac{M\omega_{cM}^2}{2}|\vec{\rho}|^2 - \frac{eB}{M}K_\perp y \tag{5.25}$$

It is possible to remove the explicit dependence on the magnetic field by scaling all the variables using $r_{cM} = [M/(4\pi\epsilon_0 B^2)]^{1/3}$, $\omega_{cM}^{-1}$, and $M$ as the units of length,

time, and mass respectively. Then we have the following relations

$$\tilde{H} = \frac{H}{M\omega_{cM}^2 r_{cM}} = \frac{1}{2}\left(\tilde{K}_\perp - \tilde{p}_y\right)^2 + \frac{1}{2}\tilde{y}^2 - \frac{1}{\sqrt{\tilde{p}_y^2 + \tilde{y}^2}} \tag{5.26a}$$

$$\tilde{y} = \frac{y}{r_{cM}} \tag{5.26b}$$

$$\tilde{p}_y = \frac{p_y}{M\omega_{cM} r_{cM}} \tag{5.26c}$$

$$\tilde{K}_\perp = \frac{K_\perp}{M\omega_{cM} r_{cM}} \tag{5.26d}$$

Figure 5.20 shows phase trajectories in the $\tilde{y} - \tilde{p}_y$ plane (which are equivalent to trajectories in $\tilde{y} - \tilde{x}$ plane due to the guiding center approximation) and plots of $\tilde{H}$ along $\tilde{y} = 0$ for different values of $\tilde{K}$. Above $\tilde{K}_c = 3/4^{1/3} \approx 1.89$, a second outer well appears. Trajectories contained in this well are giant dipole orbits (Fig. 5.19b) where the atom exhibits a permanent electric dipole moment while trajectories surrounding the Coulomb potential at $\tilde{y} = \tilde{p}_y = 0$ are standard guiding center orbits (Fig. 5.19a). In our 5.3 T field, $K_c$ corresponds to a $\overline{\mathrm{H}}$ transverse velocity of 800 m/s.

As discussed previously, the guiding center Hamiltonian (Eq. 5.24) is only valid when $\omega_{c\mu} \gg \omega_z \gg \omega_m$. Figure 5.21 shows a comparison of orbits calculated from the guiding center Hamiltonian (Eq. 5.24) versus those calculated from the full Hamiltonian (Eq. 5.14) as a function of average radius, $\bar{\rho}$. The dashed lines correspond to the criterions that either $\omega_{c\mu} = \omega_z$ or $\omega_{c\mu} = 3\omega_z$. The tighter constraint, $\omega_{c\mu} = 3\omega_z$, reflects the beginning of the deviation of the orbit from a simple guiding center orbit much more closely. At this point, energy is beginning to be traded between the motions due to close collisions and the individual motions are no longer separable.

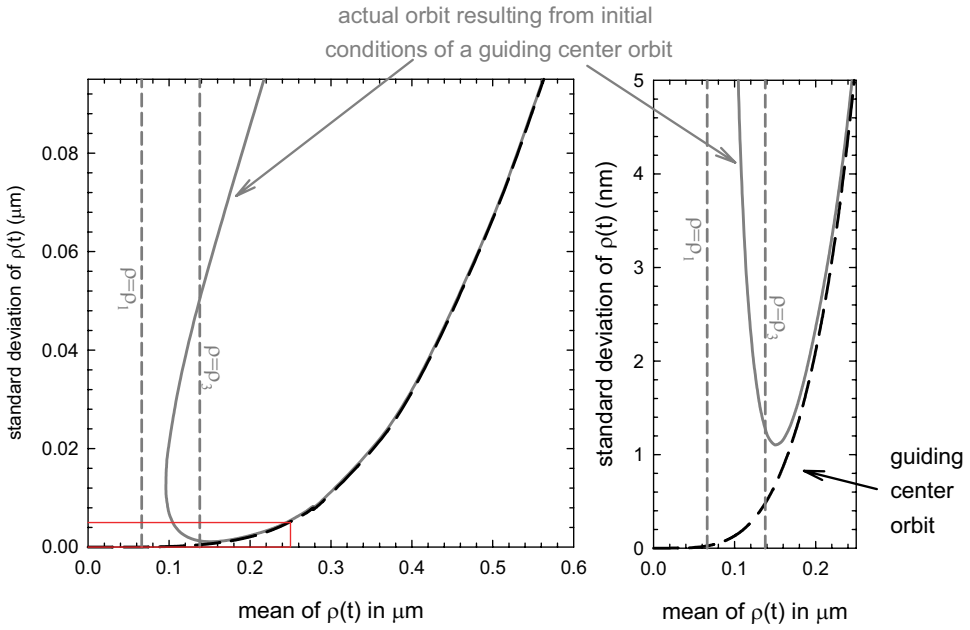


Figure 5.21: The guiding center approximation breaks down when $\rho < \rho_3$ as illustrated by a comparison of the standard deviations of orbits calculated from the guiding center Hamiltonian and the full Hamiltonian. In these simulations $\vec{K} = 0$.

### 5.6.1 Field Ionization

Figure 5.22 shows the effect of the electric field on the axial potential. For an atom near the ground state a saddle point forms and at a certain value of the electric field the positron is no longer bound axially. Classically this value is given by [89]:

$$E_z > \frac{3.21 \times 10^8\,\mathrm{V/cm}}{n^4} = 0.803\,\mathrm{V/cm}\left(\frac{\mu\mathrm{m}}{\rho}\right)^2 \tag{5.27}$$

where $n$ is the principal quantum number of the atom. Note that this equation does not account for the Stark shift in the energy levels due to the electric field or quantum mechanical effects. In practice, Eq. 5.27 is only accurate to a factor of 3 due to these limitations. For $\bar{\rho} \neq 0$, the axial well actually disappears when $\mathcal{E}_z > (5.54\,\mathrm{V/cm})(\,\mu\mathrm{m}/\rho)^2$.

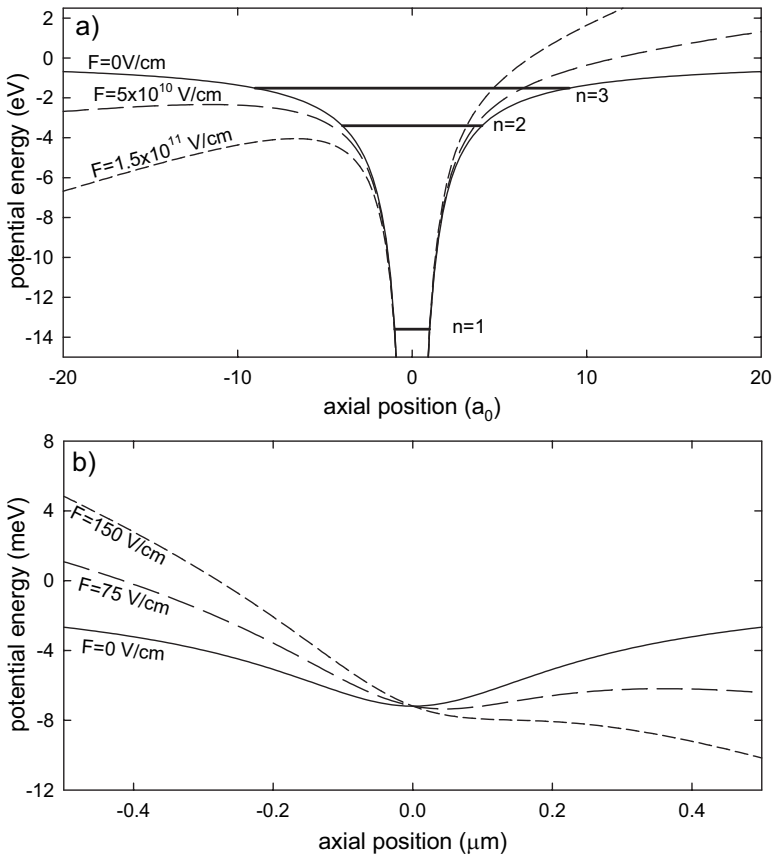


Figure 5.22: Simple classical picture of field ionization for (a) $\rho = 0$ and (b) $\rho = 0.2\,\mu\text{m}$.

We now wish to consider the effect on an atom as the axial electric field is slowly turned on which mimics the situation in our experiments closely. Inside the $e^+$ plasma, the external electric field is quite small on average, however, as the neutral atom escapes it can encounter much stronger fields. As long as the time scale of the change in the electric field is slow compared to the axial frequency, the axial action, $I_z$, is conserved even though the axial energy is not. $I_z$ is given by

$$\begin{aligned} I_z &= \frac{1}{2\pi}\oint p_z dz \\ &= \frac{1}{2\pi}\oint dz\sqrt{2\mu}\left[H_z + \frac{e^2}{4\pi\epsilon_0\sqrt{\rho^2+z^2}} + e\mathcal{E}_z z\right]^{1/2} \end{aligned} \tag{5.28}$$

and

$$H_z = \frac{p_z^2}{2\mu} - \frac{e^2}{4\pi\epsilon_0\sqrt{\rho^2+z^2}} - e\mathcal{E}_z z \tag{5.29}$$

Henceforth we will restrict ourselves to only the cases where $I_z = 0$ (*i.e.* where the atom has no axial energy). Initially, the primary effect of the electric field is to pull the positron and antiproton apart resulting in an electric dipole moment of the atom given by $d_z = \alpha\mathcal{E}_z$ where, for $I_z = 0$, $\alpha \approx 4\pi\epsilon_0\rho^3$ [90]. Eventually it is impossible to maintain a constant $I_z$ as one of the axial turning points disappear. At this point the $e^+$ is no longer bound and the atom ionizes. For $I_z = 0$ and $K_\perp = 0$, this occurs when $\mathcal{E}_z > 5.54\,\mathrm{V/cm}(\,\mu\mathrm{m}/\rho)^2$. Numerical calculations for the mean $K_\perp$ value expected for recombination at 4.2 K ($K_\perp = 1.0\times10^{-24}\,\mathrm{kg\cdot m/s}$) show that the field ionization occurs at a smaller field [90]

$$\mathcal{E}_z > 3.60\,\mathrm{V/cm}\left(\frac{\mu\mathrm{m}}{\rho}\right)^2 \tag{5.30}$$

The effect of a radial electric field on an atom is quite different from an axial electric field due to the axial magnetic field. In this situation the positron can never

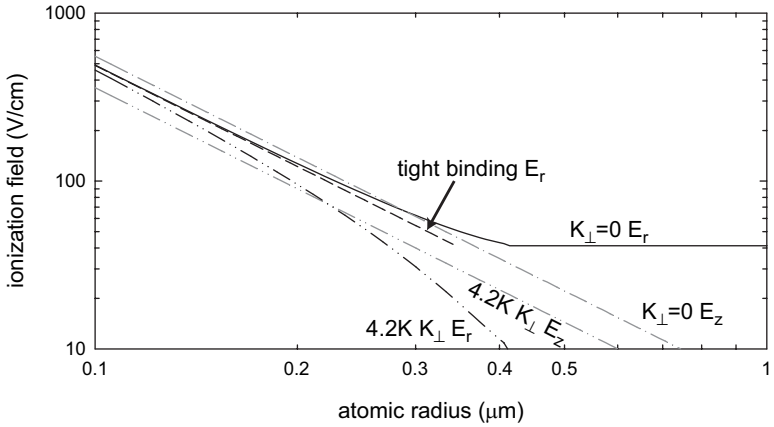


Figure 5.23: The electric field at which ionization occurs for $I_z = 0$. The two curves for axial ionization corresponds to when either $K_\perp = 0$ or $K_\perp$ is given by the mean 4.2 K thermal value. The curves for radial ionization correspond to a full numerical calculation (for $K_\perp = 0$ or $K_\perp$) and the value calculated from the tight binding assumption.

escape to infinity, so field ionization is not possible in the radial direction. However a radial electric field is equivalent to an increased perpendicular center of mass motion (Eq. 5.18). Hence as the radial electric field (or equivalently $K_\perp$) increases, the separatrix in Fig. 5.20 moves closer to the orbit. Eventually the orbit passes over the separatrix resulting in a giant dipole moment atom which is then immediately ionized by any remnant axial electric field within the trap. In the same manner as the axial field case, the radial energy is not conserved during this process but the transverse action,

$$I_m = \frac{1}{2\pi} \oint p_y[y, H, I_z, K_\perp] dy \tag{5.31}$$

is nearly constant until the separatrix crossing. Figure 5.23 shows the numerical application of these ideas. Note that the horizontal segment in the radial field ionization curve reflects the fact that the large outer well does not exist until a critical pseudomomentum is reached corresponding to $E_\perp = 41.2\,\mathrm{V/cm}$. For tightly bound atoms,

where $(\rho/r_{cM})^3 \ll 1$, an analytical expression can be found [87]

$$\mathcal{E}_\perp > 4.9\,\mathrm{V/cm}\left(\frac{\mu\mathrm{m}}{\rho}\right)^2 - \frac{KB}{M} \tag{5.32}$$

For the expected thermal $K_\perp$ value at 4.2 K of $1.0 \times 10^{-24}\,\mathrm{kg \cdot m/s}$ [90], this becomes

$$\mathcal{E}_\perp > 4.9\,\mathrm{V/cm}\left(\frac{\mu\mathrm{m}}{\rho}\right)^2 - 31.6\,\mathrm{V/cm} \tag{5.33}$$

### 5.6.2 Coupling between Center-of-Mass Motion and an Electric Field

Prior to ionizing, the atom becomes polarized in a similar manner to that described for the axial field case. For a radial electric field, the linear polarizability for small $E$ and $I_z = 0$ is given by [91]

$$\alpha_\perp = \frac{5}{2}(4\pi\epsilon_0\rho^3)\frac{1+\frac{2}{5}\rho^3 r_{CM}^3}{\left(1+\frac{\rho^3}{r_{CM}^3}\right)} \tag{5.34}$$

Due to the induced electric dipole moment, $\vec{d} = \alpha\vec{E}$, an electric field applies a force on the center of mass of the atom given by

$$\frac{d<\vec{K}>}{dt} = \nabla\alpha|\vec{E}|^2| \tag{5.35}$$

To gain insight into this force we consider a simple estimate of the change in axial velocity of a $\overline{\mathrm{H}}^*$ atom. The force can be expanded about the electrode where the electric field used for field ionization is generated giving

$$F \approx \alpha_z \left.\frac{\partial E^2(0,z)}{\partial z}\right|_{z=z_e} \tag{5.36}$$

The axial length of a high electric field generated by one electrode is comparable to the radius of the electrode, $\rho_0$, so the change in velocity is approximately

$$\Delta v_z = \frac{F}{M}\Delta t \approx \alpha \frac{E_{FI}^2}{M\rho_0}\frac{\rho_0}{v_z} \tag{5.37}$$

As $\alpha \approx 4\pi\epsilon_0\rho^3$ and $E_{FI} \approx e/(4\pi\epsilon_0\rho^2)$,

$$\frac{\Delta v_z}{v_z} \approx \frac{e^2/(4\pi\epsilon_0\rho)}{Mv_z^2} \tag{5.38}$$

Thus large fractional changes in velocity only occur when the binding energy of the atom is comparable to the energy of the center of mass motion.

## 5.7 Summary of Current Status

Over 7500 $\overline{\mathrm{H}}^*$ atoms have thus been produced in a one hour experiment by driving antiprotons within a nested Penning trap. Our field ionization analysis then indicates that the $\overline{\mathrm{H}}$ state distribution extends to atomic states with radius less than 0.1 µm. Atoms with this small of a radius can no longer be described by the simple guiding center atom model. Instead the motions of the atom are no longer separable and likely exhibit chaotic behavior [92, 93].

The axial velocity of the produced $\overline{\mathrm{H}}$ atoms was also measured for the first time. While the currently measured velocity of over 6000 m/s is much too high for the atoms to be successfully trapped and utilized for spectroscopy, the development of this technique for measuring axial velocity will allow for future optimization and hopefully a much reduced axial velocity. Furthermore, since we only measured the velocity of the weakest bound states, the deeper bound states may have slower velocities which

is consistent with the antihydrogen atom further de-exciting to lower states the more time it spends in the positron cloud.

While great progress has thus been made in the understanding of this production mechanism, to produce atoms that are usable for spectroscopic comparisons will require a technique to de-excite these atoms. Once atoms are de-excited, field ionizing them requires field magnitudes that are impossible to apply in our Penning trap. As such, a new detection method will be required. A promising candidate is photoionization as it is both state-selective and can ionize atoms in low-lying states. A first trial detected no atoms in the $n = 3$ or $n = 4$ states but with an active method to de-excite $\overline{\mathrm{H}}$ atoms this will likely change.

# Chapter 6

# Laser-Controlled Production of Antihydrogen

An alternative method to produce antihydrogen in a controlled state distribution was also investigated during this work. Here a charge exchange reaction that intrinsically conserves binding energy results in a process whereby the $\overline{\mathrm{H}}$ final state distribution is determined by the initial state distribution of the positronium atoms:

$$\mathrm{Ps} + \overline{\mathrm{p}} \longrightarrow \overline{\mathrm{H}} + \mathrm{e}^- \tag{6.1}$$

This reaction was first proposed utilizing ground state positronium in 1987 [28] and was soon demonstrated using protons instead of $\overline{\mathrm{p}}$ [94]. Unfortunately the cross section for the reaction in ground state atoms is very small so it is has not been tried for $\overline{\mathrm{p}}$. Utilizing excited positronium atoms, $\mathrm{Ps}^*$, increases the cross section as the cross section for charge exchange scales as the atomic radius squared, *i.e.* as $n_{\mathrm{Ps}}^4$ where $n_{\mathrm{Ps}}$ is the positronium principal quantum number [29].

To be efficient this reaction requires large numbers of $\mathrm{Ps}^*$ atoms. Hence it was

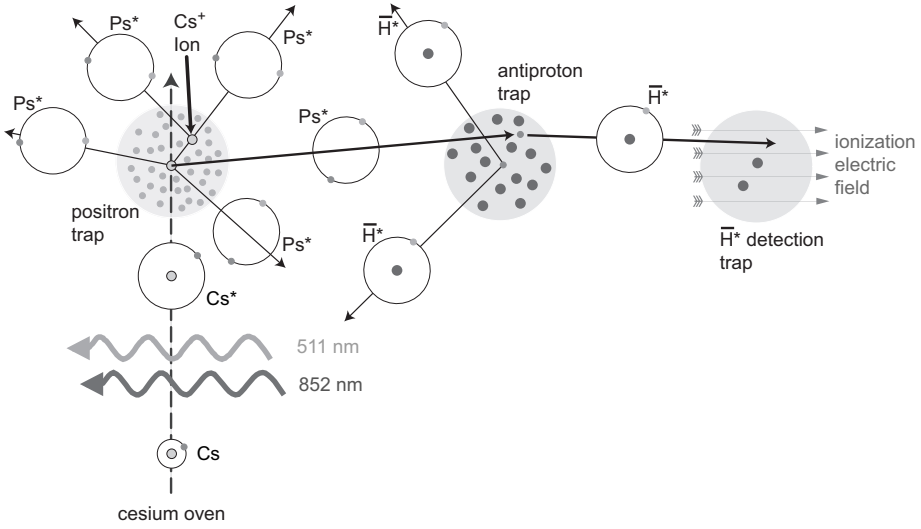


Figure 6.1: Schematic of the dual charge exchange process used for laser-controlled $\overline{\mathrm{H}}$ production.

suggested to produced $\mathrm{Ps}^*$ by an additional charge exchange reaction utilizing an alkali atom (in particular we use Cs) [11]:

$$\mathrm{Cs} + h\nu \rightarrow \mathrm{Cs}^* \tag{6.2a}$$

$$\mathrm{Cs}^* + \mathrm{e}^+ \rightarrow \mathrm{Ps}^* + \mathrm{Cs}^+ \tag{6.2b}$$

$$\mathrm{Ps}^* + \overline{\mathrm{p}} \rightarrow \overline{\mathrm{H}}^* + \mathrm{e}^- \tag{6.2c}$$

As shown in Fig. 6.1, a cesium beam must thus be produced in the 4.2 K trap, excited to a Rydberg state, and directed onto a trapped $\mathrm{e}^+$ cloud. The trapped $\mathrm{e}^+$ can then capture the valence electron of the $\mathrm{Cs}^*$ forming $\mathrm{Ps}^*$. Some of the $\mathrm{Ps}^*$ travel perpendicular to the axis of the trap and encounter a trapped $\overline{\mathrm{p}}$ cloud producing $\overline{\mathrm{H}}^*$.

This technique is likely to produce $\overline{\mathrm{H}}^*$ at the temperature of the trapped $\overline{\mathrm{p}}$ which is set by the initial collisions with 4.2 K electrons during stacking. Subsequent collisions with the much lighter $\mathrm{Ps}^*$ atoms during the charge exchange process should not substantially change the energy of the resultant $\overline{\mathrm{H}}^*$ atoms from that of the trapped

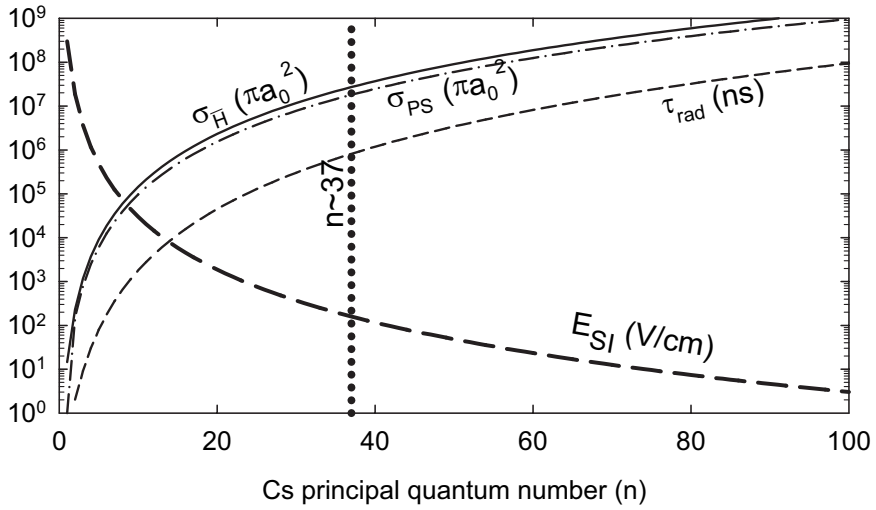


Figure 6.2: Tradeoffs involved in the choice of the principal quantum number for Cs atoms in the dual charge-exchange process. $\sigma_{\overline{\mathrm{H}}^*}$ and $\sigma_{\mathrm{Ps}^*}$ are the cross-sections for the two charge-exchange reactions, $\tau_{rad}$ is the radiative lifetime of the excited state, and $\mathrm{E_{SI}}$ is the field at which the given state ionizes.

antiprotons. This is quite different than the techniques described previously in which additional energy had to be given to the antiprotons in order to produce antihydrogen atoms so this technique will likely produce much colder $\overline{\mathrm{H}}^*$ atoms.

This charge exchange process also allows control over the final state distribution of $\overline{\mathrm{H}}^*$ by changing the initial $\mathrm{Cs}^*$ state distribution. Several parameters are traded off in the choice of the Cs principal quantum number, $n_{\mathrm{Cs}}$ (Fig. 6.2). First the cross sections for the two charge exchange processes both scale as $n_{\mathrm{Cs}}^4$. In particular from classical trajectory Monte Carlo calculations (CTMC) made with zero magnetic field,

$$\sigma_{\mathrm{Ps}} = 9.7 n_{\mathrm{Cs}}^4 \pi a_0^2 \tag{6.3}$$

$$\sigma_{\overline{\mathrm{H}}} = 14.5 n_{\mathrm{Cs}}^4 \pi a_0^2 \tag{6.4}$$

where $a_0 = 0.529\,\text{Å}$ is the Bohr radius [11] and the binding energy of the atom is assumed to be conserved throughout these reactions requiring that $n_{Ps} = n_{Cs}/\sqrt{2}$.

In these CTMC calculations, the trajectories of the incoming charged particle, the core of the Rydberg atom, and the Rydberg electron are obtained by integrating the Newtonian equations of motion. Previous predictions for other Rydberg systems agree quite well with experiments [95]. Second, excited states have a finite lifetime which for completely $\ell$-mixed states, as expected in a strong magnetic field, is given by [96]:

$$\tau_{rad} = 46.8\,\mathrm{ps}\frac{n^5}{\ln(2n-1) - 0.36} \tag{6.5}$$

Note that this equation omits the $n$-mixing which occurs as well for highly excited states and thus is only a rough estimate. For both of these reasons a higher principal quantum number is better. However, as $n_{\mathrm{Cs}}$ increases, the required field to ionize the $\mathrm{Cs}^*$ atom decreases thus if $n_{\mathrm{Cs}}$ is too high atoms will not survive the intrinsic electric field of the Penning trap. The choice of $n_{Cs} = 37$ was chosen both as a reasonable tradeoff of the parameters as well as for the availability of an inexpensive laser system to excite the atoms. This choice results in a enormous cross section — the size of a disc of diameter 30 µm.

The calculations of these cross-sections has been performed only for zero magnetic field. The addition of a strong magnetic field complicates the motion of the Rydberg atoms involved in these charge exchange processes and could have a large effect on the cross-sections. In particular, the center of mass motion of positronium in a strong magnetic field is unstable on a much larger scale than the primarily regular motion of a typical Rydberg atom with an "infinitely heavy" proton nucleus [97]. A calculation of proton impact onto a Rydberg atom revealed up to a factor of two decrease in the cross-section for charge exchange [98]. A further calculation considered the impact of

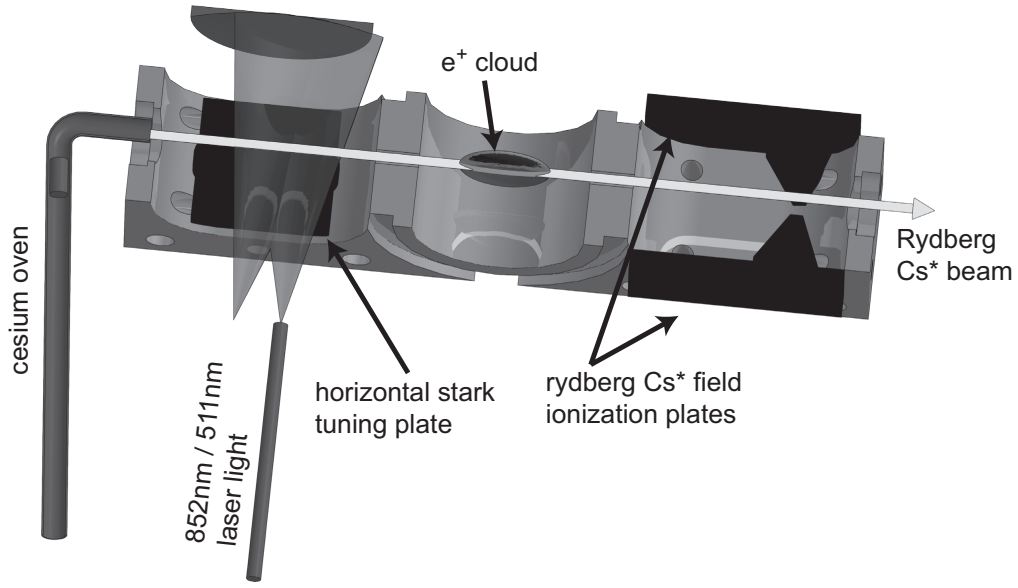


Figure 6.3: The cesium beam electrode showing its important elements.

giant dipole Ps* atoms onto antiprotons and found another factor of two reduction in the cross-section [30]. However neither of these studies exactly match the conditions in our two stage charge exchange process and, in fact, giant dipole Ps* atoms will not survive the electric fields within the Penning trap and thus cannot be responsible for the observed charge exchanges. It is thus important for a calculation following the entire process to be performed.

## 6.1 Production of Rydberg Cesium

The production of a Rydberg cesium beam inside a 4.2 K vacuum enclosure is a large technical challenge. Figure 6.3 shows the apparatus designed to overcome these difficulties. The various pieces will be discussed next.

Cesium does not produce an appreciable vapor pressure until it melts at 302 K. As

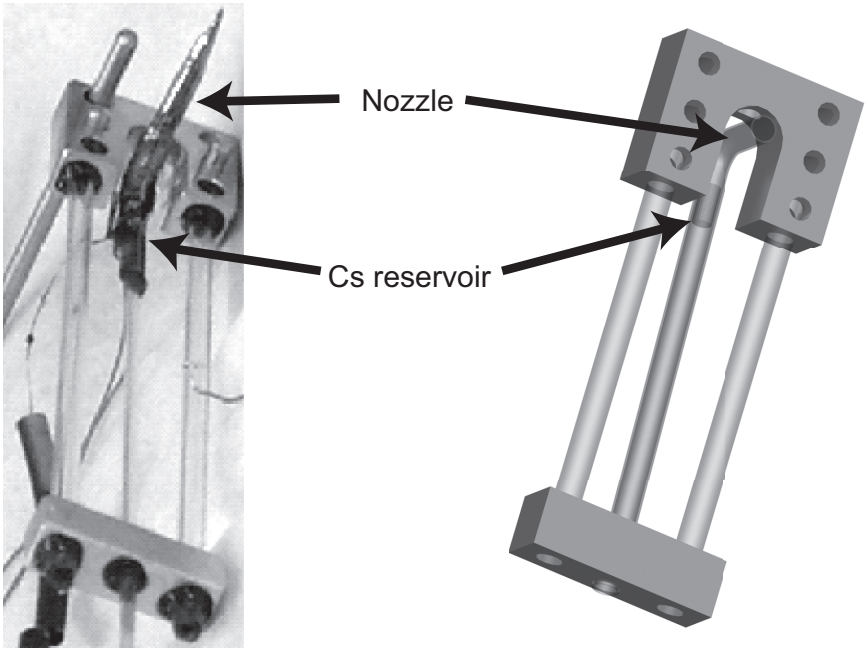


Figure 6.4: The cesium oven used in our 4.2 K Penning trap.

such the oven must be designed to warm a macroscopic quantity of cesium to higher than its melting point without raising the temperature of the electrode stack as this would heat particles trapped within and eventually cause particle losses. The final oven design contains approximately 5 $mm^3$ of Cs and is mounted on a series of glass tubes to thermally isolate the oven from the electrode (Fig. 6.4). Gold plating around the 3.8 mm Evenohm heater wire used on the oven reduces the thermal radiation load on the 4.2 K environment. During a typical experiment, the temperature of the *Cs* electrode only reaches 8 K while the oven reaches over 350 K (Fig. 6.5).

Cesium's high reactivity with the oxygen and water in air requires careful handling. The oven's nozzle is broken open only after the trap vacuum enclosure is completely ready to be evacuated and the entire trap has been surrounded by $N_2$ gas contained in a plastic bag. The vacuum enclosure is then immediately evacuated. This method

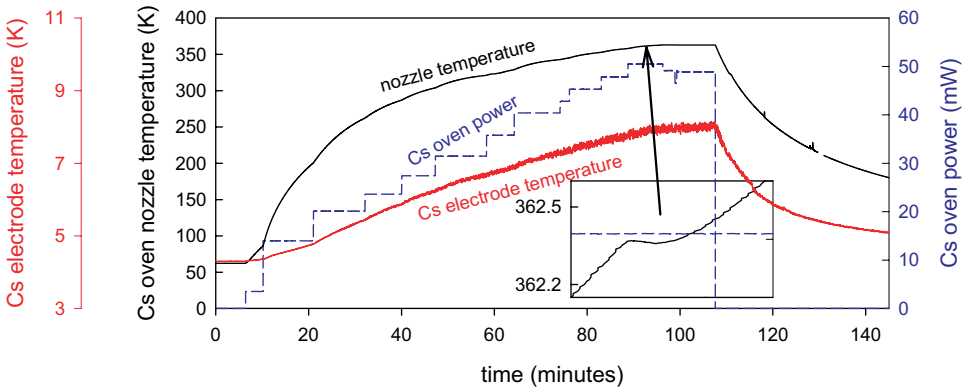


Figure 6.5: Typical temperatures during an $\overline{\mathrm{H}}^*$ production experiment. The inset shows the small decrease in temperature observed when the cesium in the reservoir melts.

has been a robust technique and resulted in a useable oven on every attempt so far provided that there was no vacuum leak. However when the trap warms up above 77 K, the previously cryopumped gas is no longer stuck to the walls and reacts with the cesium forming a crust on the oven that prevents proper operation. In general only approximately 1 in 2 ovens are useable after a thermal cycle even with a 10 hour heating time to slowly break through the crust.

### 6.1.1 Laser Excitation

To excite the cesium atoms to $n_{\mathrm{Cs}} = 37$, we utilize a two step laser excitation scheme (Fig. 6.6). First, an 852 nm, 20 mW infrared diode laser transfers atoms from the ground state, $6S_{1/2}$, to the excited state, $6P_{3/2}$. Atoms in $6P_{3/2}$ are then excited by a pulsed 511 nm copper vapor laser (Spektronika CU-BR5) to $n_{\mathrm{Cs}} \approx 37$. The basic layout of the optical system at CERN and at Harvard is shown in Fig. 6.7.

A magnetic field perturbs the atomic Hamiltonian to

$$H_B = A_{HFS}\vec{I}\cdot\vec{J} + g_J\mu_B\vec{J}\cdot\vec{B} + g_I\mu_B\vec{I}\cdot\vec{B} \tag{6.6}$$

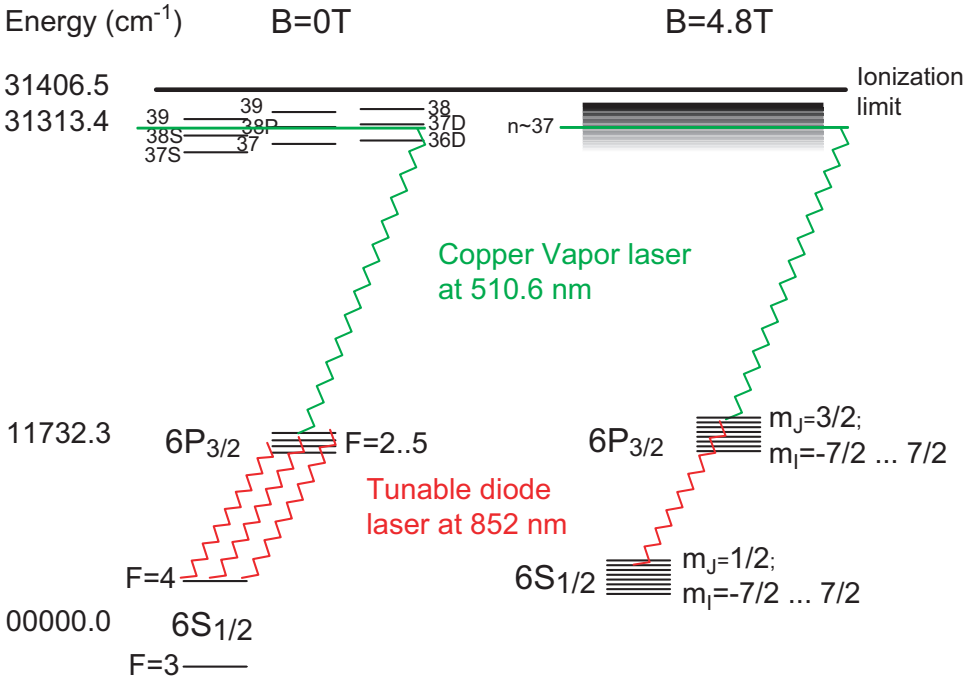


Figure 6.6: Simplified cesium energy level structure in a magnetic field of (a) 0 T and (b) 4.8 T.

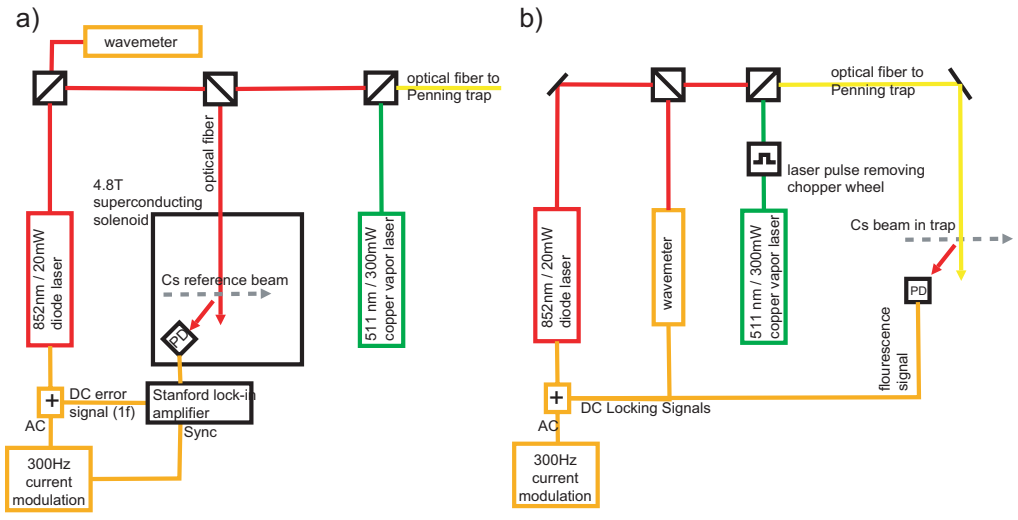


Figure 6.7: Optical system schematic for cesium excitation at (a) Harvard and at (b) CERN.

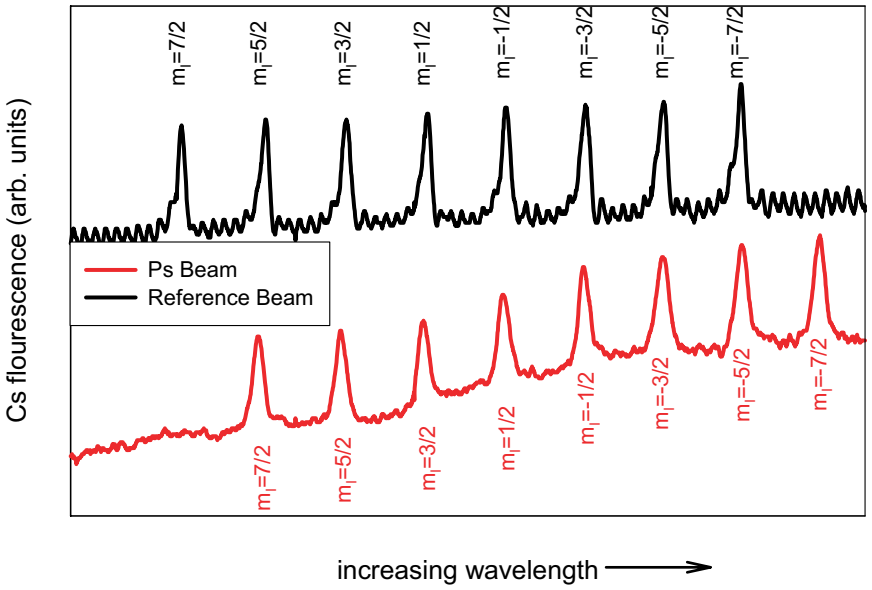


Figure 6.8: Laser scan showing the 8 fluorescence peaks of the Cs $|6S, J = 1/2, m_j = 1/2, I = 7/2\rangle \rightarrow |6P, J = 3/2, m_j = 3/2, I = 7/2\rangle$ manifold.

where $\vec{J}$ and $\vec{I}$ are the electron's angular momentum, $\vec{J} = \vec{L} + \vec{S}$, and nucleus's angular momentum respectively, $g_J$ and $g_I$ are the corresponding "g" factors that convert between angular momentum and the particular magnetic dipole moment, $\mu_B$ is the Bohr magneton, and $A_{HFS}$ is the coupling parameter describing the hyperfine structure. In a magnetic field where $g_J\mu_B\vec{J}\cdot\vec{B} \gg a_{HFS}\vec{I}\cdot\vec{J}$, $\vec{J}$ is quantized along $\vec{B}$ and Eq. 6.6 can be rewritten as

$$H_B = A_{HFS}m_I m_J + g_J\mu_B m_j B_0 + g_I\mu_B m_I B_0 \tag{6.7}$$

Since an electric dipole transition cannot change the nucleus's angular momentum (for cesium, $I = 7/2$), at 4.8 T we expect 16 possible closed cycling transitions from $6S_{1/2}$ to $6P_{3/2}$ separated into two manifolds of 8 transitions each. These two manifolds consist either of the transitions $|6S, J = 1/2, m_j = 1/2\rangle \rightarrow |6P, J = 3/2, m_j = 3/2\rangle$ or $|6S, J = 3/2, m_j = -1/2\rangle \rightarrow |6P, J = 3/2, m_j = -3/2\rangle$ (Fig. 6.8).

| | | |
|---|---|---|
| Fine structure $g$-factor | $g_j\left(6S_{1/2}\right)$ | 2.0025 |
| | $g_j\left(6P_{3/2}\right)$ | 1.3340 |
| Nuclear g-factor | $g_I$ | -0.0003989 |
| Hyperfine constant | $A_{6S_{1/2}}$ | $h \cdot 2.298\,\mathrm{GHz}$ |
| | $A_{6P_{3/2}}$ | $h \cdot 50.275\,\mathrm{MHz}$ |
| Saturation intensity | $I_{sat}$ | $2.706\ \mathrm{mW/cm^2}$ |
| Bohr magneton | $\mu_B$ | $h \cdot 13.996\,\mathrm{GHz/\,T}$ |

Table 6.1: Parameters for the $D_2$ $6S_{1/2} \rightarrow 6P_{3/2}$ transition in Cesium.

For reasonable excitation rates, the infrared diode laser must be locked to the correct wavelength which is shifted from the zero field value as determined by Eq. 6.7. At Harvard, a second cesium beam was placed in an additional superconducting magnet whose field was adjusted to offset the observed manifold by one transition (Fig. 6.8). When modulating the diode laser's wavelength at 300 Hz, the first harmonic signal from the reference beam's fluorescence is zero when the mean wavelength is centered on a transition. This signal can thus be used as an error signal to lock the diode laser to the transition. At CERN, a second superconducting magnet was not available so the diode laser was either locked by hand to the appropriate transition or for later experiments by using a wavelength meter (HighFinesse WS/7) to constantly measure the diode laser's frequency and adjust it to the previously measured value of the chosen transition [84]. This could be done to an accuracy of better than 100 MHz and the continuous locking to a Cs transition was confirmed through the measured fluorescence. In both cases the chosen transition was $|6S, J = 1/2, m_j = 1/2, m_I = -5/2\rangle \rightarrow |6P, J = 3/2, m_j = 3/2, m_I = -5/2\rangle$.

Approximately 10 mW of the infrared 852 nm light is transmitted through an

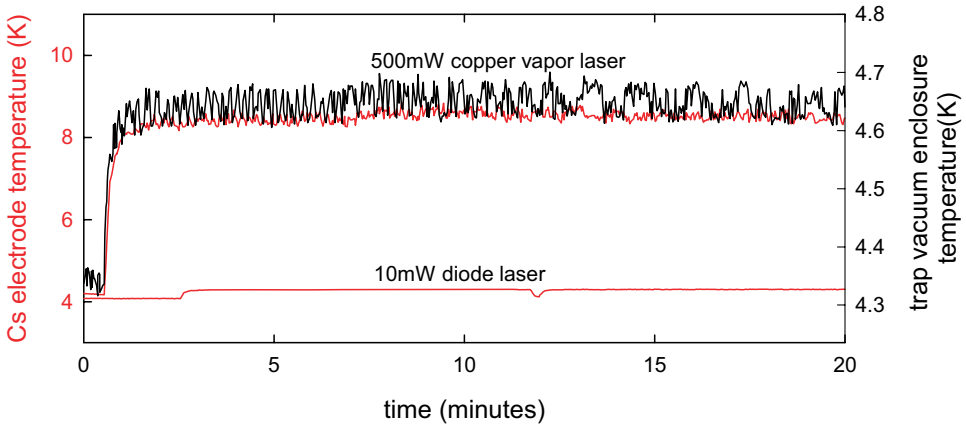


Figure 6.9: Temperature increases caused by applying the copper vapor and diode lasers to the Penning trap.

optical fiber to the *Cs* electrode within the Penning trap. Due to the double pass geometry, this corresponds to an intensity of 37.8 mW/cm$^2$ which, as it is much larger than the saturation intensity, would correspond to the maximum 50 %/16 excitation to $6P_{3/2}$ where the factor of 16 is due to the fact that only one ground state of Cs is excited. However the locking scheme at Harvard has a duty cycle of only 20 % on resonance reducing the average intensity to 6.4 mW/cm$^2$ which corresponds to a 43 %/16 excitation. This reduction does not occur in the CERN locking scheme.

Copper vapor laser pulses at 511 nm, 20 ns pulses with a repetition rate of 20 kHz then excite the $6P_{3/2}$ atoms to a state containing some $37d$ character. In a strong magnetic field, many $n, \ell$ states up to and including continuum states are mixed together rendering a simple description of the final state impossible. As the copper vapor laser has a fixed wavelength, an applied electric field is used to empirically tune the Cs atoms into resonance (Fig. 6.10). This electric field can be created either using the horizontal plates shown in 6.3 or through additional plates aligned parallel to the magnetic field. From comparisons of Cs fluorescence and Cs$^*$ ionization current

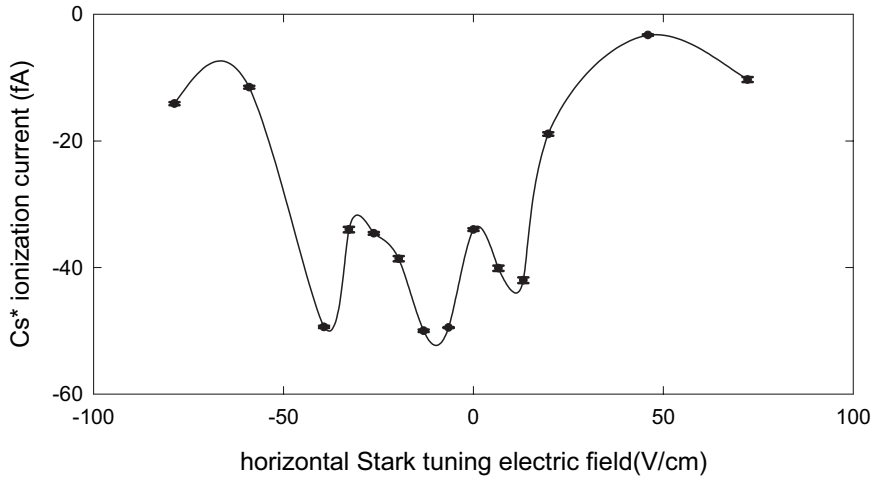


Figure 6.10: Optimization of $Cs^*$ flux through application of a Stark tuning electric field perpendicular to the Cs beam and axial magnetic field.

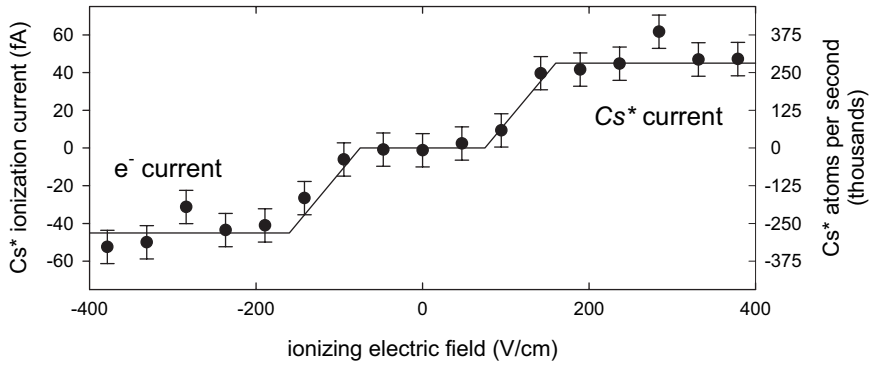


Figure 6.11: Current from $Cs^*$ atoms that field ionize after passing through the electrode stack.

as discussed below, approximately 1 in 2500 Cs atoms are excited to $n \approx 37$. The copper vapor laser pulses have an average power of 300 mW at Harvard and 500 mW at CERN. This presents a large heat load on the trap resulting in an approximately 4 K increase of the temperature of the *Cs* electrode (Fig. 6.9).

The $Cs^*$ atoms then enter the electrode stack through a 0.3 mm diameter hole in the side of the *Cs* electrode. Approximately 95 % will then leave through a 1 mm hole on the opposing side. The flux of $Cs^*$ leaving the electrode can be measured by field

ionizing these atoms with the electric field created by applying a potential difference to the field ionization plates (Fig. 6.11). The antisymmetric curve measured as a function of electric field is consistent with the current turning on as the electric field becomes strong enough to ionize $Cs^*$ atoms and saturating at fields strong enough to ionize all of the $Cs^*$. The antisymmetry occurs due to the collection of either negative $e^-$ or the positive ion cores depending on the direction of the applied electric field. Hence reversing the electric field flips the sign of the observed current.

## 6.2 Production of Rydberg Positronium

A positron cloud containing 200,000 particles was next placed in the center of the $Cs^*$ beam within the Cesium-Positronium trap at Harvard (Fig. 2.8). Using Eq. 4.28, we estimate the average cloud to have a 6.4 mm diameter, 0.8 mm axial extent, and central density of $1.4 \times 10^7\, e^+/cm^3$. The $Cs^*$ intensity in these experiments as compared to the $Cs^*$ flux measured in Fig. 6.11 was reduced by a factor of 50 to minimize Cs collection on electrode surfaces. The average flux was thus $6500 \pm 1300\ Cs^*/\,s$. As trapped positrons capture $e^-$ from $Cs^*$ atoms, neutral $Ps^*$ atoms are formed which are no longer trapped by the electrostatic well and escape isotropically. $Ps^*$ can then enter the detection wells on either side of the central $e^+$ well which have a combined solid angle of $4\pi/32$. Those atoms that enter the detection well are field ionized due to the strong entry electric field and the $e^+$ from the $Ps^*$ atom is captured if it encounters a confining electric potential at the ionization point. The number of ionized $Ps^*$ are finally determined by counting the trapped $e^+$ using the RF detection technique described in Section 4.2.1.

### 6.2.1 Excited State Distribution

The electric field range in which $Ps^*$ are detected can be varied as shown in Fig. 6.12. Only those atoms who ionize in the potential range between the lower horizontal dashed lines have positrons which encounter a confining potential and are trapped. This corresponds to an electric field range given by the upper horizontal dashed lines. The maximum electric field is set by the potential depth of the detection well. However, the minimum electric field can be varied by changing only the potentials at the ends of the trap. This technique has the advantage of not perturbing the potentials at the center of the trap and thus maintains the same initial positron cloud shape. In all cases the potential at the ends of the trap is lower than the minimum positron potential in the central well. This ensures that any positrons that escape the central trap by means other than within a neutral $Ps^*$ atom will have enough energy to escape the trap entirely and annihilate without being mistakenly counted as an ionized $Ps^*$ atom.

Figure 6.13 shows the results of mapping the number of ionized $Ps^*$ as a function of minimum axial field. The grey points are taken with exactly the same experimental parameters except that the infrared diode laser is detuned just off of the $6S_{1/2} \rightarrow 6P_{3/2}$ resonance. $Cs^*$ is no longer excited and as expected no $Ps^*$ is produced. The dashed lines show the number of $Ps^*$ atoms expected to be detected for atoms that ionize at a given electric field magnitude. This is calculated by assuming ballistic $Ps^*$ trajectories leaving the central $e^+$ well toward the detection well and then scaling the fraction of trajectories whose $Ps^*$ atom ionize before hitting the electrode surfaces to the maximum number experimentally detected.

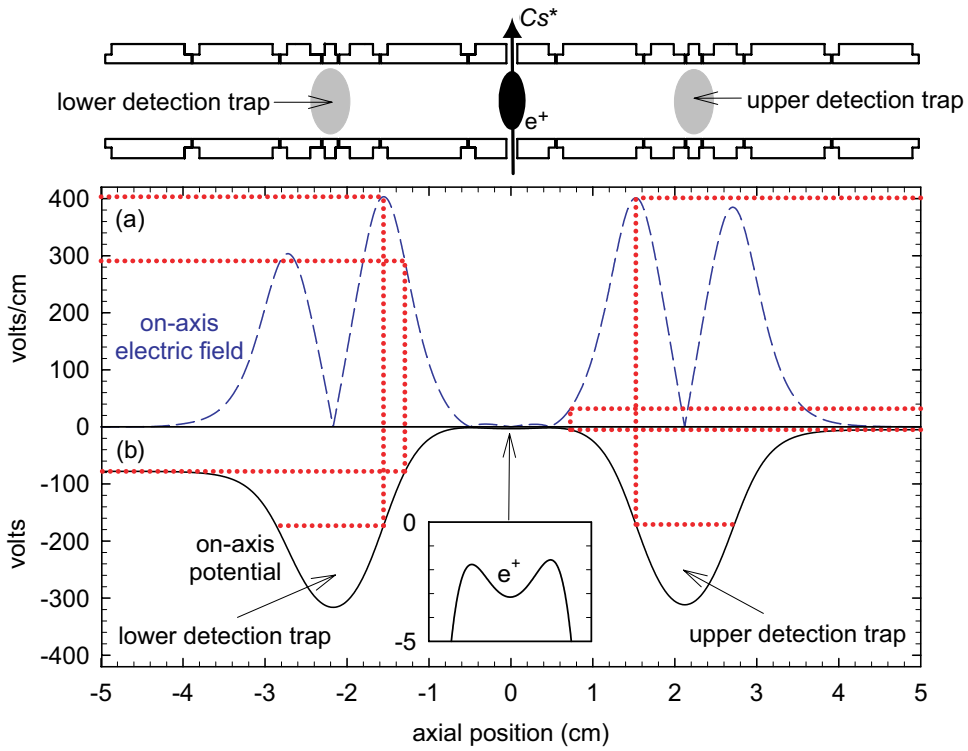


Figure 6.12: Potentials used to confine positrons in the center of the Cs* beam along with upper and lower Ps* detection traps. Dotted lines show the maximum and minimum on-axis electric field for which Ps* would be detected.

The shape of the spectrum indicates that the $Ps^*$ ionize primarily in two segments. One is between 100 V/cm and 200 V/cm and the other is between 300 V/cm and 400 V/cm. From the conservation of binding energy within the charge exchange reaction, we expect the spectrum to match that of the $Cs^*$ shown in Fig. 6.11 and thus the atoms that ionize between 100 V/cm and 200 V/cm are expected. However the more tightly bound atoms which ionize between 300 V/cm and 400 V/cm are not expected and we do not have an explanation yet for this phenomenon. As discussed previously, different quantum states with the same principal quantum number ionize at fields within a factor of 2 so this feature could be from two different angular momentum states being produced. An alternative explanation is that the $Ps^*$ travels much faster than $Cs^*$ due to its lighter weight. Thus the rate of change of the electric field experienced by the positronium atoms is much higher and the probability of a diabatic passage through an avoided crossing of two Stark levels is larger. Atoms that ionize through diabatic passage to the ionize state typically ionized at a factor of 2 higher field than those that ionize due to adiabatic passage [89].

From the calculation of ballistic $Ps^*$ trajectories, if all the initial $e^+$ formed $Ps^*$ we would expect a maximum of 3.12 % to be detected in the wells. Instead only 0.8 % of the initial positrons are detected as $Ps^*$ implying that 75 % of the beginning $e^+$ do not form excited positronium atoms. Likely this effect is due to a second channel whereby positrons can be lost from the central well without forming Rydberg positronium. This channel is not from the formation of ground state Ps through collisions with the background ground state Cs atoms in the beam as the cross section is approximately $5 \times 10^{-16}\,\mathrm{cm}^2$ [99]. This small cross-section, even with the factor of 2500 more ground

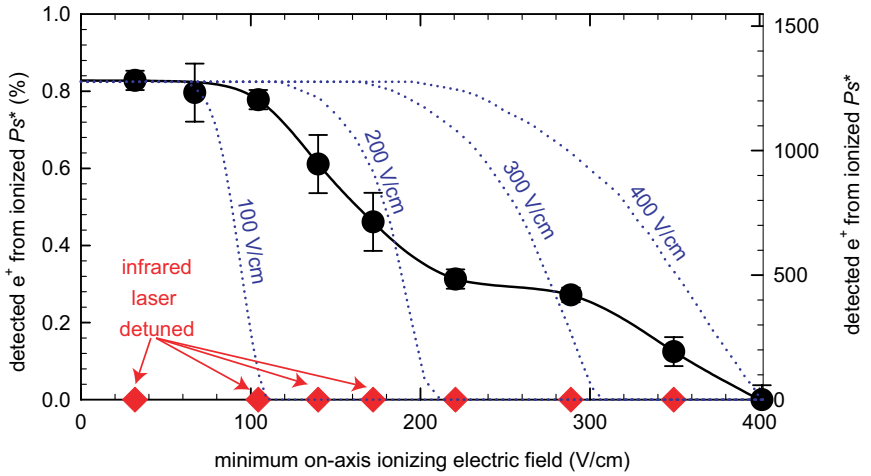


Figure 6.13: Detected Ps* as a function of the minimum axial field in the detection well. The dotted curves are obtained by averaging over all possible ballistic trajectories to the detection trap for Ps* atoms that ionize at the electric field magnitudes given.

state Cs atoms than excited Cs*, results in a 3 orders of magnitude smaller rate of ground state Ps formation than for excited Ps*. The total cross-section for ground state Cs-$e^+$ scattering which could also account for this loss through heating of the trapped $e^+$ is an order of magnitude larger but again this does not result in a rate comparable to the production of Ps*. The most plausible explanation is that multiple collisions with the trapped 300 K $Cs^+$ ion cores remaining in the central $e^+$ well after the formation of Ps* eject positrons from the well.

### 6.2.2 Production Cross-Section

By changing the length of time that the Cs beam is exposed to the copper vapor laser, we can determine the amount of time Cs* interacts with the trapped positrons. From Fig. 6.14, the fractional detection rate of Ps* for a flux of 6500 Cs*/ s is given

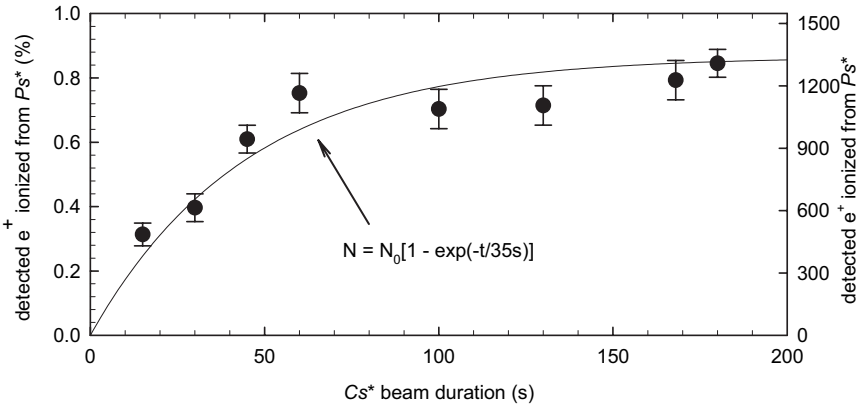


Figure 6.14: $Ps^*$ production as a function of $Cs^*$ beam duration shows a 45 second time constant. The error bars represent average measurement uncertainties.

by

$$f_{e^+} = 8.66 \times 10^{-3} \left[ 1 - \exp\left( \frac{-t}{45\,\mathrm{s}} \right) \right] \tag{6.8}$$

which when corrected for the small solid angle of the detection wells, $\Omega = 4\pi/32$, corresponds to an initial total fractional $Ps^*$ production rate of

$$\Gamma_{Ps^*} = \frac{4\pi}{\Omega} \left. \frac{df_{e^+}}{dt} \right|_{t=0} = 6(2) \times 10^{-3}/\,\mathrm{s} \tag{6.9}$$

The fractional production rate is related to the cross-section by the standard formula

$$\Gamma_{Ps^*} = \sigma_{Ps^*} \rho_{Cs^*} v_{Cs^*} = \sigma_{Ps^*} \frac{N_{Cs^*}/\,\mathrm{s}}{A_{Cs^*}} \tag{6.10}$$

where $\rho_{Cs^*}$ is the density, $v_{Cs^*} \approx 240\,\mathrm{m/s}$ is the velocity, and $A_{Cs^*} \approx 70\,\mathrm{nm}^2$ is the cross-sectional area of the 320 K $Cs^*$ beam. The measured cross section is thus

$$\sigma_{Ps^*} = 7(3) \times 10^{-10}\,\mathrm{cm}^2 \tag{6.11}$$

Note that this cross section only gives a lower limit to the true cross section. For a typical initial cloud of 200,000 $e^+$, the measured rate corresponds to 1200 $Ps^*$ being

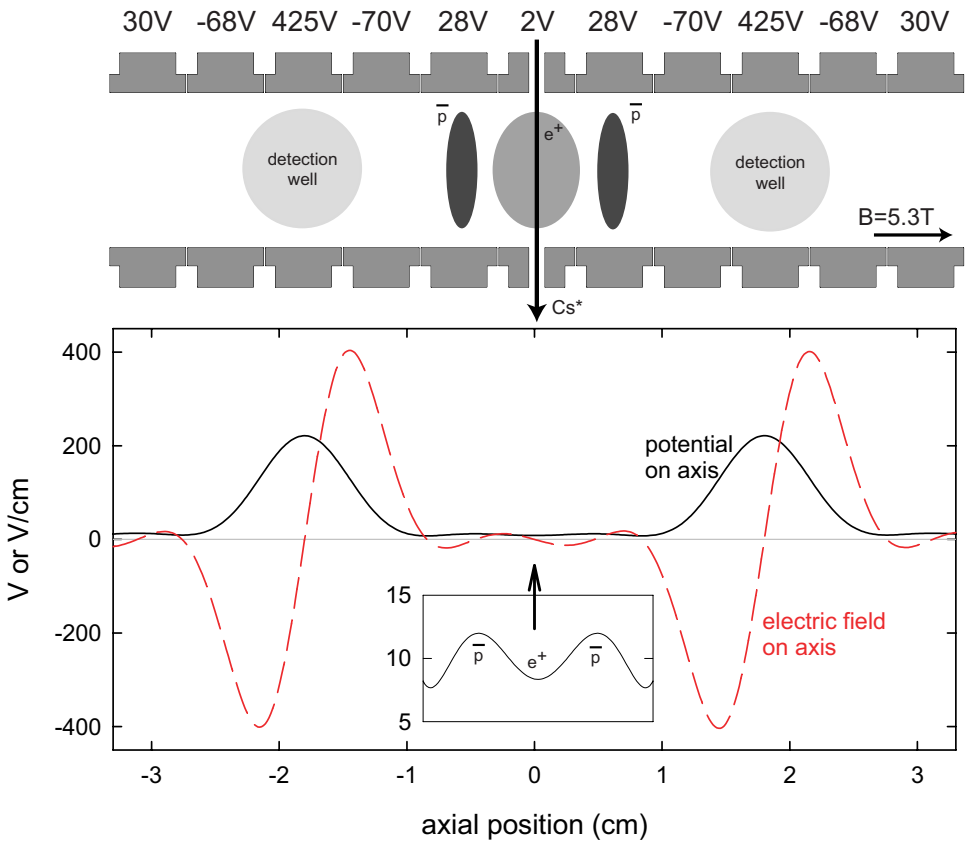


Figure 6.15: Symmetric potential structure used to confine $\overline{\mathrm{p}}$ near the $\mathrm{e}^+$ cloud as well as to ionize and detect ionized $\overline{\mathrm{H}}^*$.

formed in 1 second in which time 6500 $\mathrm{Cs}^*$ pass through the cloud. The similar numbers imply that the reaction rate could be limited by the total number of $\mathrm{Cs}^*$ available for charge exchange. Even with this caveat the measured cross section is within an order of the magnitude of the predicted $1.5\times10^{-9}\,\mathrm{cm}^2$ cross section (Eq. 6.3).

## 6.3 Production of Cold Antihydrogen

To extend this technique to produce antihydrogen through a second charge exchange requires trapping antiprotons as near as possible to the positron cloud in order

to maximize the number of $Ps^*$ that interact with the trapped $\overline{p}$. The extension of the existing potential structure to accomplish this is nontrivial due to the compressed spacing and requires several different effects to be considered.

1. The field that the $Cs^*$ encounters when entering the electrode stack must be smaller than 100 V/cm to prevent the atoms from field ionizing before they can interact with the trapped $e^+$. This requires that the potential difference between the *Cs* electrode and its nearest neighbors be as small as possible in order to reduce the radial electric field at the edge of the electrodes.

2. The depth of the $e^+$ and $\overline{p}$ potential wells must be great enough to hold large particle clouds. A 4 million $e^+$ cloud has a space charge of approximately 1 V so the well depth must be greater than this. Note this competes with the radial field requirement mentioned previously.

3. The maximum electric field on axis in the detection well must be large enough to completely ionize all incoming $\overline{H}^*$ atoms (this is at approximately 400 V/cm from Fig. 6.13).

4. Any antiprotons that escape the initial $\overline{p}$ well without forming $\overline{H}^*$ must not be trapped in a detection well. The potential barrier on the far side of the detection well must thus be lower than the barrier separating the detection well and the initial $\overline{p}$ well. Since this condition has to hold at all radii, symmetry is used to ensure this by reflecting the relative electrode potential differences across the center of the detection well (as shown in Fig. 6.15 and Fig. 6.16).

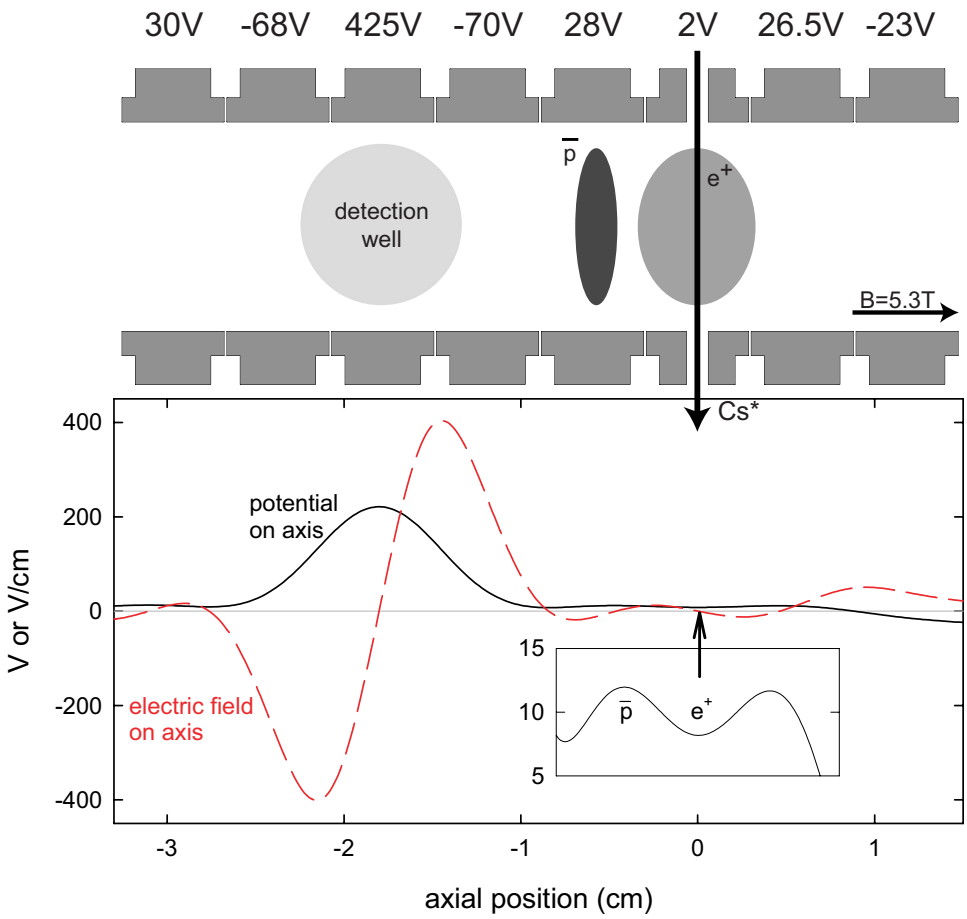


Figure 6.16: Single-sided potential structure used to confine $\overline{p}$ near the $e^+$ cloud and to ionize and detect ionized $\overline{H}^*$.

The first structure used encompasses a two sided symmetric structure which has detection wells on both sides of the $Cs^*$ beam (Fig. 6.15). While this design maximizes the solid angle of the detection well through having two wells, the large outer well for positively charged particles formed by the detection wells can trap energetic $Cs^+$ ions produced during the first charge exchange step. These are then able to collide multiple times with the trapped $\overline{p}$ transferring enough energy to the antiprotons to eject them from the trap. In fact during our attempts with this configuration all of the $\overline{p}$ were lost and no $\overline{H}^*$ was detected.

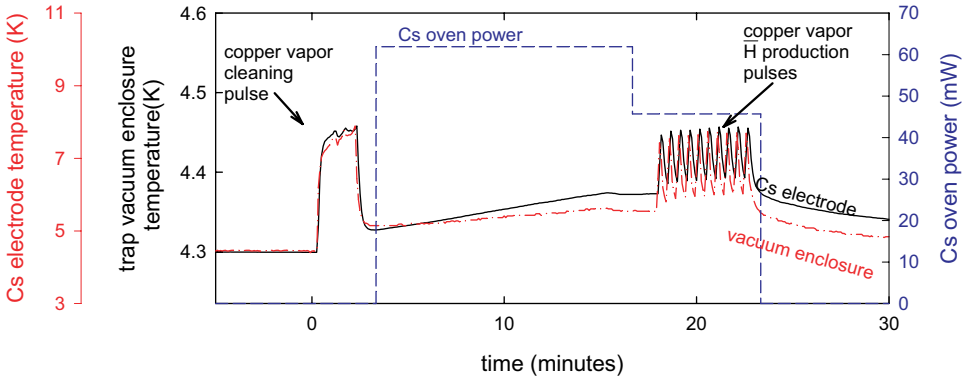


Figure 6.17: Electrode temperatures during a typical experiment producing laser-controlled $\overline{\mathrm{H}}^*$.

To prevent confined $Cs^+$ ions from heating trapped $\overline{\mathrm{p}}$, a second potential structure was employed (Fig. 6.16). While this structure does reduce the total solid angle of the detection well compared to the symmetric design, by placing all the $\overline{\mathrm{p}}$ in only one well next to the detection well this effect is minimized as the second detection well would be much farther from the trapped $\overline{\mathrm{p}}$ (and $\Omega \propto 1/r^2$). To further reduce $\overline{\mathrm{p}}$ losses during an experiment, the green 511 nm copper vapor laser is applied in ten 10 second pulses separated by cooling periods of 20 second each. Figure 6.17 shows the typical temperature profile for an experiment. These measures have reduced $\overline{\mathrm{p}}$ losses compared to the first attempts but there is still an observable increase in $\overline{\mathrm{p}}$ annihilations when $Ps^*$ is created (Fig. 6.2). While it would be tempting to attribute this to $\overline{\mathrm{H}}^*$ production, this is not consistent with the small number of $\overline{\mathrm{H}}^*$ detected as discussed next.

Figure 6.18a shows the fiber counts resulting from ionized antihydrogen atoms from 6 trials summed together. On average 1.4 million positrons and 240,000 antiprotons were used in these experiments. The 94 % efficiency of this channel implies that the 13 $\overline{\mathrm{p}}$ annihilation counts resulted from $14 \pm 4$ $\overline{\mathrm{H}}^*$ ionized in the detection

| | Initial $\overline{\mathrm{p}}$ lost |
|---|---|
| Full experiment | $87\,\% \pm 6$ |
| No $\mathrm{Ps}^*$ produced (no $\mathrm{e}^+$ trapped) | $58\,\% \pm 6$ |
| No $\mathrm{Cs}^*$ produced (diode laser off resonance) | $43\,\% \pm 22$ |
| Copper vapor laser only | $24\,\% \pm 8$ |

Table 6.2: Antiproton losses during charge exchange experiments.

well and the error bar is from the assumption of a Poissonian statistical distribution where the standard deviation is given by $\sqrt{n}$. During the 40 ms ramp time, we expect 2.2 background fiber counts when summed over the 6 experiments which is consistent with the 3 counts not located in the peak. As any $\mathrm{Ps}^*$ which does not charge exchange and form $\overline{\mathrm{H}}^*$ will ionize in the detection well and leave a trapped $\mathrm{e}^-$ in the detection well, we expect the trapped $\overline{\mathrm{p}}$ ionized from $\overline{\mathrm{H}}^*$ to cool from collisions with these electrons and be located only at the bottom of the detection well.

To determine the bottom of the detection well, a cold $\overline{\mathrm{p}}$ cloud was placed in an identical well and then ramped in the same manner as for detected $\overline{\mathrm{H}}^*$ (Fig. 6.18b). The detection window can then be defined to be only the lowest energy channels detected in the calibration ramp which as expected coincides with the detected $\overline{\mathrm{H}}^*$ peak. Within this constrained window, there is only a 3 % chance of at least one background count.

It is difficult to determine the actual solid angle of the detection well due to the large fields induced by the squashed nature of the potentials. Off-axis many $\overline{\mathrm{H}}^*$ may ionize before entering deep enough into the wall to encounter a confining potential

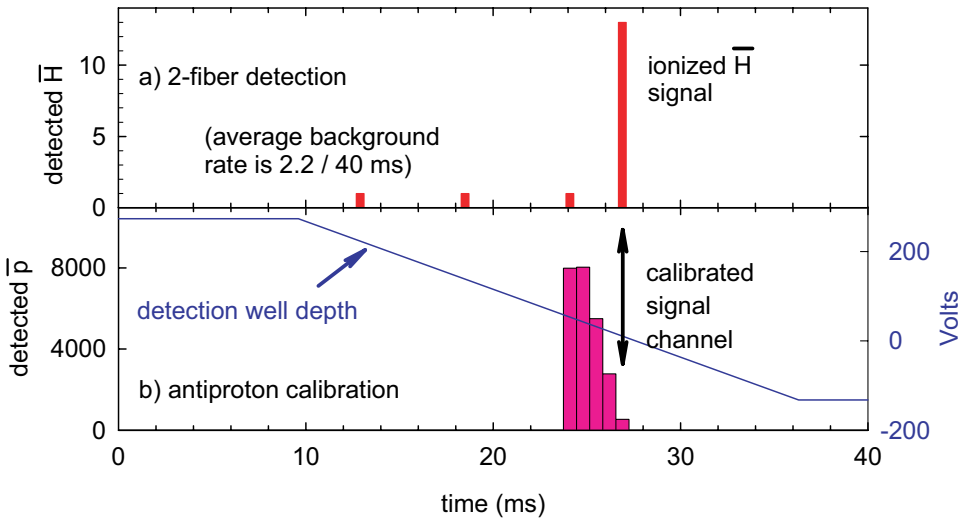


Figure 6.18: (a) Antihydrogen detected (peak) as the detection well depth is linearly decreased through 0 V. (b) Signal from $\overline{p}$ trapped in an identical well to the detection well as the well depth is decreased.

after ionization. As radial fields ionize atoms differently than axial fields, it is difficult to account correctly for the combined effects of the large radial and axial fields off-axis. With the assumption that only the axial field can ionize $\overline{H}^*$ atoms, then the solid angle is $4\pi/6$ while if the field magnitude ionizes atoms then the solid angle is $4\pi/10$. Using the average of these two values we find that approximately 100 $\overline{H}^*$ atoms were created. This corresponds to a calculated 60 $\overline{H}^*$ atoms expected from Eq. 6.2c assuming 25 % of the initial positrons formed $Ps^*$.

The most convincing evidence that these counts correspond to $\overline{p}$ ionized from $\overline{H}^*$ atoms as opposed to $\overline{p}$ trapped via some other mechanism is that the detection well is arranged so that only $\overline{p}$ ionized from $\overline{H}^*$ inside the confining detection well are trapped. Any $\overline{p}$ that escapes from the initial well without forming antihydrogen must have at least 2 eV more energy than that which would be confined by the barrier on the far side of the detection well. It is extremely unlikely during the single transit

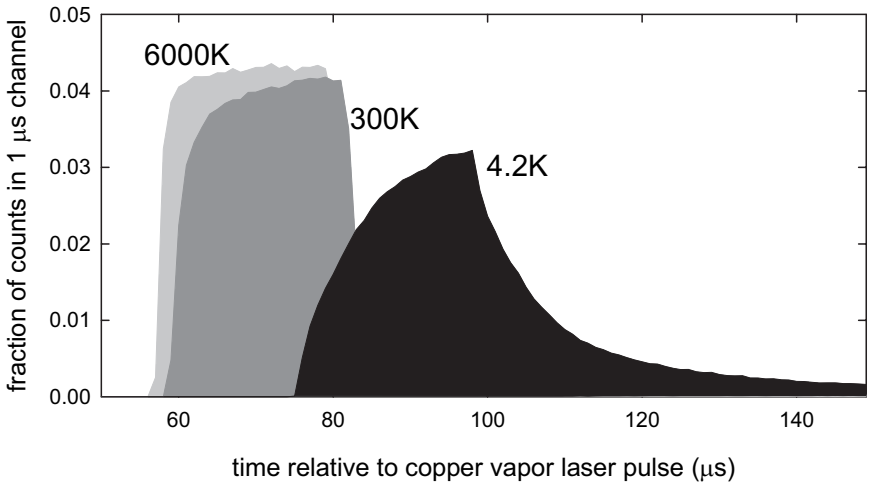


Figure 6.19: Timing of $\overline{\mathrm{H}}^*$ annihilation counts relative to a copper vapor laser pulse.

through the detection well for collisions to occur that would reduce the energy of the antiproton enough to confine it within the well. Additionally, no counts were present during the two trials made when the infrared diode laser was detuned from the $6S_{1/2} \rightarrow 6P_{3/2}$ transition (*i.e.* when no $\mathrm{Cs}^*$ or $\mathrm{Ps}^*$ was produced) or during the two trials conducted with no trapped positrons (*i.e.* when $\mathrm{Cs}^*$ but no $\mathrm{Ps}^*$ was produced).

While the total number of antihydrogen atoms produced is too small to use the velocity measurement techniques discussed in Chapter 5, by correlating $\overline{\mathrm{H}}$ annihilations with the time relative to the previous copper vapor laser pulse it is possible to estimate the $\overline{\mathrm{H}}^*$ temperature distribution. Figure 6.19 shows the expected timing distribution for antihydrogen atoms produced at 4.2 K, 300 K, and 6000 K. These are calculated assuming a cesium atom is excited somewhere in the 6 mm diameter cone created by the diverging laser light emitted from the incoming optical fiber (the numerical aperture of the fiber is 0.22). The $\mathrm{Cs}^*$ atom then proceeds to the center of the electrical stack where it charge exchanges forming $\mathrm{Ps}^*$ which travels axially to

the center of the $\overline{\mathrm{p}}$ cloud at which point the second charge exchange reaction occurs. The $\overline{\mathrm{H}}^*$ atoms formed are then given a specific temperature and allowed to travel isotropically until they encounter an electrode wall and annihilate.

Several effects make the analysis of this distribution difficult. First, the finite distance over which Cs can be excited is convolved with the $\overline{\mathrm{H}}^*$ temperature distribution and is obvious in the flat top of the 6000 K distribution. Second, in a more realistic model the location at which both charge exchange reactions occur would vary. While the $\mathrm{Ps}^*$ is traveling fast enough, $v_{\mathrm{Ps}} \approx 10^4\,\mathrm{m/s}$, that this effect is negligible, the $\mathrm{Cs}^*$ is traveling at only 250 m/s which results in a further spreading of the distribution.

A first attempt at measuring the velocity distribution was attempted in the 2004 run. In order to prevent annihilations from adjacent 20 kHz copper vapor laser pulses from stacking on top of each other, 23 out of 24 laser pulses were removed by a synchronous chopping wheel (NewFocus 3501). Trigger annihilation counts were then correlated with laser pulses utilizing a multichannel scaler (Stanford Research Systems SR430). Unfortunately the background annihilations from $\overline{\mathrm{p}}$ loss precluded seeing any signal from $\overline{\mathrm{H}}^*$ atoms. In addition the SR430 requires a minimum 400 µs dead time between the end of the acquisition of annihilations from a specific laser pulse and the beginning of the acquisition for the next pulse which limits the amount of data that can be taken. For future experiments, a better acquisition system should be developed to maximize the signal to noise ratio.

## 6.4 Conclusion

We have thus demonstrated in a proof-of-principle experiment the production of antihydrogen atoms whose internal states are entirely controlled by tuning a single laser. While only a few atoms have been detected, many more are likely to have been produced assuming an isotropic detection. The larger total number of atoms produced is the correct figure of merit by which to compare production techniques since, with a neutral atom trap, all atoms can be trapped instead of only those directed axially toward a detection well. As such more than enough atoms are likely being produced for use in spectroscopic comparisons. In addition, through the use of more initial positrons and antiprotons, an increased number of $\overline{\mathrm{H}}$ atoms should be made in a single experiment. Furthermore, the use of additional diode lasers tuned to other transitions in the $6S \rightarrow 6P$ manifold will increase the fraction of excited $\mathrm{Cs}^*$ atoms compared to ground state cesium atoms. This will hopefully reduce the number of positrons lost to other processes before forming positronium hence increasing the number of $\mathrm{Ps}^*$ atoms and producing more $\overline{\mathrm{H}}^*$ atoms.

Antihydrogen atoms produced using resonant charge exchange are also expected to have a velocity distribution given entirely by that of the $\overline{\mathrm{p}}$ from which they form which is currently 4.2 K and could be lowered much farther in principle. If future experiments demonstrate a slow 4.2 K $\overline{\mathrm{H}}$ velocity, this technique could likely become the method of choice for the production of atoms useful for spectroscopy.

# Chapter 7

# Stability of charged particles in a combined Penning-Ioffe Trap

Even at 4.2 K, $\overline{\mathrm{H}}^*$ atoms that are not confined will annihilate on electrode surfaces within approximately 50 µs. This is several order of magnitude shorter than the interaction time needed for precise laser spectroscopy or even the time needed for highly excited atoms to decay to the ground state. It has thus been proposed to first trap and store $\overline{\mathrm{H}}$ atoms before attempting an accurate comparison with H [100].

Unfortunately, the simplest magnetic neutral atom traps compatible with the axial magnetic bias field necessary for charged particle trapping destroy the cylindrical symmetry of a Penning trap. Angular momentum is no longer conserved and the confinement theorem discussed in Chapter 4 does not apply to particles trapped in this superposition of magnetic fields. An initial study [101] registered this concern and noted that despite this lack of symmetry, the three adiabatic invariants of motion in a Penning trap — the cyclotron magnetic moment, the axial harmonic motion

adiabatic invariant, and the flux enclosed by the magnetron motion — do still exist. As long as these invariants are not broken through collisions or resonances, stable particle motions exist. Plasmas, however, are ideal places for these invariants to be broken. Hence a breakdown of the single particle picture was expected as the density of charged particles was increased. A second study examined more closely the effect of collisions within the plasma and space-charge effects resulting in a flat axial potential well whereupon there would be no well-defined oscillation frequencies [102]. Experiments at very low axial magnetic field and high temperatures demonstrated that these problems result in a finite particle confinement lifetime at a high enough density.

There is thus a natural tradeoff between the ability to trap neutral atoms versus confining large numbers of charged particles. This chapter will first discuss the requirements necessary for neutral atoms to be stably trapped. We will then consider the implications a neutral atom trap has on the stability of the charged particles necessary for the production of $\overline{\mathrm{H}}$ and preliminary experimental measurements on this effect.

## 7.1 Neutral atom traps

A neutral particle with magnetic dipole moment, $\mu$, has potential energy inside a magnetic field given by $V = -\vec{\mu} \cdot \vec{B}$. If the precession frequency about the local magnetic field, $\omega_s$, is large compared to the frequency at which the magnetic field direction changes, $\omega_t$, the relative angle between the local field direction and the magnetic dipole moment is conserved. Assuming the magnetic dipole moment is

initially aligned either parallel or antiparallel with the local field lines and remains in the same alignment due to the above adiabatic condition being met, the potential energy can be rewritten as

$$V_{eff} \approx \mp \mu \left| B \right| \tag{7.1}$$

where $\mu$ is the magnitude of the magnetic dipole moment. Low (high) field seeking atoms will thus be trapped in a magnetic field configuration containing a local minimum (maximum) in the magnetic field magnitude.

Maxwell's equations, however, prevent a configuration of static fields containing a local maximum in the field magnitude [103]. The only atomic states that can be trapped in an allowed magnetic trap configuration are thus those whose magnetic dipole moment is anti-aligned with the local magnetic field direction. The resulting potential is given by:

$$V_t = \mu \left| \vec{B} \right| \tag{7.2}$$

The major contribution to the magnetic moment is from the electron's spin, since the nuclear magnetic moment is much smaller for an antihydrogen atom. Hence $\mu = \mu_B$ where $\mu_B$ is the Bohr magneton. The potential depth of the trap (in K) is then given by

$$\Delta T = \frac{\mu_B \Delta B}{k_b} = \left( \frac{0.67\,\mathrm{K}}{\mathrm{T}} \right) \Delta B \tag{7.3}$$

where $\Delta B = B_{wall} - B_0$ is the difference in magnitude field magnitude between the edge of the trap and the center.

While the atoms move throughout the trap, the magnetic dipole moment must remain anti-aligned with the local magnetic field line to avoid loss from the trap. If adiabatic motion breaks down due to the atoms encountering too low of a magnetic

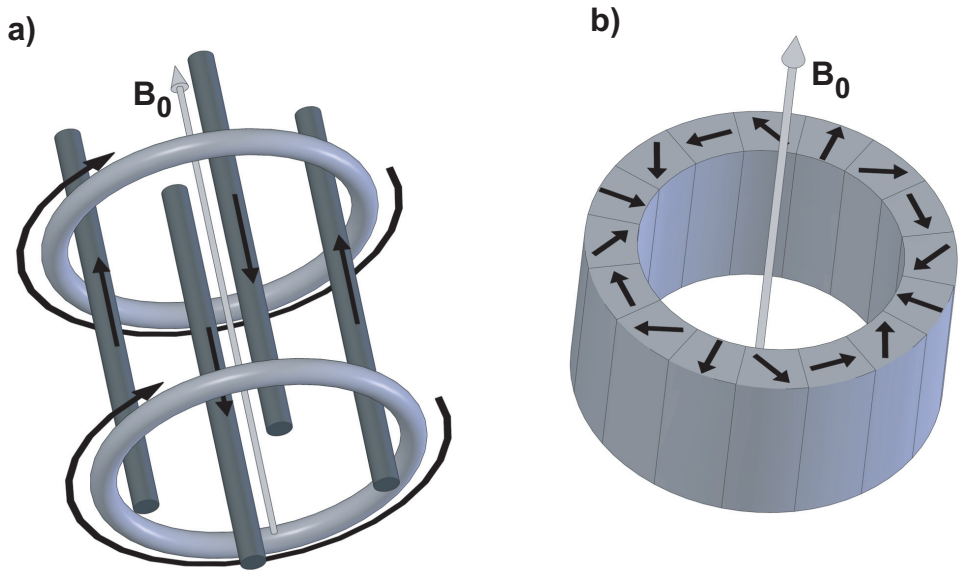


Figure 7.1: Two neutral atom Ioffe-Pritchard quadrupole trap designs — (a) a current carrying Ioffe-bar based trap (the arrows show the direction of current) and (b) a permanent magnet trap (the arrows show the magnetization axis for each permanent magnet piece). An axial pinch field must also be superimposed to confine particles axially.

field strength, a Majorana (spin-flip) transition can occur resulting in the magnetic moment becoming aligned with the field. To maintain adiabatic motion we must have for a given circular orbit of radius $\rho$ [104]

$$\omega_s = \frac{\mu B}{\hbar} \gg \frac{\left|\frac{dB}{dt}\right|}{B} = \left|\frac{dB}{d\rho}\right| \frac{v_\rho}{B} \tag{7.4}$$

where $v_\rho$ is the thermal velocity of an atom in the radial direction. This condition can not be satisfied when $B \rightarrow 0$ necessitating a trap that contains no zero field locations. The simplest design that includes no zeroes and is compatible with the axial bias field necessary for containing charged particles is the Ioffe-Pritchard quadrupole trap [105, 106] superimposed upon an axial bias field. Neglecting the axial gradient

necessary for axial confinement, the magnetic field of this trap is given by:

$$\vec{B} = B_0 \left[ \frac{x\hat{\mathbf{x}} - y\hat{\mathbf{y}}}{R} + \hat{\mathbf{z}} \right] \tag{7.5a}$$

$$= B_0 \left[ \frac{\rho}{R} \left( \cos[2\theta]\hat{\rho} - \sin[2\theta]\hat{\theta} \right) + \hat{\mathbf{z}} \right] \tag{7.5b}$$

where $B_0$ describes the overall strength of the field and $R$ is the radial length scale over which the superimposed quadrupole field becomes significant. It is obvious that this magnetic field does not have cylindrical symmetry but instead has a four-fold symmetry under rotations about the $z$-axis.

The field configuration in Eq. 7.5 can be generated either by 4 current carrying bars (Fig. 7.1a) or by a specific permanent magnet geometry (Fig. 7.1b). The adiabaticity condition (Eq. 7.4) requires that

$$B_0 \gg \frac{\hbar v_\rho}{\sqrt{8}\mu_B} \frac{1}{R} = \frac{2 \times 10^{-10}\,\mathrm{T \cdot m}}{R} \tag{7.6}$$

which is easily satisfied. For example, in the permanent magnet trap to be discussed later a quadrupole gradient resulting in $R = 7\,\mathrm{cm}$ requires only that $B_0 \gg 3 \times 10^{-9}\,\mathrm{T}$.

The bias field also reduces the radial trap depth relative to a simple quadrupole field. The difference in magnetic field modulus between the center of the trap and that at radius $\rho$ is given to lowest order in $\rho$ by

$$\Delta B = \frac{1}{2} B_0 \left( \frac{\rho}{R} \right)^2 \tag{7.7}$$

However if there were no axial bias field (but the radial gradient is the same), the trap depth would instead be given by

$$\Delta B = B_0 \left( \frac{\rho}{R} \right) \tag{7.8}$$

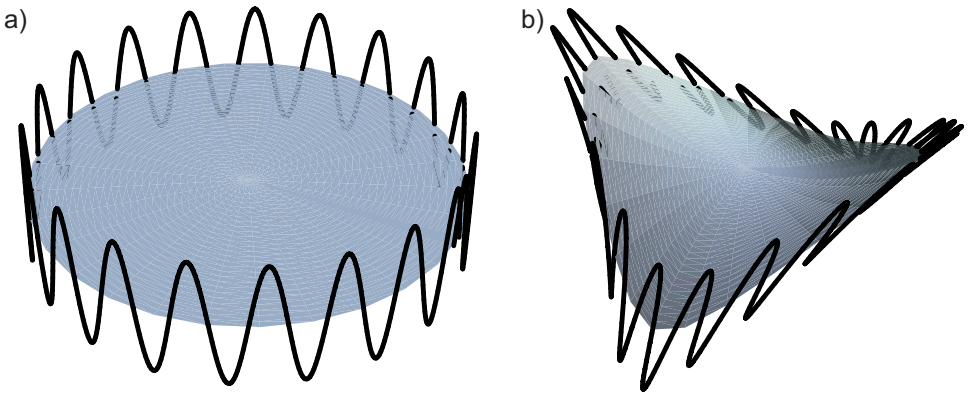


Figure 7.2: Comparison of particle motions in a Penning trap with (a) only an axial bias field and (b) a quadrupole magnetic field superimposed on axial bias field. Note the axial motion is not drawn to scale.

## 7.2 Stability of charged particles

As mentioned previously the combined Penning-Ioffe geometry is no longer cylindrically symmetric. To quantify the effect of this perturbation on the charged particles motion we first review the single particle limit [101]. The force on an electron in the combined Ioffe-Penning trap becomes

$$F = q\vec{v} \times \vec{B} - \nabla W \tag{7.9}$$

for $\vec{B}$ given by Eq. 7.5a and the electrostatic potential energy:

$$W = \frac{m\omega_z^2}{2}\left[z^2 - \frac{x^2+y^2}{2}\right] \tag{7.10}$$

The presence of the quadrupole magnetic field introduces non-linear terms to the equations of motion for a charged particle in a simple Penning trap (Eq. 2.2):

$$\ddot{z} = -\epsilon^2\omega_c^2 z + \frac{\omega_c}{R}\left(y\dot{x} + x\dot{y}\right) \tag{7.11a}$$

$$\ddot{x} = \frac{1}{2}\epsilon^2\omega_c^2 x - \omega_c\dot{y} - \frac{\omega_c}{R}y\dot{z} \tag{7.11b}$$

$$\ddot{y} = \frac{1}{2}\epsilon^2\omega_c^2 y + \omega_c\dot{x} - \frac{\omega_c}{R}x\dot{z} \tag{7.11c}$$

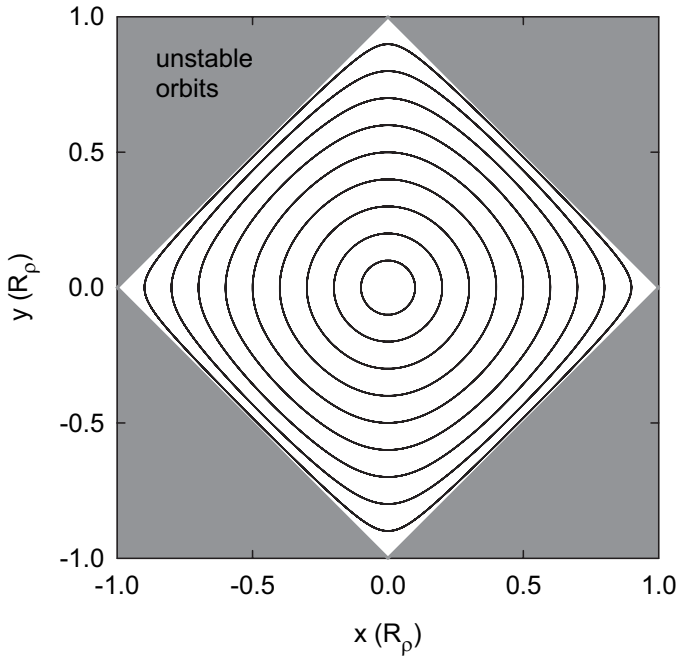


Figure 7.3: Magnetron orbits in a combined Ioffe-Penning trap projected onto the $x - y$ plane.

where $\omega_c = |e|B_0/m$, and $\epsilon = \omega_z/\omega_c$. Figure 7.2 shows the effect of these non-linear terms on an orbit of radius $\frac{4}{5}R$. Here the axial oscillations are no longer in the $z$ direction and the orbit is no longer circular.

To gain further physical insight into the particle's motion, we note that the magnetron motion must occur on a surface that is perpendicular to the local magnetic field and where there is no electrostatic force along the local field line. This condition can be expressed as

$$0 = \nabla W \cdot \hat{\mathbf{B}} \tag{7.12}$$

$$= \frac{m\epsilon^2\omega_c^2\left(x^2 - y^2 - 2Rz\right)}{\sqrt{R^2 + x^2 + y^2}} \tag{7.13}$$

so the surface is defined by

$$z = \frac{x^2 - y^2}{2R} \tag{7.14}$$

Magnetron orbits then occur on the intersection of this surface and a specified equipotential surface of Eq. 7.10. Figure 7.3 shows projections of the orbits as the radius of the magnetron motion increases.

The maximum stable orbit size occurs when $x_{y=0} = y_{x=0} = R$. Using a Taylor series expansion for small axial oscillations of the potential along a field line we see that

$$\omega_z' = \omega_z \frac{1 - x^2 - y^2}{1 + x^2 + y^2} \tag{7.15}$$

The axial well depth thus becomes negligibly small as the radius of the orbit increases eventually resulting in unconfined axial motion at $x_{y=0} = y_{x=0} = R$.

Three adiabatic invariants associated with the different motions can be identified [101]. These are the magnetic moment of the cyclotron motion, $M \approx mv_+^2/(2\left|\vec{B}\right|)$, the axial harmonic oscillator invariant, $J \approx E_z/\omega_z'$, and the magnetic flux enclosed by the magnetron orbit, $\Phi$. Particles orbits are thus stable for exponentially long times inside the projected diamond shown in Fig. 7.3 as long as no resonances are encountered that break the adiabatic invariants. The primary resonance that must be avoided is $\omega_z' = 2\omega_m'$. Due to the two-fold symmetry of the quadrupole trap, when this resonance condition occurs the magnetron motion effectively drives the axial motion by taking the axial motion through two cycles in the time of one magnetron orbit. Figure 7.4 shows how a particle that begins at a 45° angle below the $x$-axis at $z = 0$ and rotates about the trap axis by 90° during the time it takes to reach the end of the plasma and return to $z = 0$ has a radius that will grow indefinitely. If the

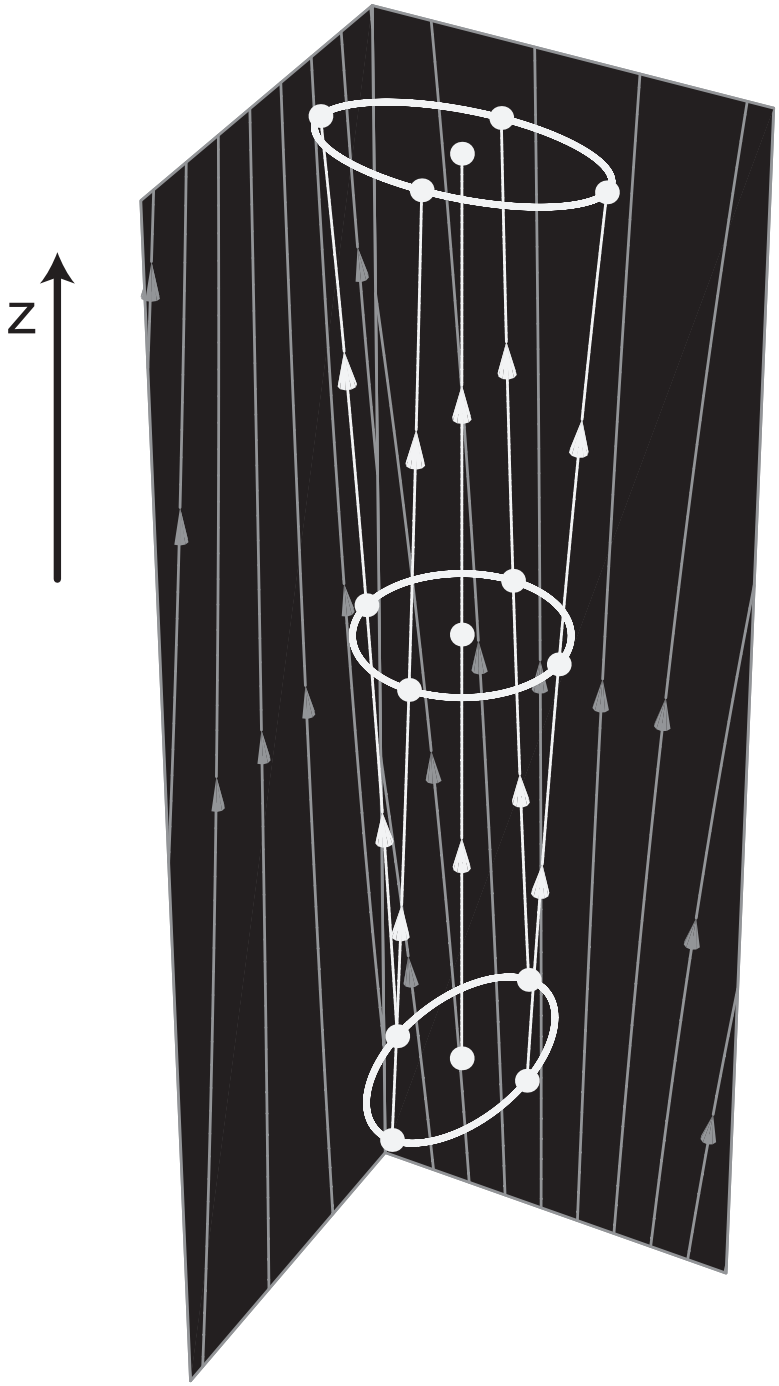


Figure 7.4: Particles follow the magnetic field lines of a combined Ioffe-Penning trap. Here the two contour plots show the magnetic field lines in the $x - z$ and $y - z$ planes. A flux tube (or plasma) that is circular at $z = 0$ becomes elliptical at the ends due to the quadrupole field.

particle instead started at 45° above the $x$-axis the same argument shows that it will move inward indefinitely. For our typical field strengths ($\epsilon \approx 10^{-4}$), resonances occur only at $x_{y=0} \approx R$ and thus are likely not to be a large effect for single particles.

In a plasma, several effects make these resonances into a larger problem. First, the flat potential along the axial direction (see Eq. 4.9) results in the axial frequency no longer being well defined but instead described by a thermal distribution. This allows more particles to be near the resonance at $\omega_z' = 2\omega_r'$ where $\omega_r'$ is the rigid rotation frequency. Second, collisions knock particles from one radial trajectory to a nearby one. These effects can be characterized through a random walk diffusion process which we will now discuss.

The diffusion coefficient, $D$, is related to the particle density function $n(\vec{r}, t)$ through Fick's law:

$$\vec{\Gamma} = -D\vec{\nabla}n \tag{7.16}$$

where $\Gamma$ is the particle flux and $n$ is the density. This is the simplest assumption possible concerning the relation of diffusion to particle flux across a surface. We can then use the continuity equation,

$$\frac{\partial n}{\partial t} = -\vec{\nabla} \cdot \vec{\Gamma}, \tag{7.17}$$

with Fick's law to obtain

$$\frac{\partial n}{\partial t} = D\nabla^2 n. \tag{7.18}$$

With the assumption that the plasma can be represented as an cylinder of uniform density with radius $\rho_p$, only radial diffusion occurs. Eq. (7.18) then reduces to

$$\frac{\partial n}{\partial t} = D\frac{1}{\rho}\frac{\partial}{\partial \rho}\rho\frac{\partial n(\rho, t)}{\partial \rho} \tag{7.19}$$

For an initial cylindrical density profile given by $n(\rho, t=0) = n_0 \left[1 - \mathrm{H}\left(r - \rho_p\right)\right]$ where H is the Heaviside step function and assuming particles are lost when they encounter the electrode walls at $\rho = \rho_W$, this equation can be integrated to find the particle fraction remaining as a function of time [107]

$$\frac{N(t)}{N(0)} = \frac{4}{k} \sum_{n=1}^{\infty} \frac{J_1\left(\alpha_{0,n} k\right)}{\alpha_{0,n}^2 J_1 \alpha_{0,n}} \exp\left[-D\left(\frac{\alpha_{0,n}}{\rho_W}\right)^2 t\right] \tag{7.20}$$

where $k = \rho_p / \rho_W$ and $\alpha_{0,n}$ is the $n$th zero of the Bessel function $J_0$. Considering the dependence of Eq. 7.20 on $\rho_p$ we note that to lowest order

$$\frac{N(t)}{N(0)} \propto 1 - \frac{\rho_p^2}{8\rho_W^2} \tag{7.21}$$

Thus the assumption of a cylindrical plasma as compared to a more accurate spheroid has only a small effect since the dependence on the radius enters as a small correction. As $\alpha_{0,n}$ increases rapidly with $n$, the first term in the series makes the largest contribution, giving a total particle lifetime:

$$\tau \approx 0.2 \frac{\rho_w^2}{D} \tag{7.22}$$

Gilson *et al.* [108, 109] proposed a model that suggests the diffusion coefficient resulting from the effect of the quadrupole field scales as

$$D \propto \left(\frac{z_p^2 \rho_0^2 \omega_r^2}{R^2 \omega_T}\right) \exp\left[\frac{-\omega_r^2}{2\omega_T^2}\right] \tag{7.23}$$

where $\rho_p$ and $z_p$ are the plasma dimensions, $\omega_r$ is the plasma rotation frequency (the analogue to $\omega_m'$ in the single particle case), and

$$\omega_T = \frac{\pi}{2 z_p} \sqrt{\frac{kT}{m}} \tag{7.24}$$

is the mean thermal axial bounce frequency for charged particles within the plasma cloud. Experiments conducted by other groups show the diffusion coefficient follows these scalings closely [102], at least for plasma axial extents and temperatures much higher than ours.

To derive this model we first note that the diffusion coefficient is given by $D = \lambda^2 \nu f$ where $\lambda$ is the radial step size caused by a collision, $\nu$ is the frequency of collisions, and $f$ is the fraction of particles that participate in these collisions. If the time between collisions, $\tau_c = \nu^{-1}$, is less than the characteristic time scale of the quadrupole perturbation, $\tau_q = \bar{v}/(2\pi R)$, where $\bar{v} = \sqrt{2k_b T/m}$ is the average thermal velocity, then frequent collisions interrupt the particle orbits each moving the particle onto a new trajectory but the individual deviations from unperturbed orbits are small and it is possible to use a perturbation approach. In this regime, the radial step size is $\lambda \approx \nu^{-1}(d\rho/dt)$.

The fraction of particles participating in the resonance is given by the integral of the thermal distribution function,

$$f(v_z) = \sqrt{\frac{m}{2\pi kT}} \exp\left[-\frac{mv_z^2}{2m}\right], \tag{7.25}$$

over the width of the resonance in velocity space which is centered at $v_z = 4\omega_r z_p/\pi$. The width of the resonance is proportional to the frequency of collisions as can be seen by observing that a lower collision frequency allows more time for the particles to move on and off of resonance thus averaging their radial extent to near zero over the time between collisions. Hence only particles whose orbit frequencies are very near the resonance exhibit linearly growing radial extents and participate in the diffusion.

Putting these results together we see that $D$ is independent of the collision fre-

quency which is the definition of plasma transport in the plateau regime [110]. In the alternative regime where $\tau_c \gg \tau_q$, charged particles can complete many orbits near resonance before a collision knocks it out of resonance. In this limit, the characteristic radial step size is the radial extent of an orbit which is independent of $\nu$ and thus $D$ is both dependent on the collision frequency and cannot be calculated using the above perturbative approach. This limit contains both the regime where the single particle picture of conserved adiabatic invariants is valid resulting in exponentially long stable orbits as well as the regime of a very strong quadrupole perturbation which results in near-instantaneous particle loss.

We will show later that the appropriate collision frequency in our experiments is approximately $360 \times 10^3/\,\mathrm{s}$ as compared to the maximum resonance frequency, $\tau_c^{-1} = 25 \times 10^3/\,\mathrm{s}$. These frequencies were calculated for 1 million $e^-$ in a 30 V well with $R = 7\,\mathrm{cm}$ which corresponds to a plasma density of $n_0 = 2 \times 10^7/\,\mathrm{cm}^3$ and a rotation frequency of $\omega_r/2\pi = 300\,\mathrm{kHz}$. We are thus in the plateau collisional regime described above and can calculate $\lambda$ in a perturbative manner. As the radial step size is then given by $\lambda \approx \rho\left(\nu^{-1}\right) - \rho(0)$ and the radial particle motion is confined to a field line:

$$\frac{d\rho}{dt} = v_z \frac{B_\rho}{B_z} = \frac{v_z}{R}\rho\cos[2\theta(t)] \tag{7.26}$$

where $v_z$ is the axial velocity of the particle. This equation can be integrated and then averaged over the rotational resonance frequency, $\omega_{res} = \omega_z/2$, resulting in

$$\rho = \rho_0 \exp\left[\frac{|v_z|}{\pi R}\frac{\cos\left(2\theta_0 + 2\Delta\omega t\right) - \cos\left(2\theta_0\right)}{\Delta\omega}\right] \tag{7.27}$$

where the electron's azimuthal position is defined as $\theta(t) = \theta_0 + \omega_{res}t + \Delta\omega t$ and its initial radius is $\rho_0$. Assuming $\theta_0 = -\pi/4$ as this results in the largest radial excursions

(as shown in Fig. 7.4) and expanding the exponent and sine term over the small mean time between collisions, $t = \nu^{-1}$, we find

$$\rho\left(\nu^{-1}\right) = \rho_0 + \frac{2\rho_0 v_z}{\pi R \nu} \tag{7.28}$$

Then using $v_z = 4\omega_r z_p/\pi$ which is true on resonance,

$$\lambda = \frac{8\rho_0 \omega_r z_p}{\pi^2 R \nu} \tag{7.29}$$

We next need to determine the fraction of particles, $f$, participating in the resonance. This can be approximated by

$$f = P\left(\omega_z = 2\omega_r\right)\Delta\omega \tag{7.30}$$

$$= \sqrt{\frac{\pi}{8}}\frac{1}{\omega_r z_p}\exp\left[\frac{-\omega_r^2}{2\omega_T^2}\right](z_p\nu) \tag{7.31}$$

where we have defined the width of the resonance by choosing $\Delta\omega$ such that $\rho\left(t = \nu^{-1}\right)$ corresponds to a maximum of Eq. 7.27 which implies that $\Delta\omega = \pi\nu/4$.

Putting these results together

$$D = \frac{16\sqrt{2}}{\pi^{7/2}}\left(\frac{z_p^2\rho_0^2\omega_r^2}{R^2\omega_T}\right)\exp\left[\frac{-\omega_r^2}{2\omega_T^2}\right] \tag{7.32}$$

Note that in this derivation we have neglected higher order resonances where $\omega_z = 2N\omega_r$ with $N$ odd. For typical cloud parameters these resonances have negligible effect due to a scaling of $N^{-5}$ in the diffusion coefficient for the $N$th order resonance.

We are now in a position to consider more fully the requirement on the collision frequency necessary for the above derivation to be applicable. In a magnetized plasma where the cyclotron radius, $r_c = \bar{v}/\omega_c = 64\,\text{nm}$ for a 1 T magnetic field at 4.2 K, is much smaller than the classical distance of closest approach, $b = e^2/(4\pi\epsilon_0 k_b T) =$

4 µm, collisions between electrons with a direction perpendicular to the magnetic field are strongly suppressed [111]. While collisions parallel to the magnetic field occur with the standard frequency, $\nu_{\|} = n_0 \bar{v} b^2 \ln(\lambda_d/b)$, the perpendicular collision frequency is only

$$\nu_{\perp} = n_0 \bar{v} b^2 \left(\frac{r_c}{b}\right)^2 = 9300/\,\mathrm{s} \tag{7.33}$$

for a 1 T magnetic bias field, 4.2 K temperature, and $n_0 = 2\times10^8/\,\mathrm{cm}^3$ in our Penning trap. However this collision rate is for approximately 90° collisions created from the sum of many smaller angle collisions. Diffusion occurs due to the individual smaller collisions so the applicable collision rate is much higher. We can estimate the actual rate by noting that while for 90° collisions, $\Delta v_{\perp}/v_{perp} \approx 1$, we have defined a collision as $\Delta\omega/\omega = \Delta v/v = \pi\nu/(4\omega)$. Assuming that these collisions are a random walk process in velocity space, $\Delta v^2 \propto t$, and hence $\Delta v^2/\Delta v_{\perp}^2 = \nu_{\perp}/\nu$. The small collision frequency is thus

$$\nu = \left(\frac{16\omega^2\nu_{\perp}}{\pi^2}\right)^{1/3} = 367\times10^3/\,\mathrm{s} \tag{7.34}$$

To determine the time scale on which the perturbative calculation of $\lambda$ is appropriate we consider Eq. 7.27 with $\theta_0 = -\pi/4$ and $\Delta\omega \cdot t = 0$:

$$\rho = \rho_0 \exp\left[\frac{|v_z|}{\pi R} 2t\right] \tag{7.35}$$

In order to need only expand the exponential to first order, we must have $\nu > 2\bar{v}/(\pi R) = 100\times10^3/\,\mathrm{s}$ for our typical experiment with $R = 7\,\mathrm{cm}$. As $\nu$ is proportional to the density of the plasma this requirement corresponds to a minimum density for large scale diffusion of $n > 6\times10^7/\,\mathrm{cm}^3$ for $R = 7\,\mathrm{cm}$ and $n > 4\times10^8/\,\mathrm{cm}^3$ for $R = 1\,\mathrm{cm}$ as we hope to achieve in a next-generation Ioffe trap.

In summary, particle loss due to the a quadrupole magnetic field perturbation can be characterized by a diffusive random walk process. This diffusion process is related to the particle lifetime through

$$\tau \approx 0.2\frac{\rho_w^2}{D} \tag{7.36}$$

The diffusion constant, $D$ scales with the perturbation strength and plasma parameters as follows:

$$D \propto \left(\frac{z_p^2\rho_p^2\omega_r^2}{R^2\omega_T}\right)\exp\left[\frac{-\omega_r^2}{2\omega_T^2}\right] \tag{7.37}$$

Due to the complicated interrelationships between $z_p$, $\rho_p$, and $\omega_r$ it is difficult to predict the optimal plasma shape but it is clear that it is important to ensure that $\omega_r \ll \omega_T$. However for our typical conditions of $R = 7\,\mathrm{cm}$ and $n_0 = 2 \times 10^7/\,\mathrm{cm}^3$, we expect a lifetime on the order of 2 minutes which as we will discuss later is approximately a factor of 50 too short. This suggests that the constant in Eq. 7.32 is not well understood; a result which was also discovered in the experiments by the Fajans group [109]

## 7.3 Electron stability in HBAR1

To experimentally investigate these effects our Jülich collaborators developed two permanent magnet trap configuration that fit inside the bore of the superconducting solenoid used for the HBAR1 trap (Fig. 7.5). Each magnet segment is composed of $Sm_2Co_{17}$ which has a remnant magnetization of 1.07 T when no external field is applied. Due to the high fields on the order of 5 T used to magnetize the pieces they show only a 10 % reduction in magnetization when placed in a 3 T bias field. On

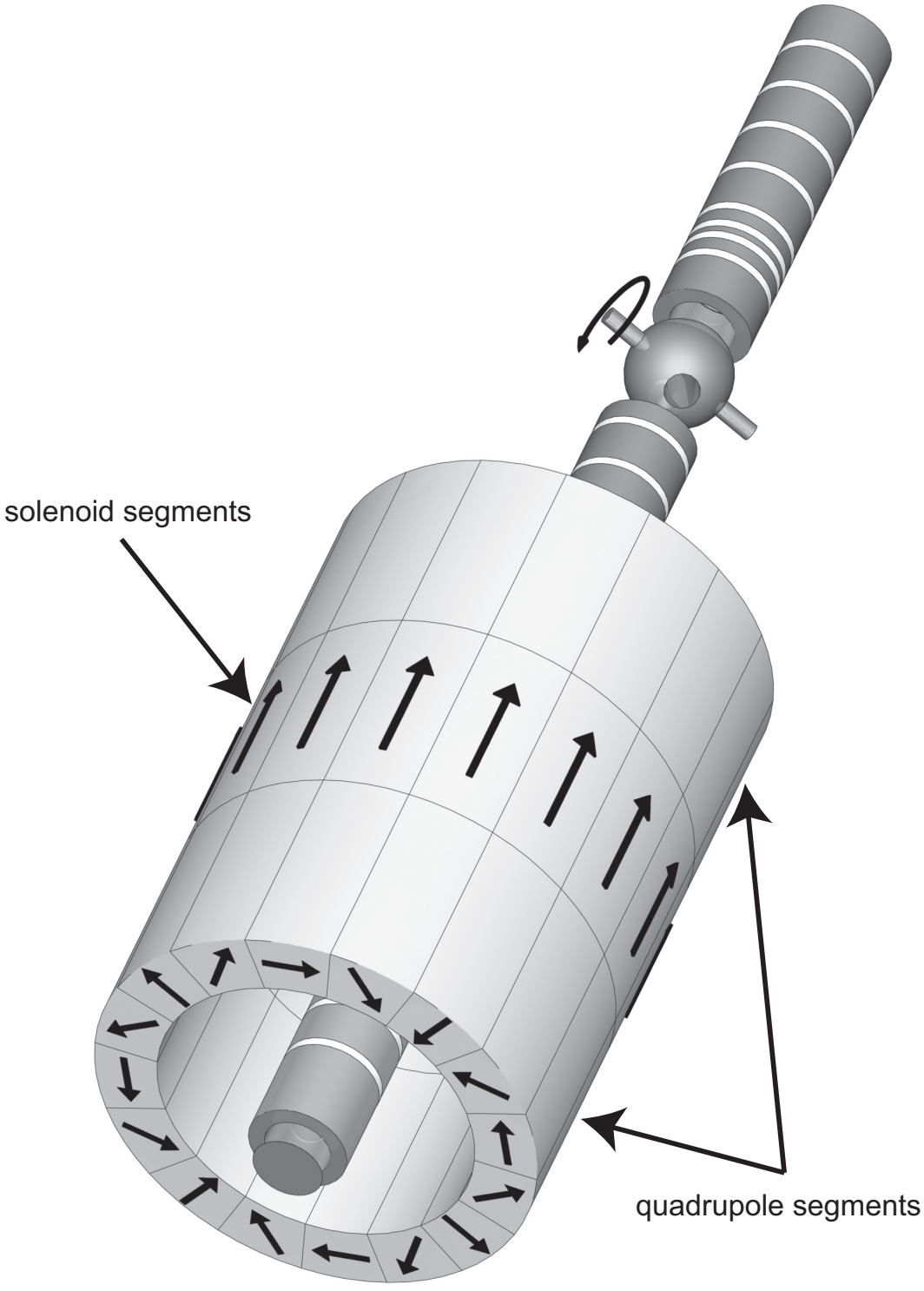


Figure 7.5: The permanent magnet Ioffe trap surrounds the electrode stack. The arrows superimposed on the permanent magnet show the axis of magnetization for each magnet.

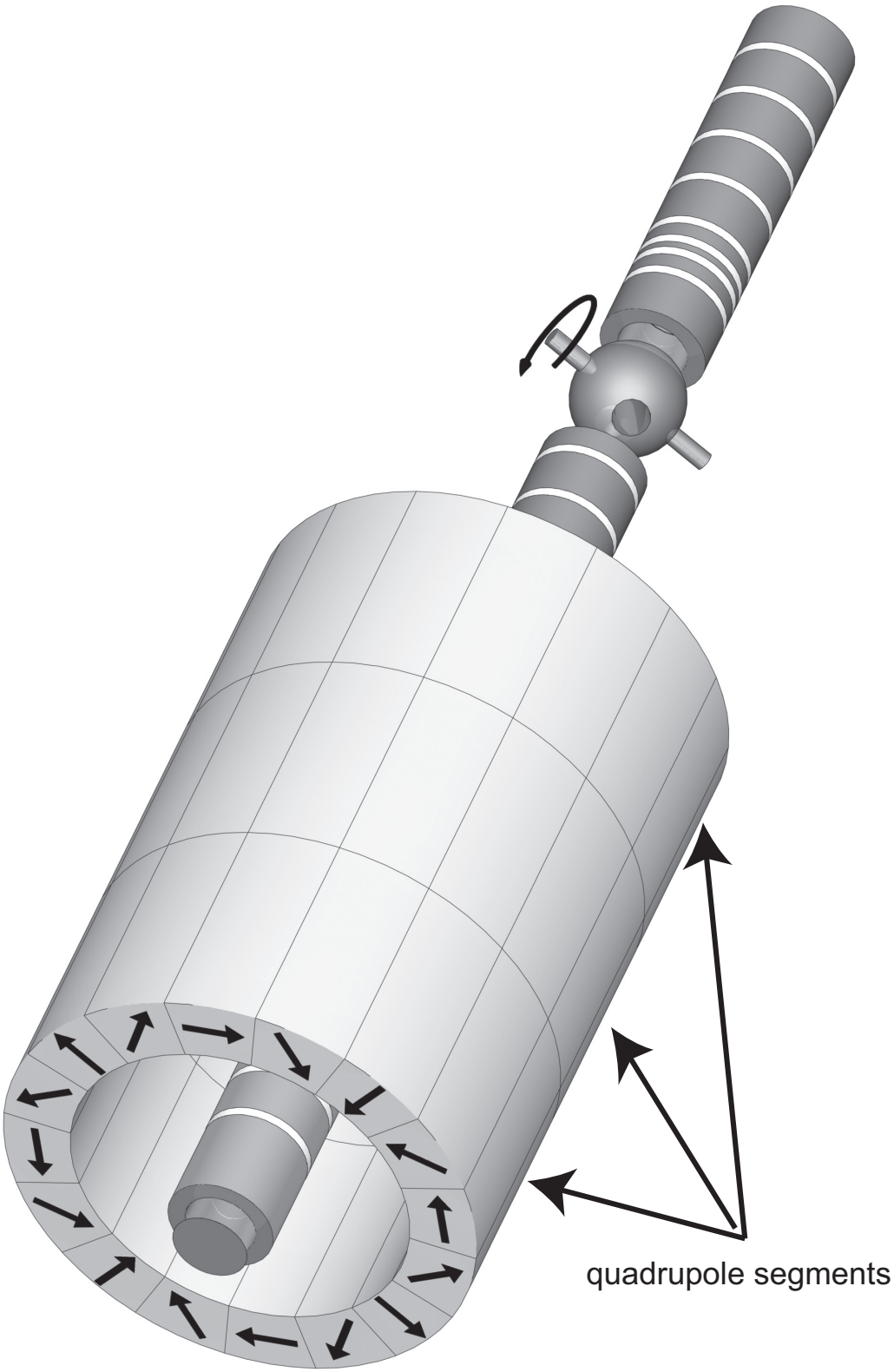


Figure 7.6: The first version design contained only permanent magnet quadrupole which cannot trap neutral atoms. The arrows superimposed on the permanent magnet show the axis of magnetization for each magnet.

| | 1 T Bias Field | | 2 T Bias Field | | 3 T Bias Field | |
|---|---|---|---|---|---|---|
| | High Gradient | Low Gradient | High Gradient | Low Gradient | High Gradient | Low Gradient |
| $B_0$ | 1.04 T | 0.90 T | 2.05 T | 1.9 T | 3.06 T | 2.94 T |
| $R$ | 7.2 cm | 85.4 cm | 14.2 cm | 174.6 cm | 21.1 cm | 256.3 cm |
| $B_0/R$ | 14.4 T/m | 1.1 T/m | 14.4 T/m | 1.1 T/m | 14.4 T/m | 1.1 T/m |

Table 7.1: Field parameters for the permanent magnetic quadrupole.

both ends are magnet rings composed of 16 segments with the magnetization axis perpendicular to the magnetic bias field and incrementing by 45° after each segment. These produce the quadrupole field necessary for radial trapping [112]. In the middle is a solenoid section with magnetization axis parallel to the bias field which is designed to reduce the axial field at the center of the trap in order to produce axial confinement. A preliminary version was also developed that consists of three quadrupole segments and thus has no axial trapping. Initial data taken with this configuration revealed long particle lifetimes similar to those that will be discussed later for the final trap design.

Due to the large radial variation in the axial field produced by the middle solenoid section, there is in general no minimum of the magnetic field strength located on axis (Fig. 7.7 and Fig. 7.8). As such, this trap is not capable of trapping neutral atoms. Instead it offers two convenient locations to perform experiments on the effects of radial gradients on charged particles. Particles in the high radial gradient location (*T6*) experience a radial gradient of 15 mT/m while particles in the low gradient (*ER*) location experience a gradient of only 1 mT/m. By varying the magnetic bias field between 1 T and 3 T, this corresponds to $R$ in *T6* between 7 cm and 21 cm (Table 7.1).

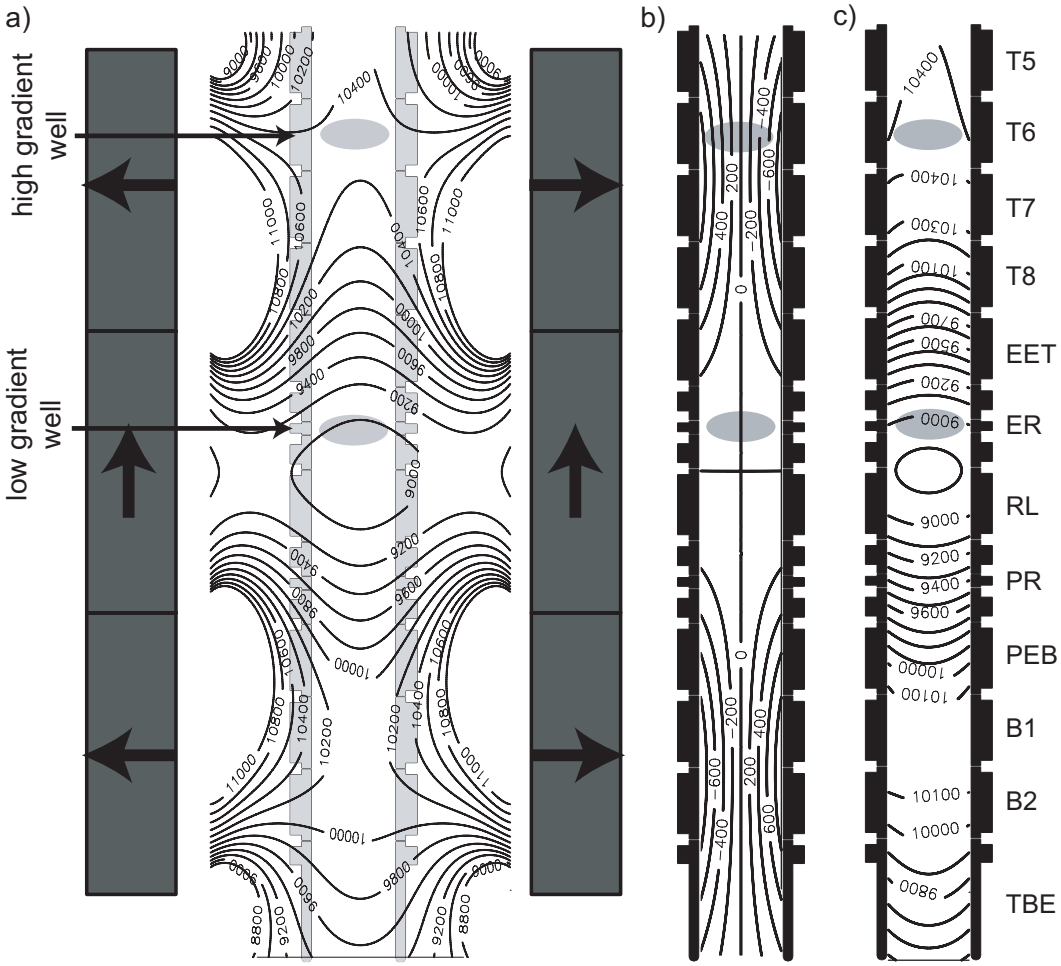


Figure 7.7: The magnetic fields produced by the permanent magnet quadrupole with a bias field of 1 T. (a) shows the field magnitude in gauss with the relevant portion of the electrode stack and permanent magnet structure superimposed (the arrows show the magnetization axis of the permanent magnets). (b) and (c) show the radial and axial field components respectively.

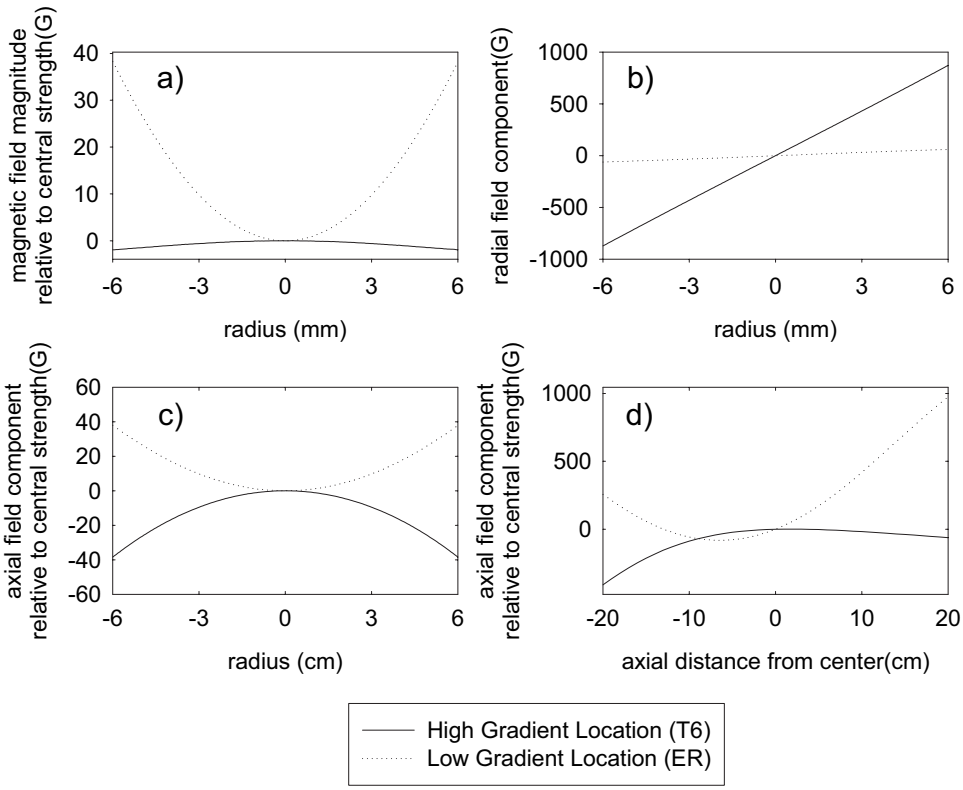


Figure 7.8: Magnetic field profile at the high and low gradient electrode locations.

An average of 1.6 million electrons (with actual numbers ranging between 650,000 and 3.2 million) were then placed in either the high and low gradient locations. Every 3 minutes, the electrons were moved to *ER*, sideband cooled and counted, and finally moved back to their initial location. This procedure was repeated over approximately one hour with an average time per point of 8 minutes. Figure 7.9 shows the results. As can be seen in the plot of the ratio of the number remaining in the high gradient location with the number in the low gradient location, the cloud is stable until the bias field is at 1 T which corresponds to $R = 7\,\mathrm{cm}$. The lifetime of 90 minutes (when adjusted for the 37.5 % duty cycle) corresponds to a diffusion coefficient calculated from the best fit to Eq. 7.20 of $D = 30(3) \times 10^{-6}\,\mathrm{cm}^2/\mathrm{s}$. The fit to the data is not great and is likely caused by the decrease of the diffusion coefficient as $\omega_r$ drops-off over time due to the reduction in central density caused by diffusion (as shown in Eq. 4.10). For this reason the higher diffusion rate curve may likely be more correct as it corresponds to the initial diffusion rate before the rotation frequency decreased.

The lifetime experiments were also repeated with the permanent magnet quadrupole removed and the bias field at 3 T and 1 T. At 3 T no particle loss was observed as expected. At 1 T we were unable to load $e^-$. Electrons were observed entering the well through the formation of a dip on the amplifier spectrum while firing the field-emission point but once the FEP was turned off the particles left the well immediately (*i.e.* on a time scale of less than 1 second). We are unable to explain this behavior by any plausible mechanism. The absence of the quadrupole perturbation should result in more stable particles and should not prevent loading when compared to the situation with the quadrupole trap in place. This behavior thus casts doubt

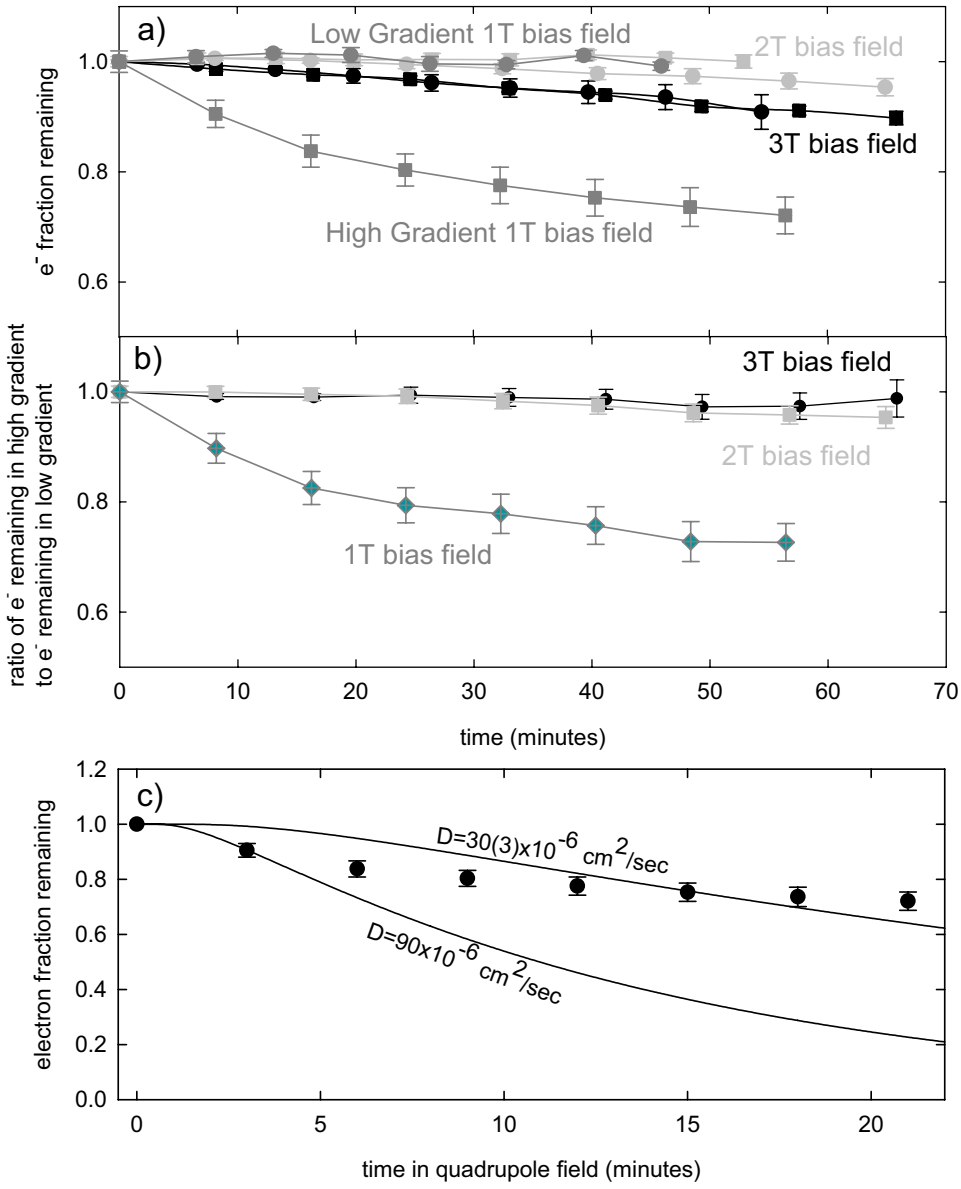


Figure 7.9: Stability of charged particles in our permanent magnet quadrupole. (a) Fractional particle loss in different Bias fields and gradients as a function of time. (b) Ratio of the particles remaining in the high and low gradient wells as a function of time. The data points represent the averaging of several different runs with both 1 and 3 million $e^-$ initially. (c) The least-squares fit for the 1 T high gradient data to Eq. 7.20 is $D = 30(3) \times 10^{-6}\,\mathrm{cm}^2/\mathrm{s}$.

on our results and needs to be understood before continuing with these experiments.

If we do believe the lifetime results in spite of this bizarre behavior, utilizing Eq. 7.23 and an estimated cloud shape based on Eq. 4.44 where $\rho_p = 3.75\,\mathrm{mm}$, $z_p = 0.24\,\mathrm{mm}$, $\omega_r = 4 \times 10^5$, and $\omega_z = 3.6 \times 10^7$, we find that the diffusion coefficient averaged over the cloud radius can be given as

$$D = 0.001 \left( \frac{z_p^2 \rho_0^2 \omega_r^2}{R^2 \omega_T} \right) \exp \left[ \frac{-\omega_r^2}{2\omega_T^2} \right] \tag{7.38}$$

This can be extrapolated to the values given in Fajans *et al.* [102] where $\omega_r = 2 \times 10^6$, $\omega_T = 4.4 \times 10^6$, $z_p = 15\,\mathrm{cm}$, $\rho_p = 1.3\,\mathrm{cm}$, and $R = 5000\,\mathrm{cm}$. The resulting calculated diffusion is $0.1\,\mathrm{cm}^2/\mathrm{s}$ while the measured diffusion is $1\,\mathrm{cm}^2/\mathrm{s}$. This agreement within an order of magnitude is striking due to the 5 orders of magnitude extrapolation required to bridge the three orders of magnitude temperature difference and two orders of magnitude difference in plasma axial extent between the two experiments and is much closer than one would expect. The reduced diffusion comparatively in HBAR1 may be due to the sideband cooling every 8 minutes which will likely drive some particles inward counteracting the diffusion due to the quadrupole field.

## 7.4 Summary

These experiments while certainly not conclusive do suggest that the superposition of a Penning trap and an Ioffe quadrupole neutral atom trap may not create any insurmountable challenges. The lack of cylindrical symmetry in this configuration does however remove the core reason for long particle confinement times. In our preliminary experiments with the strongest quadrupole perturbation we could produce,

a lifetime of only 100 minutes was observed although the inability to load electrons in the null experiment casts substantial doubts on the accuracy of these results.

Since our next generation experiment will likely use a Penning-Ioffe trap with $R \approx 1\,\mathrm{cm}$ in order to create a $1\,\mathrm{K}$ deep trap for neutral atoms and the electrode radius is increased by a factor of 3 as well, we can estimate the diffusion rate in this coefficient (for an exactly similar plasma cloud) to be $D = 0.002\,\mathrm{cm}^2/\mathrm{s}$ which corresponds to a lifetime of less than 20 minutes if one believes the results obtained in HBAR1. This is long enough for producing $\overline{\mathrm{H}}$ using either a nested well or resonant charge exchange but will require a conscience effort to minimize the amount of time the charged particles experience the quadrupole magnetic field perturbation.

# Chapter 8

# Conclusion

Just prior to this work, cold guiding center antihydrogen atoms had been made and detected [6, 7, 8]. However many fundamental questions about these atoms still remained open. What velocity were the $\overline{\mathrm{H}}$ atoms produced with? Were any deeply bound atomic states being produced? What would be required for the existing nested well techniques to produce atoms useable for spectroscopy? Could another technique produce atoms useful for spectroscopy more quickly?

ATRAP's experiments at CERN have been extremely fruitful in answering these questions during the last two years. Using the techniques developed by our collaboration and its predecessor for loading antiprotons and positrons, we can routinely accumulate and utilize up to 750,000 antiprotons and 5 million positrons [113, 93]. Employing these large numbers of positrons and antiprotons, we then demonstrated and studied two different methods of producing cold antihydrogen — a large step towards the spectroscopic comparison of hydrogen and antihydrogen.

A first method to produce slow antihydrogen utilizes a nested Penning trap to

contain antiprotons and positrons in adjacent potential wells [2]. Energy must then be given to the antiprotons in order to force them to interact with the trapped positron cloud either through the application of a RF drive or injecting them into the nested well with high energy. Over 7500 atoms have been observed in a small detection solid angle during an one hour experiment. Our field ionization analysis indicates that we have measured a $\overline{\mathrm{H}}$ state distribution that extends to atomic states less than 0.1 µm in radius. These states can no longer be described through a simple separation of motions [20] and instead will likely demonstrate chaotic behavior [92].

The axial velocity of the atoms within a nested Penning trap was also measured for the first time. A slow axial velocity is crucial in order to increase the time available for de-excitation as well as for success in trapping the resultant ground state atoms. However, the axial speed measured so far is still much faster than that needed for efficient capture into a 1 K neutral atom trap [9]. This technique should, however, allow us to minimize the velocity of the produced $\overline{\mathrm{H}}$ atoms.

A second method for producing cold antihydrogen was also demonstrated that likely is producing atoms near the ambient temperature. This technique utilizes a two step resonant charge exchange reaction which results in a final state distribution of $\overline{\mathrm{H}}$ that can be controlled simply by tuning a laser [10]. During our proof-of-principle demonstration, antihydrogen atoms were detected that are likely to be much colder than those produced in a nested Penning trap as little additional energy is likely transferred to the approximately 4.2 K antiprotons. This expectation has yet to be demonstrated.

As we can now robustly produce antihydrogen, the next logical goals are the

production of slow neutral ground state antihydrogen and then the trapping of these atoms. These goals require both colder and smaller radius atoms than have been detected so far. The refinements to the field ionization technique presented here allows us to go beyond simple $\overline{\mathrm{H}}$ counting and make progress toward meeting these two crucial challenges.

The first crucial challenge requires the development of techniques to produce much colder atoms than have been measured so far. While laser-controlled charge exchange will likely produce slow enough atoms, future experiments are needed to confirm this as well as to increase the number of $\overline{\mathrm{H}}$ produced within a single trial. Through careful optimization of the driving or injection process within the nested Penning trap scheme, it may also be possible to produce much slower atoms using this technique that will then also be useable for spectroscopy.

To meet the second crucial challenge, and produce lower lying states, will likely require the addition of an active damping technique to our experimental repertoire. Radiative decay, which is the easiest de-excitation method experimentally due to its passive nature, requires the atoms to be in a much lower state before the decay to the ground state occurs on a time scale short enough to prevent annihilation on electrode surfaces. This could be done through resonant de-excitation using laser light to stimulate downward transitions to a level below $n = 10$ which would then spontaneously decay to the ground state on a time scale of a few nanoseconds. However the broad state distribution created by the nested Penning trap method and even the smaller state distribution produced through the charge exchange reaction will make it difficult to use laser techniques to de-excite all the atoms. The use of more positrons in

the nested Penning trap may also help by allowing more time for replacement and inward diffusion collisions to occur thus lowering the produced state distribution to a range that will spontaneously decay in an acceptable length of time. Another active technique may be to employ unipolar half-cycle pulses to kick the positron to a lower energy level [114].

The final crucial challenge will necessitate the production of antihydrogen atoms inside a superposition of the neutral atom trap on top of the existing Penning trap. Our initial experiments suggest that the lack of cylindrical symmetry in this configuration dramatically reduces the stability of charged particles trapped within. However the estimated 20 minute lifetime based on these measurements in the next generation experiment with a stronger neutral atom trap should be more than long enough to produce $\overline{\mathrm{H}}$ atoms before losing the constituent charged particles to annihilations on the electrode surfaces due to the diffusion caused by the quadrupole magnetic field.

Despite these large challenges still to be overcome, the robust regular production of slow antihydrogen atoms and development of techniques to measure their speed and size are big steps forward. Even though none of these atoms yet meet the requirements for a spectroscopic comparison, their production inspires hope for rapid future progress towards trapped, ground-state atoms ready for spectroscopic tests.

# Appendix A

# Software Code

Several different software code packages were used in the course of this work. These included one that calculated potentials within the trap written by myself and another that calculated plasma equilibriums written initially by Spencer *et al.* [65]. The following sections briefly discuss how to use these software packages.

## A.1 Electrode Potentials

This code relies on the superposition of potentials calculated per electrode (with 1 V on that particular electrode and 0 V on all others) on a grid of points. The electric field can then be calculated via numerical differentiation.

### A.1.1 Grid Generation

The *gengrid* (*ggrid.exe* on Windows) program precalculates the grid files for axisymmetric electrodes whose boundaries can be defined by a series of linear line seg-

ments. Tables A.1 and A.2 show the two files that must be created to define the series of electrodes within a trap. *Gengrid* then places binary files containing all of the calculated potentials in the grid storage directory.

### A.1.2 Potential Calculation

The *voltscalc* (*vc.exe* on Windows) program utilizes these precalculated potential grid files to calculate potentials and electric fields within a given set of trapping potentials. The spacing of the output point grid is adjustable. After entering the specific trapping potentials and output grid information, the files described in Table A.3 are placed in the *output* directory located under the directory containing *voltscalc*.

### A.1.3 Trajectory Calculations

The final two programs in this suite (*hbartraj* and *cspstrajcalc*) calculate ballistic trajectories for neutral $\overline{\mathrm{H}}^*$ or $\mathrm{Cs}^*$ atoms with a given field at which they ionize. When the atom reaches either an electric field magnitude or axial field strength higher than the ionization field, the code checks where the $\overline{\mathrm{p}}$ or $\mathrm{e}^+$ is in a location with a confining potential. Repeating this process for many trajectories calculates an estimated solid angle for a specific detection well geometry.

## A.2 Plasma Thermal Equilibrium Calculation

The *equilsor2* Fortran-77 code calculates a plasma cloud's thermal equilibrium shape as discussed in Chapter 4. It was originally written by Spencer *et al.* [65] and

| | | |
|---|---|---|
| 1 | ./grids/cs/ | Path to grid storage directory |
| 2 | cslines.seg | Electrode definition file name |
| 3 | defaults.dat | Electrode potential defaults file name |
| 4 | 1000,50 | Grid size (axial points, radial points) |
| 5 | 1e-9,25000 | Convergence parameters (epsilon, maximum number of iterations) |
| 6 | TMOD | List of electrode names |
| 7 | UPHV | |
| 8 | T1 | |
| 9 | ETEC | |
| 10 | ETCE | |
| 11 | ERING | |
| 12 | EBCE | |
| 13 | EBEC | |
| 14 | CS | |
| 15 | PTEC | |
| 16 | PTCE | |
| 17 | PRING | |
| 18 | PBCE | |
| 19 | PBEC | |
| 20 | TUBE | |
| 21 | RMOD | |

Table A.1: Grid definition file for the potential calculation code.

```
1  6.1,0,5.9947,0,TMOD
2  5.9947,0.2539,5.9947,0,TMOD
3  5.9947,0.2539,5.9947,0.5999,UPHV
4  5.9947,0.2539,5.6486,0.2539,UPHV
5  5.6486,0.2539,5.6486,0.5999,UPHV
6  5.9947,0.5999,4.7596,0.5999,UPHV
7  4.7596,0.5999,3.7347,0.5999,T1
8  3.7347,0.5999,2.7098,0.5999,ETEC
9  2.7098,0.5999,2.2204,0.5999,ETCE
10 2.2204,0.5999,2.0268,0.5999,ERING
11 2.0268,0.5999,1.5374,0.5999,EBCE
12 1.5374,0.5999,0.5125,0.5999,EBEC
13 0.5125,0.5999,-0.5124,0.5999,CS
14 -0.5124,0.5999,-1.5373,0.5999,PTEC
15 -1.5373,0.5999,-2.0268,0.5999,PTCE
16 -2.0268,0.5999,-2.2203,0.5999,PRING
17 -2.2203,0.5999,-2.7098,0.5999,PBCE
18 -2.7098,0.5999,-3.7347,0.5999,PBEC
19 -3.7347,0.5999,-4.1246,0.3174,TUBE
20 -4.1246,0.3174,-5.6486,0.3174,TUBE
21 -5.6486,0.3174,-6.2836,0.4965,TUBE
22 -6.2836,0.4965,-6.2836,0.5999,TUBE
23 -6.2836,0.4965,-6.2836,0,RMOD
24 -6.2836,0,-6.3,0,RMOD
```

electrode definition segment ($z_{start}$, $\rho_{start}$, $z_{end}$, $\rho_{end}$, electrode name)

Table A.2: Electrode definition file for the potential calculation code.

| Filename | Description |
|---|---|
| axial.txt | Potentials and electric field magnitudes on axis and 3 mm off-axis |
| field.txt | Electric field components at all points specified in z, r, $E_z$, $E_\rho$, $E_{mag}$ format |
| simpleaxialfields.txt | Potentials and electric field axial component ($E_z$) in z, $V(\rho_1)$, $E_z(\rho_1)$, $V(\rho_2)$, $E_z(\rho_2)$, ... format |
| simplefields.txt | Potentials and electric field magnitude ($E_{mag}$) in z, $V(\rho_1)$, $E_{mag}(\rho_1)$, $V(\rho_2)$, $E_{mag}(\rho_2)$, ... format |
| volts.txt | Potential at all points specified in z, r, and V format |

Table A.3: *Voltscalc* output files.

modified by Parrott [115] and myself.

Table A.4 shows the input file format used for processing with descriptions of the parameters on the right hand side. The most important parameter is the equilibrium type which can be one of the items described in Table A.5. Several parameters can be adjusted to ensure convergence of the final solution. The simplest one to adjust is $\alpha$ which controls how fast the relaxation occurs. A calculated optimal value is placed in the *run.log* file when the code is run which is used when $\alpha$ is set to 0. However by entering a reduced value for $\alpha$, the relaxation is slowed down and may allow a convergent solution. Further improvements can be made by utilizing the ability to begin the calculation at a higher temperature where convergence is easier to obtain and then to slowly reduce the temperature to the desired value.

The code is capable of calculating an equilibrium containing two different particle species. If you wish to calculate an equilibrium for only one species, set the density to

| | | |
|---|---|---|
| 1 | demo5V | run ID |
| 2 | -1.602177e-19 9.10939e-31 | Species 1 charge ( C) and mass ( kg) |
| 3 | 1.602177e-19 1.67262e-27 | Species 2 charge ( C) and mass ( kg) |
| 4 | 5.3 | magnetic field ( T) |
| 5 | plmeta | ignored |
| 6 | thermalN | equilibrium type |
| 7 | peri | boundary conditions (normally peri for periodic conditions) |
| 8 | 120 1200 | grid size – radial points and axial points |
| 9 | 0.0 6.0e-3 -3.0e-2 3.52e-2 | $\rho_{\min}$( m), $\rho_{\max}$( m), $z_{\min}$( m), and $z_{\max}$( m) of computation region |
| 10 | 600000 5e-2 1.4 0.9 | maximum iterations, $\epsilon$ test for convergence, $\alpha$ (successive over-relaxation parameter; zero lets the code choose), and under-relaxation parameter |
| 11 | 1 | always 1 |
| 12 | 2.4465E+013 3.45e+0 3.45e-4 | species 1 central density ( $N_p$/m$^3$), initial |
| 13 | 10000 | temperature ( eV), final temperature ( eV), and number of iterations to reach final temperature |
| 14 | 1.0e00 3.45e+0 3.45e-4 10000 | species 2 central density ( $N_p$/m$^3$), initial temperature ( eV), final temperature ( eV), and number of iterations to reach final temperature |
| 15 | 50 1 0.6 | ignored |
| 16 | 4.4781E-003 3.8972E-003 0.0e-2 | species 1 $z_p$( m), $r_p$( m), and $z_{\text{center}}$( m) |
| 17 | 1.0e-4 3.0e-4 3.0e-2 | species 2 $z_p$( m), $r_p$( m), and $z_{\text{center}}$( m) |

Table A.4: Run definition file for the *equilsor2* plasma equilibrium calculation code.

| | | |
|---|---|---|
| 18 | 2.54e-3 5.447925E-1 1.0 5.0e-4 | aperture radius ( m), transmitted fraction (species 1), transmitted fraction (species 2), maximum fraction deviation from goal |
| 19 | 0.0 0.0 0.0 | boundary potentials — $V$(upper end), $V$(lower end), and $V$(wall) |
| 20 | -0.75e-2 0.75e-2 4.5e-3 | maximum plasma size (species 1) — $z_{start}$( m), $z_{end}$( m), and $\rho_{max}$( m) |
| 21 | 3.2e-2 2.8e-2 6.0e-3 | maximum plasma size (species 2) — $z_{start}$( m), $z_{end}$( m), and $\rho_{max}$( m) |
| 22 | 6 | number of confining rings |
| 23 | -2.52e-2 -1.512e-2 0.0 | electrode definitions — $z_{start}$( m), $z_{end}$( m), and electrode potential ( V) |
| 24 | -1.512e-2 -0.504e-2 0 | |
| 25 | -0.504e-2 0.504e-2 5 | |
| 26 | 0.504e-2 1.512e-2 0 | |
| 27 | 1.512e-2 2.52e-2 0.0 | |
| 28 | 2.52e-2 3.52e-2 -1.0 | |
| 29 | 0 | number of internal conductors |
| 30 | stop | stop processing command |

Table A.4: Continued.

| Equilibrium type | Description |
|---|---|
| thermal | Plasma radius and central density are conserved as given by input file. |
| thermalN | Plasma radius and particle number, $N$, are conserved. The conserved particle number is calculated from $N = (4/3)\pi n_0 \rho_p^2 z_p$ where $n_0$, $\rho_p$, and $z_p$ are given by the input parameters. |
| thrmcnsv | Angular momentum moment of inertia and particle number are conserved. $N$ is calculated as in thermalN and the angular momentum is calculated from $P_\theta = (2/5)N\rho_p^2$. |
| thrmaper | Particle number and the fraction of particles within the given aperture radius are conserved. $N$ is calculated as in thermalN. |
| vacuum | Solves for potential and electric fields in the absence of any particles. |

Table A.5: Equilibrium types used in the *equilsor2* code.

1.0 $N_p/\mathrm{m}^3$ and place the cloud in an out of the way location. In addition by setting the maximum plasma size for the second species to a small box will ensure that convergence issues with the nuisance second species will not disrupt the convergence of the first species.

The results from the calculation will be output in a series of data files describing the density and potentials of the equilibrium plasma cloud. A R [116] script, *equilsor2-plot.R*, automatically produces a series of plots showing the particle equilibrium in detail.

# Bibliography


[1] G. Baur, G. Boero, S. Brauksiepe, A. Buzzo, W. Eyrich, R. Geyer, D. Grzonka, J. Hauffe, K. Kilian, M. Lo Vetere, M. Macri, M. Moosburger, R. Nellen, W. Oelert, S. Passaggio, A. Pozzo, K. Rohrich, K. Sachs, G. Schepers, T. Sefzick, R.S. Simon, R. Stratmann, F. Stinzing, and M. Wolke, Phys. Lett. B **368**, 251 (1996).

[2] G. Gabrielse, S. L. Rolston, L. Haarsma, and W. Kells, Phys. Lett. A **129**, 38 (1988).

[3] D. S. Hall and G. Gabrielse, Phys. Rev. Lett. **77**, 1962 (1996).

[4] G. Gabrielse, D. S. Hall, T. Roach, P. Yesley, A. Khabbaz, J. Estrada, C. Heimann, and H. Kalinowsky, Phys. Lett. B **455**, 311 (1999).

[5] G. Gabrielse, J. Estrada, J. N. Tan, P. Yesley, N. S. Bowden, P. Oxley, T. Roach, C. H. Storry, M. Wessels, J. Tan, D. Grzonka, W. Oelert, G. Schepers, T. Sefzick, W. Breunlich, M. Cargnelli, H. Fuhrmann, R. King, R. Ursin, J. Zmeskal, H. Kalinowsky, C. Wesdorp, J. Walz, K. S. E. Eikema, and T. Haensch, Phys. Lett. B **507**, 1 (2001).

[6] G. Gabrielse, N. S. Bowden, P. Oxley, A. Speck, C. H. Storry, J. N. Tan, M. Wessels, D. Grzonka, W. Oelert, G. Schepers, T. Sefzick, J. Walz, H. Pittner, T. W. Hänsch, and E. A. Hessels, Phys. Rev. Lett. **89**, 213401 (2002).

[7] G. Gabrielse, N. S. Bowden, P. Oxley, A. Speck, C. H. Storry, J. N. Tan, M. Wessels, D. Grzonka, W. Oelert, G. Schepers, T. Sefzick, J. Walz, H. Pittner, T. W. Hänsch, and E. A. Hessels, Phys. Rev. Lett. **89**, 233401 (2002).

[8] M. Amoretti, C. Amsler, G. Bonomi, A. Bouchta, P. Bowe, C. Carraro, C. L. Cesar, M. Charlton, M. J. T. Collier, M. Doser, V. Filippini, K. S. Fine, A. Fontana, M. C. Fujiwara, R. Funakoshi, P. Genova, J. S. Hangst, R. S. Hayano, M. H. Holzscheiter, L. V. Jorgensen, V. Lagomarsino, R. Landua, D. Lindelof, E. L. Rizzini, M. Macri, N. Madsen, G. Manuzio, M. Marchesotti, P. Montagna, H. Pruys, C. Regenfus, P. Riedler, J. Rochet, A. Rotondi, G. Rouleau, G.

Testera, A. Variola, T. L. Watson, and D. P. van der Werf, Nature **419**, 456 (2002).

[9] G. Gabrielse, A. Speck, C. H. Storry, D. Le Sage, N. Guise, D. Grzonka, W. Oelert, G. Schepers, T. Sefzick, H. Pittner, J. Walz, T. W. Hänsch, D. Comeau, and E. A. Hessels, Phys. Rev. Lett. **93**, 073401 (2004).

[10] C. H. Storry, A. Speck, D. Le Sage, N. Guise, G. Gabrielse, D. Grozonka, W. Oelert, G. Scheppers, T. Sefzick, J. Walz, H. Pittner, M. Herrmann, T. W. Hänsch, D. Comeau, and E. A. Hessels, Phys. Rev. Lett. **93**, 263401 (2004).

[11] E. A. Hessels, D. M. Homan, and M. J. Cavagnero, Phys. Rev. A **57**, 1668 (1998).

[12] A. Speck, C. H. Storry, E.A. Hessels, and G. Gabrielse, Phys. Lett. B **597**, 257 (2004).

[13] Leslie E. Ballentine, *Quantum Mechanics* (World Scientific, Singapore, 1998).

[14] T. D. Lee and C. N. Yang, Phys. Rev. **104**, 254 (1956).

[15] C. S. Wu, E. Ambler, R. W. Hayward, D. D. Hoppes, and R. P. Hudson, Phys. Rev. **105**, 1413 (1957).

[16] G. Lüders, Ann. Phys. **2**, 1 (1957).

[17] S. Eidelman *et al.*, Physics Letters B **592**, 1 (2004).

[18] M. Niering, R. Holzwarth, J. Reichert, P. Pokasov, Th. Udem, M. Weitz, T. W. Hänsch, P. Lemonde, G. Santarelli, M. Abgrall, P. Laurent, C. Salomon, and A. Clairon, Phys. Rev. Lett. **84**, 5496 (2000).

[19] R. Bluhm, V. A. Kostelecký, and N. Russell, Phys. Rev. Lett. **82**, 2254 (1999).

[20] M. Glinsky and T. O'Neil, Phys. Fluids **B3**, 1279 (1991).

[21] P. O. Fedichev, Phys. Lett. A **226**, 289 (1997).

[22] L. I. Men'shikov and P. O. Fedichev, Sov. Phys. JETP **108**, 144 (1995).

[23] E. M. Bass and D. H. E. Dubin, Phys. Plas. **11**, 1240 (2004).

[24] D. R. Bates, A. E. Kingston, and R. W. P McWhirter, Proc. Roy. Soc. Lond. A **267**, 297 (1962).

[25] B. Makin and J. C. Keck, Phys. Rev. Lett. **11**, 281 (1963).

[26] F. Robicheaux and J. D. Hanson, Phys. Rev. A **69**, 010701 (2004).

[27] F. Robicheaux, Phys. Rev. A **70**, 022510 (2004).

[28] J. W. Humberston, M. Charlton, F. M. Jacobsen, and B. I. Deutch, J. Phys. B **20**, L25 (1987).

[29] M. Charlton, Phys. Lett. A **143**, 143 (1990).

[30] J. Lu, E. Y. Sidky, Z. Roller-Lutz, and H. O. Lutz, Phys. Rev. A **68**, 024702 (2003).

[31] C. Wesdorp, F. Robicheaux, and L. D. Noordam, Phys. Rev. Lett. **84**, 3799 (2000).

[32] U. Schramm, J. Berger, M. Grieser, D. Habs, E. Jaeschke, G. Kilgus, D. Schwalm, A. Wolf, R. Neumann, and R. Schuch, Phys. Rev. Lett. **67**, 22 (1991).

[33] L. S. Brown and G. Gabrielse, Rev. Mod. Phys. **58**, 233 (1986).

[34] M. Kretzschmar, Eur. J. Phys. **12**, 240 (1991).

[35] G. Gabrielse, L. Haarsma, and S. L. Rolston, Intl. J. Mass Spec. Ion Proc. **88**, 319 (1989), ibid. 93, 121 (1989).

[36] W. Press, B. Flannery, S. Teukolsky, and W. Vetterling, *Numerical Recipes in C* (Cambridge University Press, New York, 1988).

[37] G. Gabrielse, Phys. Rev. A **27**, 2277 (1983).

[38] X. Fei and W. M. Snow, Nuc. Inst. Meth. A **425**, 431 (1999).

[39] P. Oxley, Ph.D. thesis, Harvard University, 2003.

[40] P. Yesley, Ph.D. thesis, Harvard University, 2001.

[41] G. Gabrielse, X. Fei, L. A. Orozco, R. L. Tjoelker, J. Haas, H. Kalinowsky, T. A. Trainor, and W. Kells, Phys. Rev. Lett. **65**, 1317 (1990).

[42] N. Bowden, Ph.D. thesis, Harvard University, 2003.

[43] Xinrong Jiang, C. N. Berglund, Anthony E. Bell, and William A. Mackie, J. Vac. Sci. Technol. B **16**, 3374 (1998).

[44] G. Gabrielse, X. Fei, L. A. Orozco, S. L. Rolston, R. L. Tjoelker, T. A. Trainor, J. Haas, H. Kalinowsky, and W. Kells, Phys. Rev. A **40**, 481 (1989).

[45] G. Gabrielse, X. Fei, K. Helmerson, S. L. Rolston, R. L. Tjoelker, T. A. Trainor, H. Kalinowsky, J. Haas, and W. Kells, Phys. Rev. Lett. **57**, 2504 (1986).

[46] G. Gabrielse, X. Fei, L. A. Orozco, R. L. Tjoelker, J. Haas, H. Kalinowsky, T. A. Trainor, and W. Kells, Phys. Rev. Lett. **63**, 1360 (1989).

[47] G. Gabrielse, N. S. Bowden, P. Oxley, A. Speck, C. H. Storry, J. N. Tan, M. Wessels, D. Grzonka, W. Oelert, G. Schepers, T. Sefzick, J. Walz, H. Pittner, and E. A. Hessels, Phys. Lett. B **548**, 140 (2002).

[48] S. Maury, Hyperfine Int. **109**, 43 (1997).

[49] Herbert Stelzer, Nuc. Inst. Meth. **133**, 409 (1976).

[50] L. H. Haarsma, K. Abdullah, and G. Gabrielse, Phys. Rev. Lett. **75**, 806 (1995).

[51] J. Estrada, T. Roach, J. N. Tan, P. Yesley, and G. Gabrielse, Phys. Rev. Lett. **84**, 859 (2000).

[52] R. G. Greaves, M. D. Tinkle, and C. M. Surko, Phys. Plas. **1**, 1439 (1994).

[53] B. M. Jelenkovic, A. S. Newbury, J. J. Bollinger, W. M. Itano, and T. B. Mitchell, Phys. Rev. A **67**, 063406 (2003).

[54] N. Oshima, T. M. Kojima, M. Niigaki, A. Mohri, K. Komaki, and Y. Yamazaki, Phys. Rev. Lett. **93**, 195001 (2004).

[55] K. G. Lynn, B. Nielsen, and J. H. Quateman, Appl. Phys. Lett. **47**, 239 (1985).

[56] J. D. Jackson, *Classical Electrodynamics, 3rd Edition* (John Wiley and Sons, Inc., New York, 1975).

[57] H. Goldstein, C. Poole, and J. Safko, *Classical Mechanics*, 3rd ed. (Addison Wesley, Reading, MA, 2002).

[58] T. M. O'Neil, Phys. Fluids **23**, 2216 (1980).

[59] D. H. E. Dubin and T. M. O'Neil, Rev. Mod. Phys. **71**, 87 (1999).

[60] L. D. Landau and E. M. Lifshitz, *Statistical Physics*, 2nd ed. (Pergamon Press, New York, 1969).

[61] J. J. Bollinger, D. J. Wineland, and D. H. E. Dubin, Phys. Plas. **1**, 1403 (1994).

[62] Ronald C. Davidson and Nicholas A. Krall, Phys. Fluids **13**, 1543 (1970).

[63] Leaf Turner, Phys. Fluids **30**, 3196 (1987).

[64] D. H. E. Dubin, Phys. Fluids B **5**, 295 (1993).

[65] R. L. Spencer, S. N. Rasband, and R. R. Vanfleet, Phys. Fluids B **5**, 4267 (1993).

[66] M. D. Tinkle, R. G. Greaves, C. M. Surko, R. L. Spencer, and G. W. Mason, Phys. Rev. Lett. **40**, 352 (1994).

[67] D. H. E. Dubin, Phys. Rev. Lett. **66**, 2076 (1991).

[68] W. Shockley, J. Appl. Phys. **9**, 635 (1938).

[69] D. J. Wineland and H. G. Dehmelt, J. Appl. Phys. **46**, 919 (1975).

[70] G. Gabrielse, Phys. Rev. A **29**, 462 (1984).

[71] H. Nyquist, Phys. Rev. **32**, 110 (1928).

[72] D. S. Hall, Ph.D. thesis, Harvard University, 1997.

[73] X. Feng, M. Charlton, M. Holzscheiter, R. A. Lewis, and Y. Yamazaki, J. Appl. Phys. **79**, 8 (1996).

[74] T. M. O'Neil and P. G. Hjorth, Phys. Fluids **28**, 3241 (1985).

[75] B. D'Urso, Ph.D. thesis, Harvard Univ., 2003.

[76] M. Komaru, K. Yajima, H. Sasaki, T. Katoh, T. Kashiwa, T. Asano, T. Takagi, Y. Mitsui, K. Matsuzaki, and N. Nemoto, Solid-State Electron. **41**, 1481 (1997).

[77] M. Amoretti, G. Bonomi, A. Bouchta, P. D. Bowe, C. Carraro, C. L. Cesar, M. Charlton, M. Doser, A. Fontana, M. C. Fujiwara, R. Funakoshi, P. Genova, J. S. Hangst, R. S. Hayano, L. V. Jorgensen, V. Lagomarsino, R. Landua, E. L. Rizzini, M. Macri, N. Madsen, G. Manuzio, G. Testera, A. Variola, and D. P. van der Werf, Phys. Plas. **10**, 3056 (2003).

[78] *Handbook of Chemistry and Physics*, 77 ed., edited by David R. Lide (CRC Press, Boca Raton, Florida, 1996).

[79] Claude Amsler, Rev. Mod. Phys. **70**, 1293 (1998).

[80] P. Oxley, N. S. Bowden, R. Parrott, A. Speck, C. Storry, J. N. Tan, M. Wessels, G. Gabrielse, D. Grzonka, W. Oelert, G. Schepers, T. Sefzick, J. Walz, H. Pittner, T. W. Hänsch, and E. A. Hessels, Phys. Lett. B **595**, 60 (2004).

[81] S. G. Kuzmin and T. M. O'Neil, Phys. Plas. **12**, 012101 (2005).

[82] N. Madsen, M. Amoretti, C. Amsler, G. Bonomi, P. D. Bowe, C. Carraro, C. L. Cesar, M. Charlton, M. Doser, A. Fontana, M. C. Fujiwara, R. Funakoshi, P. Genova, J. S. Hangst, R. S. Hayano, L. V. Jorgensen, A. Kellerbauer, V. Lagomarsino, R. Landua, E. Lodi-Rizzini, M. Macri, D. Mitchard, P. Montagna, H. Pruys, C. Regenfus, A. Rotondi, G. Testera, A. Variola, L. Venturelli, D. P. van der Werf, Y. Yamazaki, and N. Zurlo, Phys. Rev. Lett. **94**, 033403 (2005).

[83] I.I. Sobelman, *Atomic Spectra and Radiative Transitions* (Springer-Verlag, New York, 1979).

[84] Heiko Pittner, Ph.D. thesis, Ludwig-Maximilians-Universität, 2005.

[85] J. E. Avron, I. W. Herbst, and B. Simon, Ann. Phys. **114**, 431 (1978).

[86] B. P. Carter, J. Math. Phys. **10**, 788 (1969).

[87] S. G. Kuzmin, T. M. O'Neil, and M.E. Glinsky, Phys. Plas. **11**, 2382 (2004).

[88] J. B. Taylor, Phys. Fluids **7**, 767 (1964).

[89] T. F. Gallagher, *Rydberg Atoms* (Cambridge Univ. Press, New York, 1994).

[90] D. Vrinceanu, B. E. Granger, R. Parrott, H. R. Sadeghpour, L. Cederbaum, A. Mody, J. Tan, and G. Gabrielse, Phys. Rev. Lett. **92**, 133402 (2004).

[91] S. G. Kuzmin and T. M. O'Neil, Phys. Rev. Lett. **92**, 243401 (2004).

[92] J. R. Guest and G. Raithel, Phys. Rev. A **68**, 052502 (2003).

[93] G. Gabrielse, Adv. At. Mol. Opt. Phys. **50**, (2005).

[94] J. P. Merrison, H. Bluhme, J. Chevallier, B. I. Deutch, P. Hvelplund, L. V. Jorgensen, H. Knudsen, M. R. Poulsen, and M. Charlton, Phys. Rev. Lett. **78**, 2728 (1997).

[95] S Bradenbrink, H Reihl, T Wormann, Z Roller-Lutz, and H O Lutz, J. Phys. B **27**, L391 (1994).

[96] Edward S. Chang, Phys. Rev. A **31**, 495 (1985).

[97] P. Schmelcher, J. Phys. B **25**, 2697 (1992).

[98] S. Bradenbrink, E. Y. Sidky, Z. RollerLutz, H. Reihl, and H. O. Lutz, Phys. Rev. A **55**, 4290 (1997).

[99] E. Surdutovich, W. E. Kauppila, C. K. Kwan, E. G. Miller, S. P. Parikh, K. A. Price, and T. S. Stein, Nuc. Inst. Meth. B **221**, 97 (2004).

[100] G. Gabrielse, in *Fundamental Symmetries*, edited by (P.Bloch, P. Paulopoulos, and eds.) R. Klapisch (Plenum, New York, 1987), pp. 59–75.

[101] T. M. Squires, P. Yesley, and G. Gabrielse, Phys. Rev. Lett. **86**, 5266 (2001).

[102] E. P. Gilson and J. Fajans, Phys. Rev. Lett. **90**, 015001 (2003).

[103] William H. Wing, Progr. Quant. Electr. **8**, 181 (1984).

[104] Harold J. Metcalf and Peter van der Straten, *Laser Cooling and Trapping* (Springer, New York, 1999).

[105] Y. V. Gott, M. S. Ioffe, and V. G. Tel'kovskii, Nuc. Fusion 1962 Suppl. Pt. **3**, 1045 (1962).

[106] D. E. Pritchard, Phys. Rev. Lett. **51**, 1336 (1983).

[107] M. Amoretti, G. Bettega, F. Cavaliere, M. Cavenago, F. De Luca, R. Pozzoli, and M. Rome, Rev. Sci. Instrum. **74**, 3991 (2003).

[108] E. Gilson and J. Fajans, in *Non-neutral Plasma Physics IV*, edited by F. Anderegg, L. Schweikhard, and C. F. Driscoll (AIP, New York, 2002), Vol. 606, p. 378.

[109] E. Gilson, Ph.D. thesis, University of California at Berkeley, 2001.

[110] A. A. Galeev and R. Z. Sagdeev, Sov. Phys. JETP **26**, 233 (1968).

[111] T. M. ONeil, Phys. Fluids **26**, 2128 (1983).

[112] K. Halbach, Nuc. Inst. Meth. **169**, 1 (1980).

[113] G. Gabrielse, Adv. At. Mol. Opt. Phys. **45**, 1 (2001).

[114] S. X. Hu and L. A. Collins, Phys. Rev. A **69**, 041402(R) (2004).

[115] R. Parrott, Ph.D. thesis, Harvard University, to be published.

[116] R Development Core Team, *R: A language and environment for statistical computing*, R Foundation for Statistical Computing, Vienna, Austria, 2004, 3-900051-07-0.